Non-Invasive Vaccination by Nanoparticle-based Messenger RNA (mRNA) Delivery via the Transfollicular Route

Dissertation

zur Erlangung des Grades
des Doktors der Naturwissenschaften
der Naturwissenschaftlich-Technischen Fakultät
der Universität des Saarlandes

von
Hanzey Yasar

Saarbrücken
2018

Tag des Kolloquiums:	08. April 2019
Dekan:	Prof. Dr. Guido Kickelbick
Berichterstatter:	Prof. Dr. Claus-Michael Lehr
	Prof. Dr. Alexandra K. Kiemer
Vorsitz:	Prof. Dr. Anna K. H. Hirsch
Akademischer Mitarbeiter:	Dr. Stefan Böttcher

Die vorliegende Arbeit wurde vom Dezember 2014 bis September 2018 unter der Leitung von Herrn Prof. Dr. Claus-Michael Lehr am Institut für Pharmazeutische Technologie der Universität des Saarlandes und Helmholtz-Institut für Pharmazeutische Forschung Saarland (HIPS) in der Abteilung für Wirkstoff-Transport angefertigt.

„Wer ganz gerichtet ist auf eine einseitige Betrachtung der Erscheinungswelt,
wird durch die tiefe Einseitigkeit der wissenschaftlichen Bildung geblendet.
Er erkennt nicht mehr, daß nicht die Erscheinungen selbst die Wahrheit sind,
sondern das hinter ihnen liegende Leben;
solches Wissen wird dann zu einem Halbwissen,
weil es von der Erkenntnis der höchsten Wahrheit, des Ewigen, abführt.“

- Platon (427 – 348 v. Chr.)

Table of Contents

I. Short Summary

In search for alternative strategies to replace the traditionally used syringe and needle for vaccine administrations and to overcome related disadvantages, the non-invasive approach using nanoparticles (NPs) via the transfollicular route appeared as a promising method to improve patient compliance.

As a cargo for NPs, mRNA gained remarkable attention, carrying genetic information of different antigens, proteins or peptides. Hence, the thesis presents a detailed characterization of the mechanistic behind NP-penetration into hair follicles and NP-cellular internalization. Furthermore, advanced delivery systems for mRNA delivery using pharmaceutical safe excipients were designed and mRNA complexed NPs were explored for their potential to efficiently transfect immune cells.

In vitro transfection studies in dendritic cells revealed a high transgene expression rate of approx. 80% for novel developed lipid-polymer nanoparticles (LPNs) when compared to an established polymeric system made of PLGA with a chitosan surface coating (CS-PLGA NPs).

Based on such encouraging *in vitro* results, mRNA encoding the influenza antigen hemagglutinin was loaded onto the LPNs and further characterized for their potential to induce effective immunity in *in vivo* adoptive transfer experiments using HA-transgenic mouse. However, the lack of the expected immune response in this model indicated several challenges related to transfollicular mRNA-vaccination and consequently demand optimization strategies for this administration site to pursue such non-invasive antigen delivery in the future.

II. Kurze Zusammenfassung

Alternative Strategien zum Ersatz von Spritzen und Nadeln bei Vakzinierungen würden die damit verbundenen Nachteile beseitigen und somit die Patienten-Compliance verbessern. Der nicht-invasive Ansatz unter Zuhilfenahme von Nanopartikeln (NPs) über die transfollikuläre Route hat sich als eine vielversprechende Methode dafür gezeigt.

Der Benutzung von mRNAs als Cargo für Nanopartikel kam eine beachtliche Aufmerksamkeit zu, da eine solche Technologie erlaubt unterschiedliche genetische Informationen von Antigenen, Proteinen und Peptiden zu transportieren. Diese Arbeit zeigt die Entwicklung optimierter mRNA-Trägersysteme, basierend auf pharmazeutisch sicher einzustufender Hilfsstoffe und beschreibt das Potenzial der mRNA beladenen NPs Immunzellen zu transfizieren. *In vitro* Transfektionsstudien in dendritischen Zellen zeigten eine hohe Transgen-Expressionsrate von ~80% für ein neuentwickeltes Lipid-Polymer-Hybrid NP-System (LPNs) verglichen mit einem etablierten NP-System bestehend aus PLGA und einer Chitosan Beschichtung (CS-PLGA NPs).

Ausgehend von diesen ermutigenden *in vitro* Ergebnissen wurden die LPNs mit einer mRNA beladen, die für das Influenza-Antigen Hämagglutinin kodiert und anschließend auf ihre Effektivität hin, eine Immunantwort in einem adaptiven Transferexperiment im Mäusemodell zu stimulieren, analysiert. Im Tiermodel konnte keine zufriedenstellende Immunantwort durch die transfollikuläre mRNA-basierte Vakzinierung hervorgerufen werden, was einer weiteren Optimierung dieser Administrationsroute bedarf um einen nicht-invasiven Antigen-Transport zu erlauben.

III. Abbreviations

%EE ..... *Encapsulation efficiency*
A549 ..... *Human alveolar epithelial cell line*
anCP ..... *Anionic core polyplexes*
APC ..... *Antigen presenting cell*
cCP ..... *Cationic-coated polyplexes*
c-di-AMP ..... bis-(3′,5′)-cyclic dimeric adenosine monophosphate
CFBE41o- ..... *Cystic fibrosis cell line*
CLSM ..... *Confocal laser scanning microscopy*
CP ..... *Core polyplexes*
CS ..... *Chitosan*
CS-PLGA NPs ..... *Chitosan-coated PLGA nanoparticles*
DCs ..... *Dendritic cells*
DiD ..... *1,1'-dioctadecyl-3,3,3',3'-tetramethylindodicarbocyanine perchlorate*
DOTAP *1,2-dioleoyl-3-trimethylammonium-propane*
DOTMA ..... *1, 2-di-O-octadecenyl-3-trimethylammonium propane*
FA ..... *Fluoresceinamine*
HA ..... *Hemagglutinin*
HaCaT ..... *Human keratinocyte cell line*
HBSS ..... *Hanks's Balanced Salt Solution*
LCs ..... *Langerhans cells*
LPNs ..... *Lipid-polymer hybrid nanoparticles*
MHC ..... *Major histocompatibility complex*
MMR ..... *Mannose receptor*
moDCs ..... *Monocyte-derived dendritic cells*
mRNA ..... *Messenger RNA*
mRNA:NP-systems ..... *mRNA complexed nanoparticle systems*
mRNA-HA ..... *mRNA enconding hemagglutinin*
MTT)-assay ..... *3-(4,5-dimethylthiazol-2-yl)-2,5-diphenyltetrazolium bromide assay*
M_w ..... *Molecular weight*
NPs ..... *Nanoparticles*
OVA ..... *Ovalbumin*

PBMC ..... *Peripheral mononuclear blood cells*
PDI ..... *Polydispersity index*
pDNA ..... *Plasmide DNA*
PLGA ..... *Poly(lactic-co-glycolic acid*)
PTA ..... *Phosphotungstic acid*
RNase ..... *Ribonuclease*
SC ..... *Stratum corneum*
SEM ..... *Scanning electron microscopy*
TEM ..... *Transmission electron microscopy*
TF ..... *Transfollicular route*
TPEM ..... *Two-photon excitation microscopy*

1 General Introduction

1.1 Transfollicular and Mucosal Vaccination: State of the Art

Vaccination is one of the important achievements in human history to prevent and fight infectious diseases risking the lives of millions of people each year. For over 150 years, syringes and needles (fine enough to prick the skin) have been commonly used for vaccine administration, a method associated with disadvantages concerning the lack of patient compliance, safety issues evoked from needle-stick accidents or needle reuse, logistic constraints and needle phobia [1–3]. To meet these challenges and supersede the needle-usage, a variety of different needle-free methods have been engineered by using two major application pathways, the mucosal route and the transcutaneous route, both considered as attractive target sites for eliciting effective immunity (**Figure 1**).

Transfollicular Route

The skin as the biggest organ of the human body represents the body's first line of defense to protect the body against pathogens, environmental stress factors, and toxic agents. This protective barrier function is related to the outermost "dead" layer of the skin, the stratum corneum (SC). The SC is a tough, hydrophobic and impermeable barrier and therefore represents a major challenge for drug delivery purposes. However, as a route of administration the skin is advantageous due to its easy accessibility, acceptability by patients and the prevention of obstacles associated with other routes (e.g. oral route). Until recently, the transcutaneous route appeared to be only attainable for a group of relatively small active substances with hydrophobic nature and beneficial physicochemical properties. As such, the skin itself comprises three different pathways for transcutaneous application: the transcellular, paracellular and transfollicular route [4]. While the trans- and paracellular pathways have been widely considered as the most relevant penetration routes, the transfollicular route (TF), which involves hair follicle and sebaceous gland was thought to play only a limited role for skin drug delivery [4–6]. Indeed, the TF-route has to cope with certain obstacles, as the drugs need to traverse the keratinocyte layers surrounding the hair

shaft in order to reach the epidermis and subsequently enter the circulation. This fact, along with the relatively small skin area occupied by only 0.1% of hair follicles, raised the assumption that this administration route is unworthy for future investigations [4, 7]. Therefore, a spectrum of novel strategies to facilitate drug penetration into the skin barrier in a minimally invasive manner have been adopted such as microneedles [8–10], electroporation [11, 12], jet and laser injectors [13, 14] (**Figure 1).**

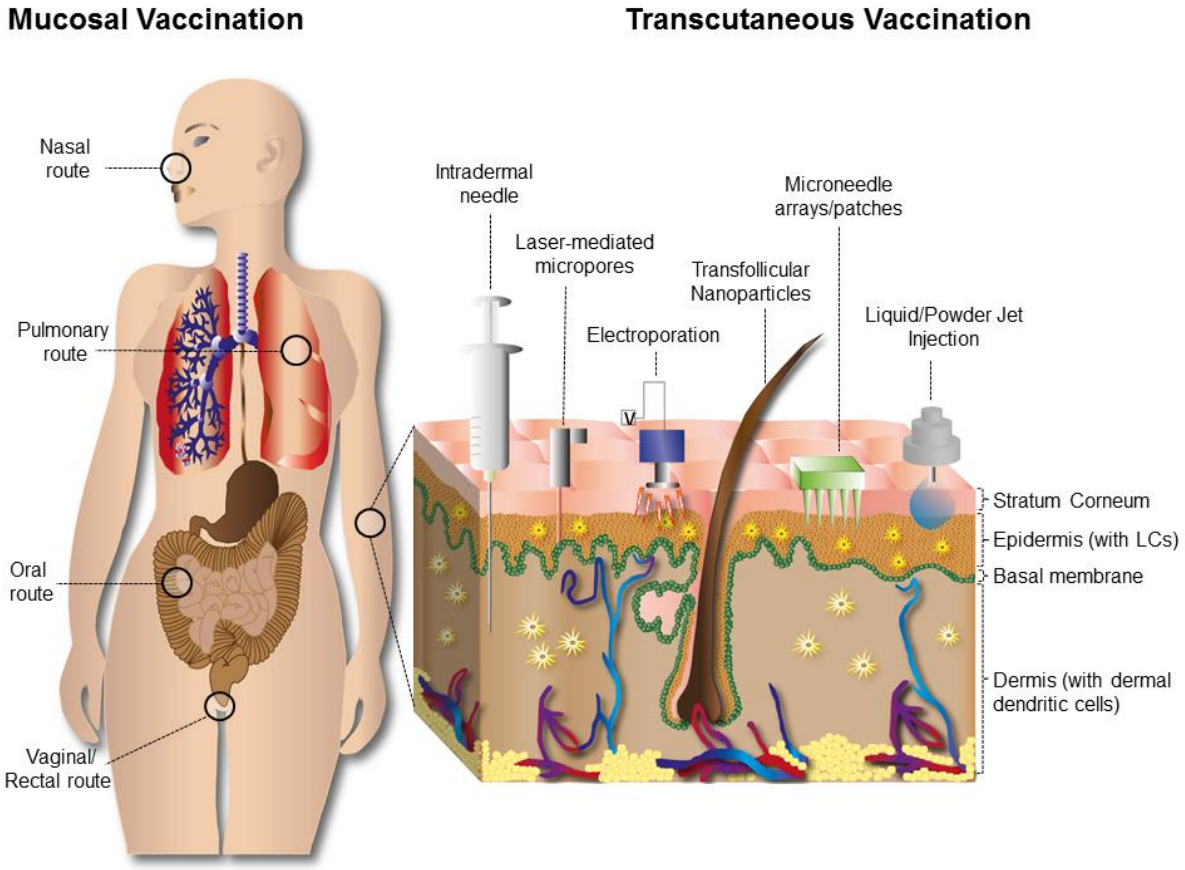

Figure 1: Schematic illustration for vaccination via the mucosal and transcutaneous route. Mucosal vaccination aims the application of vaccines through the nasal, pulmonary, oral and vaginal/rectal route. Transcutaneous vaccination comprises a variety of different strategies to deliver vaccines to the epidermal Langerhans Cells (LCs) and dermal dendritic cells with minimal impairment of the protective stratum corneum barrier. Courtesy of the Helmholtz Center for Infection Research (HZI) of Public Relations, Guzman C.A, Lehr C.-M, Gordon S. Loretz B. Schulze, K. Yasar H. “Perspectives of non-invasive vaccine Delivery” HZI Research Report 2014/15, p. 63-65.

Nevertheless, these techniques still rely on breaking or impeding the SC barrier, which makes them suboptimal for mass vaccination campaigns under critical sanitary conditions [15]. With the perspective to overcome this drawback of compromising the SC barrier, the follicular route (across the hair follicles) has recently received attention as a bypass option for drug delivery using nanoparticulate systems (nanoparticles, NPs) [16]. First studies examining the TF-route started by using liposomes in regards to their similarity with the properties of the sebaceous gland [17, 18]. However, significant progress in this field has been achieved with the growing impact of nanotechnology in cosmetics and drug delivery, particularly through toxicological studies of titanium dioxide (TiO_2) microparticles (blocks UV radiation) in sunscreens [19]. These studies revealed that most of the TiO_2 particles remained on the skin. However a small amount penetrated and accumulated in the hair follicles, indicating the potential of the hair follicle to enable drug delivery into the skin [19]. Further studies showed that particulate delivery systems accumulate in the hair follicle in a size-dependent manner and facilitate a considerable depot [20], also with the perspective to enhance this depot-effect by optimizing the design of such the particles [21].

Pollen grains as micron-sized particles [22] and microorganism [23] are also able to use the TF-route, which is why the skin represents an immunologically active site promising for vaccination [24]. Especially around the hair follicles, the skin displays an abundancy of antigen presenting cells (APCs) such as dermal dendritic cells (DCs) and Langerhans cells (LCs), crucial for antigen processing and presentation and hence important to induce effective immunity [25–27]. The existence of skin-related immune cells together with the potential of drug delivery using particulate systems through the hair follicles raised the hypothesis to use the TF-route for vaccine delivery. To facilitate vaccine penetration into the skin, pre-treatment of the skin using either cyanoacrylate stripping of the skin surface, waxing or plucking seemed to be beneficial and was applied in earlier studies. Even though skin stripping increases the permeability of the SC barrier, it also results in a stress stimulus and causes a non-specific immunomodulation [15, 28, 29].

Stripping still represents an invasive method. Therefore, a feasible non-invasive alternative without compromising the SC barrier would improve patient comfort and compliance. Ideally, such method would only involve some gentle massage to apply the particles onto the skin (**Figure 2**) without any chemical or mechanical pre-

treatment and might therefore be considered as truly non-invasive. In this context, NPs appeared as attractive vaccine delivery systems. They are small colloidal materials capable to transport different active agents to desired sites of the body and can be easily adapted regarding physiological conditions (e.g. pH-value). Thus, NPs can be developed in variable sizes and morphology, surface modification and charge depending on the biomedical target site. Vaccine antigens comprising proteins, peptides, and nucleic acids represent biological entities that are challenging to handle due to their instability, internalization behavior by the target system and moreover their antigenicity. Hence, the encapsulation of those vaccine antigens into the NPs can prevent these problematics [15].

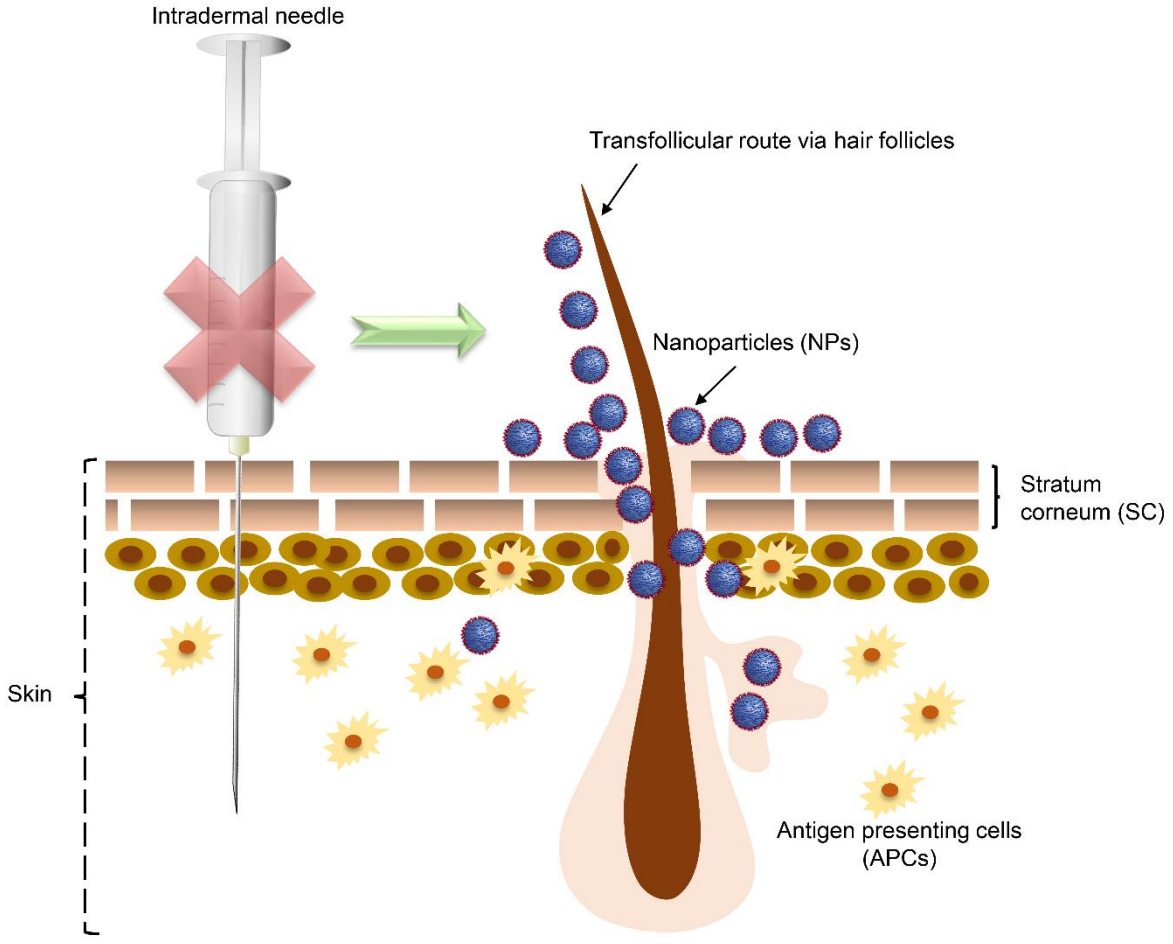

Figure 2: Non-invasive approach for vaccination using NPs. To supersede the use of intradermal needles, nanoparticles (NPs) applied via the transfollicular route appeared as a promising alternative without compromising the stratum corneum layer. Due to their small size, NPs are able to migrate across the hair follicles inside the skin structure and interact with antigen presenting cells (APCs).

NPs can improve antigen stability, protect them from the biological environment, improve cellular-internalization and tune the release profile. Baleeiero *et al*. [30] used silicon dioxide (SiO_2) particles loaded with an antigen and applied them onto the skin prior to massaging. Following this application, particles were able to penetrate into the hair follicles and were internalized by the perifollicular APCs.

Nevertheless, Mathes *et al.* [31] described the existence of tight junctions, which form an additional barrier within the hair follicles, preventing NPs from deeper penetration through the hair follicles and thus hampering their further uptake into the blood circulation. This observation demands the development of potent NP-systems for drug delivery via the hair follicles.

The materials used to design NPs as vaccine-delivery vehicles must strictly follow the requirements of the biomedical and pharmaceutical field, in order to avoid any adverse effects related with the formulation. To meet the challenges of NP-application as delivery vehicles, the used materials therefore need to be safe, biocompatible, biodegradable, and manufactured in an environmentally friendly manner [32]. Recently, a variety of different polymeric materials obtained from natural resources has been formulated as vehicles to deliver vaccine components. These vaccine components can either be encapsulated inside the polymeric matrix or coated on the colloidal surface [33] by electrostatic or chemical complexation [32]. Among these polymers, the pharmaceutical well characterized and “generally regarded as safe” (GRAS) proven net anionic charged polymer, poly(lactic-co-glycolic acid) (PLGA; Resomer® RG 503H, 50:50) with sustained release properties and the net cationic charged polysaccharide chitosan (CS) appeared as attractive materials and have been widely investigated for drug and nucleic acid delivery [34, 35].

Inspired by their properties Mittal *et al.* [2, 36] developed PLGA NPs and surface coated them with CS according to [37], which resulted in CS-PLGA NPs. Both NPs were produced using a modified double emulsion method, further stabilized by polyvinyl alcohol (PVA) and pursued for the non-invasive approach to NP-administration onto the skin without any pre-treatment measures to test the potential for transfollicular vaccine delivery. *Ex vivo* studies in excised pig ear and *in vivo* studies

on human forearm, revealed that anionic charged PLGA NPs were found in a higher amount within the hair follicles when compared to cationic CS-PLGA NPs [38]. However, when both NPs were used to encapsulate the model antigen ovalbumin (OVA) and characterized in an *in vivo* adoptive transfer experiment using OVA-specific mice, both OVA-loaded NPs exhibited a higher extent of follicular localization compared to OVA applied as a solution [2]. An *in vitro* adoptive transfer experiment further revealed the potency of CS-PLGA NPs to first stimulate APCs and further induce both CD4+ and CD8+, while PLGA NPs only stimulated CD4+ T cell proliferation [2]. Nevertheless, a higher extent of follicular localization of OVA was found when delivered by both NPs in comparison to OVA-solution [2]. A subsequent co-administration of the adjuvant bis-(3′,5′)-cyclic dimeric adenosine monophosphate (c-di-AMP) with the NPs on intact skin generated the highest IgG titer and moreover a balanced IgG subclass ratio (IgG1/IgG2c), hence a balanced cellular and humoral immune response, when compared to prior tested formulations [36]. Optimization of the NP-system by producing inverse micellar sugar glass (IMSG) NPs allowed co-encapsulation of c-di-AMP and OVA, which enabled stimulation of an immune response right after two booster vaccinations [39].

In addition, some gene-based strategies focused on the immunization via the hair follicles, due to the presence of stem cells and lineages of dividing cells capable to internalize plasmid DNA (pDNA) and induce transgene expression [40–43]. However, the immune response of topically applied pDNA remained weak even when formulated into nanoparticulate systems [44–46].
Studies using a vaccine relevant antigen against an infectious disease using the TF-route are still lacking.

Mucosal Route

The mucosal route was considered as a further non-invasive approach delivering vaccines to mucosal membranes such as those of the vagina, rectum, lung, nose, and eye (**Figure 1**), as many pathogens enter the body through the mucosal tissues [3]. However, overcoming the mucus layer to reach the underlying tissue and further affect a local or systemic action is of widespread interest, and necessitated the investigation and optimization of NPs able to penetrate the mucus layer.

Delivery vehicles must meet certain criteria to enable drug transport through the mucus barrier. Mucus is known to be a viscoelastic gel layer (composed with a high density of cross-linked and entangled mucin fibers) with limited permeability, evolved to protect the body by fast trapping and removing foreign as well as hydrophobic substances [47]. The mucins have further sialic acid-rich glycan side-chains with net negative charge resulting in strong interaction with positively charged particles and therefore their immobilization within the mucus layer [48]. As further, the mucus layer reveals strong variations in thickness depending on the anatomical site [49], especially in a disease state such as cystic fibrosis or asthma [48], which is why the development of efficient NP-system is no small task. NPs have to possess a specific degree of hydrophilicity, should avoid adhesion to the mucin fibers and additionally need to be small enough for an unhindered passage through the mucin fibers [47]. Olmsted *et al.* [50] have first described the idea of mucus-penetrating NPs, when referring to the ability of viruses to diffuse through a mucus layer and thus studied their surface properties. The surface of many viruses can carry positive and negative charged groups in a homogeneous distribution leading to a total neutral surface charge, which presumably prevents mucus-interaction [51].

In light of these studies, it was hypothesized that neutral, small and hydrophilic NPs would cross the mucus. In order to achieve such NP-systems, NPs were functionalized with the hydrophilic and uncharged polymer polyethylene glycol (PEG), which was used as a mucoadhesive agent [47, 52, 53]. However, NP-PEGylation did not bring the desired success, as the effects strongly relied on the degree of PEG surface coverage and the length of the polymer [54]. This observation was also made for CS-PEG nanocapsules used as an oral peptide delivery system [55].

Some other particulate candidates such as PLGA NPs, starch or alginate-based microcapsules have also been characterized as vaccine delivery systems for mucosal delivery, with a strong emphasis to use PLGA due to its beneficial properties [56].

Regarding the improvement in the field of nanotechnology, gene-based therapeutics focusing on RNA interference (RNAi) gene silencing by small interfering RNAs (siRNAs) have gained strong attention for mucosal delivery. Thus, Martirosyan *et al*. [57] prepared siRNA loaded CS-NPs to cross the mucosal layer. However, gene-based strategies remain challenging with low efficiency for mucosal delivery, as the NPs first need to overcome the mucus barrier and further transfect the underlying epithelial cells to achieve successful transgene expression and hence appropriate immunity.

1.2 Messenger RNA (mRNA)-Vaccination

Traditionally administered vaccines include live attenuated (weakened versions of the pathogens), inactivated (killed pathogens) or subunit vaccines (antigenic fragments of pathogens best stimulate the immune system) to combat infectious diseases [58, 59]. However, these vaccines show several restrictions as they primarily induce humoral immunity, which is disadvantageous against pathogens able to evade the adaptive immune response and additionally not applicable for immunocompromised individuals [58, 60]. A major drawback represents their limited application against fast emerging viruses, for which rapid development and large-scale deployment of vaccines are urgently required, and further against non-infectious diseases such as cancer [60].
In the search for alternative options, gene-based vaccination came initially into the focus of research, when Wolff *et al.* [61] injected pDNA and messenger RNA (mRNA) *in vivo* into mouse skeletal muscle resulting in efficient transgene expression. Nevertheless, using mRNA as vaccines was no longer proceeded due to the abundance of present ribonucleases (RNases) in the body [62], leading to mRNA instability and inefficient *in vivo* delivery, its high innate immunogenicity [60] and additionally its net negative charge preventing passive cellular entry [63]. Thus, the biomedical field continued with DNA (particularly pDNA) or protein-based therapeutics.
Despite the promotion of DNA-based vaccination in the past decades, there are still no products approved for human application, which is likely referable to several drawbacks associated with pDNA. As such, it is considered as an unsafe method for the use in humans, as it needs to cross the nuclear envelope for efficient transgene expression, which can further lead to genomic integration and hence harmful mutations [64, 65]. This additionally results in an unpredictable pDNA-protein expression, which can be transient but also last for months [66].

Therefore, mRNA-based vaccines using either non-replicating mRNA or virally derived, self-amplifying RNA (replicon) appeared as innovative, promising and safe alternative strategies, preventing the disadvantages mentioned above of pDNA application [60, 67]. Thus, mRNA does not integrate into the host genome and avoids nuclear entry, so that the transgene expression starts within the cytoplasm, which is

known to be relatively transient and consequently induces high rates of protein expression [68]. It is therefore a favorable safe cargo, specifically for non-dividing cells such as macrophages and DCs compared to pDNA, making it a beneficial candidate for immunological applications. Non-replicating mRNA is transient since the transgene expression is limited by the mRNA life-time. Moreover, it can deliver a spectrum of different antigens, proteins, peptides or cell-signaling factors and simultaneously exhibit self-adjuvanting properties by binding to pattern-recognition receptors like TLR7, to activate the cellular arm of the immune system [69, 70].

Once the mRNA is delivered to the cytosolic compartment of phagocytic cells, the encoded antigen is translated into its native form and subsequently cleaved by proteasomes to peptide-fragments. Those fragments further enter the endoplasmic reticulum (ER) from where they are loaded onto the major histocompatibility complex class I molecules (MHC-I) [69] and presented at the cell-surface to CD8+ T [65] helper cells (Th1). It is further possible that cleaved peptide-fragments can bind onto MHC class II molecules (MHC-II) and moreover presented to CD4+ T helper cells (Th2) and induce specific B-cell activation [65]. Protein or peptide-based vaccines lack this mRNA-based advantages, but contrarily they do not need to escape from the endosomes to be presented on MHC-II [69].

To benefit from mRNA-related advantages, several technologies were applied to improve the intracellular and extracellular mRNA-stability and enable the use of mRNA as cargo. The intracellular stability and therefore the subsequent translation was enhanced by structural modification on the 5’ cap analogue, the poly(A) tail and untranslated regions (UTRs) of the mRNA [71, 72]. A strategy for extracellular mRNA-stability was encapsulation of mRNA within delivery systems such as viral or non-viral vectors to enable mRNA-protection under physiological conditions. Viral vectors were initially preferred regarding their natural efficiency to transport nucleic acids, but adversely showed limitations associated with a higher immunogenic effect, production-related difficulties [69] and vector-size limitations. Thus, non-viral vectors comprising liposomes, polymeric or inorganic NPs appeared to be ideal carrier systems. Despite their lower immunogenicity over viral vectors, they contrarily revealed lower transfection rates and hence need an appropriate optimization for an efficient mRNA-transport to the intracellular compartment.

1.3 Nanoparticles as Non-Viral Vehicles to Deliver mRNA

The achievements in Nanotechnology gave rise upon the engineering and design of suitable nanoparticulate systems and thereby replaced traditional viral vectors. In light of these advances, a broad-spectrum of biomaterial-based NP-systems comprised of lipids (liposomes) [73–76] and polymers or polysaccharides (e.g. CS-PLGA NPs, starch-based polymer complexes termed as polyplexes) [77–80] were manufactured for mRNA-delivery, with both having a cationic surface potential enabling facile complexation to anionic mRNA (**Figure 3**).

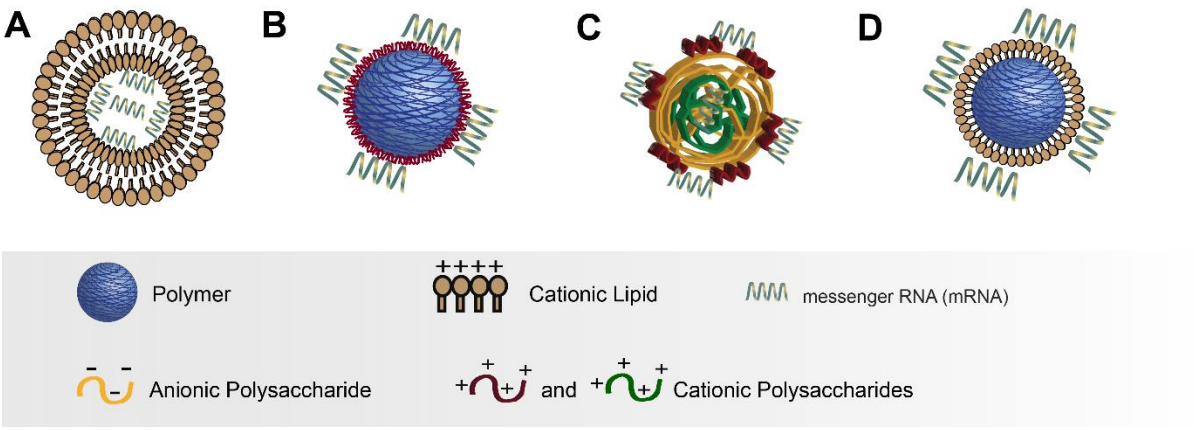

Figure 3: Selected examples of main groups for non-viral delivery of mRNA. (**A**) Lipid-based (liposomes) (**B**) polymer-based, (**C**) coacervates (polymer complexes; polyplexes) and (**D**) lipid-polymer hybrid nanoparticles (NPs).

The driving force leading to the formation of such nanoplexes is always based on the electrostatic interaction of an anionic polynucleotide and the cationic NP (**Figure 4 A**), which is either realized by the cationic head group of the lipid or the cationic amine group of the polymer as we described previously [32, 81]. Furthermore, complexation of mRNA onto the surface of nanoparticles has several advantages, as this procedure protects the mRNA from being exposed to harsh conditions during NP-production and additionally protects against RNases. As further, Su *et al*. [82] hypothesized beneficial release-kinetics of surface-loaded mRNA with a fast release upon certain physiological triggers compared to encapsulated mRNA and increased stability when compared to naked mRNA.

Despite the significant progress attained by these approaches *in vivo* and *in vitro* [63, 82, 83], appropriate NP-systems with high transfection rate and at the same time reduced cytotoxicity [84] remain crucial for mRNA-delivery. Cartiera *et al*. [85] studied the uptake-pathway of NP-systems and observed a strong co-localization of polymeric PLGA NPs within the endosomal compartment suggesting an uptake-mechanism via endocytosis.

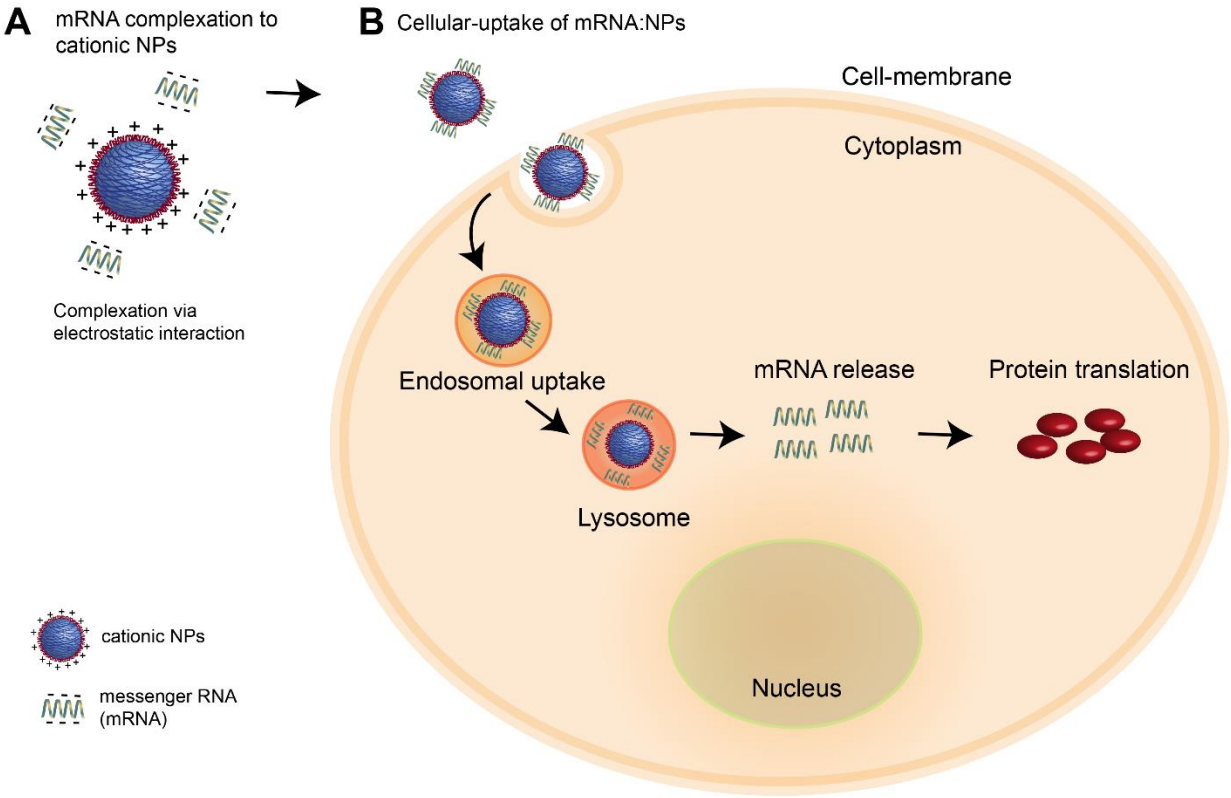

Figure 4: Cationic NPs complexed with mRNA internalized into cells. (**A**) Complexation of net anionic mRNA onto the surface of cationic NPs via electrostatic interaction. (**B**) mRNA complexed NPs (mRNA:NPs) are uptaken by cells using the endosomal pathway and finally released from the lysosomes followed by the translation of the encoding protein.

This further makes mRNA-delivery challenging since the particulate system needs to preserve functionality while transporting the mRNA through subcellular compartments. As such, the NP-systems need to overcome the cellular membrane to enable efficient cellular-uptake and further preserve the functionality of the mRNA in the acidic

conditions of the lysosomes. The NP-systems also need to escape from the lysosomal compartment and allow sufficient mRNA-release with subsequent protein translation within the cytoplasm (**Figure 4 B**).

It has been proposed that polymeric transfection systems with good pH-buffering capacity – a process known as “proton sponge effect”- play an important role in achieving a successful endosomal escape [86]. Hence, this property of transfection systems has to be taken under consideration when developing new carrier systems. Among the common mRNA-delivery systems, a new class of NPs entered the focus of research that combines the favorable features of both, lipids and polymers [87]. This new class is termed as lipid-polymer hybrid NPs (LPNs). LPNs were originally carried out as vehicles for siRNA [88–92] and pDNA [93, 94], whereas their use as vehicles for mRNA only recently started to be conducted in investigations. They usually consist of a negatively charged polymeric core surrounded by a shell of positively charged lipids. Jensen *et al.* [92] designed LPNs for siRNA-delivery by using PLGA as the polymeric-core and 1,2-dioleoyl-3-trimethylammonium-propane (DOTAP supplemented with the helper lipid 1,2-dioleoyl-sn-glycero-3-phosphoethanolamine (DOPE) as lipid-surface layer. The incorporation of helper-lipids aims to reduce agglomeration of the lipid-system and further to improve the endosomal escape [95]. As such, Su *et al*. [82] designed a phospholipid coated poly-(β-amino ester) (PBAE) hybrid system and obtained a transfection rate of up 30% tested in a dendritic cell line (DC2.4), while Perche *et al*. [96] achieved a high protein translation rate with approx. 60% using mannosylated histidylated lipoplexes. The transient translation of mRNA and hence the kinetics have been of a further focus of investigation, as the knowledge of such would aid the manufacturing of precision medicines. Therefore, first studies evaluating the mRNA transient course were described by Leonhardt et al. [78] using eGFP coded mRNA complexed with the commercially available transfection reagent Lipofectamine®. When these particles were exposed to the human alveolar epithelial cell line (A549), mRNA transgene expression reached its highest peak level shortly after 3 h of post-transfection. A similar observation was made in DCs when Stemfect® was used as transfection reagent [75]. The research field of using mRNA as cargo is fast emerging and holds strong potential for vaccination or therapeutic application. However, safe and efficient mRNA:NP-systems with detailed characterizations of the mechanistic behind the cellular-internalization and especially their translation kinetics is still missing but highly demanded for an eased enter into clinical trials.

1.4 Interaction of Nanoparticles with Immune Cells

Nanoparticles gained remarkable attention as promising and novel approaches for the treatment of various diseases, in particular where commonly applied therapeutic interventions encountered obstacles due to their low efficiency. As such, NPs have been widely studied for vaccination purposes [58], gene therapies [97], immunotherapies [98] and diagnostics [99]. However, their favorable physicochemical properties and the potential to cross biological barriers raised safety concerns upon application of nanomedicines as they may freely move throughout the body [100, 101]. It has been widely reported that NPs may cause adverse effects when entering the human body as they get inevitably in contact with human immune cells and may cause undesirable immunomodulatory effects [102, 103].

Kononenko *et al.* [101] summarized a variety of different NP-systems made of inorganic materials such as SiO_2, TiO_2 or iron oxide (Fe_2O_4) used for *in vitro* or *in vivo* studies and reported either pro- or anti-inflammatory effects, suppression of the humoral immune response, activation of the complement system or stimulation of allergic reactions. However, NPs for pharmaceutical applications should rather act as inert delivery systems with no adverse interaction with the immune system.

As further, Lunov *et al.* [104] undertook a first attempt in studying the uptake behavior of functionalized polystyrene NPs by human macrophages and monocytic cell lines. The authors concluded that the extent of NP internalization, kinetics of uptake and uptake mechanism might strongly differ between primary cells, phenotypically related tumor cell lines and differentiated tumor cells. They further reported a dependency on NP's surface charge and serum protein opsonization on these processes. As this cell line model might not be applicable on primary and differentiated cells, an adequate understanding about the NP interaction with primary immune cells and their immunological outcome is highly demanded. Therefore, human peripheral blood mononuclear cells (PBMC) were used as such models, which reflect an advanced *ex vivo* model for predicting the outcome of novel therapeutic interventions. They additionally represent the pathophysiological state of the immune cells better than tumor cell lines.

PBMC are obtained from buffy coats of blood donors using Ficoll density gradient centrifugation [105], which enables the separation between erythrocytes (red blood cells) and lymphocytes (white blood cells) further used as PBMC. They are composed of different immune cell types such as T cells (~70%), B cells (~15%), natural killer cells (NK cells; ~10%), monocytes (macrophage or dendritic cell precursor; 5%) and DCs (~2%) [106, 107]. Depending on the donor's disease state and applied treatment, the frequencies of each cell subset can significantly differ [108].

NP-systems can be internalized by cells via five different internalization routes such as phagocytosis (via mannose receptor; MMR), macropinocytosis, clathrin-mediated, caveolin-mediated and clathrin-caveolin-independent endocytosis [109]. Electrostatic interaction between some cationic nanoparticles with anionic sialic acid groups on the cell surface may facilitate their cellular-uptake. However, as T and B cells belong to the class of non-phagocytic cell types, any upcoming particulate system will be caught in the first line by the phagocytic cell types (macrophages or DCs).The MMR-mediated phagocytic pathway on macrophages leads to a more rapid uptake of charged and larger particles over smaller and neutral ones [110]. Thus, this cell type represents the first line of defense acting as a scavenger for foreign materials.

A cell-specific uptake and cell activation of monocytes isolated from PBMC was reported, when cells were exposed to silver NPs [111]. Furthermore, PBMC showed a stimulation upon treatment with TiO_2 NPs [112]. Toa *et al*. [109] used human PBMC for the characterization of NP-induced immune responses and NP-internalization behavior for their CS-coated alginate submicron vesicles. These vesicles revealed a preferential internalization by monocytes compared to non-phagocytic cell types and further induced no immuno-toxicological effect when different cell surface markers were used to quantify the activation state of these immune cells. However, adequate mechanistic information about the NPs-interaction with and the influence on human immune cells are still lacking. Especially, the interaction between the aforementioned PLGA and CS-PLGA NPs that are widely used for biomedical research and of particular interest for the intended transfollicular vaccination, and the players of the immune systems needs further investigation. This raised the question of how these charged NP-systems would interact with immune cells.

2 Aims of the Thesis

Based on the introductory part regarding the previous studies, we can conclude that NPs have shown their potential as a non-invasive approach for transfollicular vaccination without compromising the outermost protective barrier (stratum corneum) of the skin and induced an effective immune response when OVA was encapsulated as model antigen. Following up on these studies, the major aim of this thesis was the substitution of the model antigen with a vaccine-relevant antigenic fragment of the influenza virus, hemagglutinin (HA), within the NPs and stimulating a protective immune response in mouse against viral infections. To achieve this goal, two different cargos employing either the antigen hemagglutinin or a gene-based cargo using mRNA encoding for hemagglutinin were used. We herein considered the mucosal route as a back-up option for non-invasive delivery. Depending on the selected cargo and the route of administration, four different challenges had to be overcome, which are crucial for the success and application of the NP-based vaccination strategies:

(i) Preparation of NPs based on pharmaceutical safe excipients and their further characterization regarding physicochemical properties, stability, structure and morphology

(ii) Visualization of NP-penetration along the hairs of mouse *in vivo* followed by an adequate understanding about the mechanistic behind NP-cellular internalization and NP-interaction with human tracheal mucus.

(iii) Development, optimization and characterization of novel NP-systems for nucleic acid-delivery and complexation with mRNA encoding for a reporter gene or real antigen (HA), following *in vitro* assessments in a dendritic cell line of mouse origin for mRNA encoding the reporter gene.

(iv) *In vivo* adoptive transfer experiments to evaluate the potential of mRNA-HA complexed NPs to induce an effective immune response via the TF-route and in comparison to subcutaneous route.

3 Main Findings of the Thesis

3.1 Hemagglutinin as a Vaccine Relevant Antigen

Previous studies have demonstrated that vaccines can be delivered across the intact skin without compromising the outermost SC layer by employing NP delivery systems based on pharmaceutical save excipients. For this purpose, NPs composed of the biodegradable and biocompatible polymer PLGA have been produced with and without a surface coating of the polysaccharide CS and loaded with the model antigen OVA [2, 36].

Thus, when both NP-types were tested in an *in vivo* mouse model, OVA loaded CS-PLGA NPs appeared to be more effective in inducing an immune response via the TF-route and caused similar proliferation rate of CD4+ T cells like intramuscular injection [36]. Furthermore, TF immunization elicited even a balanced humoral and cellular immune response when OVA loaded CS-PLGA NPs were co-administered with c-di-AMP as adjuvant [36]. Following optimization of the NP-system, IMSG NPs were developed, which allowed co-loading of OVA and c-di-AMP. This composition and enabled higher stability of the antigen, enhanced follicular uptake and additionally the generation of an immune response after only two booster vaccinations in mouse [39].

Impressed by such data, we therefore choose to pursue the non-invasive and needle-free TF-vaccination strategy by using the viral antigen hemagglutinin (HA) as cargo for the NP-system providing the opportunity to investigate the ability of the NP-system to stimulate protective immunity against viral infection in a clinically relevant manner.

The importance of HA for vaccination relates to its function as one of the glycoproteins on the influenza virus membrane responsible for the recognition and attachment of the virus to sialic acidreceptors on the host-cell with subsequent viral internalization [113, 114]. Thus, a vaccine containing HA as antigen would cause the production of specific neutralizing antibodies that block virus entry [114] and thereby reducing viral infectivity.

Hence we wanted to replace the model antigen OVA against the real antigen HA within the NP-system and investigate their effectivity in HA-transgenic mice in cooperation with the Department of Vaccinology and Applied Microbiology at the Helmholtz Center for Infection Research (HZI) in Braunschweig. A further collaboration was settled with the Department of Structure and Function of Proteins at the HZI to produce the HA-antigen. In that regards, HA-production was attempted following two different strategies by focusing on either the baculovirus expression system [115] or a cell-culture based system employing HEK-293 cells [116], both known to be potent in the production of recombinant proteins. However, when pursuing either method, obtaining cost-effective HA-antigen at high scales necessary for the encapsulation inside the NP-system, was unattainable concerning production-related challenges. As thus, the baculovirus system provided only little amount of 2 mg/L non-glycosylated HA, while HEK-293 cells enabled scaling up to 22 mg/L of glycosylated HA. Nevertheless, the glycosylated HA revealed a non-immunogenic effect and further induced difficulties within the purification procedure.

Therefore, the production of the HA-antigen was cancelled at this stage, which influenced the initial objective of the project. This led to a switch within the objective of the project towards nucleic acid delivery, in order to carry specific genetic information by designing appropriate NPs. However, in the first step, a profound understanding of the mechanistic processes between NP-interaction within hair follicles and further NP-cell internalization was undertaken. Subsequently, a messenger RNA (mRNA) encoding the HA-antigen (mRNA-HA) was complexed with the cationic CS-PLGA NPs (mRNA-HA:CS-PLGA NPs) and evaluated for their potential to induce an immune response during *in vivo* adoptive transfer (see chapter 3.4). As mRNA-HA:CS-PLGA NPs did not cause an immune response when applied to intact skin, an attempt was made towards optimization of the nanoparticles for nucleic acid-delivery, which will be discussed in the following chapters in more detail.

3.2 Tracing the Transfollicular and Cellular Uptake of CS-PLGA NPs

3.2.1 Designing and Characterization of Plain and Fluorescently Labeled CS-PLGA NPs

As described before NP-systems showed their potential to cross the skin barrier by penetrating into the hair follicles [20, 30, 38] and they could also effectively interact with the perifollicular antigen presenting cells (APCs) by causing an effective immune response [36]. However, less is known about NP-internalization behavior with skin cells and immune cells. Detailed knowledge regarding transfollicular and cellular uptake is crucial for future non-invasive vaccination studies via hair follicles permitting a better optimization of the NP-system for this application route. In order to visualize their penetration behavior, plain and drug-free CS-PLGA NPs were chosen within these studies, as they appeared to have a favorable safety and efficiency profile. Additionally to that, CS-PLGA NPs showed their efficiency to deliver OVA and were expected to be a suitable candidate for HA and mRNA-loading. This NP-system enables the incorporation of a variety of different fluorescence dyes within the PLGA-core important for fluorescence microscopic visualization techniques e.g. confocal laser scanning microscopy (CLSM) for *in vitro* or two-photon excitation microscopy (TPEM) for *in vivo* experiments. Two different types of dyes have been included to the NP-system and tried for the visualization studies. In the first step, plain CS-PLGA NPs have been prepared using a modified double-emulsion solvent evaporation method [2, 37, 81].

Fluorescently labeled NPs were then either prepared by chemically coupling PLGA with fluoresceinamine (FA, λ_{ext} = 490 nm and λ_{em} = 525 nm) according to Weiss *et al*. [117], or by incorporating 15 µg/20µL of a lipophilic dye, 1,1'-dioctadecyl-3,3,3',3'-tetramethylindodicarbocyanine perchlorate (DiD, λ_{ext} = 644 nm and λ_{em} = 665 nm) to the initial PLGA organic phase [36].
Produced plain (CS-PLGA) and fluorescently labeled (CS-FA-PLGA or DiD_CS-PLGA) NPs were then thoroughly characterized for their morphological shape using Transmission Electron Microscopy (TEM) or Scanning Electron Microscopy (SEM).The physicochemical properties regarding hydrodynamic size, polydispersity

index (PDI) and ζ-potential were evaluated by using dynamic light scattering (DLS). All samples for the TEM-visualization were further stained with 0.5% wt/V phosphotungstic acid (PTA) prior to visualization to improve the contrast of TEM-images [32, 48].

As the morphology [118] and physicochemical properties [84] of the NPs are crucial for their cellular performance, these parameters were taken into consideration, when exploring the follicular and cellular NPs-internalization behavior. Plain and fluorescently labeled NPs indicated a smooth and evenly shaped spherical surface morphology (**Figure 5 A - C**) and a monodisperse size distribution following a PDI of ~0.1 (**Figure 5 D**).

While all NPs reveal a non-significant hydrodynamic size of approx. ~160 nm, the ζ-potential decreased from approx. +29 mV (for plain and DiD labeled NPs) to +10 mV when PLGA was covalently coupled to the FA-dye (**Figure 5 D**). This observation may relate to the fact that FA-conjugation to the PLGA carboxyl group decreased the overall PLGA anionic charge and as the chitosan coating is mainly charged driven, a smaller quantity of chitosan could bind to the PLGA surface, resulting in the reduction of the surface charge [81].

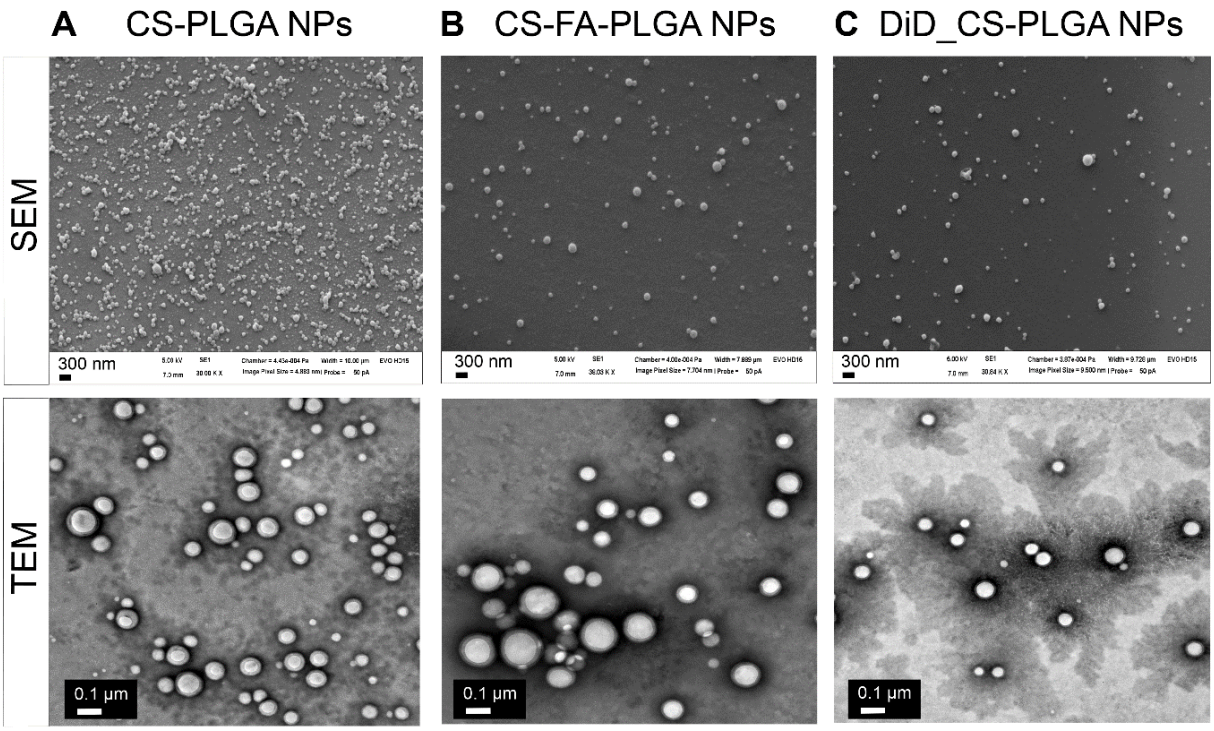

D

Nanoparticles (NPs)	Size (nm)	PDI	ζ-potential (mV)
CS-PLGA	160± 15	0.10± 0.01	+28.9± 1.2
CS-FA-PLGA	174± 6	0.09± 0.01	+10.1± 4.0
DiD_CS-PLGA	147± 16	0.12± 0.03	+29.7± 19

Figure 5: Morphological and physicochemical characteristics of plain and fluorescently labeled CS-PLGA nanoparticles (NPs). **(A – C)** Transmission Electron Microscopy (TEM) and Scanning Electron Microscopy (SEM) images indicating a spherical and evenly shaped surface morphology. **(D)** Irrespective of fluorescence labeling, all NPs reveal a similar hydrodynamic size and PDI with a cationic surface potential (ζ-potential). N = 4, mean ± SD.

3.2.2 *In Vivo* Visualization of Labeled CS-PLGA NPs in Mice using Two-Photon Excitation Microscopy

The permeation of CS-PLGA NPs into the hair follicles was visualized *in vivo* in living mice in cooperation with the Department of Vaccinology and Applied Microbiology from HZI and the Institute for Molecular and Clinical Immunology, Otto-von-Guericke-University of Magdeburg. Here, questions of how deep the NPs penetrate through hair follicle and further their distribution profile within intact skin structure (**Figure 6**) were examined.

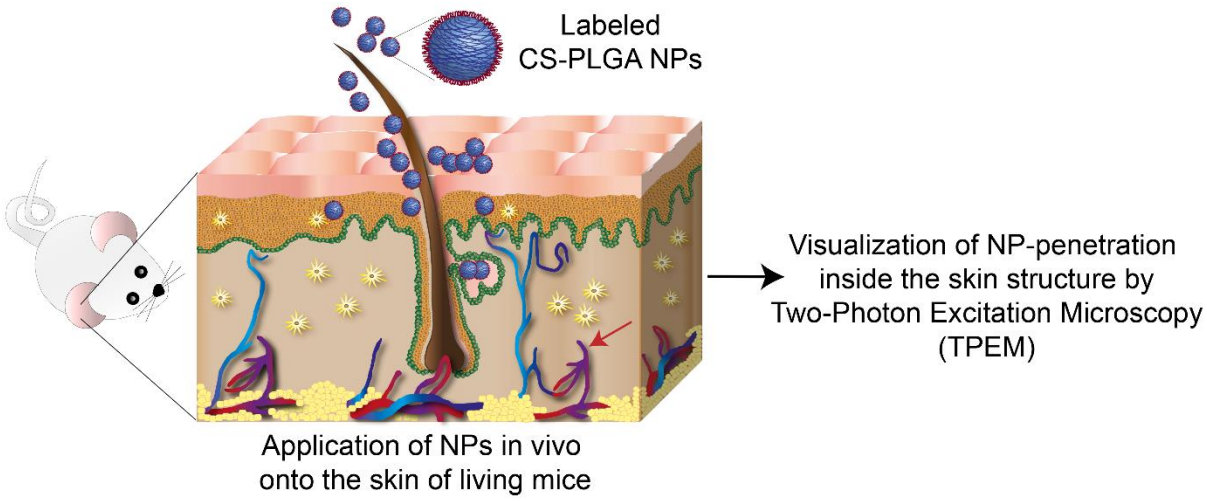

Figure 6: Schematic illustration of NP-penetration inside the skin structure. Labeled NPs were applied by gentle massaging onto the ear of living mice as application site and NP-penetration was visualized using Two-Photon Excitation Microscopy (TPEM) after 3.5 or 24 h.

The NP-permeation within the pilosebaceous unit (comprised of hair follicle and sebaceous gland [119]) was observed by Two-Photon Excitation Microscopy (TPEM), a type of non-linear microscopic technique [120] that allows the noninvasive characterization of biological samples in three dimensions with high-resolution [121]. It is an appropriate technique for the three-dimensional and deep *in vivo* visualization of cells and tissues particularly for intact thick samples (e.g. skin) as an alternative to confocal microscopy, in which the penetration-depth is limited due to out-of-focus background signal [121–123]. However, as the TPEM requires the excitation of two photons, optimal TPE-wavelength for the excitation of fluorescence dyes is obtained

by doubling the maximal excitation wavelength ($\lambda_{max/ext}$) of a single-photon [124] resulting in higher laser intensities. Consequently, a green fluorophore like FA with $\lambda_{max/ext}$ = 490 nm would have a TPE-wavelength of below 1000 nm in the infrared spectrum. However, many dyes (e.g. DiD) reveal deviation from this rule [124]. Thus, DiD, a far-red dye has a TPE-wavelength of 817 nm [125]. Furthermore, the application of higher excitation wavelengths may lead to strong autofluorescence within the biological sample, making the selection of suitable labels indispensable.

The experiments have been further conducted using C57BL/6 albino mice as the expressed melanin in the skin of C57BL/6 mouse would cause an interaction with the laser light resulting in skin burn.

In order to evaluate the extent of autofluorescence, an untreated and anesthetized mouse was placed under TPEM and the skin was excited with a laser of 850 nm. The skin was then visualized from the surface to a depth of approx. 50 µm and the obtained fluorescence microscopic images exhibit autofluorescence of a variety of different skin components (**Figure 7**). Here, the hair shaft can be recognized as a straight cylindrical shape having green autofluorescence and the keratinocytes in yellow by their characteristic polygonal shape [126].

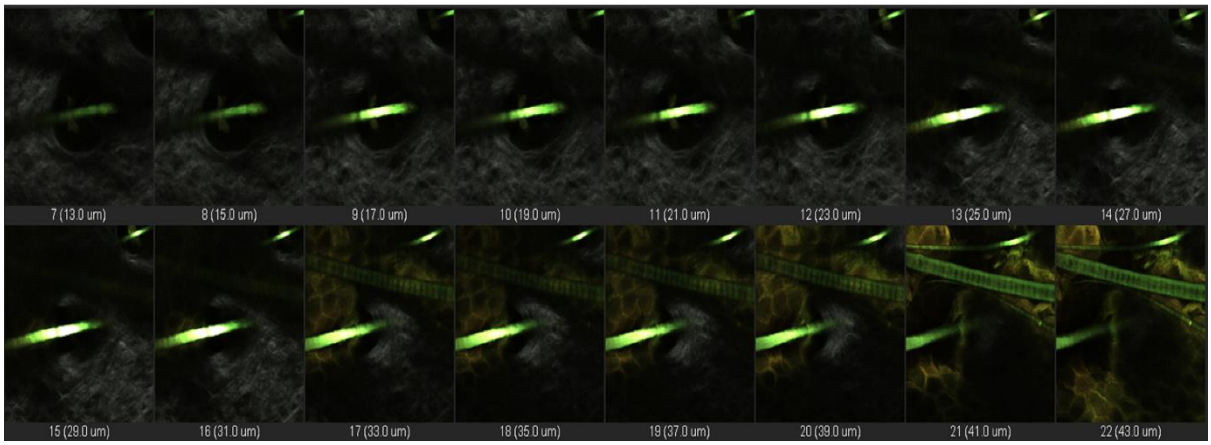

Figure 7: TPEM-images of untreated mouse skin. Thefigure shows indicate a z-stack images covering a depth of approx. 50 µm of untreated mouse skin with a TPEM-wavelength of 580 nm. Green autofluorescence represents the hair follicle and the keratinocytes of the skin can be seen in yellow. Data kindly provided by Dr. Andreas Müller and Simon Delandre.

The autofluorescence may relate to the high laser power used in TPEM [127], which emanates the excitation of endogenous chromophores in the skin structure such as flavoproteins and reduced pyridine nucleic acids [128]. As the hair shaft showed a green autofluorescence, CS-PLGA NPs labeled with the green FA-dye could not be used for the *in vivo* visualization study. Therefore, the dye was exchanged with the lipophilic dye DiD and thus DiD-labeled CS-PLGA NPs (**Figure 5**) have been further used for *in vivo* imaging. As thus, a volume of 20 µL DiD-labeled CS-PLGA NPs (2 mg/mL) was applied onto the ear of a living mouse without any pre-treatment and only by gently massaging for 2-3 min. The excess of NPs was removed afterwards, and the mouse was then placed under the TPEM microscope followed by recording the NP-penetration into the skin-structure after a predetermined time of 3.5 h or 24 h (**Figure 8**). The TPEM images clearly showed a penetration and a further accumulation of DiD-labeled CS-PLGA NPs (~150 nm) around the hair follicle 3.5 h after application (**Figure 8 A**). Deeper penetration and higher accumulation of DiD-labeled NPs was observed, when the skin was visualized after 24 h of NP-application (**Figure 8 B**). This NP-accumulation can be attributed to the creation of a depot-effect within the pilosebaceous unit, particularly favorable for various therapies, in which the encapsulated bioactive compound can benefit from the follicular reservoir to achieve the desired release profile. Previous studies discussed similar observations when TiO_2 microparticles were applied onto the skin, were a small amount penetrated as well as accumulated in the hair follicles in a size-dependent manner and facilitated a considerable depot-effect [19, 20]. The remaining of NPs within the follicular reservoir may relate to the slow clearance rate by sebum flow and hair growth [38].

When visualizing deeper skin areas, DiD-labeled CS-PLGA NPs seem to be restricted from further diffusion into the skin layer resulting in stronger localization around the keratinocytes (**Figure 8 B, lower panel**). Besides the fact that the outermost SC barrier is important for the protection of the body from external pathogens, the skin consists of so-called tight-junctions (TJs) forming a further inside-out barrier in the epidermis [129]. The existence of TJs presumably prohibited the diffusion of the applied NPs from the follicular space into the deeper viable epidermal layers. Mathes *et al.* [31] described comparable observations by characterizating the permeation behavior of polymeric nanoparticles of similar size like CS-PLGA NPs with TEM and found a distinctive NP-localization in the upper part of the HF with only a few NPs penetrating deeper into the regions of the TJ-barrier.

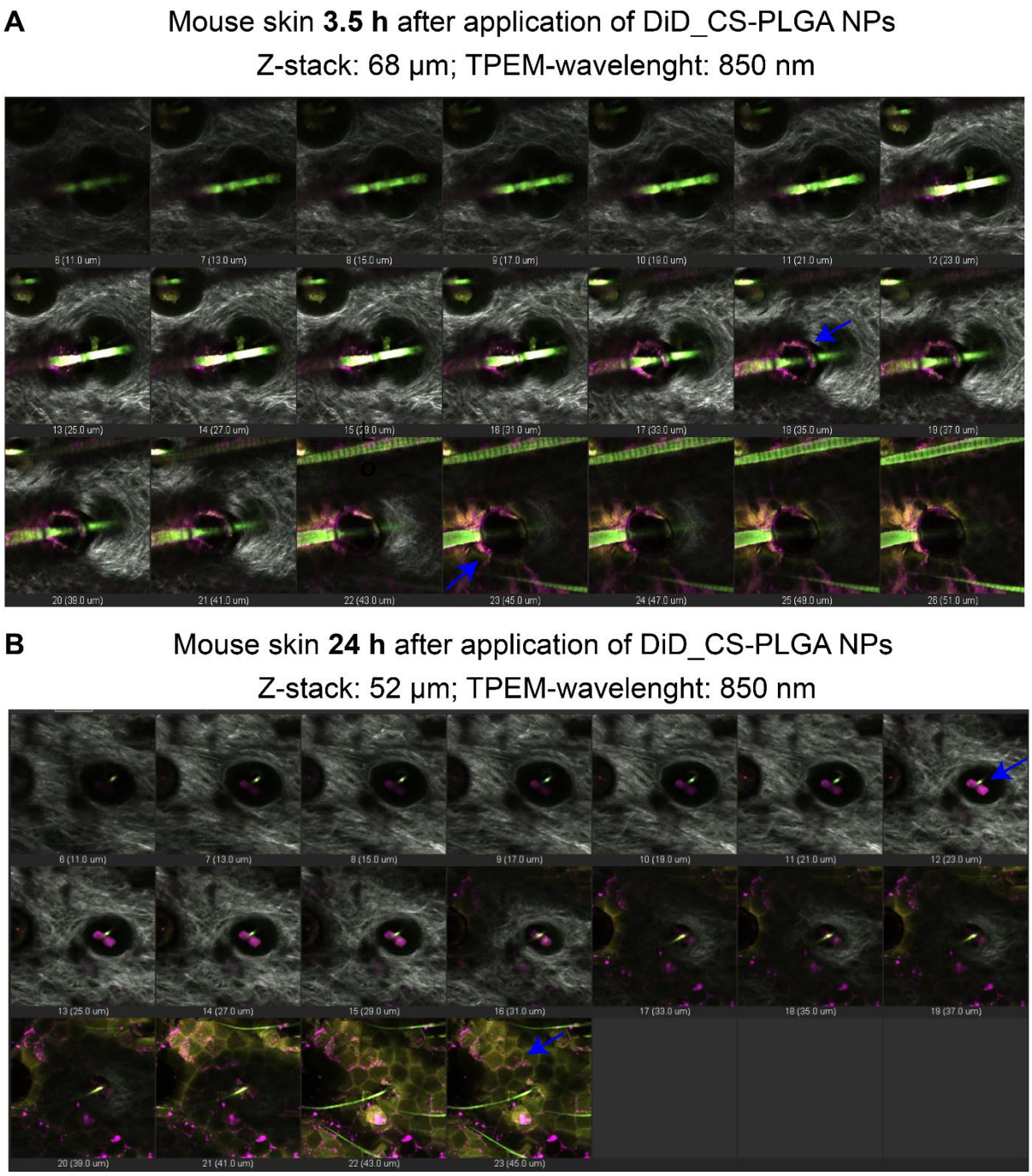

Figure 8: NP-penetration to the hair follicle and distribution behavior within the skin structure. Labeled NPs are represented in magenta and accumulate either (**A**) after 3.5 h around the hair follicle (blue arrow) or (**B**) penetrate deeper inside the skin structure after 24 h of NP-application causing a depot-effect (blue arrow in 23 µm depth). The NPs are further restricted in the diffusion through the skin as indicated by the blue arrow in the lower panel. Data kindly provided by Dr. Andreas Müller and Simon Delandre.

3.2.3 *In Vitro* Uptake Behavior of DiD labeled CS-PLGA NPs in DC2.4 and HaCaT Cell Line

Overcoming the protective SC barrier by successful permeation through the hair follicles is one of key hurdles for NPs in order reach the APCs in the epidermis via the transfollicular route [15]. Especially for mRNA-based vaccines, NPs further need to enter the cellular membrane and induce a protein expression with a subsequent presentation of protein-fragments on their surface and activation of T-cells. Therefore, this study assesses the cellular-internalization behavior of the DiD labeled CS-PLGA NPs in skin-related cells. A bone marrow derived dendritic cell line from mouse (DC2.4) as APCs and further a human keratinocyte cell line (HaCaT, non-phagocytic) were thoroughly characterized for their cytotoxicity and uptake behavior upon exposure to CS-PLGA NPs.

It is widely known that cationic NPs have a higher tendency to cause cytotoxic effects [130] based on the enhanced interaction of partially positive charged particles with the anionic charged cell membrane which also facilitates cellular uptake [131]. Thus, to ensure, that the used NP-system is safe, the cell viability of skin-related cells was determined upon exposure to plain CS-PLGA NPs for 4 h and at increasing concentrations between 10 – 160 µg/mL. A live-dead staining kit was used for DC2.4 cells, previously mentioned in Yasar *et al*. [81] and the percentage of viable cells was quantified by flow cytometry using heat-killed cells as positive control. The viability of HaCaT cells was measured as described in Yasar *et al.* [32] with a 3-(4,5-dimethylthiazol-2-yl)-2,5-diphenyltetrazolium bromide) (MTT)-assay using Triton X as a positive control. Under such conditions, both cell lines revealed high values of cell viability when exposed to plain CS-PLGA NPs even at high concentration of 160 µg/mL (**Figure 9**).

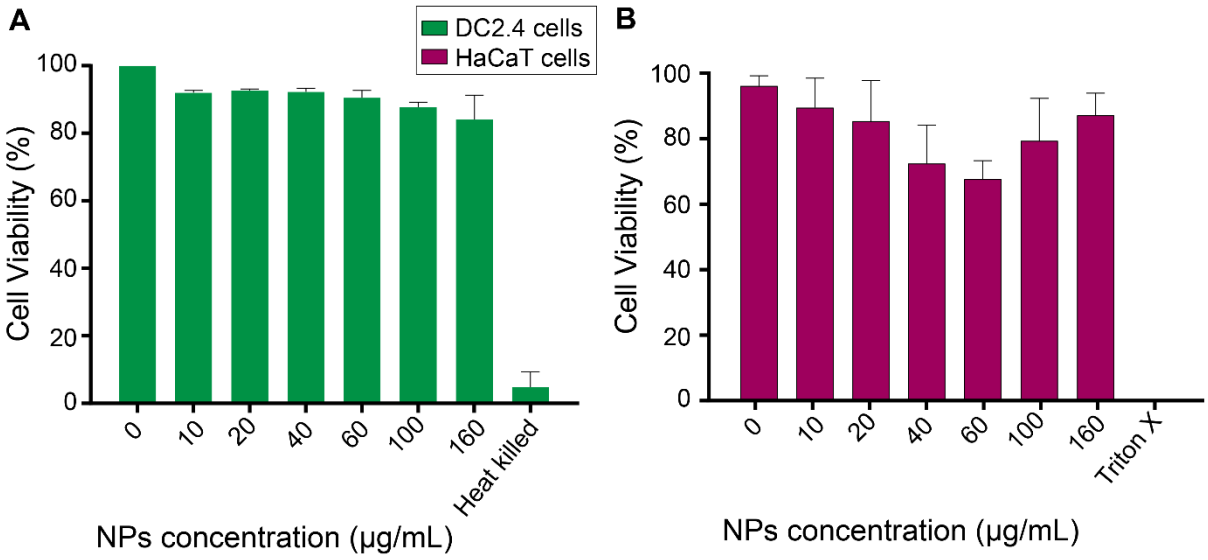

Figure 9: Cell viability of DC2.4 and HaCaT cells upon NP-exposure for 4h. Cell viability of (**A**) DC2.4 cells assayed with a live-dead staining kit and (**B**) HaCat cells by using a MTT-assay. N = 3, mean ± SD.

In order to confirm the cellular-localization of the NPs, we continued to use DiD-labeled CS-PLGA NPsat increasing concentrations (10 – 500 µg/mL) and treatedDC2.4 and HaCaT cells for 2 h at 37°C by slightly shaking. The effect of NP-internalization was quantified by flow cytometry by measuring the percentage of red fluorescent positive cells and the mean fluorescence intensity (MFI).

The dendritic cells showed a fast and significant higher internalization of fluorescently labeled NPs with ~90% positive cells for all tested concentrations above 30 µg/mL, while the keratinocytes only indicated cellular-internalization of ~40% at very high concentrations starting at 160 µg/mL (**Figure 10 A**, **B**). Fruthermore, a comparably less fluorescence shift was detected for keratinocytes (**Figure 10 C, D**). We made similar concentration-independent observations for dendritic cells when CS-PLGA NPs were fluorescently labeled with FA (CS-FA-PLGA NPs) and additionally analyzed the kinetics of cellular-internalization after 2 and 4 h of NP-incubation [81]. Here, DCs further revealed time-independent particle-uptake. This behavior of NP-internalization within the used cell lines relates to their cellular function. DCs belong to phagocytic and professional antigen presenting cells able to recognize and endocytose foreign material (pathogens), which leads to their maturation followed by a down-regulation of phagocytosis [132]. Therefore, the immature state of DCs is correlated with a higher

uptake-activity in comparison to the non-phagocytic cells [131]. The phagocytic activity and hence particle uptake is reduced after reaching a saturation state [81].

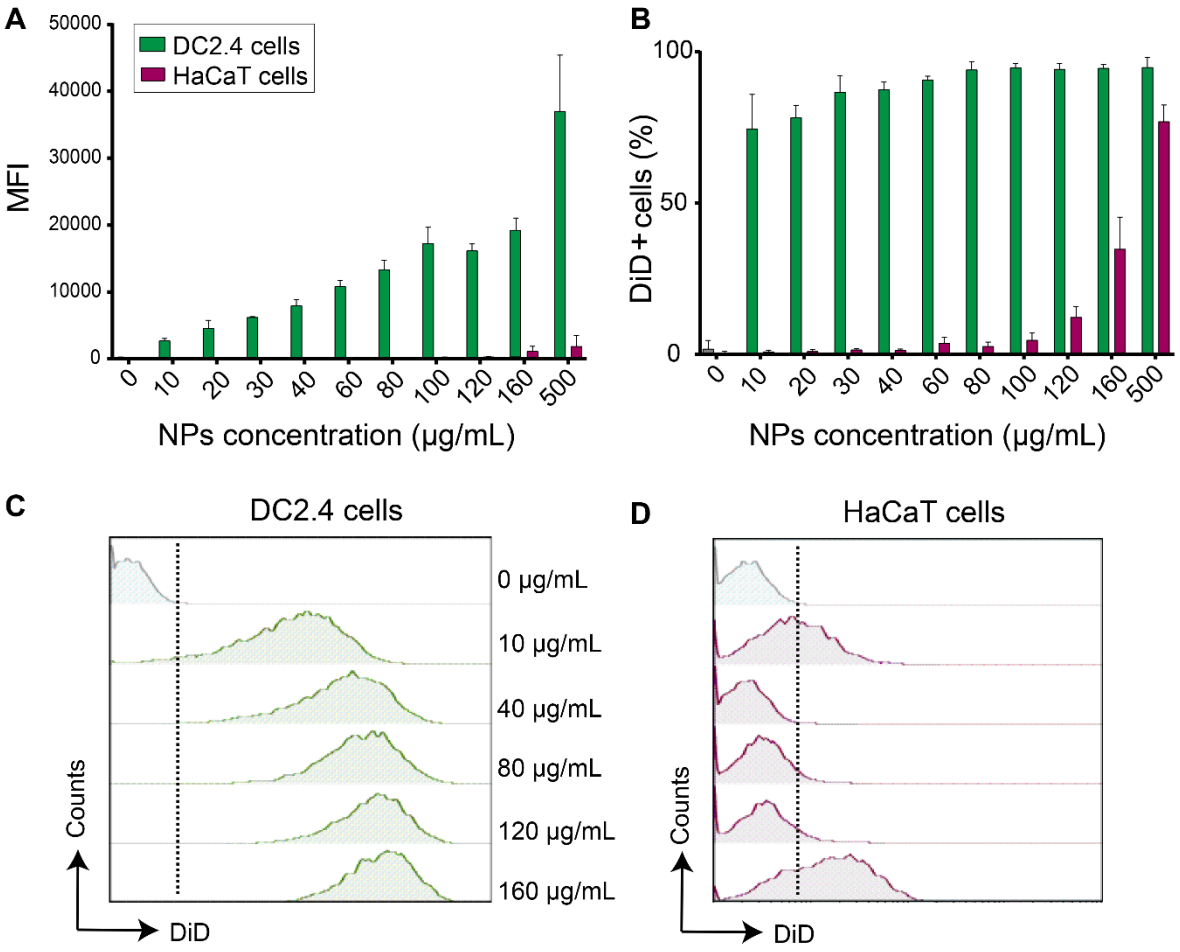

Figure 10: Cellular-association of DiD labeled CS-PLGA NPs. Fluorescently labeled CS-PLGA NPs were incubated for 2 h and quantified with flow cytometry for their cellular-internalization behavior. (**A**) Mean fluorescence intensity (MFI) upon NP-exposure at different concentrations and (**B**) DiD positive cells. Representative graphs depicting a concentration-dependent fluorescence shift for (**C**) DC2.4 cells, while (**D**) HaCaT cells only reveal a strong shift at higher concentrations. N = 3, mean ± SD.

To distinguish between cellular-association and real uptake of CS-PLGA NPs, DC2.4 and HaCaT cells were incubated with DiD_CS-PLGA NPs for 2 h at 37°C and visualized by CLSM. The NP-excess was removed and cells were washed by using Hanks's Balanced Salt Solution (HBSS-buffer, pH 7.4). Cell membranes were stained with fluoresceine labeled germ agglutinin (WGA, 10 µg/mL) linked to Alexa Fluor 488

fluorescent dye, fixed with 3% paraformaldehyde.Cell nuclei were afterwards stained with 4′,6-diamidino-2-phenylindole (DAPI, 0.1 µg/mL). Cells without any treatment were used as a control. CLSM-images were acquired with a 64x water immersion objective at 1024 x 1024 resolution and presented either a 3D or a vertical section (cross-section) across a specific region of the sample. Different image-representations were necessary for a decent assessment of NP-uptake within the cells.

After cells were washed with HBSS-buffer to remove remaining NPs, still a high amount of fluorescently labeled DiD_CS-PLGA NPs were evident in the images either strongly attached to the cell membranes or by causing a strong background signal worsen the image-quality (**Figure 11**). Thus, the internalized NPs could not be distinguished from NPs adsorbed to the cell membrane. We, therefore, used a method described by Bishop *et al.* [133], where heparin was added to the buffer and further used as the washing buffer. This method was slightly adapted for our experimental settings.

Here, DCs were exposed to labeled NPs as mentioned above for 2 h and the excess of NPs were removed by incubating the cells afterwards for 5 min (repeated twice) with cooled HBSS-buffer supplemented with heparin (100 Units/mL) followed bywashing steps with pre-warmed HBSS alone. Using cooled buffer would prevent endocytosis [133] of NPs. The obtained confocal-images with the HBSS-heparin washing method demonstrated a definite improvement (**Figure 12**) when compared to the normal treated ones (**Figure 11).** The image-quality was significantly improved, which allowed a simple differentiation between internalized and uninternalized NPs to the DCs in either represented images. The same HBSS-heparin washing method was applied to HaCaT cells after 2 h of NP-exposure (**Figure 13**). Qualitative analysis of the NP-uptake behavior with CLSM using the HBSS-heparin washing method matched with the quantitative data obtained by flow cytometry. Both methods revealed a higher NP-internalization for DCs over HaCaT cells.

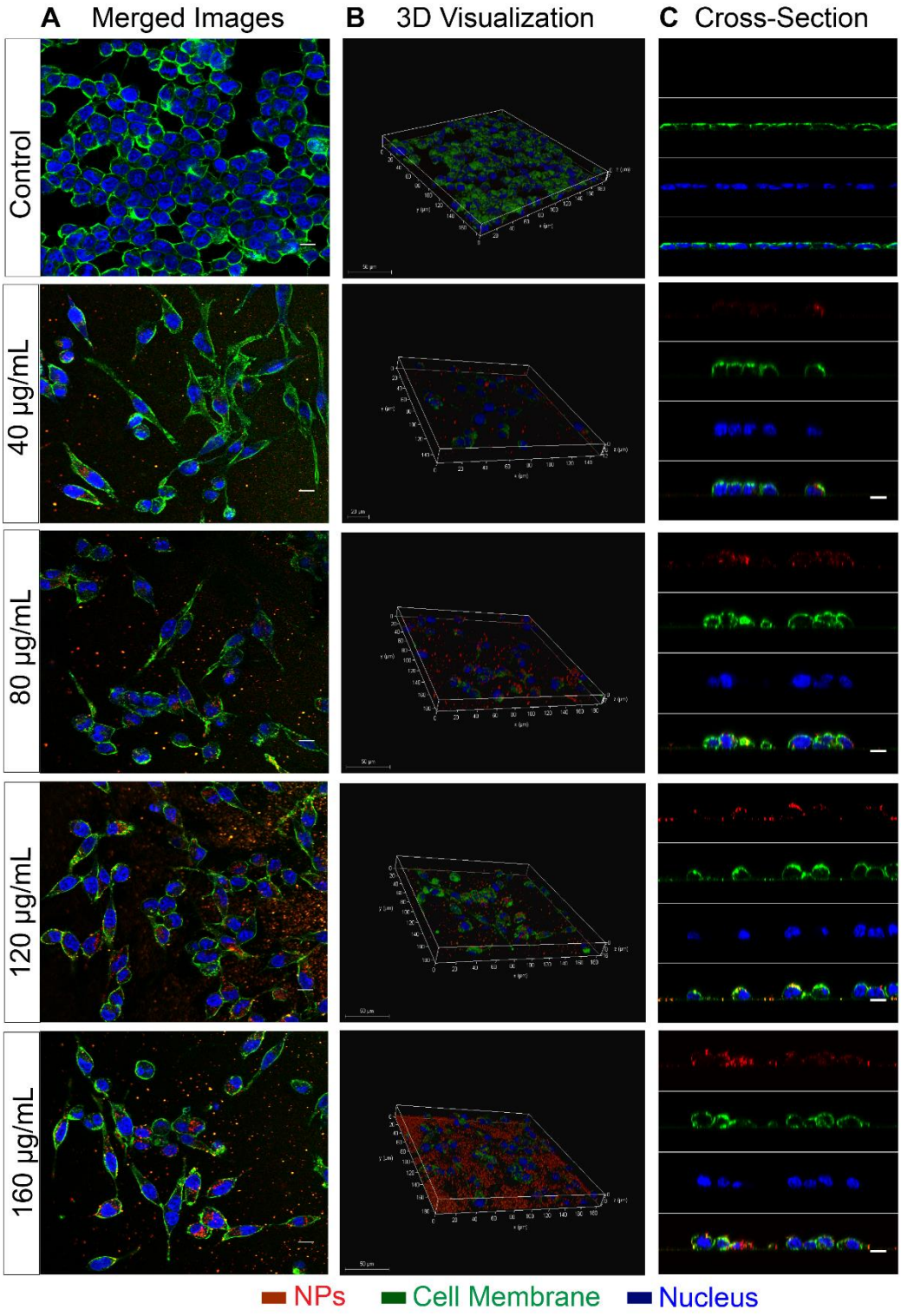

Figure 11: Representative confocal microscopy images for DC2.4 cells exposed to DiD_CS-PLGA NPs. DC2.4 cells were incubated for 2 h with labeled NPs of different concentrations (40 – 160 µg/mL) and NP-excess was removed by pre-warmed HBSS-buffer. Control images show cells without any treatment. (**A**) Merged images, (**B**) 3-dimensional (3D) visualization and (**C**) Cross-section. Scale bar 50 µm.

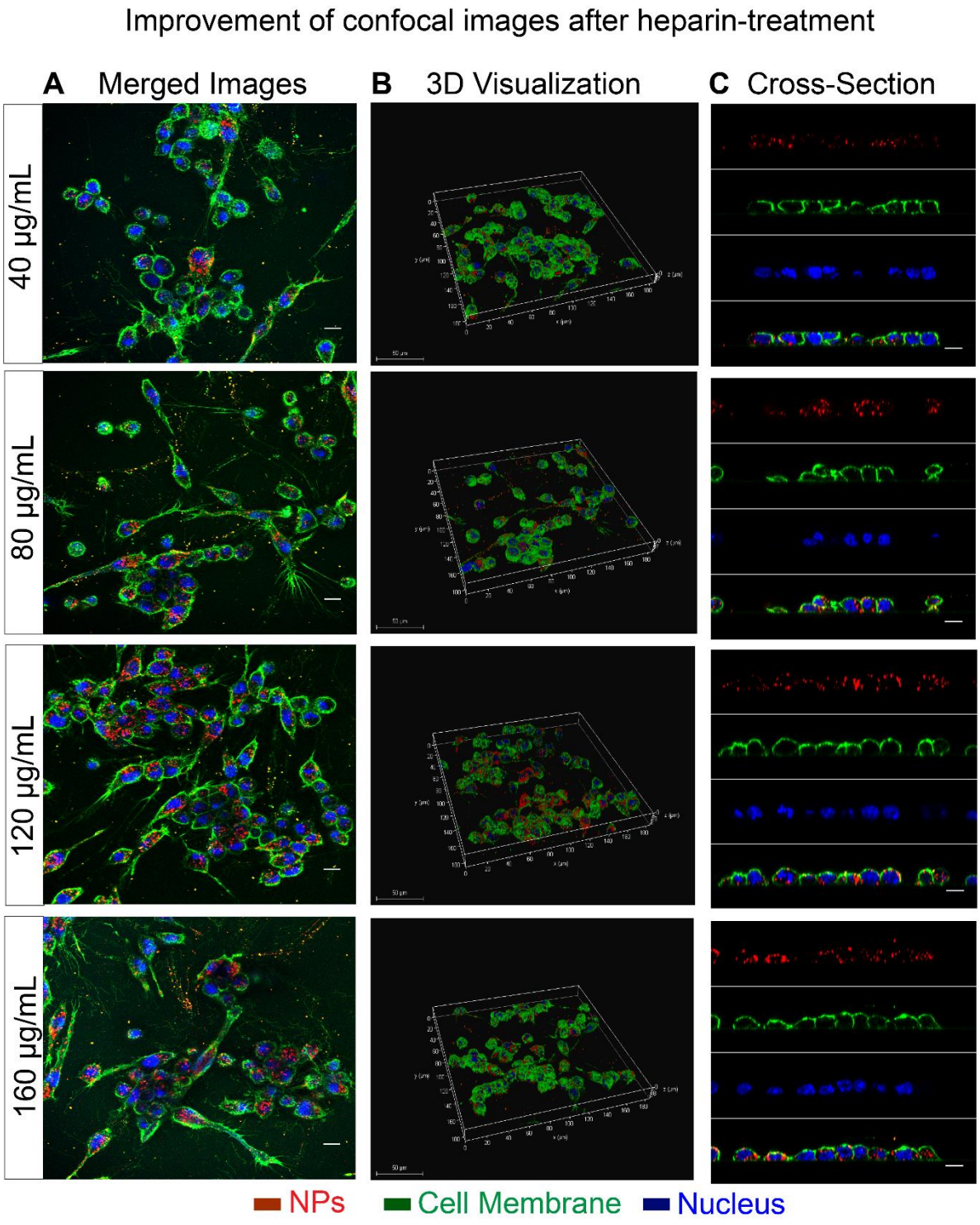

Figure 12: Representative confocal microscopy images for DC2.4 cells after treatment with the HBSS- heparin method. Using HBSS supplemented with heparin in the washing step, improved image quality and aided to the differentiation between internalized DiD_CS-PLGA NPs (applied in different concentrations) to DCs from non-internalized NPs in all images and for all tested concentration ranges. (**A**) Merged images, (**B**) 3-dimensional (3D) visualization and (**C**) Cross-section. Scale bar 50 µm.

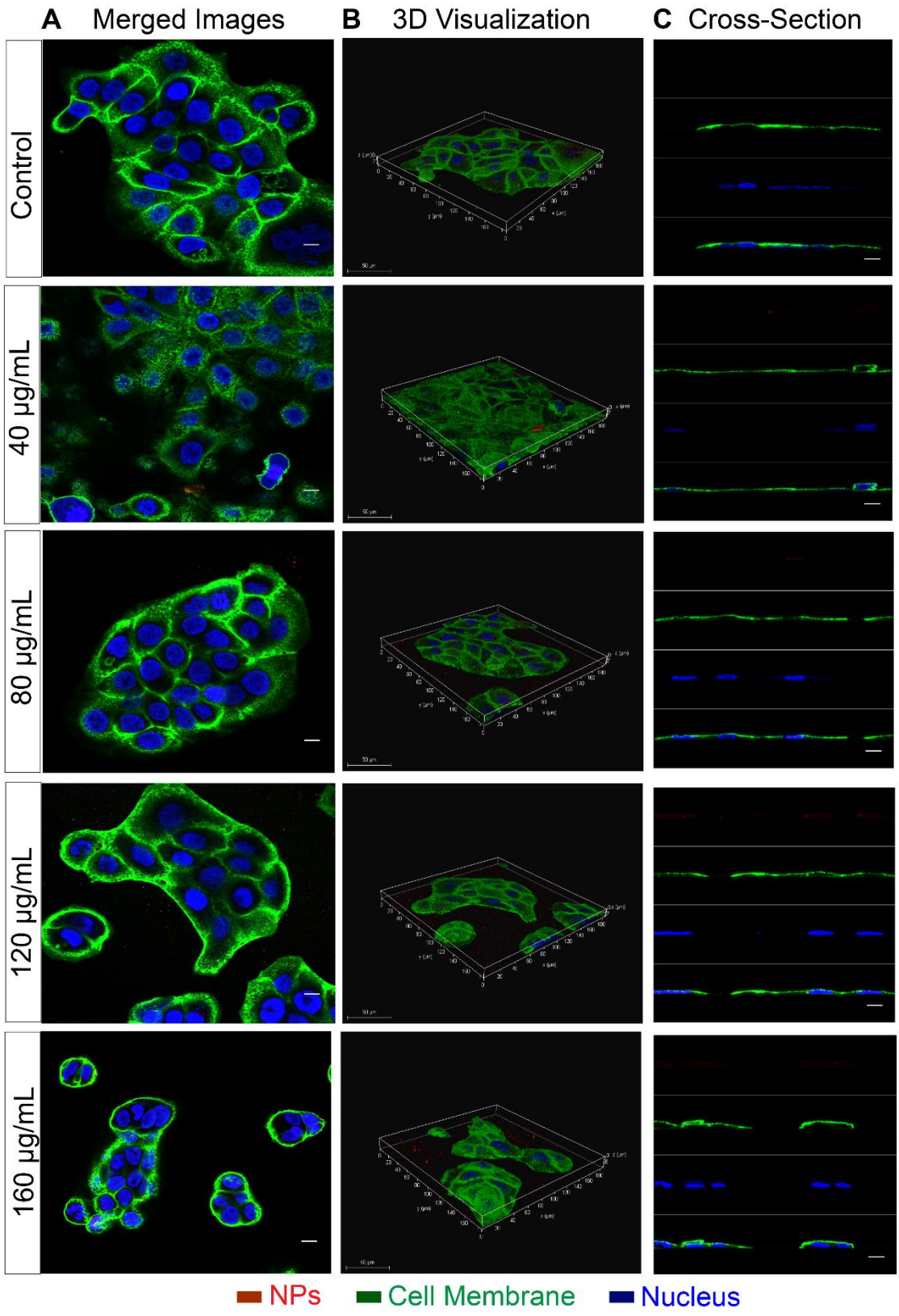

Figure 13: Representative confocal microscopy images for HaCaT cells. Cells were exposed to different concentrations of DiD labeled NPs and NP-excess was removed using HBSS-heparin in the washing step and images were obtained by CLSM. (**A**) Merged images, (**B**) 3-dimensional (3D) visualization and (**C**) Cross-section. Scale bar 50 µm.

3.2.4 Uptake Behavior of PLGA and CS-PLGA NPs in Primary Human Immune Cells from PBMC

*See also chapter 6.1, Yasar and Duran et al. (**2018**) Nanomedicine: NBM; in reply.*

The studies in section 3.2.2 and 3.2.3 ought to give an in-depth understanding about the NP cell-interaction once they enter the body and encounter cells. However, adequate knowledge about the mechanistic of cellular-internalization after topical application purposing transfollicular vaccination requires a more profound analysis of NP-effects on primary cells isolated from skin.

As the availability of fresh skin is limited, we pursued to use fresh blood from healthy donors, isolated immune cells and characterized the influence of our NPs in cooperation with the Center for Experimental and Clinical Infection Research, Twincore in Hannover.

It has been widely described that nanoparticles made of inorganic materials may cause a variety of different immune effects (e.g. activation of the complement system, anti-inflammatory effects) observed either *in vivo* or *in vitro* [101] or act as adjuvants which would be beneficial for vaccination purposes. However, in most nanomedicine particles should be employed as delivery systems for a variety of cargos, but not interact with the immune system in order to avoid any adverse immunological effects. Therefore, it is of crucial knowledge to understand the behavior of those materials on immune cells obtained from human origin to attain quick translation into clinical studies as a further perspective. Such knowledge is also important for carriers intended for vaccination, as it may affect the type of immune response and help in selection of a suitable adjuvant type and amount.

This study aimed to employ peripheral mononuclear blood cells (PBMC) from human origin as an attractive *ex vivo* model for the in-depth characterization of our drug-free NPs. We herein used two opposite charged drug-free NPs, cationic CS-PLGA NPs and anionic PLGA NPs systematically compared them with each other. Either type of NP has been previously used for transfollicular vaccination [2].

Thus, NP-internalization behavior in PBMC, intracellular fate and immunomodulating properties towards monocyte-derived dendritic cells (moDCs) were assessed by using FA- labeled PLGA and CS-PLGA NPs for the analysis with flow cytometry and CLSM. The produced anionic PLGA (PDI of ~0.01 and ζ-potential of approx. -20 mV) and cationic CS-PLGA NPs showed a narrow size distribution and a hydrodynamic size below 200 nm with spherical and smooth surface morphology.

As the physicochemical properties of nanosized materials, their morphology and aggregation behavior under physiological conditions are crucial for the NP-cell interaction [84, 91, 134], the physical stability was assessed in CellGro® cell culture and conditioned medium harvested from cultured cells. NPs were tested at different concentrations (10 – 120 µg/mL) in the appropriate medium for 2 or 4 h at 37°C. Independent from surface-potential, the NPs at 60 µg/mL remained overall stable under both medium conditions (**Figure 14**), which were also used for all *ex vivo* studies.

We then continued to analyze the kinetics of NP-internalization for both NP-types in primary human immune cells within PBMC, which were isolated by a Ficoll density gradient (**Figure 15**). As PBMC comprise a variety of immune cell types, the frequencies of each immune cell subset were first quantified by immunolabeling of PMBC with fluorescent-coupled antibodies against CD3, CD19, MHC-II, as well as CD14, and the samples were measured by flow cytometry. When single cells were selected, T cells were defined as CD3+ CD19- cells and B cells as CD19+ CD3- cells, whereas the CD3- CD19- population was further discriminated in MHC-II+ CD14+ monocytes and MHC-II+ CD14- DC. Thus, PBMC comprised ~60% T cells, ~5% B cells, ~20% monocytes, and ~15% dendritic cells (**Figure 15**).

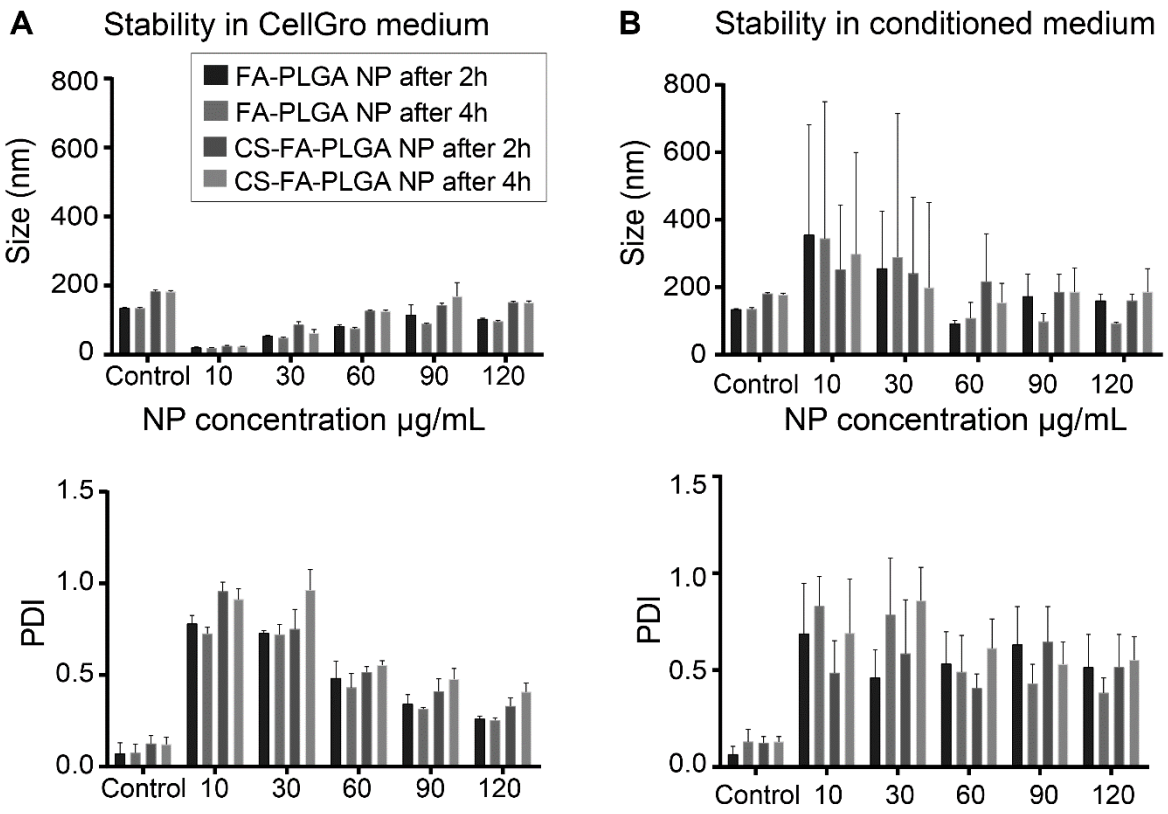

Figure 14: Physical stability of opposite charged NPs under physiological conditions. Stability test for non-labeled PLGA and CS-PLGA NPs in (**A**) CellGro® medium and (**B**) conditioned medium harvested from cultured moDCs. Hydrodynamic size and PDI were measured by DLS. N = 3, mean ± SD.

Impressively, despite the higher frequencies of lymphocytes (T cells and B cells) within the PBMC, they revealed almost no uptake when in contact with either type of NPs. Monocytes and DCs though, indicated the highest uptake with nearly 80% after 4 h of NP-exposure (**Figure 16**), indicating a preferential NP-uptake by APCs.

A similar observation has been earlier reported by Greulich *et al*. [111] where the cell-specific response of PBMC to silver nanoparticles was characterized, which showed preferential uptake in monocytes over T-cells.

Zolnik *et al*. [103] further described that NPs are often firstly captured by phagocytic cells, such as monocytes, which is comparable to our findings. Furthermore, a surface charge dependent uptake was not observed. Thus, the FA-PLGA and CS-FA-PLGA NPs showed preferential uptake by APCs even without further surface-functionalization needed for a specific cell targeting.

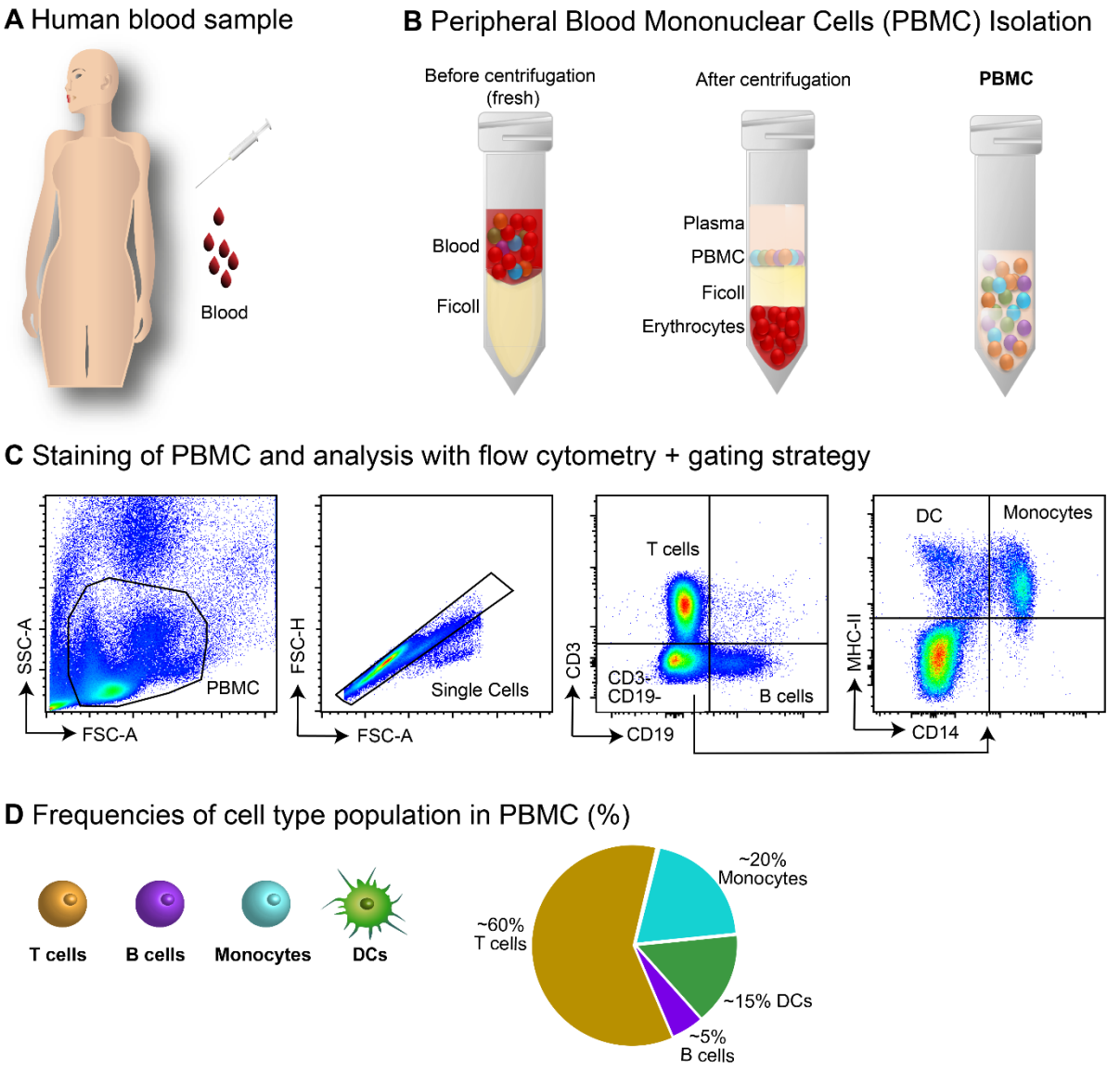

Figure 15: Human immune subsets in peripheral mononuclear blood cells (PBMC). (**A, B**) Human PBMC are isolated from blood donors using a Ficoll density gradient centrifugation. (**C**) Human PBMC were stained with fluorescent-coupled antibodies specific for CD3, CD19, MHC-II, and CD14 and T cells, B cells, monocytes and dendritic cells were each classified as indicated for one representative donor. (**D**) Frequencies of cell subsets identified within PBMC from N = 11 donors.

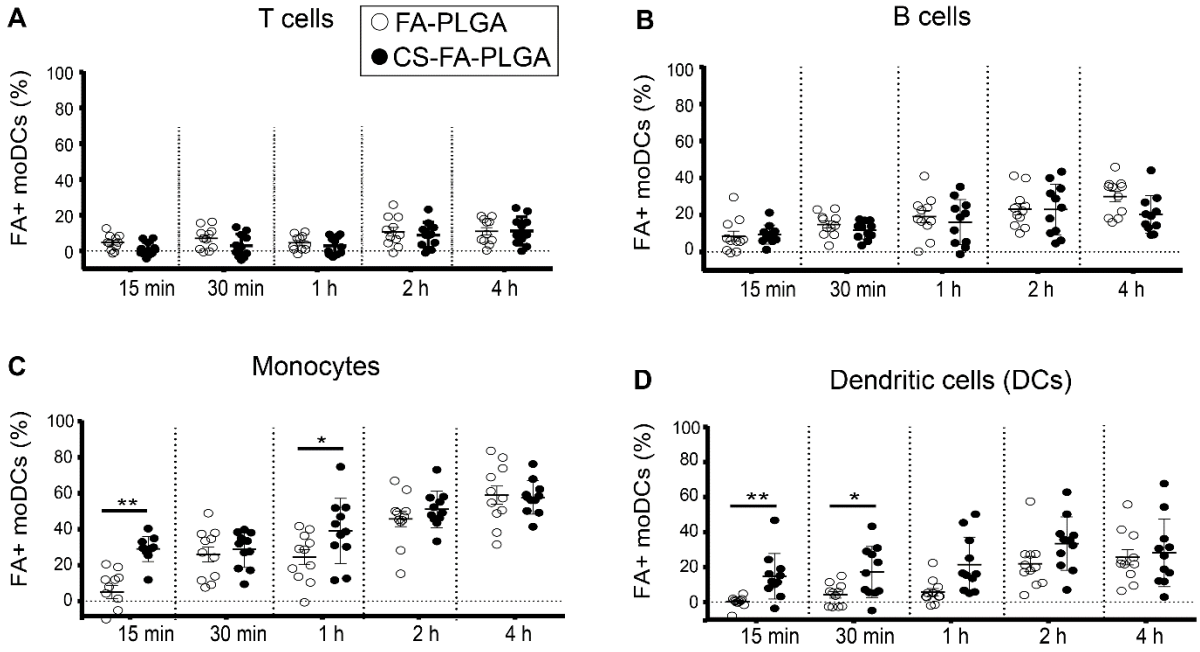

Figure 16: NP-association in PBMC subsets at 37°C. Anionic FA-PLGA and cationic CS-FA-PLGA NPs are preferentially internalized by primary human APCs. The amount NP-uptake was determined using flow cytometry by measuring the percentage of FA positive cells for (**A**) T cells, (**B**) B cells, (**C**) monocytes and (**D**) dendritic cells. N = 11, mean ± SEM (two-tailed Wilcoxon test, **p ≤0.002, *p ≤0.0322).

As both NPs-types showed similar efficient uptake in monocytes and DCs, we wanted to get a clear picture of their internalization behavior, intracellular trafficking, and immune safety profile specifically towards DCs. They represent the most professional antigen presenting cells with the capability to initiate both innate and adaptive immunity [103, 132]. Thus, CD14+ cells were isolated from PBMC by magnetic cell sorting and further differentiated into immature moDCs by using granulocyte-macrophage colony-stimulating factor (GM-CSF) as a general growth factor and interleukin-4 (IL-4) as cytokine. Cells were incubated 5 days to allow their differentiation (**Figure 17**).

We first analyzed the cell viability of moDCs exposed to different concentrations of anionic FA-PLGA and cationic CS-FA-PLGA NPs for 4 h and quantified the percentage of dead cells using a live-dead staining kit with heat-killed moDCs as a positive control.

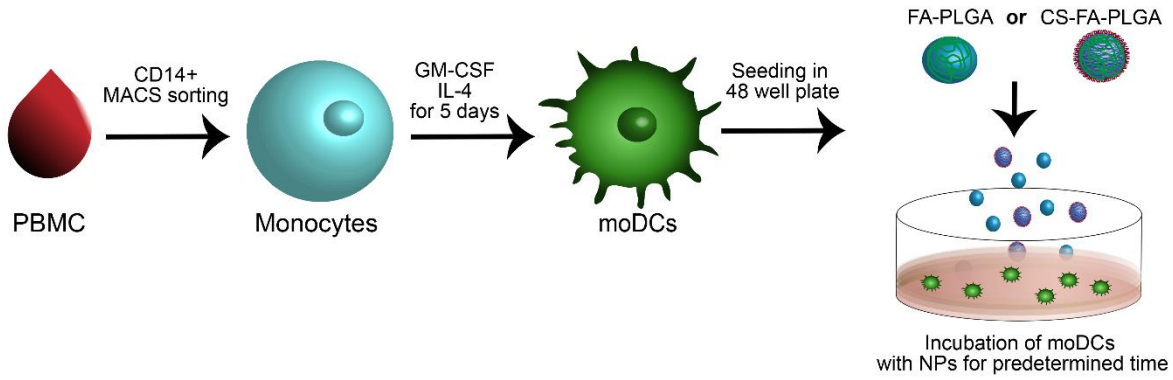

Figure 17: Differentiation of monocyte-derived DCs (moDCs) from human blood. PBMC were obtained from donors, from which the monocytes were isolated using CD14+ MACS sorting method. The isolated monocytes were further incubated with GM-CSF and IL-4 for 5 days resulting in monocyte derived dendritic cells. The moDCs were then seeded on 48 well plates and either exposed to FA-PLGA or CS-FA-PLGA NPs for predetermined time-points to characterize NP-cellular internalization behavior.

Both NP types showed a low cytotoxic effect when exposed to moDCs (**Figure 18 A**). We further characterized the kinetics of internalization by moDCs for either type of NP-system (60 µg/mL) at three different time-points. The moDCs were exposed to both types of NPs for 2, 4 or 24 h and the percentage of green fluorescent positive cells was measured by flow cytometry.

While cationic CS-PLGA NPs revealed a significant stronger fluorescence shift over the tested time-points with ~70% of fluorescence positive cells after 24 h, the anionic PLGA NPs showed a time-independent cell internalization with nearly 40% of detected positive cells (**Figure 18 B**). These results correlated with the outcome of the uptake studies performed in DC2.4 cell line [81], indicating an efficient uptake behavior of cationic CS-FA-PLGA NPs. Whereas anionic FA-PLGA NPs revealed a significantly lower uptake. This is explicable by the fact that moDCs express receptors like the mannose receptor (MMR), Dectin-1 and toll-like receptor (TLR) 2 on their surface enhancing cellular uptake [135–138] and are also associated with CS recognition. Using a CS surface coating of FA-PLGA may lead to receptor-mediated endocytosis of CS-FA-PLGA NPs in comparison to a non-specific uptake of FA-PLGA NPs.

Due to that fact, we analyzed the mechanism of uptake by studying the intracellular localization of both NP-types within moDCs, and found a higher colocalization of CS-

FA-PLGA NPs within the early and late endosomes, while FA-PLGA NPs had a tendency to localize more in the lysosomes (see chapter 6.1). These results further indicated a receptor-mediated uptake of CS-PLGA NPs.

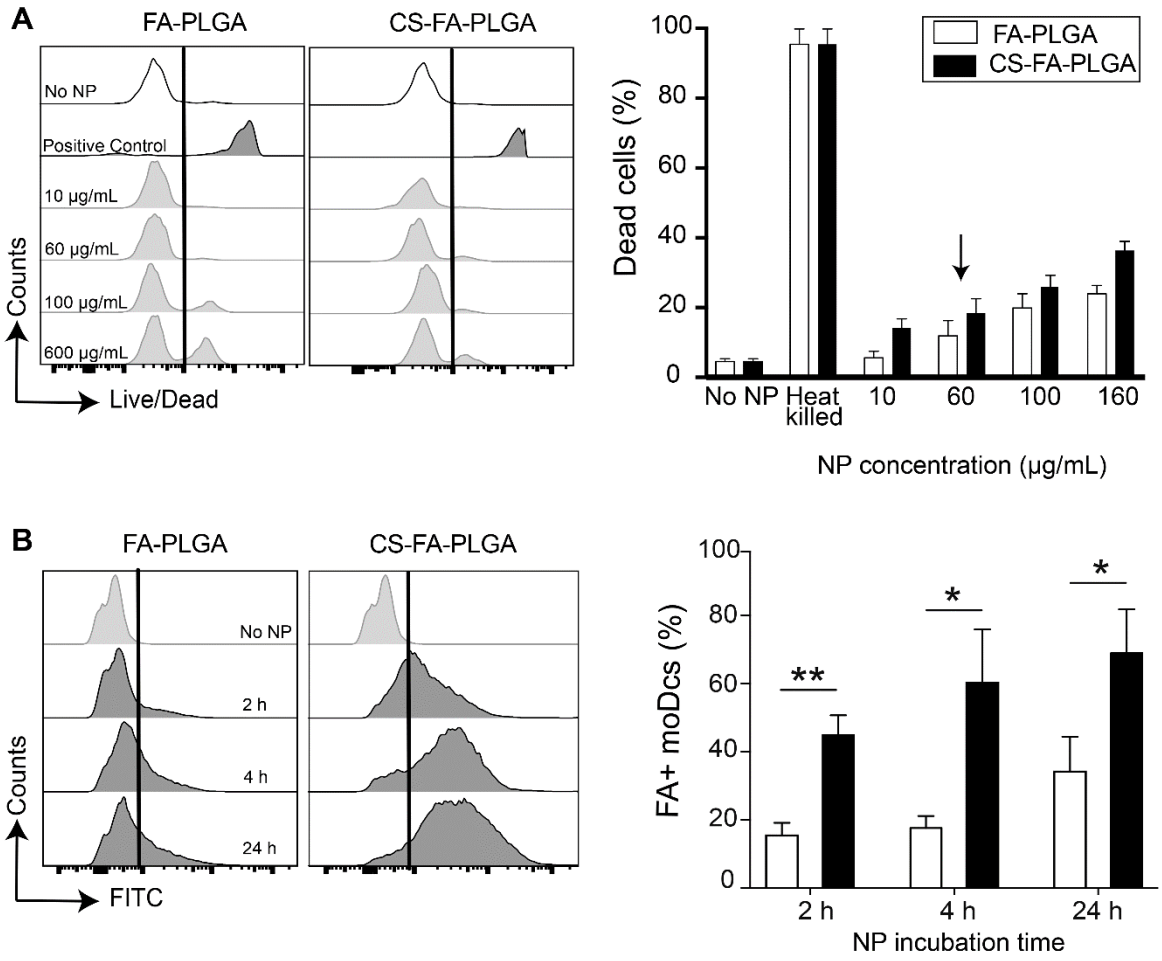

Figure 18: NP-association in moDCs. (**A**) The cytotoxicity of moDCs upon NP-exposure was assayed using a Zombie Aqua™ dye to evaluate the percentage of dead cells. Black arrow points to the used concentration. Data kindly provided by Veronica Duran. (**B**) Kinetics of NP-uptake were performed for both NP-types at different time-points. N = 3 donors, mean ± SD.

Additionally, we did not observe any immune activation of moDC according to the expression MHC-I, MHC-II, CD11c, CD86, CD40 and MMR after treatment with both types of NPs (see chapter 3.5.1). The observed up- and down-regulation of the MMR upon CS-FA PLGA-treatment may correlate with the hypothesis of Han *et al*. [138] describing the MMR as the main receptor involved in the recognition of chitosan derivatives.

These results demonstrated that the plain NPs are safe vehicles attractive for antigen-delivery preferentially to APCs, revealing an efficient uptake in APCs without immunostimulatory or -modulatory effects. With its cationic surface charge, CS-PLGA NPs would enable complexation with anionic mRNA, which is an interesting cargo to be delivered to APCs in order to ensure mRNA-based vaccination. This mRNA-based approach is the focus of the upcoming chapters.

3.3 Interaction of CS-PLGA NPs with Mucus

*See also chapter 6.2, Murgia et al. (**2017**), EJPB*

In the chapters before, we discussed how NP-delivery systems could overcome the skin (via the hair follicles) as well as cellular barriers and performed in-depth characterizations of their internalization behavior *in vivo*, *in vitro* and *ex vivo* pointing towards the application of the NPs for mRNA-based vaccination via the transfollicular route. However, the mucus barrier has been often neglected in *in vitro* studies [48] especially for the assessment of drug delivery systems aiming towards mucosal vaccination. Overcoming the mucus barrier in order to reach the underlying tissue and evoke either a local or a further systemic action is no small task.

Due to the cross-linking of mucin fibers, the mucus attains a mesh-like structure [48], in which pore-sizes are highly heterogeneous with variable size distribution [139] causing steric hindrance to NP-penetration. In the current case of mRNA delivery, overcoming the mucus layer would lead to NP-uptake by underlying epithelial cells and hence ensure their transfection. Therefore, the present study aimed among others to analyze the interaction of the previously described cationic coated CS-PLGA NPs with a novel established *in vitro* model based on the cystic fibrosis cell line CFBE41o- grown under liquid-liquid conditions with subsequent addition of freeze-dried native human mucus on the surface.

Hereby, DiD-labeled CS-PLGA NPs were used to visualize the uptake. When the NPs were exposed to naked CFBE41o- cells, a significantly higher uptake was observable in comparison to CFBE41o- cells with an additional mucus layer on the surface [48]. This observation could be explained by the fact, that our cationic CS-PLGA NPs with the size of approx. 160 nm might stuck inside the mucin fiber mesh, and could further interact with their negative charged sialic acid-rich glycan side-chains hindering the subsequent cellular uptake [48, 140]. As thus, the efficiency of our NP-system to deliver specific bioactive would be dramatically reduced for mucus-covered epithelia.

Considering the transport of mRNA to the underlying epithelial cells, mucosal delivery represents even a bigger challenge and sets the requirement to enhance our NP-system in order to cross the mucosal barrier.

3.4 mRNA-HA:CS-PLGA NPs for Transfollicular Vaccination: *In Vivo* Adoptive Transfer in HA-Transgenic Mice

The performed studies described in the previous chapters supported the comprehension about the mechanistic behind the cellular and transfollicular uptake of our cationic CS-PLGA NPs. We showed that CS-PLGA NPs were efficiently internalized into immune cells causing no adverse immunological effects. The *in vivo* data further suggested that CS-PLGA NPs were able to penetrate inside the lower hair follicle and showed signs of accumulation. These characteristics make the cationic NPs an efficient and safe delivery system for transfollicular vaccination. As we could not pursue with the idea to incorporate the HA-antigen into the NP-system, we continued with nucleic acids as cargo for our NPs and evaluated the potential of our NP-system for TF-vaccination.

Nucleic acid-based therapeutics gained strong attention as alternatives for conventional vaccine strategies using either killed pathogens, pathogen subunits or live-attenuated viruses [141, 142]. As thus, the first attempt was made using pDNA encoding a specific antigen as a vaccine component delivered by liposomes or microparticles resulting in an increased uptake of pDNA by cells [142]. However, pDNA-based delivery systems permitted low transgene expression especially in non-dividing and hard-to-transfect cells e.g. DCs and macrophages [141], which constitute an interesting target for the induction and regulation of antigen-specific immune responses. To ensure a safe and potent cargo with facilitated transgene expression, we therefore focused on the incorporation of a mRNA to the NP-system. The selected mRNA encodes the vaccine-relevant antigen hemagglutinin (mRNA-HA). In comparison to pDNA, mRNA permits unique advantages as it starts the protein translation within the cytoplasm and yields faster protein expression [60, 81].

We kindly received the mRNA-HA from CureVac-the RNA people® from Tübingen/Germany and complexed it with CS-PLGA NPs. The cationic amine group of chitosan facilitates electrostatic interaction with the anionic charged mRNA to the surface of cationic NPs [81] leading to the formation of mRNA-HA complexed CS-PLGA NPs (mRNA-HA:CS-PLGA NPs). As the mRNA-HA condensation to the particles might show limitations regarding particle-aggregation at lower mRNA-

HA:NPs ratios, conditions of these studies were chosen using mRNA:NPs weight ratios (w/w) ranging between 1:15, 1:20, 1:25 and 1:30. The mRNA-HA was post-loaded onto the surface of CS-PLGA NPs with the purpose to avoid exposing the mRNA to harsh conditions during the production procedure and fast release upon certain physiological triggers [81, 82]. mRNA-HA complexed NPs at all tested weight ratios revealed a spherical and evenly shaped surface morphology (**Figure 19 A - D)**. A drop of the ζ-potential from +31 mV for plain NPs to approx. +17 mV was observable for all mRNA-HA:CS-PLGA NPs ratios presumably due to a partially charge neutralization of cationic particles with the anionic polynucleotide [81]. The process of mRNA-loading may had raised the risk for particle-aggregation as observed for w/w of 1:15 (**Figure 19 A**) with an increased size of ~177 nm following a broader size distribution profile with the highest PDI of approx. 0.31 (**Figure 19 E**). We have made similar observations when CS-PLGA NPs were complexed with a mRNA encoding the reporter gene mCherry and showed that lower w/w ratios had a higher tendency to aggregate [81].

In the next step, we characterized the probability of the mRNA-HA complexed CS-PLG NPs to induce an immune response by *in vivo* adoptive transfer experiments using HA-transgenic mice. Thus, the ratio of 1:15 and 1:20 were tested with and without the co-administration of the adjuvant c-di-AMP via the transfollicular route and HA protein (from H1N1) plus c-di-AMP as positive control via the subcutaneous route (**Figure 20 A**). Two days before the immunization via the TF-route, mice hair were depilated using VEET cream. A dose of 5 µg of mRNA-HA was applied per mouse by gently massaging the mRNA-HA:CS-PLGA NPs. The positive control was injected subcutaneously using a dose of 2 µg of HA plus 1 µg c-di-AMP per mouse.

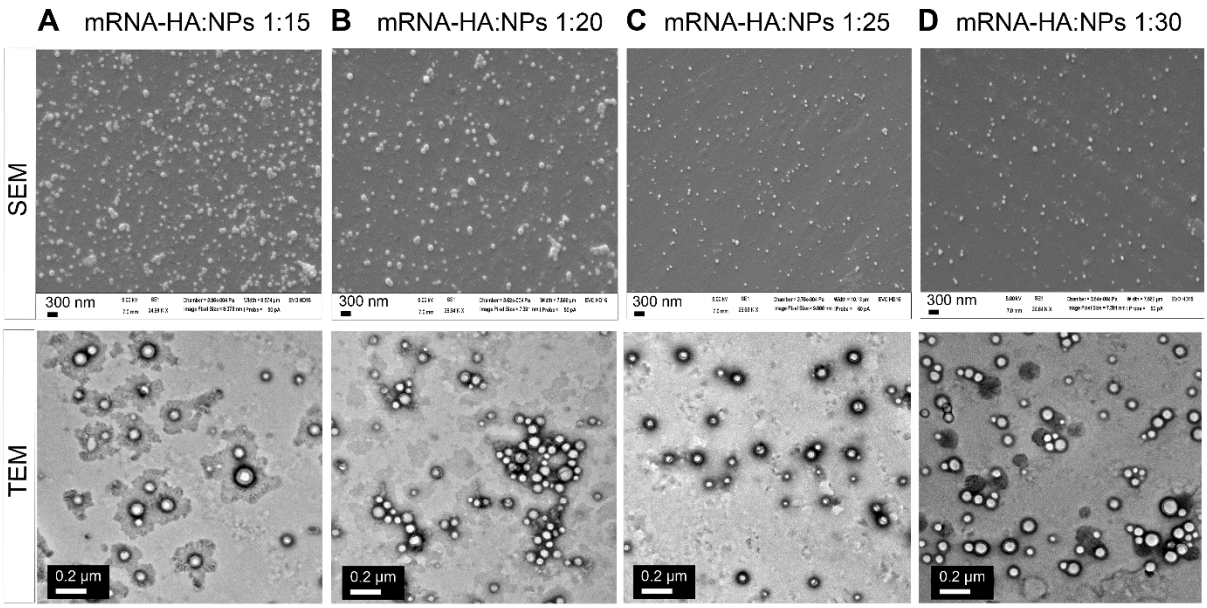

E

Nanoparticles (NPs)	mRNA-HA:NPs (w/w)	Size (nm)	PDI	ζ-potential (mV)
Plain CS-PLGA	-	138 ± 8	0.15 ± 0.01	+31.7 ± 6.3
mRNA-HA:CS-PLGA	**1:15**	**177 ± 25**	**0.31 ± 0.07**	**+15.3 ± 0.3**
mRNA-HA:CS-PLGA	**1:20**	**147 ± 3**	**0.25 ± 0.02**	**+17.1 ± 2.8**
mRNA-HA:CS-PLGA	1:25	140 ± 2	0.22 ± 0.01	+16.8 ± 0.5
mRNA-HA:CS-PLGA	1:30	139 ± 5	0.22 ± 0.03	+17.5 ± 1.0

Figure 19: Morphological appearance and colloidal properties mRNA-HA complexed CS-PLGA nanoparticles (mRNA-HA:NPs). (**A- D**) SEM and TEM-images obtained for mRNA-HA:CS-PLGA NPs at w/w ranging from 1:15 – 1:30. NPs were stained with 0.5% wt/V of PTA for TEM-images (**E**) Physicochemical properties of all tested ratios. Samples with a ratio of 1:15 and 1:20 indicated in bold were used for *in vivo* studies. n = 3, mean ± SD.

A

Groups	Nanoparticles (NPs)	mRNA:NPs (w/w)	Dose/mouse (5 µg mRNA-HA)	Route
Negative control (N = 5)	Blank CS-PLGA	-	60.0 µL	Transfollicular
Group 1 (N = 5)	mRNA-HA:CS-PLGA	1:15	42.5 µL	Transfollicular
Group 2 (N = 5)	mRNA-HA:CS-PLGA + 1 µg Adjuvant (c-di-AMP)	1:15	42.5 µL	Transfollicular
Group 3 (N = 5)	mRNA-HA:CS-PLGA	1:20	55.0 µL	Transfollicular
Group 4 (N = 5)	mRNA-HA:CS-PLGA + 1 µg Adjuvant (c-di-AMP)	1:20	55.0 µL	Transfollicular
Positive control (N = 5)	H1N1(13/164) + 1 µg Adjuvant (c-di-AMP)	-	2 µg of HA	Subcutaneous

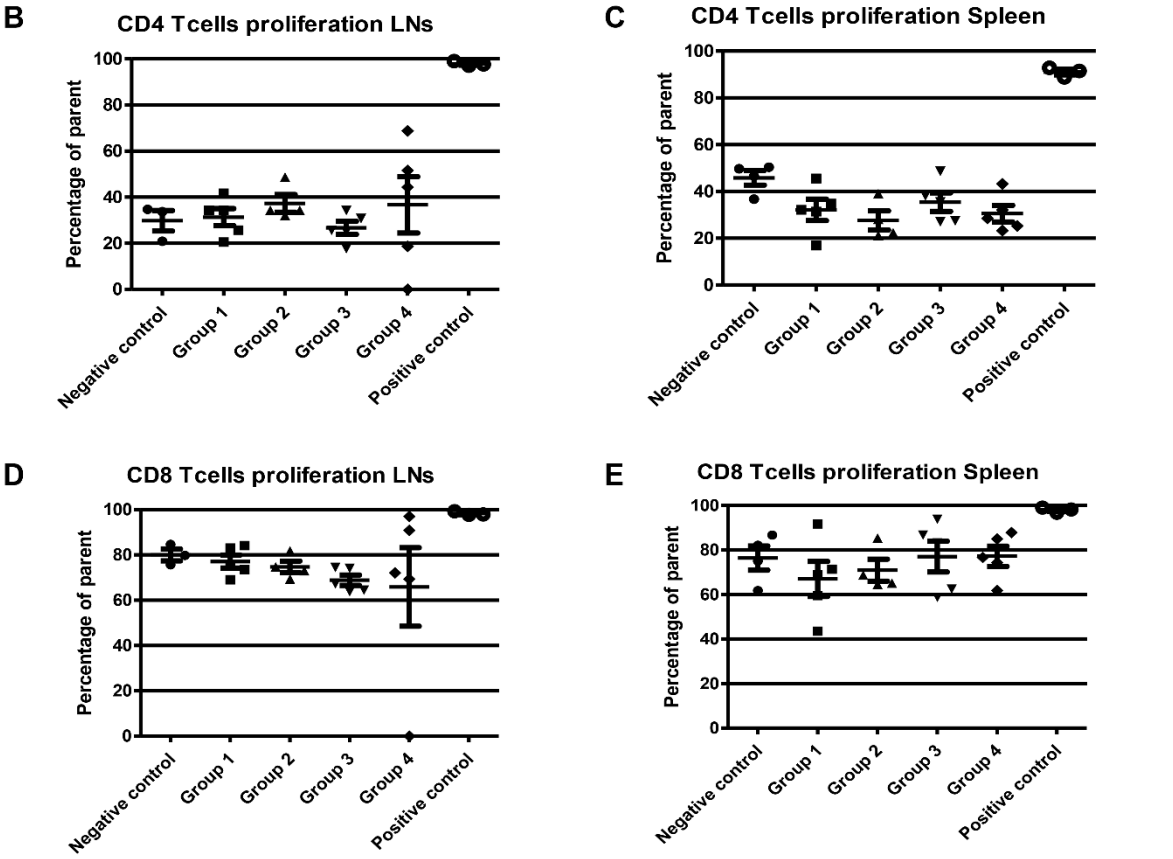

Figure 20: *In vivo* adoptive transfer experiment in HA-transgenic mice. (**A**) Experimental setup for all tested groups, either with or without the adjuvant c-di-AMP using the transfollicular route. The percentage of (**B** - **C**) CD4+ and (**D** - **E**) CD8+ T cells proliferation was quantified using flow cytometry for both the lymph nodes (LNs) and spleen of mice. N = 5, mean ± SD. Data kindly provided by Simon Delandre.

For both sampled organs, all tested groups showed low CD4+ T cells proliferation at the same level of the background (negative control) compared to the positive control (**Figure 20 B –C**). A high level of CD8+ T cells proliferation was observable for all tested groups (**Figure 20 D – E**). However, the plain CS-PLGA NPs (negative control) showed similar CD8+ titers as the other groups with mRNA and the positive control.

We encountered several factors playing a crucial role in the obtained outcome of the *in vivo* adoptive transfer experiments via the TF-route using our mRNA-HA loaded CS-PLGA NPs. As such, either (i) the used NP-system, (ii) applied dose of mRNA-HA or (iii) the transfollicular route may represent limiting parameters in the achievement of an effective immune response.

Previously, Raber *et al*. [38] analyzed the follicular uptake efficiency of different coated NP-systems applied onto the skin of human volunteers and showed that only ~2% of NPs with a cationic surface potential penetrated inside the HF, while ~81% were found on the skin surface. Whereas, lipophilic or negatively charged NPs revealed a higher tendency for follicular uptake with nearly 5%. As such, only ~1.5% of CS-PLGA NPs were found in the HF [38]. Taking this fact under consideration, applying our net positive charged mRNA:CS-PLGA NPs would similarly lead to a loss of more than 80% of NPs on the mouse skin. The penetrated small amount of mRNA:NPs further would have to be internalized by the perifollicular APCs, to cause a transgene expression of HA and subsequently a presentation of the antigen-fragments on MHC classes. Consequently, the chances for an effective *in vivo* transfection drops using cationic NPs. On the other side, a cationic surface potential of the particles is highly required for the complexation of mRNA as well as for an enhanced cellular uptake as discussed in chapter 3.2.4.
Thus, to counter this limitation, either the NP-system needs improvement to be potent enough to deliver the necessary mRNA dose to the APCs and/or the applied mRNA dose per mouse must be increased in future studies. Petsch et *al.* [143] used a high dose of 80 µg of mRNA-HA and injected intradermally to BALB/c mice. However, comparable to the intradermal or subcutaneous route, the transfollicular route is associated with higher challenges for mRNA-vaccination using NPs and therefore demands an optimal tuning of all involved parameters.

3.5 Development of Safe and Efficient NPs to Deliver Nucleic Acids

3.5.1 Starch-Chitosan Polyplexes for pDNA Delivery

*See also chapter 6.3, Yasar and Ho et al. (**2018**) Polymers.*

The aim of the present study was to design and optimize an efficient delivery system for nucleic acids made of materials from renewable resources in an organic solvent free synthesis in order to fulfill the strict requirements of the biomedical field [32]. As thus, the selected excipients should be biocompatible and biodegradable, safe, at the same time enable good drug loading capacity, and deliver genes efficiently to the target cells. In addition to that, the engineering aspects of the used materials should qualify to be environmentally friendly and facile producible. Therefore, a variety of different polymeric materials have been synthesized to develop drug delivery vehicles by either including them inside the polymeric matrix or loading them onto the surface of the particles [33]. However, the amount of such polymers with the further property of being water-soluble suitable for biomedical use is still limited, but highly desired. Particularly, natural and gently modified polysaccharides, e.g. chitosan, alginate, starch or dextrin with their synthetic derivatives have been considered as efficient candidates for nanocarrier systems [144, 145].

Hence, this work focused on the development of a flexible and facile NP-system based on the advantageous properties of the natural polysaccharides, starch and CS, and their potential to deliver pDNA. Starch is a polysaccharide, which is naturally degraded by α-amylase and widely used in pharmaceutical applications [146]. As natural starch is not water-soluble, we gently chemically modified and synthesized starch derivatives with fractional molecular weight (M_w) ratios according to Yamada *et al*. [79] , in which the preparation of partially oxidized starch derivatives was reported and further used as a platform for gene delivery.

Thus, anionic starch with M_w > 100 kDa and commercially available chitosan derivatives using either oligo chitosan M_w ~5 kDa or Protasan^{TM} M_w ~90 kDa were used as the main components to formulate the nanocarrier systems. The partially oxidized starch carries a carboxylate functional group with a net negative charge that

facilitates complex coacervation with the net positive charged amine functional group of chitosan in aqueous solution resulting in polyplexes. In order to obtain particles with high colloidal stability, we carefully tuned the molar ratio between the carboxylate and amine functional group, the polymer concentration and further the polymer type. The preparation within this study represents a step forward from the approach reported by Barthold *et al.* [147].

In the first step, we engineered plain starch-chitosan polyplexes composed of starch (M_w > 100 kDa) and oligo chitosan leading to anionic core polyplexes (anCP) carrying a negative ζ-potential (**Figure 21 A**), which enabled a further surface coating with Protasan resulting in cationic-coated polyplexes (cCP) (**Figure 21 B**). The plain polyplexes revealed a smooth and spherical surface shape with a narrow size-distribution profile and low cytotoxic effects tested on A549 cells (see chapter 6.3). The colloidal stability of both polyplexes was explored at different pH values (from 3.5 to 8.0) relevant for various administration routes. Regarding our TF-application, the particles have to be stable under slightly acidic conditions, since the natural pH value of the skin is approx. 5 [148]. Both polyplexes were stable under these conditions, making them suitable for skin application purposes. The produced anCP further retained their stability under storage conditions for over 27 days.
In the next step, we assessed the potential of the novel NP-system to deliver pDNA efficiently by *in vitro* transfection studies in A549 cells. Thus, we used pDNA encoding the green fluorescence protein pAmCyan as a model nucleic acid and incorporated it inside the anCP with an additional pDNA complexation (w/w of 1:30) onto the surface of cCP resulting in pAmCyan double loaded cCP (**Figure 21 C**), achieving a encapsulation efficiency (%EE) of 94% [32].

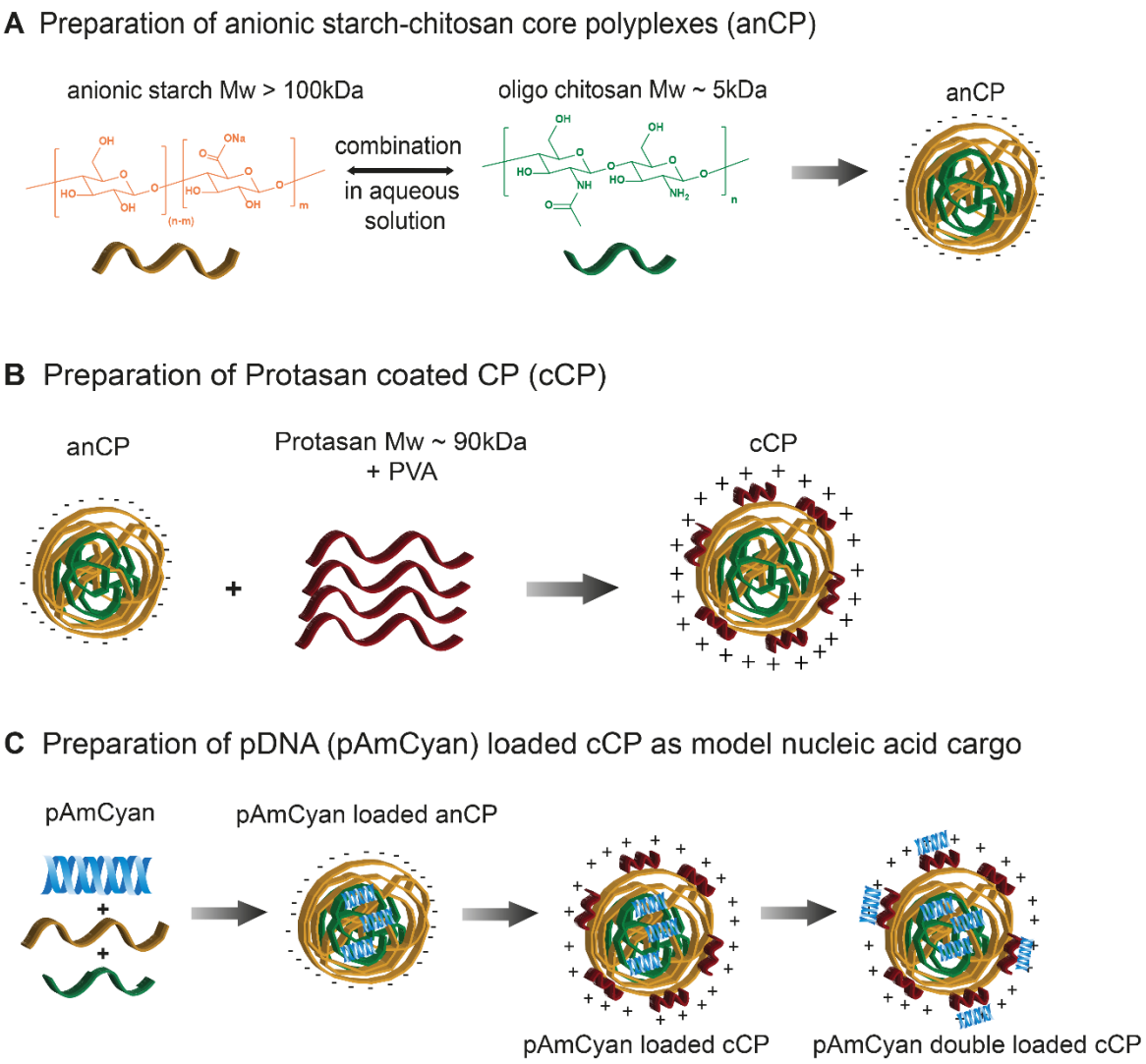

Figure 21: Preparation of starch-chitosan polyplexes for gene delivery. Represented schematic illustration has been published in Yasar *et al.* [32].

The transfection efficiency was evaluated after 48 – 96 h post-transfection using CLSM and flow cytometry. pAmCyan double loaded cCP mediated a protein expression rate of 5% after 48 h, whereas the positive control jetPRIME® (commercially available transfection reagent) caused a transfection efficiency of 45%, which rapidly decreased after 96 h to only 25% (**Figure 22**). Presumably, the high stability of the condensed pDNA within the polyplexes may have led to an incomplete release within the cytoplasm and hence less transfection rate [149, 150]. As mentioned in the chapters before, the amount of positive charged particles found within the hair follicles is very low, which in return means that only a low rate can be further internalized by perifollicular APCs. An additional low transfection rate of 5 % using our polyplexes

would reduce the chance for an efficient transfection by the administration route. We therefore focused in the upcoming study to design a more efficient NP-system with high transfection rate in an *in vitro* based assay.

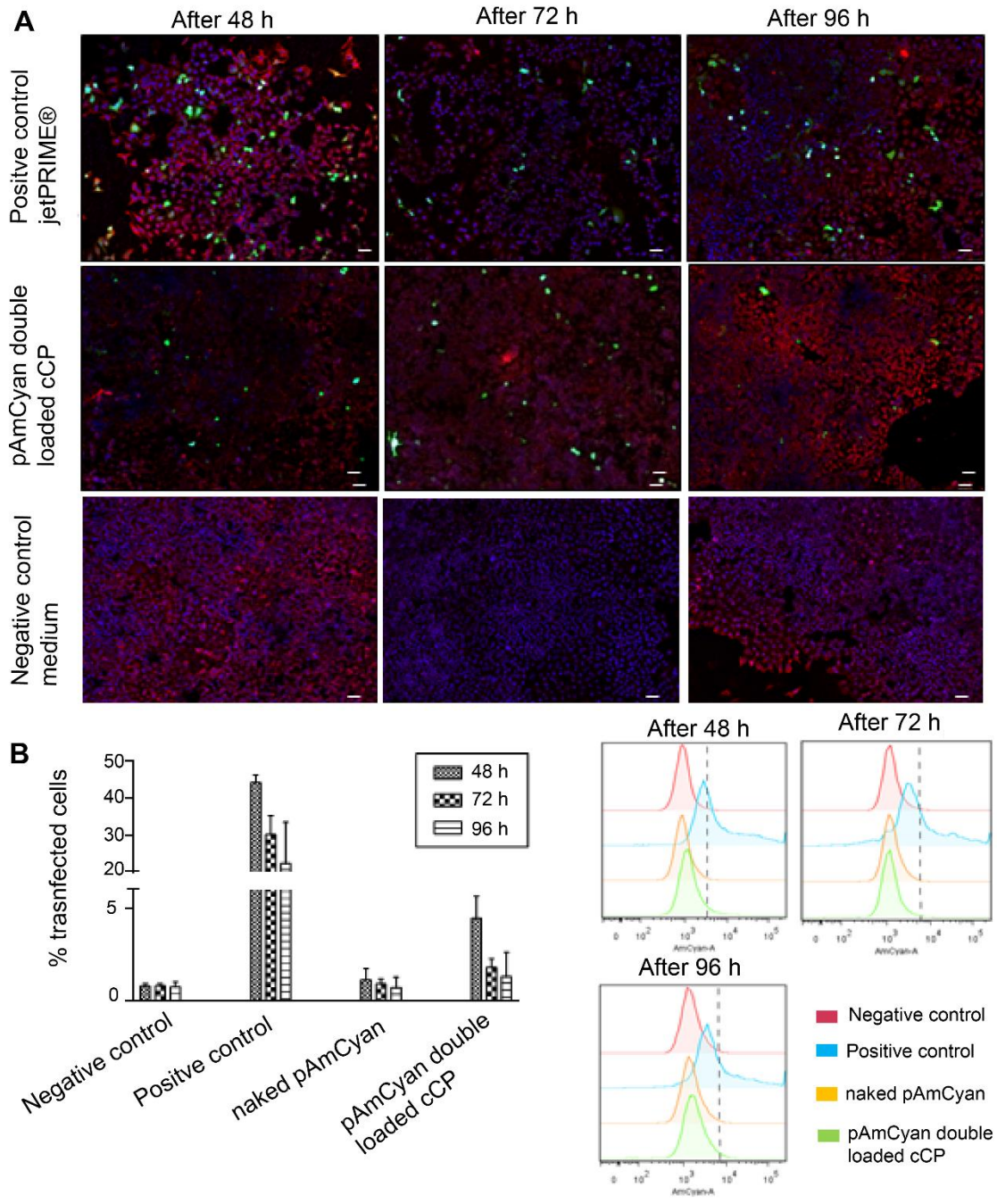

Figure 22: Transfection studies in A549 cells using pAmCyan double loaded cCP. (**A**) CLSM-images of transfected cells (green fluorescence signal: successful transfected cells; red: cell membrane; blue: cell nucleus; scale bar 50 µm). (**B**) Quantification of the transfection efficiency by flow cytometry. N = 3, mean ± SD. Images are modified from Yasar *et al.* [32].

3.5.2 Lipid-Polymer Hybrid NPs Carrying mRNA-mCherry as Reporter Gene to DC2.4 Cell Line

*See also chapter 6.4, Yasar et al. (**2018**) Journal of Nanobiotechnology*

As discussed in chapter 3.4, mRNA-based vaccination represents an innovative and promising alternative to pDNA-based strategies. Hence, a variety of different NP-systems have been manufactured using either polymer-based [77, 78] or lipid-based [73–76] NP-systems to replace the traditionally used viral-vectors for mRNA-delivery [68]. Nevertheless, the development of appropriate mRNA-delivery systems with high transfection efficiency and low cytotoxicity remains a challenge. Therefore, the objective of this study was to design a potent and safe NP-system that would efficiently deliver mRNA and should induce a high transgene expression rate in APCs. We focused on a new class of NP-system combining the beneficial properties of lipid and polymer carriers, hence we produced a lipid-polymer hybrid system (LPNs) [82, 87] and analyzed the kinetics of their cellular-internalization behavior within DCs.
Additionally to that, Raber *et al.* [38] discussed the tendency of cationic and lipophilic NPs to preferentially accumulate within the hair follicle in a higher amount. The before mentioned findings concerning the surface characteristics are important for a successful TF-vaccination.

The LPNs were designed using PLGA as the main core with a cationic surface coating using the lipid 1, 2-di-O-octadecenyl-3-trimethylammonium propane (DOTMA) [81]. These lipid-coated PLGA NPs were produced using a modified double-emulsion method as described earlier by Jensen *et al*. [92]. We further compared the lipid-coated PLGA NPs with the well-established CS-PLGA NPs and kept all processes during the production equal to allow for comparison. All plain NPs were characterized for their morphological structure, physicochemical properties, and colloidal stability under physiological as well as storage conditions. Further, their cytotoxic effects were evaluated *in vitro* in DC2.4 cells. The plain NP-systems revealed a spherical and evenly shaped surface morphology and additionally indicated a core-shell structure with both particles having a positive ζ-potential and a narrow size-distribution profile with a hydrodynamic size of ~230 nm (PDI ~0.1) for LPNs and ~150 nm (PDI ~0.1) for CS-PLGA NPs [81]. As important for biopharmaceutical application, both NP-systems

retained their colloidal stability in different physiological media (HBSS-buffer, cell culture medium DMEM, and DMEM plus 10% FCS). The LPNs remained stable when tested under storage conditions exposed to room temperature and 4°C and revealed low cytotoxic effects with up to 80% cell viability at 100 µg/mL particle concentration, when tested with a live-dead staining kit in DC2.4 cells.

To evaluate the potential of the lipid-coated PLGA NPs to deliver mRNA, a model mRNA encoding for the fluorescent protein mCherry was complexed onto the cationic surface of the NP-system at various ratios and the kinetics of cellular-uptake and further transgene expression were assessed at pre-determined time-points. The mRNA complexed NPs showed positive ζ-potential for w/w ratios of 1:20 and 1:30, while the tested w/w ratio of 1:10 had slightly lower surface potential with a broader size-distribution profile respectively [81].

While cellular-association of either type of NPs with (**Figure 23 A**) and without (**Figure 23 B**) mRNA-complexation was comparable, protein expression rate was significantly different.

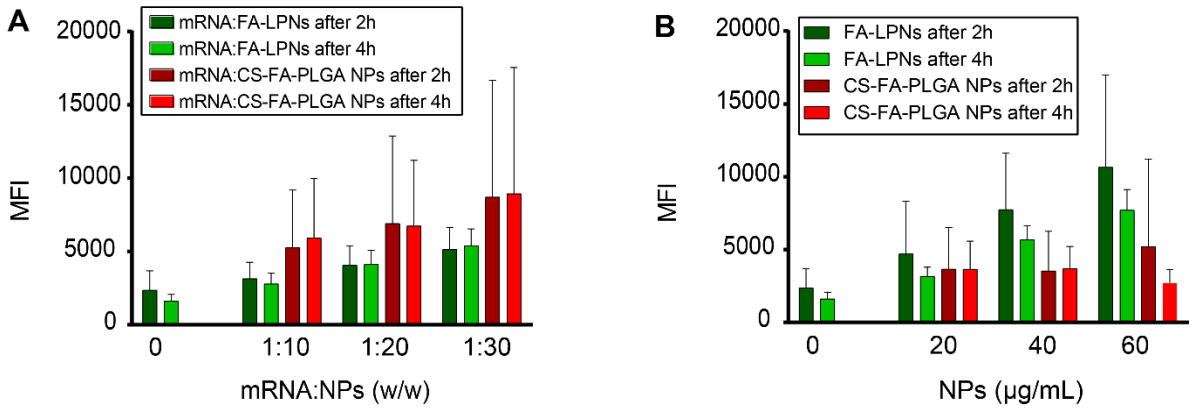

Figure 23: Cellular association of LPNs and CS-PLGA NPs in DC2.4 cells. The association of either NP-type was measured using the mean fluorescence intensity (MFI) of FA-labeled particles (**A**) with and (**B**) without mRNA complexation in the FITC-channel. N = 4, mean ± SD. Histograms were modified from Yasar *et al.* [81].

However, unlike mRNA:CS-PLGA NPs, mRNA:LPNs indicated an impressive transfection efficiency of ~80 % already after a 4 h time-course with a decay after 24 and 48 h post-transfection (**Figure 24 A**), while mRNA:CS-PLGA NPs in comparison

showed the highest transfection rate of nearly 5% 24 h post-transfection (**Figure 24 B**). However, CS-PLGA NPs had earlier shown their efficiency to delivery nuclease-encoding mRNA following an intratracheal administration in an *in vivo* transgenic mouse model resulting in an efficient genome editing [151]. In another setting, intratracheal and intravenous application of our CS-PLGA NPs together with chemically modified mRNA encoding for the cystic fibrosis transmembrane and conductance regulator (CFTR) – used as a highly potent pulmonary drug – revealed a significant improvement of the lung function in *in vivo* mouse, indicating a promising approach for cystic fibrosis patients [80]. That implicates the importance of the administration route for mRNA-delivery. The differences within the transfection rates of both NP-types may relate to higher stability of condensed mRNA within LPNs over CS-PLGA NPs and consequently a complete release within the cytoplasm [81].

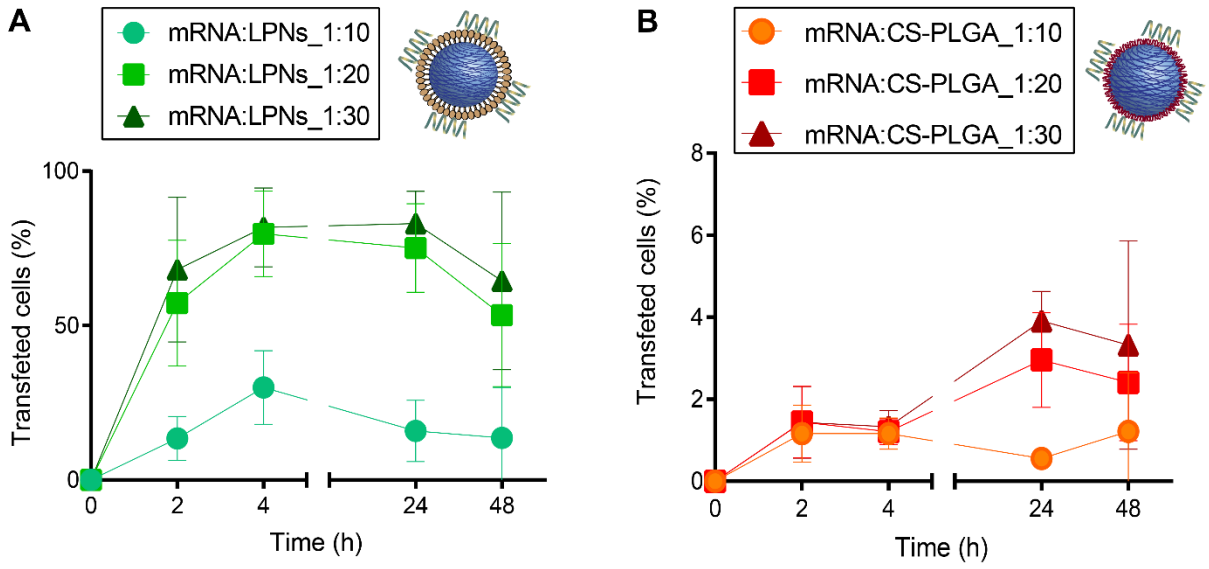

Figure 24: Kinetics of mCherry transgene expression in DCs after exposure to LPNs and CS-PLGA NPs. (**A**) mRNA complexed LPNs (**B**) CS-PLGA NPs were quantified at different w/w ratios for their efficiency to transfect DC2.4 cell line. While LPNs showed a high transfection rate after 2 h upon particles exposure, CS-PLGA NPs revealed a slight transfection efficiency 24 h post-transfection. N = 4, mean ± SD. Histograms were modified from Yasar *et al*. [81].

When we tested a simultaneous uptake and protein translation of labeled and mRNA complexed LPNs for 4 h using a live cell fluorescence microscopy, we observed an

independent protein translation rate from the NP-uptake, with an exponential increase over a time-course of 4 h (**Figure 25 A**). Whereas, the uptake remained comparably similar over the same time for transfected and non-transfected cells (**Figure 25 B**). Meaning that the NP-uptake does not play a crucial role to induce subsequent transfection. As such, even if CS-PLGA NPs were efficiently taken up by the cells, they only caused a low transfection rate. Leonhardt *et al.* [78] described earlier a similar observation, in which eGFP coded mRNA was complexed to the commercially available transfection reagent Lipofectamine2000® that further induced a fast protein expression after 3 h upon exposure to A549 cells. Our studies clearly underline the transient nature of mRNA [75, 78] as the protein translation starts within the cytoplasm and the importance to evaluate the kinetics of mRNA translation delivered by NP-systems. The knowledge about the kinetics may foster the generation of precise mRNA-based vaccines.

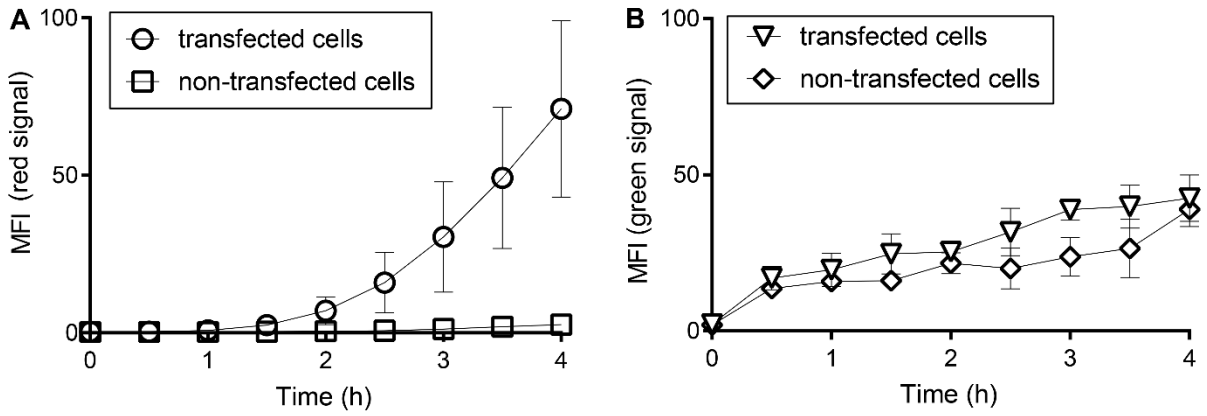

Figure 25: Live cell fluorescence microscopy of DCs when exposed for 4 h to labeled and mRNA complexed LPNs. (**A**) Time-dependent increase of mCherry protein translation (red signal) with mRNA complexed LPNs. (**B**) Transfected and non-transfected cells reveal similar time-independent cellular-uptake. n = 3, mean ± SD. Histograms were modified from Yasar *et al.* [81].

Our transfection studies using three different NP-types indicated that the cationic LPNs outperform the CS-PLGA NPs as well as starch-chitosan polyplexes when delivering nucleic acids. Quite impressed by such data, the LPNs were complexed with the mRNA-HA and analyzed for their potential to induce HA transgene expression and hence an immune response via the transfollicular route.

3.5.3 mRNA-HA:LPNs for *In Vivo* Adoptive Transfer in Mice: Comparing Transfollicular with Subcutaneous Route

This study aimed to evaluate the potential of the novel NP-system, lipid-coated PLGA NPs as delivery vehicle for mRNA-HA *in vivo* in adoptive transfer experiments. Thus, mRNA-HA complexed LPNs (mRNA-HA:LPNs) with a w/w of 1:20 were tested via the TF-route, and the outcome was additionally compared to the subcutaneous route with and without adjuvantation (**Figure 26 A**).

A

Groups	Formulation	mRNA:NPs (w/w)	Amount of mRNA-HA (µg)	Route
PBS	-	-	-	-
Blank LPNs	NPs + Adj	-	-	Transfollicular (TF)
mRNA:LPNs	NPs + mRNA-HA	1:20	20	Transfollicular (TF)
mRNA:LPNs	NPs + mRNA-HA + Adj	1:20	20	Transfollicular (TF)
mRNA:LPNs	NPs + mRNA-HA	1:20	20	Subcutaneous (SuC)
mRNA:LPNs	NPs + mRNA-HA + Adj	1:20	20	Subcutaneous (SuC)

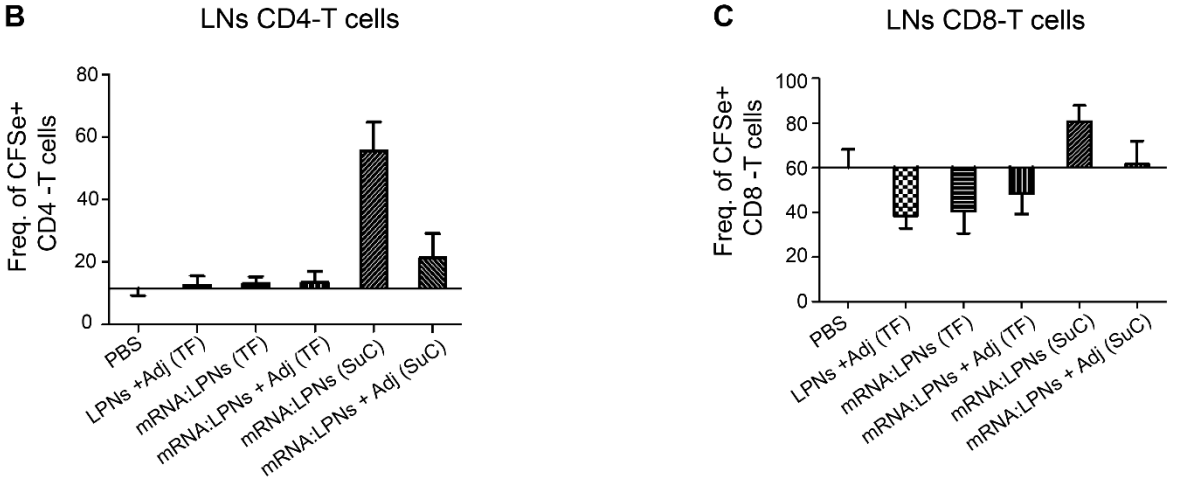

Figure 26: *In vivo* adoptive transfer using mRNA:LPNs via transfollicular and subcutaneous route in HA-transgenic mice. (**A**) Experimental setup for *in vivo* adoptive transfer studies (Adj stands for the adjuvant c-di-AMP), (**B**) CD4+ and (**C**) CD8+ T cells proliferation obtained lymph nodes (LNs). Data kindly provided by Simon Delandre.

We further increased the applied mRNA-HA dose per mouse up to 20 µg (**Figure 26 A**). The lymph nodes (LNs) were sampled 6 days post-immunization and the percentage of CD4+ and CD8+ T cells proliferation rate was quantified by flow cytometry. Even here, the TF-route could not induce a significant T cells proliferation, when compared to the subcutaneous route, which elicited nearly 60% CD4+ and approx. 80% CD8+ T cells proliferation when applied without an adjuvant (**Figure 26 B, C**).

Even our, according to the *in vitro* assessment in DCs, potent LPNs was not able to induce sufficient immune response *in vivo* via the transfollicular route, which further underlines the challenge for this administration pathway. Apart from the fact that only a few percentages of NPs would penetrate inside the hair follicle, it further represents also an immune-privileged area as described by Christoph *et al*. [152], upon characterization of the amount of various immune cells around human hair follicles. It was reported that the proximal hair follicle contains low number of macrophages and Langerhans cells, which are mainly in charge of MHC-I or MHC-II antigen presentation.

Thus, mRNA-delivery using the TF-administration route seems quite challenging as mRNA with its transgene products is recognized as intracellular or endogenous antigen by APCs continuing with their presentation on the MHC-I class. Lack of this type of APCs around the hair follicles consequently may have reduced the chances for successful transfection. However, even if the skin would hold abundant APCs, the present tight junctions presumably would restrict their smooth migration along the hair follicles, which likely prevents the further NP-cellular internalization. This may explain the observed results, when comparing the TF-route to the SuC one, in which the mRNA was directly injected to the skin, which certainly facilitates NP-cell uptake and hence antigen-presentation to CD4+ or CD8+ T cells.

4 Conclusion and Perspectives for Future Investigations

Skin-targeted NP-systems without weakening the protective stratum corneum barrier remain the most attractive approach for simplified future vaccinations. The studies performed within this thesis report detailed investigations of NP-cell interactions with an immune cell line of mouse origin (DC2.4), human epithelial cell lines (HaCaT and A549) and primary human immune cells. We further developed successfully new NP-systems composed of biodegradable and biocompatible polymers and assessed their potential for nucleic acid delivery, with the focus on mRNA, which remains a demanding cargo to deliver.

Not unexpectedly, several challenges for mRNA-delivery were encountered, specifically by aiming for the transfollicular route. A very potent NP-system to sufficiently deliver mRNA was needed and hence we produced two new carrier systems comprising starch-chitosan polyplexes and lipid-polymer hybrid nanoparticles and compared them with the well-established chitosan-coated PLGA NPs. When assessing all NP-systems, the LPNs revealed a higher potency to deliver mRNA. *In vitro* experiments with dendritic cells revealed a superior and rapid protein translation rate for LPNs complexing mRNA (coding for a reporter gene) in comparison to CS-PLGA NPs. We further conducted an in-depth characterization of the mRNA protein translation kinetics within DCs aiming to improve the understanding of mRNA's transient nature as needed for future manufacturing of precision nanomedicines. With the focus on using our particles for non-invasive transfollicular vaccination, we replaced the mCherry reporter gene with a mRNA encoding the vaccine relevant antigenic fragment of the influenza virus (hemagglutinin; HA). The potential of this system to induce an effective immune response was evaluated *in vivo* in adoptive transfer experiments using HA-transgenic mice. Unfortunately, an immune response was only detected for the control condition by using our system via the subcutaneous route, but not for the non-invasive approach via the TF-route.

Gene-vaccination by mRNA via the TF-route turned out to be challenging and obviously requires a more profound understanding of skin-structure around the hair follicles, NP-systems, and their subsequent cellular-internalization behavior.

Therefore, future investigations for transcutaneous mRNA-vaccination strategies should also consider alternative experimental settings.
In order to still allow a minimally invasive vaccination-strategy, the produced nanoparticles complexing mRNA can be tested on the skin following the generation of micropores within the skin structure. A system for dermatological skin-microporation is commercially available and uses precise laser-light to create small pores in the skin. These pores would act as gates inside the skin, facilitate NP-skin permeation and may activate the innate immune system. By not relying on the immune-privileged hair follicles, this approach could possibly facilitate the internalization of NPs by skin-immune cells, which seemed to be difficult via the hair follicles.

As an alternative to generating immunity via the antigen encoding mRNA, the number of immunization boosts can be further minimized by using self-amplifying RNA as cargo. Such so-called replicons can drive high level expression of recombinant antigens, which stimulates both the innate and adaptive immune system and represents a benefit for influenza vaccinations [153].

A better characterization of the NP-uptake mechanism and safety profile in primary human immune cells is mandatory, for future production of safe nanoparticles easy to translate into clinical trials. Combining genome editing tools like clustered regularly interspaced short palindromic repeats (CRISPR) and CRISPR- associated (Cas) biochemical methods with nanoparticulate delivery systems may foster the understanding of uptake and activation mechanism of immune cells, when specific pattern recognition receptors (PRR) are knocked down following the subsequent measurement of NP-influence on these cells.

5 References

[1] Kendall, M.A.F. Needle-free vaccine injection. *Handbook of experimental pharmacology*, **2010,** 193–219.

[2] Mittal, A.; Raber, A.S.; Schaefer, U.F.; Weissmann, S.; Ebensen, T.; Schulze, K.; Guzmán, C.A.; Lehr, C.-M.; Hansen, S. Non-invasive delivery of nanoparticles to hair follicles: A perspective for transcutaneous immunization. *Vaccine*, **2013**, *31,* 3442–3451.

[3] Mitragotri, S. Immunization without needles. *Nat Rev Immunol*, **2005**, *5,* 905–916.

[4] Schaefer, H.E. *Skin barrier : principles of percutaneous absorption;* Karger: Basel, New York, **1996**.

[5] Illel, B.; Schaefer, H. Transfollicular percutaneous absorption. Skin model for quantitative studies. *Acta Dermato-Venereologica*, **1988**, *68,* 427–430.

[6] Schaefer, H., Watts, F., Brod, J. and Illel, B. Follicular penetration: In: R.c., Scott, R.H Guy and I. Hadgraft (Eds), Prediction of Percutaneous Penetration: Methods, Measurements, and Modelling. *IBC Technical Services. London*, **1990,** 163–173.

[7] Scheuplein, R.J. Mechanism of percutaneous absorption. II. Transient diffusion and the relative importance of various routes of skin penetration. *The Journal of investigative dermatology*, **1967**, *48,* 79–88.

[8] van der Maaden, K.; Varypataki, E.M.; Romeijn, S.; Ossendorp, F.; Jiskoot, W.; Bouwstra, J. Ovalbumin-coated pH-sensitive microneedle arrays effectively induce ovalbumin-specific antibody and T-cell responses in mice. *European journal of pharmaceutics and biopharmaceutics : official journal of Arbeitsgemeinschaft fur Pharmazeutische Verfahrenstechnik e.V*, **2014**, *88,* 310–315.

[9] Prausnitz, M.R. Microneedles for transdermal drug delivery. *Advanced drug delivery reviews*, **2004**, *56,* 581–587.

[10] Römgens, A.M.; Bader, D.L.; Bouwstra, J.A.; Baaijens, F.P.T.; Oomens, C.W.J. Monitoring the penetration process of single microneedles with varying tip diameters. *Journal of the mechanical behavior of biomedical materials*, **2014**, *40,* 397–405.

[11] Denet, A.-R.; Vanbever, R.; Préat, V. Skin electroporation for transdermal and topical delivery. *Advanced drug delivery reviews*, **2004**, *56,* 659–674.

[12] Prausnitz, M.R.; Edelman, E.R.; Gimm, J.A.; Langer, R.; Weaver, J.C. Transdermal Delivery of Heparin by Skin Electroporation. *Nature biotechnology*, **1995**, *13,* 1205.

[13] HINGSON, R.A.; HUGHES, J.G. Clinical studies with jet injection; a new method of drug administration. *Current researches in anesthesia & analgesia*, **1947**, *26,* 221–230.

[14] Han, T.-h.; Yoh, J.J. A laser based reusable microjet injector for transdermal drug delivery. *Journal of Applied Physics*, **2010**, *107,* 103110.

[15] Mittal, A.; Raber, A.S.; Lehr, C.-M.; Hansen, S. Particle based vaccine formulations for transcutaneous immunization. *Human vaccines & immunotherapeutics*, **2013**, *9,* 1950–1955.

[16] Lademann, J.; Knorr, F.; Richter, H.; Jung, S.; Meinke, M.C.; Rühl, E.; Alexiev, U.; Calderon, M.; Patzelt, A. Hair follicles as a target structure for nanoparticles. *J. Innov. Opt. Health Sci.*, **2015**, *08,* 1530004.

[17] Lieb, L.M.; Ramachandran, C.; Egbaria, K.; Weiner, N. Topical delivery enhancement with multilamellar liposomes into pilosebaceous units: I. In vitro evaluation using fluorescent techniques with the hamster ear model. *Journal of Investigative Dermatology*, **1992**, *99,* 108–113.

[18] Li, L.; Margolis, L.B.; Lishko, V.K.; Hoffman, R.M. Product-delivering liposomes specifically target hair follicles in histocultured intact skin. *In Vitro Cellular and Developmental Biology - Animal*, **1992**, *28 A,* 679–681.

[19] Lademann, J.; Weigmann, H.; Rickmeyer, C.; Barthelmes, H.; Schaefer, H.; Mueller, G.; Sterry, W. Penetration of titanium dioxide microparticles in a sunscreen formulation into the horny layer and the follicular orifice. *Skin pharmacology and applied skin physiology*, **1999**, *12,* 247–256.

[20] Lademann, J.; Richter, H.; Teichmann, A.; Otberg, N.; Blume-Peytavi, U.; Luengo, J.; Weiss, B.; Schaefer, U.F.; Lehr, C.-M.; Wepf, R.; Sterry, W. Nanoparticles--an efficient carrier for drug delivery into the hair follicles. *European journal of pharmaceutics and biopharmaceutics : official journal of Arbeitsgemeinschaft fur Pharmazeutische Verfahrenstechnik e.V*, **2007**, *66,* 159–164.

[21] Mak, W.C.; Patzelt, A.; Richter, H.; Renneberg, R.; Lai, K.K.; Rühl, E.; Sterry, W.; Lademann, J. Triggering of drug release of particles in hair follicles. *Journal of controlled release : official journal of the Controlled Release Society*, **2012**, *160,* 509–514.

[22] Jacobi, U.; Engel, K.; Patzelt, A.; Worm, M.; Sterry, W.; Lademann, J. Penetration of pollen proteins into the skin. *Skin pharmacology and physiology*, **2007**, *20,* 297–304.

[23] Janeway, C.A. *Immunobiology 5: The immune system in health and disease / Charles A. Janeway … [et al.],* 5th ed.; Garland; Edinburgh : Churchill Livingstone: New York, **2001**.

[24] Gupta, P.N.; Mishra, V.; Rawat, A.; Dubey, P.; Mahor, S.; Jain, S.; Chatterji, D.P.; Vyas, S.P. Non-invasive vaccine delivery in transfersomes, niosomes and liposomes: A comparative study. *International journal of pharmaceutics*, **2005**, *293,* 73–82.

[25] Combadière, B.; Mahé, B. Particle-based vaccines for transcutaneous vaccination. *Comparative immunology, microbiology and infectious diseases*, **2008**, *31,* 293–315.

[26] Hansen, S.; Lehr, C.-M. Nanoparticles for transcutaneous vaccination. *Microbial biotechnology*, **2012**, *5,* 156–167.

[27] Palucka, K.; Banchereau, J. Dendritic Cells: A Link Between Innate and Adaptive Immunity. *Journal of Clinical Immunology*, **1999**, *19,* 12–25.

[28] Toll, R.; Jacobi, U.; Richter, H.; Lademann, J.; Schaefer, H.; Blume-Peytavi, U. Penetration profile of microspheres in follicular targeting of terminal hair follicles. *The Journal of investigative dermatology*, **2004**, *123,* 168–176.

[29] Vogt, A.; Combadiere, B.; Hadam, S.; Stieler, K.M.; Lademann, J.; Schaefer, H.; Autran, B.; Sterry, W.; Blume-Peytavi, U. 40 nm, but not 750 or 1,500 nm, nanoparticles enter epidermal CD1a+ cells after transcutaneous application on human skin. *The Journal of investigative dermatology*, **2006**, *126,* 1316–1322.

[30] Baleeiro, R.B.; Wiesmüller, K.-H.; Reiter, Y.; Baude, B.; Dähne, L.; Patzelt, A.; Lademann, J.; Barbuto, J.A.; Walden, P. Topical vaccination with functionalized particles targeting dendritic cells. *The Journal of investigative dermatology*, **2013**, *133,* 1933–1941.

[31] Mathes, C.; Brandner, J.M.; Laue, M.; Raesch, S.S.; Hansen, S.; Failla, A.V.; Vidal, S.; Moll, I.; Schaefer, U.F.; Lehr, C.-M. Tight junctions form a barrier in porcine hair follicles. *European journal of cell biology*, **2016**, *95,* 89–99.

[32] Yasar, H.; Ho, D.-K.; Rossi, C. de; Herrmann, J.; Gordon, S.; Loretz, B.; Lehr, C.-M. Starch-Chitosan Polyplexes: A Versatile Carrier System for Anti-Infectives and Gene Delivery. *Polymers*, **2018**, *10,* 252.

[33] Mahapatro, A.; Singh, D.K. Biodegradable nanoparticles are excellent vehicle for site directed in-vivo delivery of drugs and vaccines. *Journal of nanobiotechnology*, **2011**, *9,* 55.

[34] Danhier, F.; Ansorena, E.; Silva, J.M.; Coco, R.; Le Breton, A.; Préat, V. PLGA-based nanoparticles: An overview of biomedical applications. *Journal of controlled release : official journal of the Controlled Release Society*, **2012**, *161,* 505–522.

[35] Divya, K.; Jisha, M.S. Chitosan nanoparticles preparation and applications. *Environmental Chemistry Letters*, **2018**, *16,* 101–112.

[36] Mittal, A.; Schulze, K.; Ebensen, T.; Weißmann, S.; Hansen, S.; Lehr, C.M.; Guzmán, C.A. Efficient nanoparticle-mediated needle-free transcutaneous vaccination via hair follicles requires adjuvantation. *Nanomedicine : nanotechnology, biology, and medicine*, **2015**, *11,* 147–154.

[37] Ravi Kumar, M.N.V.; Bakowsky, U.; Lehr, C.M. Preparation and characterization of cationic PLGA nanospheres as DNA carriers. *Biomaterials*, **2004**, *25,* 1771–1777.

[38] Raber, A.S.; Mittal, A.; Schäfer, J.; Bakowsky, U.; Reichrath, J.; Vogt, T.; Schaefer, U.F.; Hansen, S.; Lehr, C.-M. Quantification of nanoparticle uptake into hair follicles in pig ear and human forearm. *Journal of controlled release : official journal of the Controlled Release Society*, **2014**, *179,* 25–32.

[39] Mittal, A.; Schulze, K.; Ebensen, T.; Weissmann, S.; Hansen, S.; Guzmán, C.A.; Lehr, C.-M. Inverse micellar sugar glass (IMSG) nanoparticles for transfollicular vaccination. *Journal of controlled release : official journal of the Controlled Release Society*, **2015**, *206,* 140–152.

[40] Li, L.; Hoffman, R.M. The feasibility of targeted selective gene therapy of the hair follicle. *Nature Medicine*, **1995**, *1,* 705–706.

[41] Li, L.; Margolis, L.B.; Lishko, V.K.; Hoffman, R.M. Product-delivering liposomes specifically target hair follicles in histocultured intact skin. *In Vitro Cellular and Developmental Biology - Animal*, **1992**, *28 A,* 679–681.

[42] Fan, H.; Lin, Q.; Morrissey, G.R.; Khavari, P.A. Immunization via hair follicles by topical application of naked DNA to normal skin. *Nature biotechnology*, **1999**, *17,* 870.

[43] Hoffman, R.M. The hair follicle as a gene therapy target. *Nature biotechnology*, **2000**, *18,* 20–21.

[44] Yu, Z.; Chung, W.-G.; Sloat, B.R.; Löhr, C.V.; Weiss, R.; Rodriguez, B.L.; Li, X.; Cui, Z. The extent of the uptake of plasmid into the skin determines the immune responses induced by a DNA vaccine applied topically onto the skin. *The Journal of pharmacy and pharmacology*, **2011**, *63,* 199–205.

[45] Shi, Z.; Curiel, D.T.; Tang, D.-c. DNA-based non-invasive vaccination onto the skin. *Vaccine*, **1999**, *17,* 2136–2141.

[46] Cui, Z.; Mumper, R.J. Topical immunization using nanoengineered genetic vaccines. *Journal of controlled release : official journal of the Controlled Release Society*, **2002**, *81,* 173–184.

[47] Lai, S.K.; Wang, Y.-Y.; Hanes, J. Mucus-penetrating nanoparticles for drug and gene delivery to mucosal tissues. *Advanced drug delivery reviews*, **2009**, *61,* 158–171.

[48] Murgia, X.; Yasar, H.; Carvalho-Wodarz, C.; Loretz, B.; Gordon, S.; Schwarzkopf, K.; Schaefer, U.; Lehr, C.-M. Modelling the bronchial barrier in pulmonary drug delivery: A human bronchial epithelial cell line supplemented with human tracheal mucus. *European journal of pharmaceutics and biopharmaceutics : official journal of Arbeitsgemeinschaft fur Pharmazeutische Verfahrenstechnik e.V*, **2017**, *118,* 79–88.

[49] Cone, R.A. Barrier properties of mucus. *Advanced drug delivery reviews*, **2009**, *61,* 75–85.

[50] Olmsted, S.S.; Padgett, J.L.; Yudin, A.I.; Whaley, K.J.; Moench, T.R.; Cone, R.A. Diffusion of macromolecules and virus-like particles in human cervical mucus. *Biophysical Journal*, **2001**, *81,* 1930–1937.

[51] Boegh, M.; Nielsen, H.M. Mucus as a barrier to drug delivery – understanding and mimicking the barrier properties. *Basic & clinical pharmacology & toxicology*, **2015**, *116,* 179–186.

[52] Bures, P.; Huang, Y.; Oral, E.; Peppas, N.A. Surface modifications and molecular imprinting of polymers in medical and pharmaceutical applications. *Journal of controlled release : official journal of the Controlled Release Society*, **2001**, *72,* 25–33.

[53] Huang, Y.; Leobandung, W.; Foss, A.; Peppas, N.A. Molecular aspects of muco- and bioadhesion: Tethered structures and site-specific surfaces. *Journal of controlled release : official journal of the Controlled Release Society*, **2000**, *65,* 63–71.

[54] Wang, Y.-Y.; Lai, S.K.; Suk, J.S.; Pace, A.; Cone, R.; Hanes, J. Addressing the PEG mucoadhesivity paradox to engineer nanoparticles that "slip" through the human mucus barrier. *Angewandte Chemie (International ed. in English)*, **2008**, *47,* 9726–9729.

[55] Prego, C.; Torres, D.; Fernandez-Megia, E.; Novoa-Carballal, R.; Quiñoá, E.; Alonso, M.J. Chitosan-PEG nanocapsules as new carriers for oral peptide delivery. Effect of chitosan pegylation degree. *Journal of controlled release : official journal of the Controlled Release Society*, **2006**, *111,* 299–308.

[56] Sharma, R.; Agrawal, U.; Mody, N.; Vyas, S.P. Polymer nanotechnology based approaches in mucosal vaccine delivery: Challenges and opportunities. *Biotechnology advances*, **2015**, *33,* 64–79.

[57] Martirosyan, A.; Olesen, M.J.; Howard, K.A. Chitosan-based nanoparticles for mucosal delivery of RNAi therapeutics. *Advances in genetics*, **2014**, *88,* 325–352.

[58] Gregory, A.E.; Titball, R.; Williamson, D. Vaccine delivery using nanoparticles. *Frontiers in cellular and infection microbiology*, **2013**, *3,* 13.

[59] Pulendran, B.; Ahmed, R. Immunological mechanisms of vaccination. *Nature immunology*, **2011**, *12,* 509–517.

[60] Pardi, N.; Hogan, M.J.; Porter, F.W.; Weissman, D. mRNA vaccines - a new era in vaccinology. *Nature reviews. Drug discovery*, **2018**, *17,* 261–279.

[61] Wolff, J.A.; Malone, R.W.; Williams, P.; Chong, W.; Acsadi, G.; Jani, A.; Felgner, P.L. Direct gene transfer into mouse muscle in vivo. *Science*, **1990**, *247,* 1465–1468.

[62] Sorrentino, S. Human extracellular ribonucleases: multiplicity, molecular diversity and catalytic properties of the major RNase types. *Cellular and Molecular Life Sciences CMLS*, **1998**, *54,* 785–794.

[63] Kaczmarek, J.C.; Kowalski, P.S.; Anderson, D.G. Advances in the delivery of RNA therapeutics: from concept to clinical reality. *Genome medicine*, **2017**, *9,* 60.

[64] Würtele, H.; Little, K.C.E.; Chartrand, P. Illegitimate DNA integration in mammalian cells. *Gene therapy*, **2003**, *10,* 1791–1799.

[65] Pascolo, S. Messenger RNA-based vaccines. *Expert opinion on biological therapy*, **2004**, *4,* 1285–1294.

[66] Pascolo, S. Vaccination with Messenger RNA (mRNA). In: *Toll-like receptors (TLRs) and innate immunity*. Akira, S., Bauer, S., Hartmann, G., Eds.; Springer: Berlin, **2008**; pp. 221–235.

[67] McCullough, K.C.; Milona, P.; Thomann-Harwood, L.; Démoulins, T.; Englezou, P.; Suter, R.; Ruggli, N. Self-Amplifying Replicon RNA Vaccine Delivery to Dendritic Cells by Synthetic Nanoparticles. *Vaccines*, **2014**, *2,* 735–754.

[68] Palamà, I.E.; Cortese, B.; D'Amone, S.; Gigli, G. mRNA delivery using non-viral PCL nanoparticles. *Biomaterials science*, **2015**, *3,* 144–151.

[69] Reichmuth, A.M.; Oberli, M.A.; Jaklenec, A.; Langer, R.; Blankschtein, D. mRNA vaccine delivery using lipid nanoparticles. *Therapeutic delivery*, **2016**, *7,* 319–334.

[70] Fotin-Mleczek, M.; Duchardt, K.M.; Lorenz, C.; Pfeiffer, R.; Ojkić-Zrna, S.; Probst, J.; Kallen, K.-J. Messenger RNA-based vaccines with dual activity induce balanced TLR-7 dependent adaptive immune responses and provide antitumor activity. *Journal of immunotherapy (Hagerstown, Md. : 1997)*, **2011**, *34,* 1–15.

[71] Pollard, C.; Koker, S. de; Saelens, X.; Vanham, G.; Grooten, J. Challenges and advances towards the rational design of mRNA vaccines. *Trends in molecular medicine*, **2013**, *19,* 705–713.

[72] Kallen, K.-J.; Heidenreich, R.; Schnee, M.; Petsch, B.; Schlake, T.; Thess, A.; Baumhof, P.; Scheel, B.; Koch, S.D.; Fotin-Mleczek, M. A novel, disruptive vaccination technology: self-adjuvanted RNActive(®) vaccines. *Human vaccines & immunotherapeutics*, **2013**, *9,* 2263–2276.

[73] Malone, R.W.; Felgner, P.L.; Verma, I.M. Cationic liposome-mediated RNA transfection. *Proceedings of the National Academy of Sciences of the United States of America*, **1989**, *86,* 6077–6081.

[74] Temmerman, M.-L. de; Dewitte, H.; Vandenbroucke, R.E.; Lucas, B.; Libert, C.; Demeester, J.; Smedt, S.C. de; Lentacker, I.; Rejman, J. mRNA-Lipoplex loaded microbubble contrast agents for ultrasound-assisted transfection of dendritic cells. *Biomaterials*, **2011**, *32,* 9128–9135.

[75] Phua, K.K.L.; Leong, K.W.; Nair, S.K. Transfection efficiency and transgene expression kinetics of mRNA delivered in naked and nanoparticle format. *Journal of controlled release : official journal of the Controlled Release Society*, **2013**, *166,* 227–233.

[76] Haes, W. de; van Mol, G.; Merlin, C.; Smedt, S.C. de; Vanham, G.; Rejman, J. Internalization of mRNA lipoplexes by dendritic cells. *Molecular pharmaceutics*, **2012**, *9,* 2942–2949.

[77] Rejman, J.; Tavernier, G.; Bavarsad, N.; Demeester, J.; Smedt, S.C. de. mRNA transfection of cervical carcinoma and mesenchymal stem cells mediated by cationic carriers. *Journal of controlled release : official journal of the Controlled Release Society*, **2010**, *147,* 385–391.

[78] Leonhardt, C.; Schwake, G.; Stögbauer, T.R.; Rappl, S.; Kuhr, J.-T.; Ligon, T.S.; Rädler, J.O. Single-cell mRNA transfection studies: Delivery, kinetics and statistics by numbers. *Nanomedicine : nanotechnology, biology, and medicine*, **2014**, *10,* 679–688.

[79] Yamada, H.; Loretz, B.; Lehr, C.-M. Design of starch-graft-PEI polymers: An effective and biodegradable gene delivery platform. *Biomacromolecules*, **2014**, *15,* 1753–1761.

[80] Haque, A. K. M. Ashiqul; Dewerth, A.; Antony, J.S.; Riethmüller, J.; Schweizer, G.R.; Weinmann, P.; Latifi, N.; Yasar, H.; Pedemonte, N.; Sondo, E.; Weidensee, B.; Ralhan, A.; Laval, J.; Schlegel, P.; Seitz, C.; Loretz, B.; Lehr, C.-M.; Handgretinger, R.; Kormann, M.S.D. Chemically modified h CFTR mRNAs recuperate lung function in a mouse model of cystic fibrosis. *Scientific Reports*, *8,* 16776.

[81] Yasar, H.; Biehl, A.; Rossi, C. de; Koch, M.; Murgia, X.; Loretz, B.; Lehr, C.-M. Kinetics of mRNA delivery and protein translation in dendritic cells using lipid-coated PLGA nanoparticles. *Journal of nanobiotechnology*, **2018**, *16,* 72.

[82] Su, X.; Fricke, J.; Kavanagh, D.G.; Irvine, D.J. In vitro and in vivo mRNA delivery using lipid-enveloped pH-responsive polymer nanoparticles. *Molecular pharmaceutics*, **2011**, *8,* 774–787.

[83] Cheng, C.; Convertine, A.J.; Stayton, P.S.; Bryers, J.D. Multifunctional triblock copolymers for intracellular messenger RNA delivery. *Biomaterials*, **2012**, *33,* 6868–6876.

[84] Lv, H.; Zhang, S.; Wang, B.; Cui, S.; Yan, J. Toxicity of cationic lipids and cationic polymers in gene delivery. *Journal of controlled release : official journal of the Controlled Release Society*, **2006**, *114,* 100–109.

[85] Cartiera, M.S.; Johnson, K.M.; Rajendran, V.; Caplan, M.J.; Saltzman, W.M. The uptake and intracellular fate of PLGA nanoparticles in epithelial cells. *Biomaterials*, **2009**, *30,* 2790–2798.

[86] Akinc, A.; Thomas, M.; Klibanov, A.M.; Langer, R. Exploring polyethylenimine-mediated DNA transfection and the proton sponge hypothesis. *The journal of gene medicine*, **2005**, *7,* 657–663.

[87] Hadinoto, K.; Sundaresan, A.; Cheow, W.S. Lipid-polymer hybrid nanoparticles as a new generation therapeutic delivery platform: A review. *European journal of pharmaceutics and biopharmaceutics : official journal of Arbeitsgemeinschaft fur Pharmazeutische Verfahrenstechnik e.V*, **2013**, *85,* 427–443.

[88] Groot, A.M. de; Thanki, K.; Gangloff, M.; Falkenberg, E.; Zeng, X.; van Bijnen, D.C.J.; van Eden, W.; Franzyk, H.; Nielsen, H.M.; Broere, F.; Gay, N.J.; Foged, C.; Sijts, A.J.A.M. Immunogenicity Testing of Lipidoids In Vitro and In Silico: Modulating Lipidoid-Mediated TLR4 Activation by Nanoparticle Design. *Molecular therapy. Nucleic acids*, **2018**, *11,* 159–169.

[89] Colombo, S.; Cun, D.; Remaut, K.; Bunker, M.; Zhang, J.; Martin-Bertelsen, B.; Yaghmur, A.; Braeckmans, K.; Nielsen, H.M.; Foged, C. Mechanistic profiling of the siRNA delivery dynamics of lipid-polymer hybrid nanoparticles. *Journal of controlled release : official journal of the Controlled Release Society*, **2015**, *201,* 22–31.

[90] Hasan, W.; Chu, K.; Gullapalli, A.; Dunn, S.S.; Enlow, E.M.; Luft, J.C.; Tian, S.; Napier, M.E.; Pohlhaus, P.D.; Rolland, J.P.; DeSimone, J.M. Delivery of multiple siRNAs using lipid-coated PLGA nanoparticles for treatment of prostate cancer. *Nano letters*, **2012**, *12,* 287–292.

[91] Thanki, K.; Zeng, X.; Justesen, S.; Tejlmann, S.; Falkenberg, E.; van Driessche, E.; Mørck Nielsen, H.; Franzyk, H.; Foged, C. Engineering of small interfering RNA-loaded lipidoid-poly(DL-lactic-co-glycolic acid) hybrid nanoparticles for highly efficient and safe gene silencing: A quality by design-based approach.

European journal of pharmaceutics and biopharmaceutics : official journal of Arbeitsgemeinschaft fur Pharmazeutische Verfahrenstechnik e.V, **2017**, *120,* 22–33.

[92] Jensen, D.K.; Jensen, L.B.; Koocheki, S.; Bengtson, L.; Cun, D.; Nielsen, H.M.; Foged, C. Design of an inhalable dry powder formulation of DOTAP-modified PLGA nanoparticles loaded with siRNA. *Journal of controlled release : official journal of the Controlled Release Society*, **2012**, *157,* 141–148.

[93] Díez, S.; Miguéliz, I.; Tros de Ilarduya, C. Targeted cationic poly(D,L-lactic-co-glycolic acid) nanoparticles for gene delivery to cultured cells. *Cellular & molecular biology letters*, **2009**, *14,* 347–362.

[94] Bose, R.J.C.; Arai, Y.; Ahn, J.C.; Park, H.; Lee, S.-H. Influence of cationic lipid concentration on properties of lipid–polymer hybrid nanospheres for gene delivery. *International journal of nanomedicine*, **2015**, *10,* 5367–5382.

[95] Wasungu, L.; Hoekstra, D. Cationic lipids, lipoplexes and intracellular delivery of genes. *Journal of controlled release : official journal of the Controlled Release Society*, **2006**, *116,* 255–264.

[96] Perche, F.; Benvegnu, T.; Berchel, M.; Lebegue, L.; Pichon, C.; Jaffrès, P.-A.; Midoux, P. Enhancement of dendritic cells transfection in vivo and of vaccination against B16F10 melanoma with mannosylated histidylated lipopolyplexes loaded with tumor antigen messenger RNA. *Nanomedicine : nanotechnology, biology, and medicine*, **2011**, *7,* 445–453.

[97] Wong, J.K.L.; Mohseni, R.; Hamidieh, A.A.; MacLaren, R.E.; Habib, N.; Seifalian, A.M. Will Nanotechnology Bring New Hope for Gene Delivery? *Trends in biotechnology*, **2017**, *35,* 434–451.

[98] Schmid, D.; Park, C.G.; Hartl, C.A.; Subedi, N.; Cartwright, A.N.; Puerto, R.B.; Zheng, Y.; Maiarana, J.; Freeman, G.J.; Wucherpfennig, K.W.; Irvine, D.J.; Goldberg, M.S. T cell-targeting nanoparticles focus delivery of immunotherapy to improve antitumor immunity. *Nature communications*, **2017**, *8,* 1747.

[99] Parveen, S.; Misra, R.; Sahoo, S.K. Nanoparticles: A boon to drug delivery, therapeutics, diagnostics and imaging. *Nanomedicine : nanotechnology, biology, and medicine*, **2012**, *8,* 147–166.

[100] Oberdörster, G. Safety assessment for nanotechnology and nanomedicine: Concepts of nanotoxicology. *Journal of internal medicine*, **2010**, *267,* 89–105.

[101] Kononenko, V.; Narat, M.; Drobne, D. Nanoparticle interaction with the immune system. *Arhiv za higijenu rada i toksikologiju*, **2015**, *66,* 97–108.

[102] Dobrovolskaia, M.A.; Shurin, M.; Shvedova, A.A. Current understanding of interactions between nanoparticles and the immune system. *Toxicology and applied pharmacology*, **2016**, *299,* 78–89.

[103] Zolnik, B.S.; González-Fernández, A.; Sadrieh, N.; Dobrovolskaia, M.A. Nanoparticles and the immune system. *Endocrinology*, **2010**, *151,* 458–465.

[104] Lunov, O.; Syrovets, T.; Loos, C.; Beil, J.; Delacher, M.; Tron, K.; Nienhaus, G.U.; Musyanovych, A.; Mailänder, V.; Landfester, K.; Simmet, T. Differential uptake of functionalized polystyrene nanoparticles by human macrophages and a monocytic cell line. *ACS Nano*, **2011**, *5,* 1657–1669.

[105] Fischbach, H.; Döring, M.; Nikles, D.; Lehnert, E.; Baldauf, C.; Kalinke, U.; Tampé, R. Ultrasensitive quantification of TAP-dependent antigen compartmentalization in scarce primary immune cell subsets. *Nature communications*, **2015**, *6*.

[106] Autissier, P.; Soulas, C.; Burdo, T.H.; Williams, K.C. Evaluation of a 12-color flow cytometry panel to study lymphocyte, monocyte, and dendritic cell subsets in humans. *Cytometry. Part A : the journal of the International Society for Analytical Cytology*, **2010**, *77,* 410–419.

[107] Corkum, C.P.; Ings, D.P.; Burgess, C.; Karwowska, S.; Kroll, W.; Michalak, T.I. Immune cell subsets and their gene expression profiles from human PBMC isolated by Vacutainer Cell Preparation Tube (CPT™) and standard density gradient. *BMC immunology*, **2015**, *16,* 48.

[108] Sasaki, Y.; Darmochwal-Kolarz, D.; Suzuki, D.; Sakai, M.; Ito, M.; Shima, T.; Shiozaki, A.; Rolinski, J.; Saito, S. Proportion of peripheral blood and decidual CD4(+) CD25(bright) regulatory T cells in pre-eclampsia. *Clinical and experimental immunology*, **2007**, *149,* 139–145.

[109] Toma, C.C.; Aloisi, A.; Bordoni, V.; Di Corato, R.; Rauner, M.; Cuniberti, G.; Delogu, L.G.; Rinaldi, R. Immune Profiling of Polysaccharide Submicron Vesicles. *Biomacromolecules*, **2018**, *19,* 3560–3571.

[110] Hussain, S.; Vanoirbeek, J.A.J.; Hoet, P.H.M. Interactions of nanomaterials with the immune system. *Wiley interdisciplinary reviews. Nanomedicine and nanobiotechnology*, **2012**, *4,* 169–183.

[111] Greulich, C.; Diendorf, J.; Gessmann, J.; Simon, T.; Habijan, T.; Eggeler, G.; Schildhauer, T.A.; Epple, M.; Köller, M. Cell type-specific responses of peripheral blood mononuclear cells to silver nanoparticles. *Acta biomaterialia*, **2011**, *7,* 3505–3514.

[112] Becker, K.; Schroecksnadel, S.; Geisler, S.; Carriere, M.; Gostner, J.M.; Schennach, H.; Herlin, N.; Fuchs, D. TiO(2) nanoparticles and bulk material stimulate human peripheral blood mononuclear cells. *Food and chemical toxicology : an international journal published for the British Industrial Biological Research Association*, **2014**, *65,* 63–69.

[113] Gamblin, S.J.; Skehel, J.J. Influenza hemagglutinin and neuraminidase membrane glycoproteins. *The Journal of biological chemistry*, **2010**, *285,* 28403–28409.

[114] Lee, Y.-T.; Kim, K.-H.; Ko, E.-J.; Lee, Y.-N.; Kim, M.-C.; Kwon, Y.-M.; Tang, Y.; Cho, M.-K.; Lee, Y.-J.; Kang, S.-M. New vaccines against influenza virus. *Clinical and experimental vaccine research*, **2014**, *3,* 12–28.

[115] Margine, I.; Palese, P.; Krammer, F. Expression of functional recombinant hemagglutinin and neuraminidase proteins from the novel H7N9 influenza virus using the baculovirus expression system. *Journal of visualized experiments : JoVE*, **2013,** e51112.

[116] Le Ru, A.; Jacob, D.; Transfiguracion, J.; Ansorge, S.; Henry, O.; Kamen, A.A. Scalable production of influenza virus in HEK-293 cells for efficient vaccine manufacturing. *Vaccine*, **2010**, *28,* 3661–3671.

[117] Weiss, B.; Schaefer, U.F.; Zapp, J.; Lamprecht, A.; Stallmach, A.; Lehr, C.-M. Nanoparticles made of Fluorescence-Labelled Poly(L-lactide-co-glycolide): Preparation, Stability, and Biocompatibility. *j nanosci nanotechnol*, **2006**, *6,* 3048–3056.

[118] Salatin, S.; Maleki Dizaj, S.; Yari Khosroushahi, A. Effect of the surface modification, size, and shape on cellular uptake of nanoparticles. *Cell biology international*, **2015**, *39,* 881–890.

[119] Schneider, M.R.; Schmidt-Ullrich, R.; Paus, R. The hair follicle as a dynamic miniorgan. *Current biology : CB*, **2009**, *19,* R132-42.

[120] Denk, W.; Strickler, J.; Webb, W. Two-photon laser scanning fluorescence microscopy. *Science*, **1990**, *248,* 73–76.

[121] So, P.T.; Dong, C.Y.; Masters, B.R.; Berland, K.M. Two-photon excitation fluorescence microscopy. *Annual review of biomedical engineering*, **2000**, *2,* 399–429.

[122] Benninger, R.K.P.; Piston, D.W. Two-photon excitation microscopy for the study of living cells and tissues. *Current protocols in cell biology*, **2013**, *Chapter 4,* Unit 4.11.1-24.

[123] Svoboda, K.; Yasuda, R. Principles of two-photon excitation microscopy and its applications to neuroscience. *Neuron*, **2006**, *50,* 823–839.

[124] Zipfel, W.R.; Williams, R.M.; Webb, W.W. Nonlinear magic: Multiphoton microscopy in the biosciences. *Nature biotechnology*, **2003**, *21,* 1369–1377.

[125] Evans, C.L.; Potma, E.O.; Puoris'haag, M.; Côté, D.; Lin, C.P.; Xie, X.S. Chemical imaging of tissue in vivo with video-rate coherent anti-Stokes Raman scattering microscopy. *Proceedings of the National Academy of Sciences of the United States of America*, **2005**, *102,* 16807–16812.

[126] Carrer, D.C.; Vermehren, C.; Bagatolli, L.A. Pig skin structure and transdermal delivery of liposomes: A two photon microscopy study. *Journal of controlled release : official journal of the Controlled Release Society*, **2008**, *132,* 12–20.

[127] Pineda, C.M.; Park, S.; Mesa, K.R.; Wolfel, M.; Gonzalez, D.G.; Haberman, A.M.; Rompolas, P.; Greco, V. Intravital imaging of hair follicle regeneration in the mouse. *Nature protocols*, **2015**, *10,* 1116–1130.

[128] Masters, B.R.; So, P.T.; Gratton, E. Multiphoton excitation fluorescence microscopy and spectroscopy of in vivo human skin. *Biophysical Journal*, **1997**, *72,* 2405–2412.

[129] Bäsler, K.; Bergmann, S.; Heisig, M.; Naegel, A.; Zorn-Kruppa, M.; Brandner, J.M. The role of tight junctions in skin barrier function and dermal absorption. *Journal of controlled release : official journal of the Controlled Release Society*, **2016**, *242,* 105–118.

[130] Fischer, D.; Li, Y.; Ahlemeyer, B.; Krieglstein, J.; Kissel, T. In vitro cytotoxicity testing of polycations: Influence of polymer structure on cell viability and hemolysis. *Biomaterials*, **2003**, *24,* 1121–1131.

[131] Fröhlich, E. The role of surface charge in cellular uptake and cytotoxicity of medical nanoparticles. *International journal of nanomedicine*, **2012**, *7,* 5577–5591.

[132] Lipscomb, M.F.; Masten, B.J. Dendritic cells: Immune regulators in health and disease. *Physiological reviews*, **2002**, *82,* 97–130.

[133] Bishop, C.J.; Majewski, R.L.; Guiriba, T.-R.M.; Wilson, D.R.; Bhise, N.S.; Quiñones-Hinojosa, A.; Green, J.J. Quantification of cellular and nuclear uptake rates of polymeric gene delivery nanoparticles and DNA plasmids via flow cytometry. *Acta biomaterialia*, **2016**, *37,* 120–130.

[134] Shang, L.; Nienhaus, K.; Nienhaus, G.U. Engineered nanoparticles interacting with cells: Size matters. *Journal of nanobiotechnology*, **2014**, *12,* 5.

[135] van Kooyk, Y. C-type lectins on dendritic cells: Key modulators for the induction of immune responses. *Biochm. Soc. Trans.*, **2008**, *36,* 1478–1481.

[136] Burgdorf, S.; Kurts, C. Endocytosis mechanisms and the cell biology of antigen presentation. *Current Opinion in Immunology*, **2008**, *20,* 89–95.

[137] Moseman, A.P.; Moseman, E.A.; Schworer, S.; Smirnova, I.; Volkova, T.; Andrian, U. von; Poltorak, A. Mannose Receptor 1 Mediates Cellular Uptake and Endosomal Delivery of CpG-Motif Containing Oligodeoxynucleotides. *The Journal of Immunology*, **2013**, *191,* 5615–5624.

[138] Han, Y.; Zhao, L.; Yu, Z.; Feng, J.; Yu, Q. Role of mannose receptor in oligochitosan-mediated stimulation of macrophage function. *International Immunopharmacology*, **2005**, *5,* 1533–1542.

[139] Murgia, X.; Pawelzyk, P.; Schaefer, U.F.; Wagner, C.; Willenbacher, N.; Lehr, C.-M. Size-Limited Penetration of Nanoparticles into Porcine Respiratory Mucus after Aerosol Deposition. *Biomacromolecules*, **2016**, *17,* 1536–1542.

[140] LUDWIG, A. The use of mucoadhesive polymers in ocular drug delivery. *Advanced drug delivery reviews*, **2005**, *57,* 1595–1639.

[141] Islam, M.A.; Reesor, E.K.G.; Xu, Y.; Zope, H.R.; Zetter, B.R.; Shi, J. Biomaterials for mRNA delivery. *Biomaterials science*, **2015**, *3,* 1519–1533.

[142] Ferraro, B.; Morrow, M.P.; Hutnick, N.A.; Shin, T.H.; Lucke, C.E.; Weiner, D.B. Clinical applications of DNA vaccines: Current progress. *Clinical infectious diseases : an official publication of the Infectious Diseases Society of America*, **2011**, *53,* 296–302.

[143] Petsch, B.; Schnee, M.; Vogel, A.B.; Lange, E.; Hoffmann, B.; Voss, D.; Schlake, T.; Thess, A.; Kallen, K.-J.; Stitz, L.; Kramps, T. Protective efficacy of in vitro synthesized, specific mRNA vaccines against influenza A virus infection. *Nature biotechnology*, **2012**, *30,* 1210–1216.

[144] Kang, B.; Opatz, T.; Landfester, K.; Wurm, F.R. Carbohydrate nanocarriers in biomedical applications: Functionalization and construction. *Chemical Society reviews*, **2015**, *44,* 8301–8325.

[145] Baldwin, A.D.; Kiick, K.L. Polysaccharide-modified synthetic polymeric biomaterials. *Biopolymers*, **2010**, *94,* 128–140.

[146] Builders, P.F.; Arhewoh, M.I. Pharmaceutical applications of native starch in conventional drug delivery. *Starch - Stärke*, **2016**, *68,* 864–873.

[147] Barthold, S.; Kletting, S.; Taffner, J.; Souza Carvalho-Wodarz, C. de; Lepeltier, E.; Loretz, B.; Lehr, C.-M. Preparation of nanosized coacervates of positive and negative starch derivatives intended for pulmonary delivery of proteins. *J. Mater. Chem. B*, **2016**, *4,* 2377–2386.

[148] Lambers, H.; Piessens, S.; Bloem, A.; Pronk, H.; Finkel, P. Natural skin surface pH is on average below 5, which is beneficial for its resident flora. *International journal of cosmetic science*, **2006**, *28,* 359–370.

[149] Hartono, S.B.; Phuoc, N.T.; Yu, M.; Jia, Z.; Monteiro, M.J.; Qiao, S.; Yu, C. Functionalized large pore mesoporous silica nanoparticles for gene delivery featuring controlled release and co-delivery. *J. Mater. Chem. B*, **2014**, *2,* 718–726.

[150] Truong, N.P.; Jia, Z.; Burgess, M.; Payne, L.; McMillan, N.A.J.; Monteiro, M.J. Self-catalyzed degradable cationic polymer for release of DNA. *Biomacromolecules*, **2011**, *12,* 3540–3548.

[151] Mahiny, A.J.; Dewerth, A.; Mays, L.E.; Alkhaled, M.; Mothes, B.; Malaeksefat, E.; Loretz, B.; Rottenberger, J.; Brosch, D.M.; Reautschnig, P.; Surapolchai, P.; Zeyer, F.; Schams, A.; Carevic, M.; Bakele, M.; Griese, M.; Schwab, M.; Nürnberg, B.; Beer-Hammer, S.; Handgretinger, R.; Hartl, D.; Lehr, C.-M.; Kormann, M.S.D. In vivo genome editing using nuclease-encoding mRNA corrects SP-B deficiency. *Nature biotechnology*, **2015**, *33,* 584–586.

[152] Christoph, T.; Müller-Röver, S.; Audring, H.; Tobin, D.J.; Hermes, B.; Cotsarelis, G.; Rückert, R.; Paus, R. The human hair follicle immune system: cellular composition and immune privilege. *British Journal of Dermatology*, **2000**, *142,* 862–873.

[153] Zimmer, G. RNA Replicons - A New Approach for Influenza Virus Immunoprophylaxis. *Viruses*, **2010**, *2,* 413–434.

6 Scientific Output - Original Research Papers

6.1 Preferential Uptake of Chitosan-Coated PLGA Nanoparticles by Antigen Presenting Cells

Preferential uptake of chitosan-coated PLGA nanoparticles by antigen presenting cells

Hanzey Yasar[§], Veronica Duran[§], Jenny Becker, Brigitta Loretz, Ulrich Kalinke, Claus-Michael Lehr, Nanomedicine-Nanotechnology, Biology and Medicine (**2018**) in reply.

[§]*Equally contributing authors*

Preferential uptake of chitosan-coated PLGA nanoparticles by antigen presenting cells

Hanzey Yasar[1, 2, §], Veronica Duran[3, §], Jennifer Becker[3], Brigitta Loretz[1], Ulrich Kalinke[3, *] and Claus-Michael Lehr[1, 2, *]

[1] Helmholtz-Institute for Pharmaceutical Research Saarland (HIPS) - Helmholtz Center for Infection Research (HZI) Department of Drug Delivery (DDEL), Campus E8.1, 66123 Saarbrücken, Germany. Phone: +49 681 98806 1000, E-Mail: Claus-Michael.Lehr@helmholtz-hzi.de

[2] Department of Pharmacy, Saarland University, 66123 Saarbrücken, Germany

[3] Institute for Experimental Infection Research, TWINCORE, Centre for Experimental and Clinical Infection Research, a joint venture between the Hannover Medical School and the Helmholtz Centre for Infection Research, 30625 Hannover, Germany. Phone: +49 511 220027 100, E-Mail: Ulrich.Kalinke@twincore.de

[$]equally contributing authors

***Correspondence to**: Claus-Michael Lehr, PhD, Department of Drug Delivery, Helmholtz-Institute for Pharmaceutical Research Saarland, University of Saarland, Campus E8.1, 66123 Saarbrücken, Germany. Phone: +49 681 98806 1000, E-Mail Claus-Michael.Lehr@helmholtz-hzi.de,

Ulrich Kalinke, PhD, Instiute for Experimental Infection Research, TWINCORE, Center for Experimental and Clinical Infection Research, 30625 Hannover, Germany. Phone: +49 511 220027 100, E-Mail: Ulrich.Kalinke@twincore.de

Keywords: Nanoparticles, PLGA NP, chitosan-PLGA NP, PBMC, monocyte-derived DC, intracellular trafficking.

Work count manuscript (incl. figure legends): 4559 without references

Number of figures: 6

Word count abstract: 136

Abstract

Biodegradable polymeric nanoparticles (NP) made from poly (lactid-co-glycolide) acid (PLGA) and chitosan (CS) hold promise as innovative formulations for targeted delivery. Since interactions of such NP with primary human immune cells have not been characterized, yet, here we assessed the effect of PLGA or CS-PLGA NP treatment on human peripheral blood mononuclear cells (PBMC), as well as on monocyte-derived DC (moDC). Amongst PBMC, antigen presenting cells (APC) showed higher uptake of both NP preparations than lymphocytes. Furthermore, moDC internalized CS-PLGA NP more efficiently than PLGA NP, presumably because of receptor-mediated endocytosis. Consequently, CS-PLGA NP were delivered mostly to endosomal compartments, whereas PLGA NP primarily ended up in lysosomes. Thus, CS-PLGA NP confer enhanced delivery to endosomal compartments of APC, offering new therapeutic options to either modulate APC function or to inhibit pathogens that preferentially infect APC.

Background

Over the past few decades nanoparticles (NP) gained increased attention as an innovative approach to improve drug delivery. In particular for the treatment of diseases such as infections and cancer, where normally applied therapeutics often show low efficiency, NP formulations are promising new strategies (1). Due to their physicochemical properties which facilitate interactions with biological systems (2), their morphological structure that allows for efficient uptake by different cell types (3), and the alternative to functionalize their surface with a variety of different structures (4), NP formulations represent a versatile tool to improve delivery of a whole variety of cargos to their site of action. As such, NP have been widely studied for vaccine formulations (5), cancer treatment (6), gene therapeutic purposes (7), immunotherapies (8), and diagnostics (9). Tuning their physicochemical properties resulted in enhanced crossing of biological barriers and increased bioavailability. However, these developments have also raised safety concerns as they enable NP to travel freely throughout the body (10, 11). It has been reported that NP may cause adverse effects when entering the human body, as the contact with human immune cells is inevitable and may cause undesirable immunomodulatory effects (12, 13). This sets strict requirements for the selection of materials and excipients when designing NP. We therefore focused on the analysis of two delivery systems that have been described in previous studies, which are composed of poly (lactid-co-glycolide) acid (PLGA). Such anionic PLGA NP can be subjected to chitosan-surface coating, thus resulting in cationic chitosan-coated PLGA (CS-PLGA) NP (14, 15). These polymers are biodegradable and biocompatible and therefore were already approved by regulatory authorities as pharmaceutically safe materials for clinical and cosmetic use (16, 17).

PLGA and CS-PLGA NP have been successfully applied in one of our previous studies for vaccination via the transfollicular route (15). Interestingly, this vaccination approach induced immune responses against the model antigen ovalbumin only when an adjuvant was additionally used (18). Further studies using CS-PLGA NP revealed their potential for messenger RNA (mRNA) delivery when applied intravenously in an *in vivo* mouse setting (19, 20).

The delivery potential of NP to antigen presenting cells (APC) has gained increased interest due to the function of APC as first line defense against pathogens as well as for their key role in triggering antigen-specific immune responses (21). When targeting APC, NP should allow for delivery of immune-modulating molecules as well as for provision of antimicrobial compounds, without inducing adverse immune reactions. Here, we studied the interaction of PLGA and CS-PLGA NP with primary human immune cells. Importantly, cells derived from human PBMC more faithfully reflect the pathophysiological state of immune cells in humans than tumor cell lines, thus representing a better predictive model for the characterization of new therapeutic interventions. Hence, (i) we prepared anionic PLGA and cationic CS-PLGA NP and fluorescently labeled them for cellular visualization purposes and (ii) we tested the uptake of both NP preparations by different immune cell subsets contained within human PBMC. (iii) To more specifically study NP uptake by APC, we isolated monocytes from PBMC, differentiated them to monocyte-derived dendritic cells (moDC), and tested the uptake and cytotoxic effect following NP treatment. (iv) Furthermore, we studied the immunological safety profile of NP treatment by analyzing the activation status of moDC upon NP treatment, and (v) we analyzed to which

subcellular compartments the NP traveled after cellular uptake. In brief, these studies indicated that in particular CS-PLGA NP are a versatile tool to selectively deliver drugs to APC via the uptake into endosomal compartments.

Methods

Preparation and Characterization of PLGA and chitosan-coated PLGA nanoparticles

For the production of plain (anionic) PLGA or chitosan-coated (cationic) CS-PLGA NP, a modified double-emulsion method was used as described previously (15, 22). In brief, 50 mg of PLGA (50:50; Resomer RG 503H, Evonik Industries AG, Darmstadt, Germany) was dissolved in ethyl acetate. Then 400 µl of milli-Q water (Merck Millipore, Billerica, MA) was added to the PLGA organic phase. This solution was sonicated with an ultrasound device (Branson Ultrasonic Corporation, USA) for 30 s at a 30% amplitude. Next, a solution of 2% (w/V) polyvinyl alcohol (PVA; Mowiol® 4-88, Sigma-Aldrich, Darmstadt, Germany) was prepared with milli-Q water. A volume of 4 ml PVA solution was applied to the initial PLGA solution and sonicated at the above settings. After continuous stirring overnight, the solution was purified by using a dialysis membrane (MWCO 1 kDa, Spectrum Labs, CA, USA) to obtain a final solution of 2 mg/ml PLGA NP. Similarly, chitosan-coated PLGA NP were produced by supplementing the PVA solution with 0.2% (w/v) chitosan (Protasan UP CL 113, FMC Biopolymer AS Novamatrix, Sandvika, Norway). For visualization purposes, the NP were fluorescently labeled by covalently coupling fluoresceinamine to the NP surface (FA; Sigma-Aldrich, Darmstadt, Germany), as previously described (23). In this study, all *in vitro* experiments were conducted with FA-labeled PLGA (FA-PLGA) or CS-PLGA (CS-FA-PLGA) NP.

All NP used in this study were thoroughly characterized for their quality attributes. Using dynamic light scattering (Zetasizer, Malvern Instruments, Malvern, UK), three colloidal properties were analyzed: the hydrodynamic size, the polydispersity index (PDI) and the ζ-potential. The morphology of NP was determined by using transmission electron microscopy (TEM; JEOL JEM 2011, St. Andrews, UK), as reported previously (22). All excipients, including materials and polymers, as well as the produced NP were in house tested for their endotoxins content by using the EndoLISA® detection assay (Hyglos GmbH, Bernried am Starnberger See, Germany).

Isolation of primary human immune cells

Human PBMC were isolated from buffy coats of healthy blood donors provided by the Blutbank Springe (Germany) using Ficoll density gradient centrifugation (Biocoll, Biochrom AG). CD14-positive monocytes were isolated by MACS selection using CD14 MicroBeads (Miltenyi). To differentiate monocyte-derived dendritic cells (moDC), purified monocytes were cultivated for 5 days in serum-free DC CellGro® medium (CellGenix, Freiburg, Germany) enriched with 1000 U/ml GM-CSF (granulocyte macrophage-colony stimulating factor, CellGenix) and 1000 U/ml IL-4 (CellGenix).

Flow cytometry analysis

$1x10^6$ PBMC were immunolabeled with anti-CD3-PerCP (UCHT1, Biolegend), anti-CD14-PacBlue (M5E2,Biolegend), anti-CD19-Amcyan (HIB19, BD Biosciences), and anti-HLA-DR-APC-Cy7 (L243; Biolegend) for 15 min at 4°C. For immune activation studies in moDC, $5x10^5$ cells were harvested and immunolabeled with anti-CD40-PE (5C3, Biolegend), anti-CD86-PacBlue (IT2.2, Biolegend), anti-HLA-AB-PeCy5

(W6/32, BD Biosciences), anti HLA-DR-APC-Cy7 (L243, Biolegend), anti-CD11c-PeCy7 (3.9, Biolegend) and anti-CD206-APC (15-2;Biolegend). Unspecific immunolabeling of PBMC and moDC conferred by Fc receptor binding was blocked by the addition of 10% Gamunex (Grifols Deutschland GmbH, Frankfurt am Main, Germany) solution. Data were acquired on a LSRII flow cytometer (BD Biosciences) and analyzed with the FlowJo software (Tree Star).

Nanoparticle binding and uptake studies

Uptake of NP was tested in PBMC. To this end, 60 µg/ml of FA-PLGA or CS-FA-PLGA NP were added to $1x10^6$ PBMC and incubated either at 4ºC or 37ºC. Cells were harvested, immunolabeled and NP-derived FA fluorescence was assessed by flow cytometry. Binding of NP to the cell surface was determined as the percentage of FA positive cells observed in PBMC incubated at 4ºC and net uptake of NP was calculated by subtracting the NP binding from the percentage of FA positive cells observed at 37ºC.

Confocal fluorescence microscopy

For confocal imaging, moDC were seeded in coverslip-bottom LabTeK® culture chambers (Sigma-Aldrich, Darmstadt, Germany) during the five days of moDC differentiation. After NP treatment, cells were fixed with 3% paraformaldehyde for 10 min at room temperature, washed three times with PBS and blocked with glycine-containing blocking buffer for 1 hour. Cells were washed again three times with PBS and incubated with primary antibodies of interest for 24 hours at 4ºC. After PBS washing, fluorophore-conjugated secondary antibodies were added and the samples were incubated for 2 hours at room temperature. Finally, DAPI was added for nuclear

staining, cells were washed and mounted with DAKO fluorescent mounting medium. Confocal microscopy was then performed with the Olympus FV1000-IX81 laser-scanning microscope using the 60x oil immersion objective, NA 1.35.

Statistical analysis

All data analyses were performed using the GraphPad Prism Software (La Jolla CA). To compare matched samples, two tailed Wilcoxon test was used with a p-value <0.05 set as statistically significant and for colocalization studies, a two-way ANOVA was performed with a p-value <0.05 set as significant. All measurements were performed at least 3 times.

Results

Production and characterization of PLGA and chitosan-coated PLGA nanoparticles

For this study two oppositely charged delivery systems, PLGA (anionic) and chitosan-coated PLGA (cationic) NP, were generated as described earlier (13, 14). As even minor variations in the physicochemical properties of NP preparations can influence their functionality and bioavailability, we thoroughly characterized the NP morphology, the NP size, the polidispersity index (PDI), the ζ-potential, the endotoxin content, and the stability under cell culture conditions of NP preparations used in this study. PLGA and CS-PLGA NP with and without FA-labelling revealed a smooth and evenly shaped spherical morphology (Figure 1, *A-D*), with a hydrodynamic size of approx. 130 nm for PLGA and 150 nm for CS-PLGA NP (Figure 1, *E*). Both NP preparations had a monodisperse particle-size distribution as indicated by a PDI of approx. 0.1. PLGA NP showed an anionic surface charge with a ζ-potential of approx. -18 mV, whereas CS-PLGA NP were cationic with a ζ-potential of approx. +26 mV (Figure 1, *E* and Supplementary Table 1). FA-labelling only slightly increased the size of both NP preparations and reduced the ζ-potential of CS-PLGA NP from +26 to +13 mV. Nevertheless, both non-labeled as well as FA-labeled CS-PLGA NP had a clear positive charge.

As for immunological assays it is of key relevance to avoid impurities, only pharmaceutical grade materials were used to generate NP preparations. Additionally, each excipient used for NP production as well as the final NP preparations were tested for their endotoxin content (Supplementary Table 2). Furthermore, the stability and aggregation behavior of PLGA and CS-PLGA NP was tested under cell culture

conditions. For this, both NP preparations were incubated in fresh CellGro® medium or in medium harvested after 5 days of moDC culture (conditioned medium) and the hydrodynamic size as well as the PDI were measured. PLGA and CS-PLGA NP showed a similar size and PDI after incubation in PBS or fresh medium. In contrast, following incubation in conditioned medium both NP showed moderately increased size and PDI (Supplementary Figure 1). For this reason, a medium exchange was performed prior to NP treatment of cells in the following *in vitro* experiments.

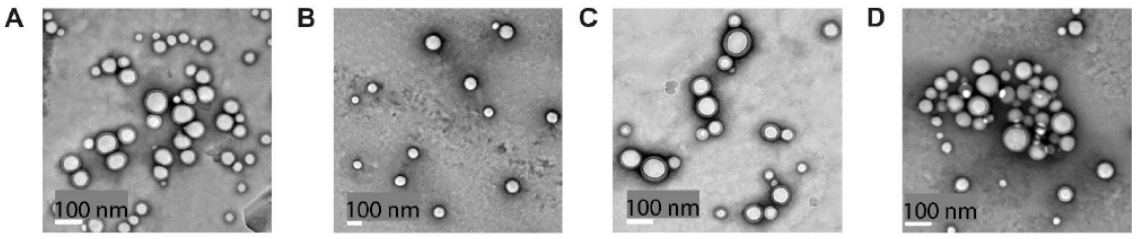

E

Nanoparticle	Size (nm)	PDI	ζ-potential (mV)
PLGA	127 ± 12	0.12 ± 0.07	-18.4 ± 3.8
FA-PLGA	162 ± 34	0.05 ± 0.03	-16.3 ± 5.6
CS-PLGA	151 ± 20	0.17 ± 0.08	26.8 ± 1.5
CS-FA-PLGA	183 ± 26	0.09 ± 0.00	13.1 ± 6.2

Figure 1: Morphological and physicochemical characterization of PLGA and chitosan-coated PLGA nanoparticles. Transmission electron micrographs of **(A)** non-labeled PLGA NP, **(B)** FA-PLGA NP, **(C)** non-labeled CS-PLGA NP and **(D)** CS-FA-PLGA NP. **(E)** The NP preparations were characterized for their size, polydispersity index (PDI) and ζ-potential. Data presented as mean ± SD *(n = 3)*.

Among PBMC, antigen presenting cells show enhanced uptake of PLGA and chitosan-coated PLGA nanoparticles

To study the NP uptake by primary human immune cells, blood samples were drawn from healthy donors and PBMC were isolated by Ficoll density gradient centrifugation (Figure 2, *A*).

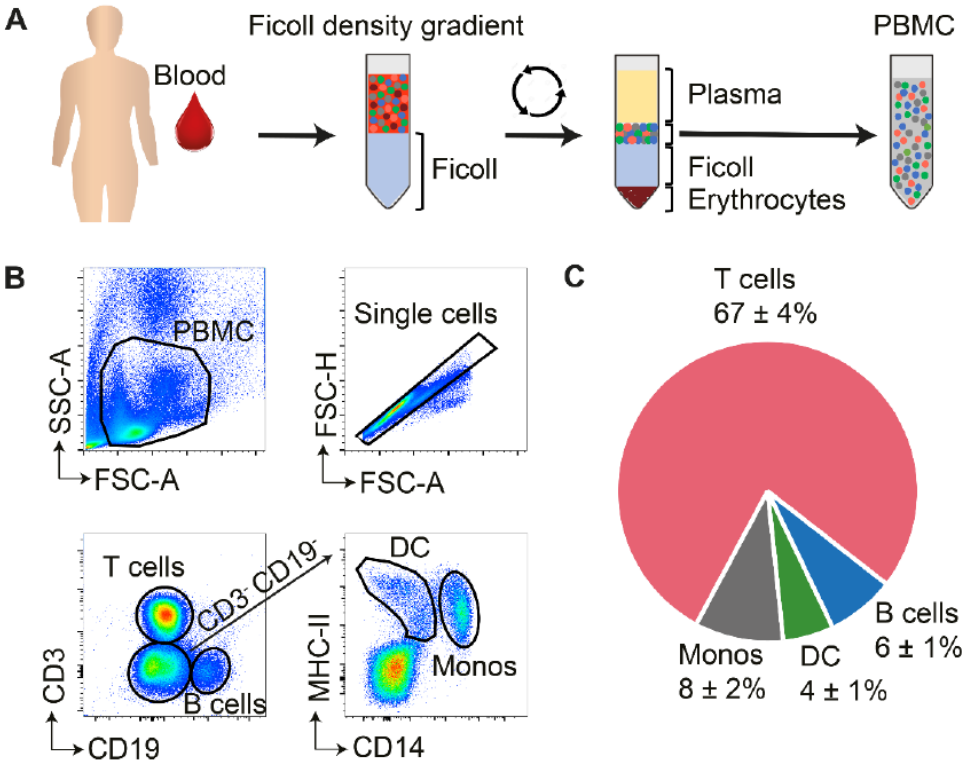

Figure 2: Characterization of immune cell subsets in human PBMC. (A) Blood was drawn from healthy donors and human PBMC were isolated by Ficoll density gradient centrifugation. **(B)** Human PBMC were immunolabeled with fluorescent-coupled antibodies specific for CD3, CD19, MHC-II, and CD14. $CD3^{+}CD19^{-}$ T cells, $CD3^{-}CD19^{+}$ B cells, $CD3^{-}CD19^{-}MHCII^{+}CD14^{+}$ monocytes (monos) and $CD3^{-}CD19^{-}MHCII^{+}CD14^{-}$ dendritic cells (DC) were gated as indicated for one representative donor. **(C)** Cell subset distribution amongst PBMC from 11 healthy donors. Values indicate mean percentage ± SD.

To determine the immune cell subset distribution amongst PBMC, cells prepared from 11 different donors were immunolabeled with fluorescent-coupled antibodies directed against CD3, CD19, MHC-II, and CD14, and the samples were analyzed by flow cytometry. Amongst single cells, T cells were defined as $CD3^+CD19^-$ cells and B cells as $CD19^+CD3^-$ cells, whereas the $CD3^-CD19^-$ population was further dissected in MHC-II^+CD14^+ monocytes and MHC-II^+CD14^- DC (Figure 2, *B*). This analysis revealed that PBMC comprise approx. 67% T cells, 6% B cells, 4% dendritic cells (DC), and 8% dendritic monocytes (Figure 2, *C*). To investigate the kinetics of NP uptake, PBMC were treated with 60 µg/ml of FA-PLGA or CS-FA-PLGA NP and after incubation at 37°C for the indicated times, cells were harvested, immunolabeled as described above, and the percentages of FA positive cells were determined by flow cytometry. Incubation at 4°C was performed as a control to determine the FA signal derived from binding of nanoparticles to the cell surface (Supplementary Figure 2). Under such conditions, T cells did not show abundant FA positive cells, neither upon treatment with FA-PLGA or CS-FA-PLGA NP, and not even after 4 h of incubation (Figure 3, *A*), whereas less than 20% of the B cells were FA positive after 4 h treatment with FA-PLGA NP, but not after treatment with CS-FA-PLGA NP (Figure 3, *B*). In contrast, DC and monocytes showed increased fluorescence already after 15 min of incubation with CS-FA-PLGA NP, but not after FA-PLGA NP treatment (Figure 3, *C and D*). After prolonged incubation of up to 4 h, approx. 40% of the DC were FA positive upon treatment with CS-FA-PLGA NP while only 20% were positive upon FA-PLGA NP treatment (Figure 3, *C*). Interestingly, after 4 h of incubation, approx. 60% of the monocytes were FA positive, irrespective of whether the PBMC were treated with FA-PLGA or CS-FA-PLGA NP (Figure 3, *D*).

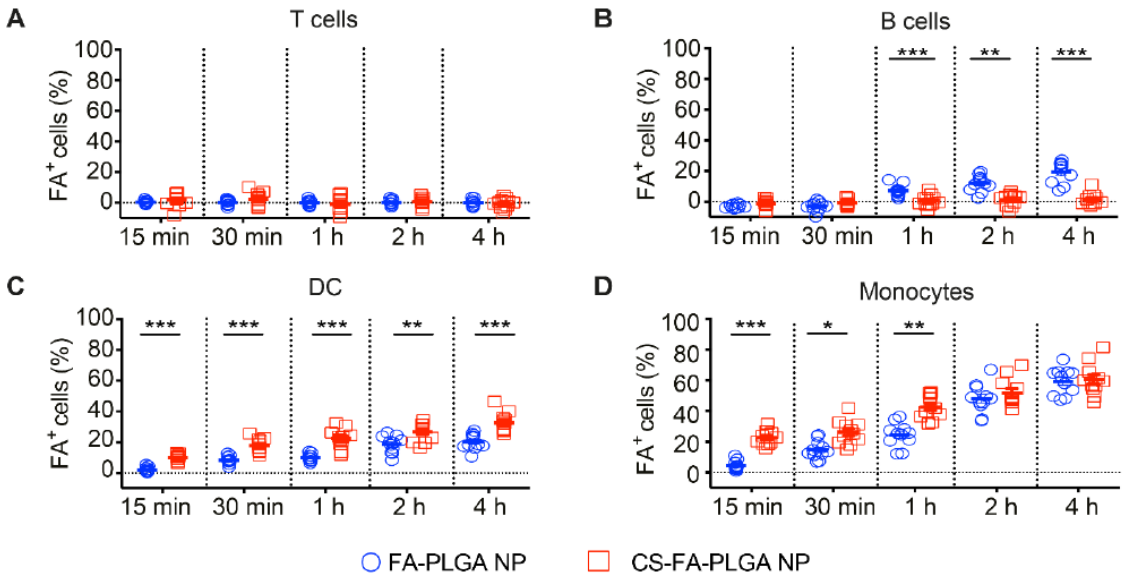

Figure 3: FA-PLGA and CS-FA-PLGA nanoparticles are preferentially taken up by APC in human PBMC. PBMC prepared as described in Figure 2 were treated with 60 µg/ml of FA-PLGA or CS-FA-PLGA NP at 37°C for the indicated times. Percentages of FA positive cells were determined for **(A)** T cells, **(B)** B cells, **(C)** DC and **(D)** monocytes. Values were normalized to the fluorescence signal detected after incubation at 4°C (Supplementary Figure 1). Error bars indicate mean ± SEM (two-tailed Wilcoxon test, ***$P \leq 0.0010$, **$P \leq 0.0068$, *$P \leq 0.0137$, n=11).

Thus, upon treatment of PBMC with FA-PLGA or CS-FA-PLGA NP, primarily myeloid cells including DC and monocytes, but not lymphocytes, showed enhanced NP uptake. Of note, monocytes took up NP even more efficiently than DC and after short incubation times, both myeloid cell subsets showed enhanced uptake of CS-FA-PLGA NP when compared with FA-PLGA NP.

Chitosan-coated PLGA nanoparticles are effectively internalized by monocyte-derived dendritic cells and do not show toxic effects

As DC are of key relevance for the induction and regulation of antigen-specific immune responses and thus constitute an interesting pharmacological target, the delivery of NP in DC was studied in greater detail. To this end, $CD14^+$ cells were isolated from PBMC by magnetic cell sorting and further differentiated to monocyte-derived dendritic cells (moDC) by incubation in medium enriched with GM-CSF and IL-4 for 5 days (Figure 4, *A*). To analyze the effect of NP treatment on cell viability, moDC were exposed to increasing concentrations of FA-PLGA or CS-FA-PLGA NP for 24 h and the percentage of dead cells was quantified using the Zombie Aqua™ dye, with heat-killed moDC as a positive control (Supplementary Figure 3). These experiments indicated that up to a concentration of 100 µg/ml only low toxicity was detected for both NP. At the highest concentration of 600 µg/ml, approx. 20% and 40% of the moDC were dead upon treatment with FA-PLGA and CS-FA-PLGA NP, respectively (Supplementary Figure 3). Therefore, moDC were exposed to 60 µg/ml of either type of NP preparation for 2, 4, or 24 h and the percentage of FA positive cells was determined by flow cytometry. Incubation with CS-FA-PLGA NP resulted in significantly increased percentages of FA positive cells at all the tested time points, with approx. 70% FA positive cells after 24 h of incubation. In contrast, treatment with FA-PLGA NP resulted only in approx. 30% FA positive cells after 24 h of incubation (Figure 4, *C*). These results demonstrated that CS-FA-PLGA NP are more efficiently taken up by moDC than FA-PLGA NP.

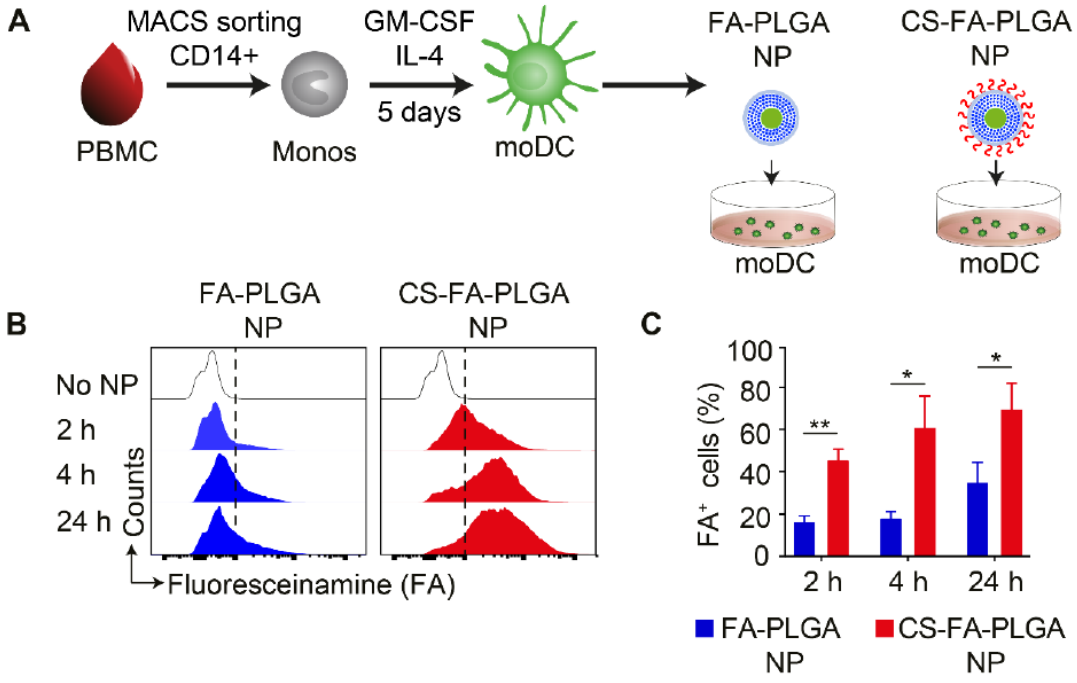

Figure 4: CS-FA-PLGA nanoparticles are effectively internalized by human moDC. (A) Monocytes were isolated from PBMC by magnetic activated cell sorting (MACS) for CD14+ cells, differentiated to monocyte-derived DC (moDC), and were then treated with FA-PLGA or CS-FA-PLGA NP. **(B)** moDC were treated with 60 µg/ml FA-PLGA or CS-FA-PLGA NP for 2, 4 and 24 h at 37°C, and the percentage of FA positive cells was determined by flow cytometry. Representative data of moDC from one donor is shown. **(C)** Quantification of FA positive moDC from 5 donors. The error bars indicate mean ± SEM (two tailed Wilcoxon test, $^{**}P \leq 0.0015$, $^{*}P \leq 0.0309$, n=5).

Treatment with FA-labeled PLGA or chitosan-coated PLGA nanoparticles does not induce upregulation of surface activation markers on moDC

In order to evaluate whether treatment with FA-PLGA or CS-FA-PLGA NP would activate moDC, surface activation markers were analyzed by flow cytometry before and after 2, 4, and 24 h of NP treatment. Upon LPS treatment, moDC showed a 2.5-fold increased mean fluorescent intensity (MFI) of MHC-I expression when compared with non-treated moDC. In contrast, neither upon FA-PLGA nor CS-FA-PLGA NP treatment moDC showed significant MHC-I up-regulation. Similarly, CD11c, MHC-II, CD86, and CD40 were not up-regulated after FA-PLGA or CS-FA-PLGA NP treatment, whereas after LPS treatment the highest fold increase was detected after 24 h of incubation for CD11c and MHC-II (approx. 4-fold), CD86 (approx. 8-fold) and CD40 (approx. 7-fold). Interestingly, the mannose-receptor (MR) surface expression remained at basal levels after 24 h of incubation with FA-PLGA NP, whereas after exposure to CS-FA-PLGA NP it increased after 2 h of incubation, then decreased below basal levels after 4 h, and after 24 h of incubation it finally increased again by 2.5-fold (Figure 5, *A* and *B*). Thus, our results revealed that even after 24 h of incubation with FA-PLGA or CS-FA-PLGA NP there was no significant up-regulation of activation markers on the surface of moDC, except for the MR, which was differentially regulated upon CS-PLGA NP treatment.

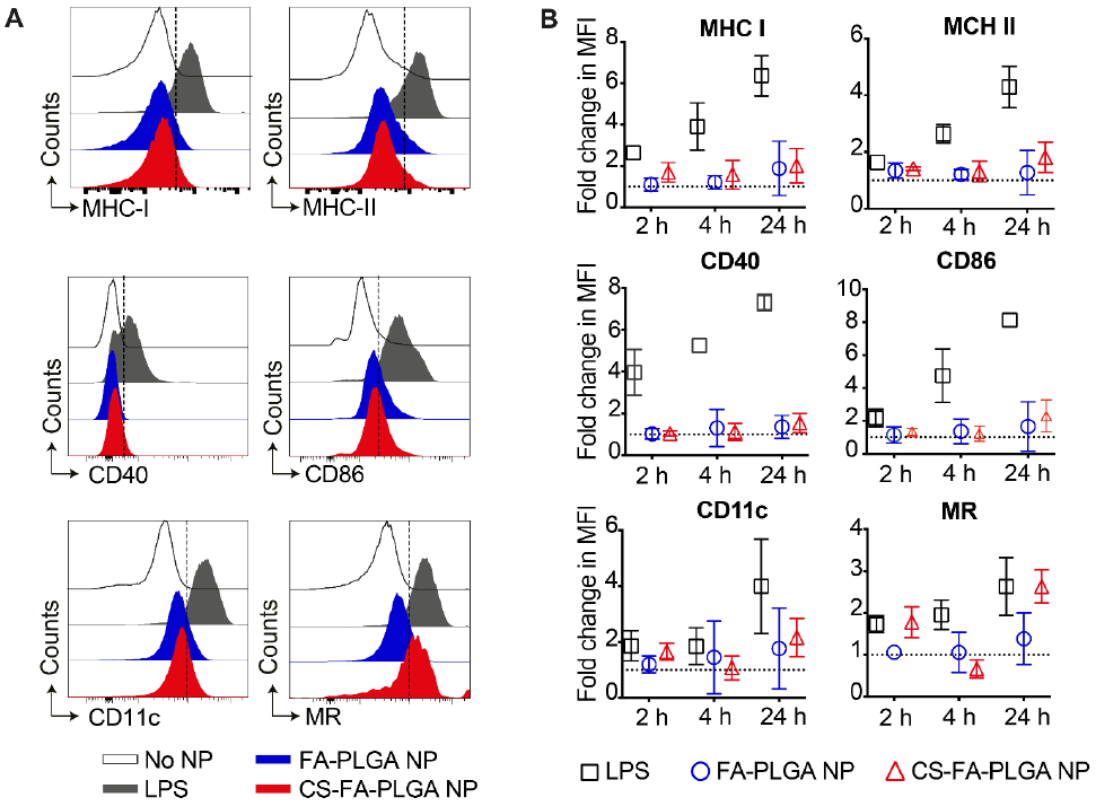

Figure 5: Human moDC are not activated upon treatment with FA-PLGA or CS-FA-PLGA nanoparticle. moDC prepared as described in Figure 4 were treated with 60 µg/ml of FA-PLGA or CS-FA-PLGA NP at 37°C for 2, 4 and 24 h, stained for surface activation markers and analyzed by flow cytometry. LPS (100 ng/ml) was used as a positive control. **(A)** Histograms correspond to surface expression of MHC-I, CD11c, MHC-II, CD86, mannose receptor (MR) and CD40 for one representative donor. **(B)** Values shown correspond to fold increase in mean fluorescent intensity (MFI) compared to basal conditions (no NP treatment). N=5 from 3 independent experiments.

Within moDC, FA-labeled chitosan-coated PLGA nanoparticles are preferentially delivered to early and late endosomes

To further study the intracellular localization after NP uptake, moDC were incubated for 2 h with FA-PLGA or CS-FA-PLGA NP, the cells were fixed, markers for intracellular organelles were immunolabeled with specific antibodies and confocal microscopic analysis was performed. All images were further analyzed with ImageJ to determine the colocalization between FA fluorescence derived from internalized NP and labeled subcellular compartments, as indicated by the Pearson's correlation coefficient (PCC). In these assays, Rab5a was used as a marker for early endosomes, which appear in early stages of endocytosis, whereas Rab7 was used to identify late endosomes, which develop after acidification of early endosomes (Figure 6, *A*). Upon treatment of moDC with FA-PLGA NP, a PCC with Rab5a and Rab7 of approx. 0.3 was detected, whereas upon treatment with CS-FA-PLGA NP a significantly enhanced value of approx. 0.5 was obtained. Interestingly, Lamp1 that was used as a marker for lysosomes, which are the most acidic organelle of cells, gave a PCC of approx. 0.4 with FA-PLGA NP, while with CS-FA-PLGA NP a value of 0.2 was obtained (Figure 6, *B* and *C*). To identify recycling endosomes, the marker Rab11 was analyzed, which resulted in PCC values below 0.2 for both NP. This was also the case for BiP, which was used as a marker for the endoplasmic reticulum (ER), and for GM130, which is a marker for the Golgi bodies (Supplementary Figure 4). Thus, while both NP preparations colocalized similarly low with recycling endosomes, the ER, and Golgi bodies, CS-FA-PLGA NP showed a higher colocalization with early and late endosomes than FA-PLGA NP, which colocalized to a higher extent with lysosomes.

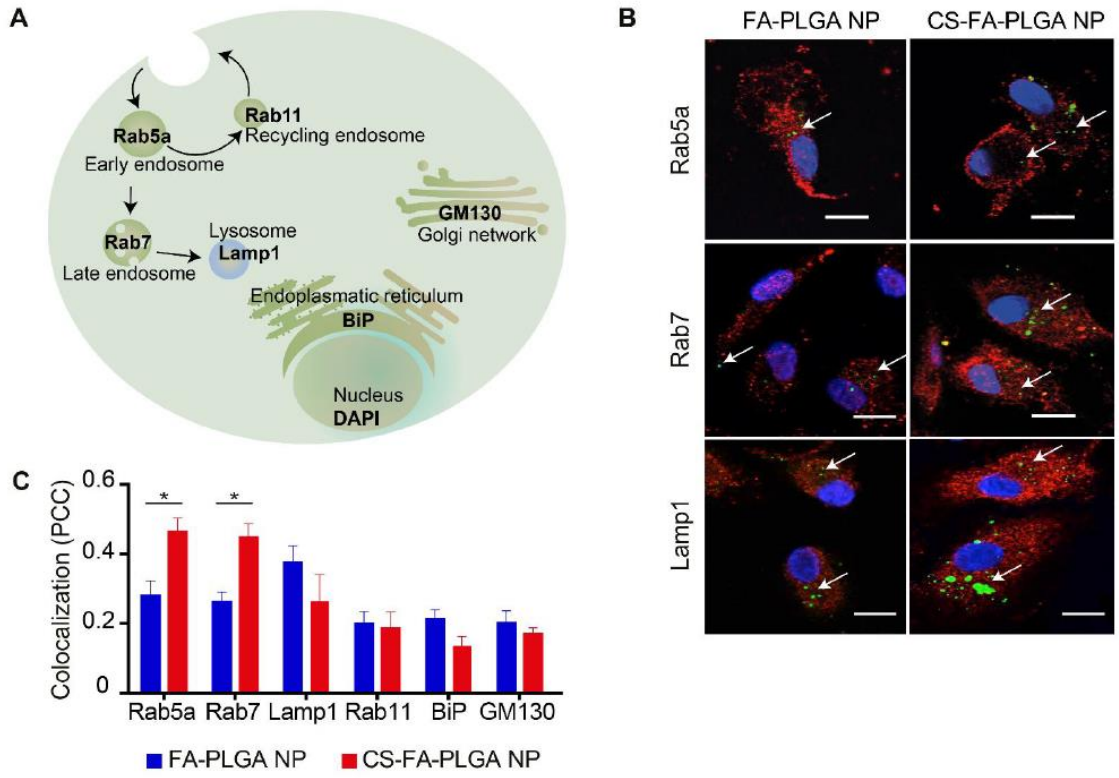

Figure 6: CS-FA-PLGA nanoparticles are preferentially delivered to endosomal compartments. **(A)** Schematic depiction of organelle-specific markers used to label cellular compartments within moDC (early endosomes (Rab5a), late endosomes (Rab7), lysosomes (Lamp1), recycling endosomes (Rab11), endoplasmatic reticulum (BiP), and Golgi bodies (GM130)). **(B)** Human moDC generated as described in Figure 4 were treated with 60 µg/ml of FA-PLGA or CS-FA-PLGA NP for 2 h at 37°C, fixed, and intracellular organelles were immunolabeled and counter-stained with an Alexa Fluor 647-coupled secondary antibody. DAPI staining was performed to identify the cell nuclei and samples were analyzed by confocal microscopy. Scale bar represents 1 µm. **(C)** Pearson's correlation coefficient (PCC) between organelle markers and FA-fluorescence derived from CS-FA-PLGA or FA-PLGA NP. For each donor a minimum of 3 photos was analyzed, each image comprising 5-10 cells. The error bars indicate mean ± SD (two-way ANOVA $*p \leq 0.033$, N=3 donors from 2 independent experiments).

Discussion

Nanoparticulated delivery systems hold promise as innovative formulations to enhance efficacy and reduce adverse effects of new drugs. As drug delivery vehicles, ideally they should be able to target specific cells without inducing adverse reactions. Furthermore, an in-depth understanding of the interaction of nanoparticle formulations with human immune cells is of key relevance, as regardless of the application route that eventually will be chosen, such nanoparticle drug formulations will come in direct contact with blood or tissue-resident immune cells. Here we found that amongst PBMC, APC effectively internalize FA-PLGA and CS-FA-PLGA NP. In moDC, these NP caused low cytotoxic effects and they did not confer immunostimulatory effects. We additionally discovered that moDC show a preferential uptake of CS-FA-PLGA NP, which upon internalization are mostly delivered to early and late endosomes.

PLGA and CS-PLGA NP were generated by using pharmaceutical grade excipients. Additionally, the raw materials as well as the final products were thoroughly tested for LPS contaminations. NP generated under such conditions showed high quality, including absence of any detectable LPS contamination, as well as consistent physicochemical and morphological properties, even after addition of the FA fluorescent dye. Additionally, both NP had only minor toxic effects at concentrations below 100 µg/ml and only a moderate increase in cytotoxicity was observed at very high doses.

Therefore, we proceeded with experiments in human PBMC to assess the internalization of FA-PLGA and CS-FA-PLGA NP. We observed that despite the far more abundant presence of T cells, both NP were preferentially taken up by APC.

Amongst APC, monocytes showed an enhanced uptake of both NP preparations when compared with DC. Presumably, this is due to the innate phagocytic function of APC, which is basically absent in lymphocytes. Interestingly, after short incubation times APC showed more efficient internalization of CS-FA-PLGA NP than of FA-PLGA NP. Such faster uptake kinetics of CS-FA-PLGA NP can be attributed to specific chitosan interactions with endocytic receptors that are expressed by APC (24) as well as to the electrostatic attraction caused by the positively charged chitosan and the negatively charged cell surface (25). These traits could be exploited, e.g., during i.v. injection of CS-PLGA NP to selectively target recirculating APC within the blood, whereas upon i.m. injection of PLGA NP enhanced interaction times between the NP and the APC might be available in the draining lymph node, which might allow NP uptake independent of the functionalization with chitosan. Nevertheless, such strategies would have to be carefully studied in relevant animal models before applications in humans can be considered.

Moreover, we observed a strong preference in the uptake of CS-FA-PLGA NP by moDC when compared with FA-PLGA NP. Beyond the electrostatic advantage that CS-FA-PLGA NP have over FA-PLGA NP, this can be explained by the fact that moDC show high expression of receptors involved in chitosan sensing. Amongst these, TLR2, Dectin-1 and the mannose receptor (MR) (26, 27) play major roles and are known to enhance cellular uptake upon involvement (28). In this context, chitosan functionalization of PLGA NP might promote receptor-mediated endocytosis, which seems to be more efficient than non-specific uptake of non-functionalized PLGA NP.

As suspected from the consistent quality of both NP preparations, we did not observe any activation of moDC following FA-PLGA or CS-FA-PLGA NP treatment in moDC. Nevertheless, a slight regulation in the surface expression of the MR was observed upon treatment with CS-FA-PLGA NP. MR surface expression was first increased, then decreased and later increased again. These results are compatible with the hypothesis that the MR is the main receptor involved in the recognition of chitosan derivatives (31) and as it is an endocytic receptor, it is also internalized to endosomal compartments and further re-shuttled in its empty form back to the plasma membrane (32). Of note, other studies have shown that the efficacy of DC-targeted delivery might be enhanced using natural ligands that bind DC-specific receptors, compared with approaches using specific antibodies. The strategy to use natural receptor ligands for NP functionalization promotes receptor recycling and thus, increases the rate of antigen internalization (37).

Furthermore, we found that CS-FA-PLGA NP are mostly delivered to early and late endosomes, while non-functionalized FA-PLGA NP mostly end up in other subcellular compartments, such as lysosomes. This further points towards receptor-mediated endocytosis of CS-FA-PLGA NP, as it has been proven that recognition via the abovementioned receptors mediates delivery into endosomal compartments via a tyrosine-based motif in the receptor cytoplasmic tail (29, 30).

Interestingly, moDC showed a higher uptake of CS-FA-PLGA NP when compared with DC within PBMC. As *in vitro* generated moDC resemble DC generated under inflammatory conditions *in vivo*, they are known to have a higher endocytic capacity as well as higher expression of surface receptors such as the MR, in comparison to

As suspected from the consistent quality of both NP preparations, we did not observe any activation of moDC following FA-PLGA or CS-FA-PLGA NP treatment in moDC. Nevertheless, a slight regulation in the surface expression of the MR was observed upon treatment with CS-FA-PLGA NP. MR surface expression was first increased, then decreased and later increased again. These results are compatible with the hypothesis that the MR is the main receptor involved in the recognition of chitosan derivatives (31) and as it is an endocytic receptor, it is also internalized to endosomal compartments and further re-shuttled in its empty form back to the plasma membrane (32). Of note, other studies have shown that the efficacy of DC-targeted delivery might be enhanced using natural ligands that bind DC-specific receptors, compared with approaches using specific antibodies. The strategy to use natural receptor ligands for NP functionalization promotes receptor recycling and thus, increases the rate of antigen internalization (37).

Furthermore, we found that CS-FA-PLGA NP are mostly delivered to early and late endosomes, while non-functionalized FA-PLGA NP mostly end up in other subcellular compartments, such as lysosomes. This further points towards receptor-mediated endocytosis of CS-FA-PLGA NP, as it has been proven that recognition via the abovementioned receptors mediates delivery into endosomal compartments via a tyrosine-based motif in the receptor cytoplasmic tail (29, 30).

Interestingly, moDC showed a higher uptake of CS-FA-PLGA NP when compared with DC within PBMC. As *in vitro* generated moDC resemble DC generated under inflammatory conditions *in vivo*, they are known to have a higher endocytic capacity as well as higher expression of surface receptors such as the MR, in comparison to

partially supported by the Helmholtz “Zukunftsthema Immunology & Inflammation” (ZT-0027) (to U.K.).

Conflict of interest: The authors declare no conflict of interest

References

1. Senapati S, Mahanta AK, Kumar S, Maiti P. Controlled drug delivery vehicles for cancer treatment and their performance. Signal Transduction and Targeted Therapy. 2018;3(1):7.
2. Getts DR, Shea LD, Miller SD, King NJC. Harnessing nanoparticles for immune modulation. Trends in immunology. 2015;36(7):419-27.
3. Du J, Zhang YS, Hobson D, Hydbring P. Nanoparticles for immune system targeting. Drug Discovery Today. 2017;22(9):1295-301.
4. Sussman E, Clark M, Shastri VP. Functionalized Polymeric Nanoparticles. MRS Proceedings. 2004;818:M12.9.1.
5. Gregory AE, Titball R, Williamson D. Vaccine delivery using nanoparticles. Frontiers in Cellular and Infection Microbiology. 2013;3:13.
6. Hartshorn CM, Bradbury MS, Lanza GM, Nel AE, Rao J, Wang AZ, et al. Nanotechnology Strategies To Advance Outcomes in Clinical Cancer Care. ACS nano. 2018;12(1):24-43.
7. Wong JKL, Mohseni R, Hamidieh AA, MacLaren RE, Habib N, Seifalian AM. Will Nanotechnology Bring New Hope for Gene Delivery? Trends in Biotechnology. 2017;35(5):434-51.
8. Schmid D, Park CG, Hartl CA, Subedi N, Cartwright AN, Puerto RB, et al. T cell-targeting nanoparticles focus delivery of immunotherapy to improve antitumor immunity. Nature Communications. 2017;8(1):1747.
9. Parveen S, Misra R, Sahoo SK. Nanoparticles: a boon to drug delivery, therapeutics, diagnostics and imaging. Nanomedicine: Nanotechnology, Biology and Medicine. 2012;8(2):147-66.
10. Oberdörster G. Safety assessment for nanotechnology and nanomedicine: concepts of nanotoxicology. Journal of Internal Medicine. 2009;267(1):89-105.
11. Veno K, Mojca N, Damjana D. Nanoparticle interaction with the immune system / Interakcije nanodelcev z imunskim sistemom. Archives of Industrial Hygiene and Toxicology. 2015;66(2):97-108.
12. Zolnik BS, González-Fernández Á, Sadrieh N, Dobrovolskaia MA. Nanoparticles and the Immune System. Endocrinology. 2010;151(2):458-65.
13. Dobrovolskaia MA, Shurin M, Shvedova AA. Current understanding of interactions between nanoparticles and the immune system. Toxicology and Applied Pharmacology. 2016;299:78-89.
14. Ravi Kumar MNV, Bakowsky U, Lehr CM. Preparation and characterization of cationic PLGA nanospheres as DNA carriers. Biomaterials. 2004;25(10):1771-7.
15. Mittal A, Raber AS, Schaefer UF, Weissmann S, Ebensen T, Schulze K, et al. Non-invasive delivery of nanoparticles to hair follicles: A perspective for transcutaneous immunization. Vaccine. 2013;31(34):3442-51.
16. Jayakumar R, Nwe N, Tokura S, Tamura H. Sulfated chitin and chitosan as novel biomaterials. International Journal of Biological Macromolecules. 2007;40(3):175-81.
17. Makadia HK, Siegel SJ. Poly Lactic-co-Glycolic Acid (PLGA) as Biodegradable Controlled Drug Delivery Carrier. Polymers. 2011;3(3):1377-97.
18. Mittal A, Schulze K, Ebensen T, Weißmann S, Hansen S, Lehr CM, et al. Efficient nanoparticle-mediated needle-free transcutaneous vaccination via hair follicles requires adjuvantation. Nanomedicine: Nanotechnology, Biology and Medicine. 2015;11(1):147-54.

19. Haque AKMA, Dewerth A, Antony JS, Riethmüller J, Latifi N, Yasar H, et al. Modified hCFTR mRNA restores normal lung function in a mouse model of cystic fibrosis. bioRxiv. 2017.
20. Mahiny AJ, Dewerth A, Mays LE, Alkhaled M, Mothes B, Malaeksefat E, et al. In vivo genome editing using nuclease-encoding mRNA corrects SP-B deficiency. Nature Biotechnology. 2015;33:584.
21. Zupančič E, Curato C, Paisana M, Rodrigues C, Porat Z, Viana AS, et al. Rational design of nanoparticles towards targeting antigen-presenting cells and improved T cell priming. Journal of Controlled Release. 2017;258:182-95.
22. Yasar H, Ho D-K, De Rossi C, Herrmann J, Gordon S, Loretz B, et al. Starch-Chitosan Polyplexes: A Versatile Carrier System for Anti-Infectives and Gene Delivery.
23. Weiss B, Schaefer UF, Zapp J, Lamprecht A, Stallmach A, Lehr CM. Nanoparticles made of fluorescence-labelled Poly(L-lactide-co-glycolide): preparation, stability, and biocompatibility. Journal of nanoscience and nanotechnology. 2006;6(9-10):3048-56.
24. Dumitriu S. Polymeric Biomaterials, Revised and Expanded: CRC Press; 2001.
25. Duck Weon L, Hosun L, Ha Na C, Woo Sub S. Advances in chitosan material and its hybrid derivatives: a review. The Open Biomaterials Journal. 2009;1(1):10-20.
26. Bueter CL, Specht CA, Levitz SM. Innate Sensing of Chitin and Chitosan. PLOS Pathogens. 2013;9(1):e1003080.
27. van Kooyk Y. C-type lectins on dendritic cells: key modulators for the induction of immune responses. Biochemical Society Transactions. 2008;36(6):1478.
28. Kerrigan AM, Brown GD. C-type lectins and phagocytosis. Immunobiology. 2009;214(7):562-75.
29. Burgdorf S, Kurts C. Endocytosis mechanisms and the cell biology of antigen presentation. Current Opinion in Immunology. 2008;20(1):89-95.
30. Moseman AP, Moseman EA, Schworer S, Smirnova I, Volkova T, von Andrian U, et al. Mannose receptor (MRC1) mediates cellular uptake and endosomal delivery of CpG-ODN. Journal of immunology (Baltimore, Md : 1950). 2013;191(11):10.4049/jimmunol.1301438.
31. Han Y, Zhao L, Yu Z, Feng J, Yu Q. Role of mannose receptor in oligochitosan-mediated stimulation of macrophage function. International Immunopharmacology. 2005;5(10):1533-42.
32. Taylor PR, Gordon S, Martinez-Pomares L. The mannose receptor: linking homeostasis and immunity through sugar recognition. Trends in Immunology. 2005;26(2):104-10.
33. Tacken PJ, de Vries IJM, Torensma R, Figdor CG. Dendritic-cell immunotherapy: from ex vivo loading to in vivo targeting. Nature Reviews Immunology. 2007;7:790.
34. Segura E, Amigorena S. Inflammatory dendritic cells in mice and humans. Trends in Immunology. 2013;34(9):440-5.
35. Min J, Yang D, Kim M, Haam K, Yoo A, Choi JH, et al. Inflammation induces two types of inflammatory dendritic cells in inflamed lymph nodes. Experimental & molecular medicine. 2018;50(3):e458.
36. Savina A, Amigorena S. Phagocytosis and antigen presentation in dendritic cells. Immunological reviews. 2007;219(1):143-56.

37. Tacken PJ, ter Huurne M, Torensma R, Figdor CG. Antibodies and carbohydrate ligands binding to DC-SIGN differentially modulate receptor trafficking. 2012;42(8):1989-98.
38. Lambricht L, Peres C, Florindo H, Préat V, Vandermeulen G. Chapter Ten - Polymer-Based Nanoparticles as Modern Vaccine Delivery Systems. In: Skwarczynski M, Toth I, editors. Micro and Nanotechnology in Vaccine Development: William Andrew Publishing; 2017. p. 185-203.
39. Klippstein R, Pozo D. Nanotechnology-based manipulation of dendritic cells for enhanced immunotherapy strategies. Nanomedicine: Nanotechnology, Biology and Medicine. 2010;6(4):523-9.
40. Kishimoto TK, Maldonado RA. Nanoparticles for the Induction of Antigen-Specific Immunological Tolerance. Frontiers in Immunology. 2018;9:230.
41. Unanue ER. Intracellular Pathogens and Antigen Presentation—New Challenges with Legionella Pneumophila. Immunity. 2003;18(6):722-4.
42. Khan N, Gowthaman U, Pahari S, Agrewala JN. Manipulation of Costimulatory Molecules by Intracellular Pathogens: Veni, Vidi, Vici!! PLOS Pathogens. 2012;8(6):e1002676.

6.2 Modelling the Bronchial Barrier in Pulmonary Drug Delivery: A Human Bronchial Epithelial Cell Line Supplemented with Human Tracheal Mucus

Modelling the bronchial barrier in pulmonary drug delivery: a human bronchial epithelial cell line supplemented with human tracheal mucus

Xabi Murgia, Hanzey Yasar, Cristiane Carvalho-Wodarz, Brigitta Loretz, Sarah Gordon, Konrad Schwarzkopf, Ulrich Schaefer, Claus-Michael Lehr; European Journal of Pharmaceutics Biopharmaceutics 118 (**2017**) 79–88.

DOI: 10.1016/j.ejpb.2017.03.020

European Journal of Pharmaceutics and Biopharmaceutics 118 (2017) 79–88

Contents lists available at ScienceDirect

European Journal of Pharmaceutics and Biopharmaceutics

journal homepage: www.elsevier.com/locate/ejpb

Modelling the bronchial barrier in pulmonary drug delivery: A human bronchial epithelial cell line supplemented with human tracheal mucus

Xabi Murgia [a], Hanzey Yasar [a], Cristiane Carvalho-Wodarz [a], Brigitta Loretz [a], Sarah Gordon [a], Konrad Schwarzkopf [b], Ulrich Schaefer [c], Claus-Michael Lehr [a,c,*]

[a] Helmholtz Institute for Pharmaceutical Research Saarland (HIPS), Helmholtz Centre for Infection Research (HZI), Saarland University, 66123 Saarbrücken, Germany
[b] Department of Anesthesia and Intensive Care, Klinikum Saarbrücken, 66119 Saarbrücken, Germany
[c] Biopharmaceutics and Pharmaceutical Technology, Department of Pharmacy, Saarland University, 66123 Saarbrücken, Germany

ARTICLE INFO

Article history:
Received 28 November 2016
Revised 16 March 2017
Accepted in revised form 28 March 2017
Available online 1 April 2017

Keywords:
Cystic fibrosis
Pulmonary mucus
Epithelial drug delivery
Nanoparticles

ABSTRACT

The airway epithelium together with the mucus layer coating it forms a protective system that efficiently filters and removes potentially harmful particles contained in inhaled air. The same mechanism, however, serves to entrap particulate drug carriers, precluding their interaction with their target. The mucus barrier is often neglected in *in vitro* testing setups employed for the assessment of pulmonary drug delivery strategies. Therefore, our aim was to more accurately model the bronchial barrier, by developing an *in vitro* system comprising a tight epithelial cell layer which may be optionally supplemented with a layer of human tracheal mucus. To form the epithelium *in vitro*, we used the cystic fibrosis cell line CFBE41o-, which can be grown as monolayers on Transwell® supports, expressing tight junctions as well as relevant transport proteins. In contrast to the cell line Calu-3, however, CFBE41o- does not produce mucus. Therefore, native human mucus, obtained from tracheal tubes of patients undergoing elective surgery, was used as a supplement. The compatibility of CFBE41o- cells with the human mucus was addressed with the MTT assay, and confirmed by fluorescein diacetate/propidium iodide live/dead staining. Moreover, the CFBE41o- cells retained their epithelial barrier properties after being supplemented with mucus, as evidenced by the high trans-epithelial electrical resistance values (~1000 Ω cm^2) together with a continued low level of paracellular transport of sodium fluorescein. Fluorescently-labeled chitosan-coated PLGA nanoparticles (NP, ~168 nm) were used as a model drug delivery system to evaluate the suitability of this *in vitro* model for studying mucus permeation and cell uptake. Comparing CFBE41o- cell monolayers with and without mucus, resp., showed that the NP uptake was dramatically reduced in the presence of mucus. This model may therefore be used as a tool to study potential mucus interactions of aerosolized drugs, and more specifically NP-based drug delivery systems designed to exert their effect in the bronchial region.

1. Introduction

The conducting airways of the lungs are coated with a viscoelastic secretion, the pulmonary mucus, which moisturizes the inhaled air and acts as a filter for inhaled particles. In the healthy state, mucus is composed of water (95% w/w), glycoproteins (mucins, 2–5%), salts, non-mucin proteins, lipids, DNA, enzymes, cells and bacteria [1–3]. The mucins are continuously secreted into the airway lumen by specialized secretory cells, and polymerize to form a mesh-like structure that is constantly being propelled out of the lungs by the ciliary beating of the airway epithelial cells – this creates a dynamic barrier termed as mucociliary clearance [4–6]. In disease states such as asthma, chronic obstructive pulmonary disease (COPD), and in particular cystic fibrosis (CF) considerable changes in the mucus can occur, leading to mucus oversecretion and mucus thickening [7–10]; this in turn can compromise the mucus clearance mechanism, providing optimal conditions for bacterial growth and chronic infection [11].

CF is a lethal genetic disease caused by a mutation of the CF transmembrane conductance regulator (CFTR). This results in numerous irregularities including an abnormal hydration of the airways, which leads to an impairment of the mucociliary machinery, recurrent infections, and eventually premature death [11]. The clinical management of CF focuses primarily on improving the mucociliary clearance and combating chronic infections rather

* Corresponding author at: Helmholtz Institute for Pharmaceutical Research Saarland (HIPS), Helmholtz Centre for Infection Research (HZI), Saarland University, 66123 Saarbrücken, Germany.
E-mail address: claus-michael.lehr@helmholtz-hzi.de (C.-M. Lehr).

http://dx.doi.org/10.1016/j.ejpb.2017.03.020
0939-6411/

than targeting the primary cause, namely correcting the genetic disease. The potential of nanomedicine to improve the efficiency of gene-therapy in such diseases by using nanoparticle (NP)-based drug delivery systems is considerable, as evidenced by efficient transfection of cell-based *in vitro* models including the CF cell line CFBE41o- [12–14]. This cell line was generated by transformation of CF airway cells with the SV40 virus and is homozygous for the most common CF mutation, the F508-CFTR mutation. Of particular interest to pharmaceutical research is the ability of this cell line to express tight-junction proteins such as claudin-1, ZO-1, and occludin [15], which confer on CFBE41o- monolayers significant epithelial barrier properties evidenced by high transepithelial electrical resistance (TEER) values [15–18]. This cell line also expresses a number of proteins relevant for pulmonary drug transport, including P-glycoprotein (P-gp), lung resistance-related P protein (LRP), and caveolin-1 [15]. Unfortunately, unlike other pulmonary cell lines such as Calu-3, which are able to secrete mucus [19–21], the CFBE41o- cell line lacks the capacity to synthesize and secret mucus onto the cell monolayer – a key feature that must be taken into account in the context of airway research. In particular, with regard to the use of NP-based drug delivery systems to treat bronchial diseases, our work and that of others has previously shown that particles with a diameter above 200 nm are almost exclusively trapped within the pulmonary mucus [3,22,23]. Moreover, with a net negative charge under physiological conditions [24,25], mucus represents a significant barrier to positively charged nanocarriers [21,26], which are often used in the context of nucleic acid delivery for transfection purposes [27–29].

Therefore, in the present study we explored the possibility to develop an *in vitro* model of the airways composed of a CFBE41o- cell layer coated with human tracheal mucus. Our aim was to take a step forward in accurately mimicking the scenario within the CF lung, by utilizing the positive features of the CFBE41o- cell line in the context of pharmaceutical research and further introducing mucus as a key non-cellular barrier of the airways. For this purpose we cultured CFBE41o- cells in Transwell® supports and added a layer of human tracheal mucus on top of the cell monolayer, creating an air-mucus interface. The biocompatibility of CFBE41o- cells with the human tracheal mucus was investigated by measurement of epithelial barrier properties upon incubation with the exogenous mucus. Ultimately, as a proof-of-concept validation of the implemented *in vitro* model, we produced chitosan-poly(D,L-lactide-co-glycolide; PLGA) nanoparticles and determined the effect of the mucus layer on the cellular uptake of such particles.

2. Methods

2.1. Human mucus sample collection

Undiluted human tracheal mucus samples were collected by the endotracheal tube method [3,30,31], after obtaining informed consent from patients and in compliance with a protocol approved by the Ethics Commission of The Chamber of Medicine Doctors of the Saarland (file number 19/15). The tracheal tube of patients undergoing elective surgery with general anesthesia, non-related to pulmonary conditions, was collected after surgery. The distal portion of the tracheal tube (5–10 cm), including the balloon, was cut and placed in a 50 ml centrifuge tube. The mucus of each tracheal tube was collected by centrifuging the samples at 190*g* for 30 s. Samples with visible blood contamination were excluded from the analysis. Mucus samples were stored at −20 °C until further use. In total 16 mucus samples from independent patients were used in this study. The mean age of the patients was 56.8 ± 4.8 years, the male: female ratio was 12:4, and 6 out of 16 patients were smokers.

2.2. Freeze-dried mucus disk preparation

Mucus samples frozen and stored at −20 °C were thawed gradually and allowed to reach room temperature. Thereafter, single mucus drops with an approximate weight of 30–40 mg (34.17 ± 1.82 mg, n = 45 mucus drops) were placed over a Teflon® surface and spread over delineated circular surfaces of 1.12 cm^2. The samples were then placed into an autoclavable sealing bag, stored at −80 °C for 4 h, and ultimately, freeze-dried overnight (Alpha 2-4 LSC, Christ, Germany). After completion of the preset freeze-drying program, the bag containing the mucus disks (1.7 ± 0.1 mg estimated solid content, for an estimated water content of 95%) was immediately sealed and stored in a dry atmosphere at room temperature until further use. Five different batches with 14–20 mucus disks per batch were used in this study.

2.3. Mucus characterization

2.3.1. Mucus bulk rheology

Experiments were conducted on an Anton-Paar MCR 102 rheometer (Graz, Austria) equipped with cone-plate geometry (diameter: 25 mm, cone angle: 2°) at room temperature. Strain amplitude (γ) sweeps were performed at a frequency of 1 Hz in the range of 0.1–10%. Frequency (ω) dependency of the storage modulus G' and the loss modulus G'' was measured in the range between 0.1 and 40 rad/s at a strain amplitude of 1%.

In the first set of experiments native undiluted tracheal mucus samples were gradually thawed and allowed to reach room temperature. Thereafter, an approximate volume of 150 µl of mucus was placed in the rheometer and the aforementioned protocol was conducted. In the second set of experiments previously freeze-dried and rehydrated mucus samples were analyzed. Mucus samples contained in 1.5 ml Eppendorf tubes were allowed to equilibrate to room temperature and weighed using a precision balance (CPA 224S, Sartorius, Göttingen, Germany). Afterwards, the samples were stored at −80 °C for 4 h followed by overnight freeze-drying (Alpha 2-4 LSC, Christ, Osterode am Harz, Germany). The freeze-dried (solid) content of the samples was weighed again to determine the water content of mucus. Mucus samples were then re-hydrated with exactly the same volume of sublimed water (Milli-Q water, Advantage A10, Merck Millipore, Billerica, MA), and were allowed to mix in a 360° multi-rotator (PTR-35, Grant instruments, UK) for at least two hours at room temperature. Thereafter, re-hydrated mucus samples were placed in the rheometer to perform the measurements as described above.

2.3.2. Scanning electron microscopy

The structure of pulmonary mucus was imaged by means of scanning electron microscopy (SEM). Human tracheal mucus samples were gradually thawed and spread over the surface of a SEM-imaging carbon disk. The mucus was freeze-dried *in situ* following the freeze-drying protocol as in Section 2.2. Freeze-dried mucus samples were gold-sputtered (QUORUM Q150R ES, Gala Instrumente, Germany) and then transferred to the SEM (EVO HD15, Zeiss, Germany) for imaging.

In order to image the CFBE41o- cell monolayer and the combined model comprising the cell monolayer and the overlying mucus, the cells were seeded onto Transwell® permeable supports and were cultured until a confluent monolayer was reached (see Section 2.4). The day before the SEM fixation the apical culture medium was removed and a mucus disk together with 100 µl of fresh medium were added to the apical compartment, creating an air mucus interface. The cells with the mucus disks in place were incubated for 24 h at 37 °C, 5% CO_2, in a horizontal shaker. After incubation the basolateral medium was aspirated and fixation was performed by adding 1 ml of glutaraldehyde 3% (Sigma)

in PBS to the basolateral compartment for 2 h. Subsequently, dehydration was carried out through a graded series of ethanol (30–100%, 10 min each). In the final step 150 µl of hexamethyldisilazane (Fluka) were added to the apical compartment. The filter of the Transwells® was then cut with a scalpel and mounted onto SEM-stacks. Samples were further sputtered with gold and transferred to the electron microscope.

2.4. Cell culture of CFBE41o-

CFBE41o- cells were a kind gift of Dr. Dieter C. Gruenert (University of California, San Francisco, CA, USA). Passages 78–90 were used in this study. Cells were passaged on a weekly basis (0.2×10^6 cells in a T75 flask) and grown in minimum essential medium (MEM, Gibco) supplemented with 10% fetal calf serum (FCS, Lonza), 5% non-essential amino acids (NEAA 100x, Gibco), 0.54 mg/ml of D-(+)-glucose (Sigma), and 100 µg/ml streptomycin and 100 U/ml penicillin, at 37 °C in a 5% CO_2 incubator. Unless otherwise stated, for experimental purposes cells were seeded onto Transwell® permeable supports (3640, Insert diameter 12 mm, growth area 1.12 cm^2, pore size 0.4 µm; Corning, Wiesbaden, Germany) at a density of 1.5×10^5 cells/cm^2 and grown under submerged conditions with apical/basolateral fluid volumes of 500 µl/1100 µl, respectively. The culture medium was replaced every 2–3 days.

2.5. Nanoparticle preparation and characterization

PLGA (50:50; Resomer RG 503H) was purchased from Evonik Industries AG (Darmstadt, Germany); ultrapure chitosan chloride salt (Protasan UP CL113) was obtained from FMC Biopolymer AS NovaMatrix (Sandvika, Norway). Polyvinyl alcohol (PVA) Mowiol®4-88 was purchased from Sigma-Aldrich (Germany); the lipophilic fluorescent dye 1,1′-dioctadecyl-3,3,3′,3′-tetramethylin dodicarbocyanine perchlorate (DiD) was obtained from Thermofisher Scientific (Oregon, USA). Ethyl acetate was purchased from Sigma-Aldrich (Germany), and purified water was produced freshly by a Milli-Q water purification system (Merck Millipore, Billerica, MA).

Drug free, DiD-labeled chitosan-PLGA NPs were used as a model drug delivery system to evaluate the uptake behavior on CFBE41o- cell monolayers with and without mucus. Such NPs were prepared by using a modified double-emulsion method according to Mittal et al. [32]. Briefly, a 0.2% w/v chitosan solution was first prepared by dissolving Protasan UP CL113 in a 2% w/v PVA solution. A 50 mg amount of PLGA was dissolved in 2 ml ethyl acetate and equilibrated with 15 µg/20 µl of DiD ethanolic solution under continuous stirring for 1 h at room temperature. A 400 µl volume of water was then added to the PLGA organic phase and sonicated with ultrasound (Branson Ultrasonic Corporation, USA) at 20% amplitude for 20 s to allow the primary emulsion to form. Immediately afterwards, the PVA chitosan solution was applied to the primary emulsion and sonicated using the same settings, leading to the formation of a w/o/w emulsion. Milli-Q water was added dropwise to the w/o/w emulsion to allow for the evaporation of the organic solvent. The resulting chitosan coated PLGA NPs were purified by centrifugation at 15,000*g* for 15 min and washed once with milli-Q water to remove any excess free dye. The size, polydispersity index (PDI) and ζ-potential of the DiD labeled chitosan-PLGA NPs were characterized using a Zetasizer Nano (Malvern Instruments, Malvern, UK). The morphological appearance of the carrier system was visualized using Transmission Electron Microscopy (TEM, JEM 2011, JEOL) and further with SEM (EVO HD15, Zeiss, Germany). Prior to the SEM measurements, NPs were put onto a carbon disk and gold-sputtered. In order to improve the contrast of the TEM images, NPs were further stained with 0.5% w/v phosphotungstic acid (Sigma).

2.6. Cytotoxicity assays

2.6.1. MTT assay

CFBE41o- cells were seeded in 96 well plates at a density of 20,000 cells per well and grown for 4 days. Cells were then washed twice with Hank's balanced salt solution (HBSS, Gibco) buffer, and 200 µl of fresh culture medium together with a freeze-dried mucus disk were added to the test wells. The cells were incubated for 24 h at 37 °C and 5% CO_2 in a horizontal shaker. Cells incubated with cell culture medium only served as positive controls (100% viability) and cells incubated with Triton-X 1% (Sigma) served as negative controls (0% viability). Following incubation, the mucus was removed by aspiration and the cells were washed twice with HBSS buffer. A 200 µl volume of the tetrazolium dye MTT (5 mg/ml) was added to each well, followed by 4 h incubation at 37 °C, 5% CO_2, in a horizontal shaker. Formed formazan crystals were then solubilized by adding 200 µl of dimethyl sulfoxide (DMSO, Sigma). The absorbance of each well at 560 nm was measured with a plate reader (Infinite M200 Pro, TECAN), and the percentage of viable cells in each well was calculated as previously described [33].

2.6.2. Live/dead staining with fluorescein diacetate (FDA) and propidium iodide (PI)

Cell monolayers were cultured for at least 10 days under submerged conditions. Live cells can take up and convert the non-fluorescent FDA into its fluorescent product fluorescein by means of cytosolic esterases, whereas PI cannot cross the membrane of viable cells but will stain the nuclei of non-viable cells by intercalating with the double helix DNA. Approximately 24 h before live/dead staining the apical medium was removed from each culture well and a mucus disk together with 100 µl of fresh culture medium were added to apical compartments. The cells with the mucus disks in place were incubated for 24 h at 37 °C and 5% CO_2 in a horizontal shaker. After 24 h, the mucus disks had dissolved creating an air-mucus interface in the apical compartment of each Transwell®. To proceed with the live/dead staining, medium was aspirated from mucus-containing apical compartments which were then washed twice with fresh medium. The cells were allowed to equilibrate for 30 min with 500 µl of freshly added cell culture medium, before this was replaced by 500 µl of the working solution of the FDA/PI live/dead stain (Sigma). The working solution itself was prepared in a 5 ml volume by adding 20 µl of FDA (5 mg/ml in acetone) and 100 µl of PI (2 mg/ml in PBS) to 4.88 ml of Phosphate-buffered saline (PBS, pH 7.4). The cells were incubated with the working solution for 5 min at room temperature, in the dark. The apical compartment of each well was then washed twice with cold PBS and the culture plate immediately transferred to a confocal laser scanning microscope (Leica TCS SP 8; Leica, Mannheim, Germany). Images of cell monolayers were acquired at 1024×1024 resolution, using either a 25x water immersion (Fluotar VISIR 25x/0.95) or a 63x water immersion objective (HC APO CS2 63x/1.20). Image analysis was performed using LAS X software (Leica Application Suite X; Leica, Mannheim, Germany). Non-stained cells were used to preset the initial confocal settings. Cells that were not exposed to mucus served as positive controls and cells incubated with Triton-X 1% served as negative controls.

2.7. Functional mucosal barrier property assays

2.7.1. Evolution of TEER values of CFBE41o- cells cultured under submerged conditions

TEER values were measured every 2–3 days for three weeks with an epithelial voltohmmeter equipped with STX2 chopstick

manual electrodes (EVOM, World Precision Instruments, USA). A sharp increase in TEER values is associated with a confluent cell monolayer and the development of tight-junctions between neighboring cells. The raw TEER values were corrected according to the background resistance value of the Transwell® filter itself, and the growth area of the filter (1.12 cm^2).

2.7.2. TEER measurements with and without mucus incubation

Cells were cultured for at least 10 days under submerged conditions. The apical medium was aspirated and a mucus disk together with 100 µl of fresh medium was added to the apical compartment. The cells with the mucus disks in place were incubated for 24 h at 37 °C and 5% CO_2, in a horizontal shaker. The next day, the mucus-containing apical compartment was aspirated, washed twice with fresh culture medium, and the cells were allowed to equilibrate for 30 min with 500 µl of freshly added cell culture medium in the apical compartment. Thereafter, TEER values were measured. Cells not exposed to mucus served as controls.

2.7.3. Permeability of sodium fluorescein

Cell monolayers were cultured under submerged conditions for 7 days (the time point at which CFBE41o- cells displayed the highest epithelial barrier properties, according to TEER measurements). Apical compartments were then washed with Krebs-Ringer buffer (KRB) (NaCl 142.03 mM, KCl 2.95 mM, $K_2HPO_4{*}3H_2O$ 1.49 mM, HEPES 10.07 mM, D-glucose 4.00 mM, $MgCl_2{*}6H_2O$ 1.18 mM, $CaCl_2{*}2H_2O$ 4.22 mM; pH 7.4) and a mucus disk together with 100 µl of KRB buffer were added, and incubated for 4 h. Control wells incubated with just 100 µl of KRB served as controls. After the incubation, the basolateral culture medium was aspirated and the cells were washed twice with KRB. A volume of 1.5 ml of fresh KRB was then added to the basolateral compartment. The transport study was initiated by adding 500 µl of sodium fluorescein (10 µg/ml) to the apical (donor) compartment. The paracellular transport of sodium fluorescein was determined by sampling 200 µl from the basolateral (acceptor) compartment at various time points (0, 5, 15, 30, 60, 90 and 120 min). The basolateral volume withdrawn at each sampling point was replaced by the same volume of fresh pre-warmed KRB buffer. Throughout the experiment the cells were incubated at 37 °C and 5% CO_2 on a horizontal shaker. The amount of sodium fluorescein in the acceptor compartment at each time-point was assessed by means of fluorescence intensity using a plate reader (Infinite M200PRO, Tecan, Germany) at excitation and emission wavelengths of 488 and 530 nm respectively. The apparent permeability coefficient (P_{app}) was then calculated by applying the formula:

$$P_{app} = (dQ/dt)\%(A * C_0) \quad (1)$$

where dQ/dt is the flux (µg/s of permeated sodium fluorescein, obtained from the slope of the linear region of each individual permeation profile), A the area of the filter insert (1.12 cm^2), and C_0 the initial donor concentration of sodium fluorescein. C_0 was assumed to be 8.33 µg/ml in all wells, considering that 500 µl of sodium fluorescein (10 µg/ml) were added to a pre-existing apical volume of 100 µl.

2.7.4. Permeability through mucus and cellular uptake of nanoparticles

CFBE41o- cells were cultured under submerged conditions for at least 10 days. The apical medium was then aspirated and a mucus disk with 100 µl of medium was added to the apical compartment followed by a 24 h incubation to allow for disk dissolution and creation of an air-mucus interface. Volumes of 400 µl of the DiD-labeled chitosan-PLGA NPs were then added to the apical compartment at a concentration of 40 µg/ml and were incubated for an additional 24 h. After incubation, the apical compartment, including the mucus, was aspirated and the cells were washed twice with PBS. In the following step 100 µl of wheat germ agglutinin (10 µg/ml, Vector Labs, CA, USA) were added to the apical compartment in order to stain the cell membrane. The cells were again washed twice with PBS and fixed with 3% paraformaldehyde (PFA, 15710-5, Electron Microscopy Science, USA) in PBS, for 30 min, at room temperature. After fixation cells were washed twice with PBS and then 200 µl of 4′,6-diamidino-2-phenylindole (0.1 µg/ml, DAPI, Life Technologies, Darmstadt, Germany) were added to the apical compartment (10–15 min), followed by two further washes with PBS. Cell monolayers underwent a total of 8 PBS washes, which removed almost all the mucus as well as extracellular NPs. Finally, the filter membrane of each Transwell® insert was cut out with a scalpel and mounted on a glass slide with mounting medium (DAKO, Product No 85 5302380-2, USA). Mounted samples were stored at 4 °C until analysis by confocal laser scanning microscopy (Leica TCS SP 8; Leica, Mannheim, Germany). Images were acquired at 1024 × 1024 resolution, using a 63x water immersion objective (HC APO CS2 63x/1.20). Image analysis was performed using LAS X software (Leica Application Suite X; Leica, Mannheim, Germany).

2.8. Statistical analysis

All values are given as mean ± standard error of the mean (SE). Statistical analysis was performed with the SPSS statistics software (IBM, Germany). The storage and loss moduli of the native versus the freeze-dried and re-suspended mucus were compared using one-way ANOVA. The TEER values before and after mucus addition, P_{app} values, and permeated amounts of sodium fluorescein were compared using an independent samples *t*-test with Levene's test for equality of variances. A $P < 0.05$ was accepted as significant.

3. Results and discussion

3.1. CFBE41o- monolayers display high TEER values already after 5 days in submerged culture

CFBE41o- cells grown under submerged conditions displayed high TEER values within just 5 days of being seeded on Transwell® supports (Fig. 1). The TEER values peaked between days 5–9 with values above 1500 Ω cm^2. TEER values stabilized after day 10 (with the exception of a slight decrease between days 10 and 15) at approximately 1000 Ω cm^2, indicating optimal epithelial barrier properties within this time period.

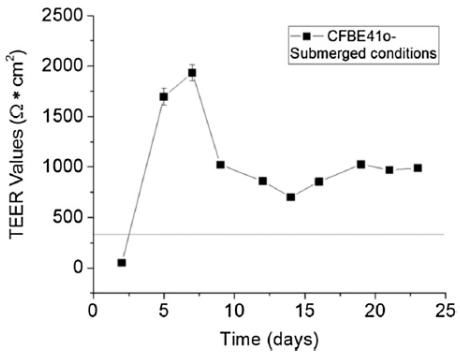

Fig. 1. Time-course of TEER values measured for the CFBE41o- cell line cultured under submerged conditions. The horizontal line at 300 Ω cm^2 indicates the threshold values deemed to indicate the presence of a tight barrier. The mean ± SE for n = 25, from 4 independent experiments are shown.

The noted TEER values are in line with previous studies and suggest the expression of functional tight junctions already within a few days of cell seeding on Transwell® membranes [15,16]. Equivalent bioelectric properties have been also described for other bronchial cell lines grown under submerged conditions such as 16HBE14o- cells, and the widely used Calu-3 cell line [34–36]. The Calu-3 cell line can secrete mucus, provided that cells are cultured at the air-liquid interface [20,21]. However, growing Calu-3 cells under this condition significantly decreases the TEER values [19,37] and significantly increases the culture time needed to achieve both a tight epithelial barrier ($\geq$300 Ω cm^2) and a confluent mucus layer on top of the cells [20,21]. The TEER values of CFBE41o- cells are similarly low when cultured at the air-liquid interface [15], bordering on the threshold values deemed to indicate the presence of a tight barrier. In order to develop a relevant model that mimics the CF airway for pharmaceutical testing purposes, we therefore sought to combine the optimal epithelial barrier properties displayed by the CFBE41o- cell line grown under submerged conditions with the option to either add, or not to add, a supplementary human mucus layer.

3.2. In vitro model concept

The concept of the novel *in vitro* model involves growing CFBE41o- cells in Transwell® supports under submerged conditions until the monolayer develops optimal barrier properties. At this time-point the overlying culture medium is removed and the apical compartment is supplemented with freeze-dried human mucus in combination with a minimal volume of medium, creating an air-mucus interface. The human tracheal mucus samples obtained for the present work were initially nonsterile and highly elastic. Mucus samples are difficult to manipulate, precluding the possibility of pipetting precise mucus volumes or efficiently distributing mucus over a cell monolayer without damaging it. To overcome this limitation, we developed a feasible alternative to freeze-dry small amounts of mucus in order to form thin disks, which could then be placed onto the cell monolayers and re-hydrated with a minimal amount of culture medium. Moreover, we speculate that the freeze-drying process may have accounted for a reduction in the microbial load of the exogenous human material.

3.3. Freeze-dried, re-suspended tracheal mucus show similar rheological properties to undiluted native mucus

The rheological properties of native undiluted mucus were compared to those of mucus samples that had undergone freeze-drying and subsequent re-hydration. With regard to the undiluted native tracheal mucus, in the tested strain range (0.1–10%) airway mucus was within the viscoelastic linear range (Fig. 2A, black symbols). Therefore a strain of 1% was chosen to determine the frequency dependence of the viscoelastic moduli. In the tested frequencies (0.1–40 rad/s) G′ dominated over G″ in all the three decades of frequencies tested (Fig. 2B, black symbols). These rheological properties are characteristic of cross-linked gels and are in line with previous studies reporting on the bulk rheological behavior of airway mucus [3,10,30]. The G″/G′ ratio of mucus determined at 1 rad/s represents a frequency value that is often used in mucus rheology to approximate the low velocities of mucociliary clearance [30,31,38]. Materials with a ratio ranging between $0 \leq G''/G' \leq 1$ are classified as viscoelastic solids. The G″/G′ ratio achieved here for the native tracheal mucus shows a mean value of 0.27 ± 0.01, in good agreement with the values reported by Schuster et al. and Rubin et al. in which a G″/G′ of 0.30 and 0.28 were respectively determined for airway mucus samples collected by the same method as employed in the current work [3,31].

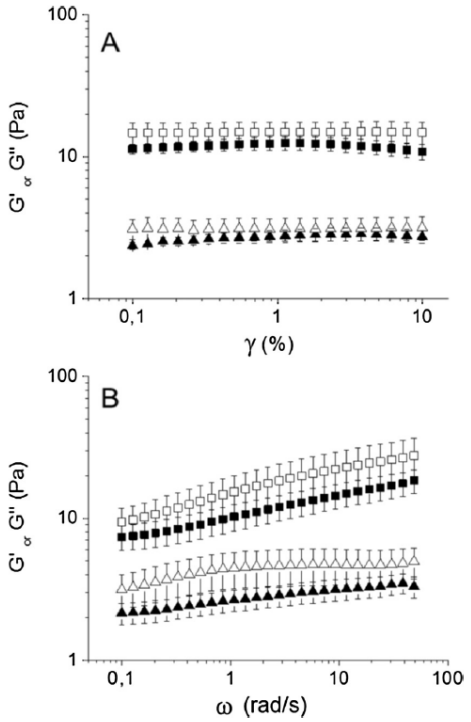

Fig. 2. Bulk rheology of native human tracheal mucus (solid symbols) compared to native airway mucus which was freeze-dried and re-suspended (open symbols). (A) Strain (γ)-dependent viscous (G″, triangles) and elastic (G′, squares) moduli from 0.1 to 10% strain at a frequency of 6.28 rad/s (1 Hz). (B) Frequency-dependent viscous (G″, triangles) and elastic (G′, squares) moduli from 0.1 to 50 rad/s at 1% strain. The mean ± SE for n = 5 independent mucus samples are shown.

Since our aim was to implement a mucus layer on top of the CFBE41o- cell monolayer using freeze-dried tracheal mucus, we investigated whether, upon re-hydration, the freeze-dried mucus would partially or completely recover the viscoelastic properties shown by the native material.

The water percentage of the mucus samples was 95.79 ± 0.62%, being the percentage of solid content of 4.20 ± 0.62. After re-hydration with exactly the same volume of sublimed water and 2 h of mixing in a 360° rotator, the freeze-dried mucus displayed very similar viscoelastic properties as the undiluted human mucus, with no statistical difference between the elastic or viscous moduli at any of the strains or frequencies tested. As with the native material, G′ exceeded G″ in both the amplitude and the frequency sweep test (Fig. 2, white symbols). The viscoelastic moduli were slightly, but not significantly, higher in the case of the freeze-dried and re-hydrated mucus in comparison to the native material. The mean G″/G′ ratio at 1 rad/s demonstrated a mean value of 0.29 ± 0.01, which confirms that intermolecular cross-linking and the characteristic mucus viscoelastic behavior were recovered after re-hydration.

3.4. CFBE41o- cells remain viable and retain their barrier properties after addition of external human freeze-dried mucus

The primary concern of adding an exogenous mucus to the CFBE41o- monolayers was a potential adverse effect that the human-derived tracheal mucus could exert on the cells. Previous studies attempting to implement exogenous mucus onto cell

monolayers, had shown a clear disruption of the epithelial barrier properties and even some cytotoxicity [39,40]. Boegh et al. found a significant barrier disruption after incubating Caco-2 cells with native porcine intestinal mucus, as evidenced by the dramatic decrease in TEER values [39], whereas Teubl et al. reported a reduced viability of the oral epithelial cell line TR146 after a 24 h incubation with mucins derived from bovine submaxillary glands [40]. We hypothesized that due to the common human origin of both the CFBE41o- cells and the tracheal mucus, the cells and the mucus would be better compatible. To assess any potential toxic effects that the exogenous freeze-dried mucus could exert on the cells, the MTT assay was performed on proliferating CFBE41o- cells. However, after 24 h of incubating the cells with mucus the viability was slightly higher than in untreated control cells, suggesting even a positive effect of human mucus on the human-derived CFBE41o- cells under such conditions (Fig. 3A).

In a subsequent step we sought to confirm the cell viability of CFBE41o- monolayers that were allowed to differentiate and to develop tight junctions in Transwell® using the so called live dead staining: in the case that cells are alive, the diffusion and subsequent esterase-mediated hydrolysis of the non-fluorescent dye FDA to the fluorescent product fluorescein will occur. In the case that cells are dead, PI will bind to DNA within the nuclei of cells in which the cell membrane is disrupted (Fig. 3B). After staining with the working solution of FDA/PI we observed tightly packed CFBE41o- cells in confluent monolayers emitting high fluorescence intensity in the fluorescein detection range (Fig. 3C–E), confirming the high cell viability previously observed in proliferating cells with the MTT assay.

Having confirmed with two different methods the compatibility of the CFBE41o- monolayers with exogenous mucus, the next step consisted of addressing whether CFBE41o- monolayers would retain their epithelial barrier properties after adding exogenous mucus. For that purpose we indirectly assessed the presence of tight junctions by comparing the TEER values of the cells before and 24 h after coating the monolayer with mucus (Fig. 4). Monolayers incubated without mucus but under the same experimental conditions were used as controls. Under both conditions the barrier properties of the CFBE41o- cell monolayers remained intact. Thus, unlike in the work of Boegh et al., where the TEER values dropped after adding external pig gastric mucus to Caco-2 cells [39], in the present constellation the barrier properties were maintained after mucus addition. The most plausible explanation for the compatibility between the CFBE41o- cells and the exogenous

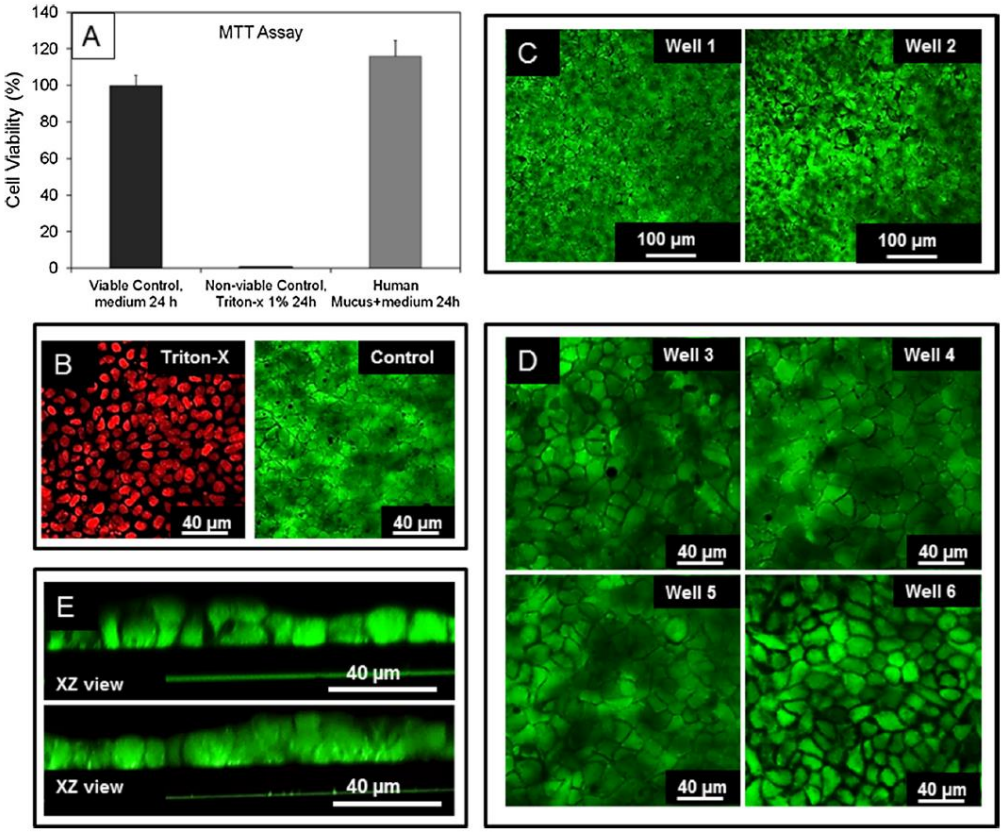

Fig. 3. The viability of CFBE41o- cells upon contact with exogenous human mucus was assessed with the MTT assay and by live/dead staining with fluorescein diacetate (FDA) and propidium iodide (PI). (A) CFBE41o- cells exposed to mucus for 24 h had a viability over 100% (grey bar), slightly greater than that of control cells incubated with the appropriate medium (black bar); CFBE41o- cells incubated with the detergent Triton-X served as a negative control with 0% viability. (B) Representative fluorescence microphotographs of the negative (left) and positive (right) controls for the live/dead staining; cells with their nuclei stained in red represent non-viable cells, whereas cells with a green cytoplasm represent viable cells. (C) and (D) Representative fluorescence microphotographs of independent experiments at different magnifications, showing different Transwells® (wells 1–6) supporting CFBE41o- monolayers that had been incubated for 24 h with human mucus in the apical compartment. (E) X-Z cross-sectional view of viable CFBE41o- monolayers that had been incubated for 24 h with human mucus.

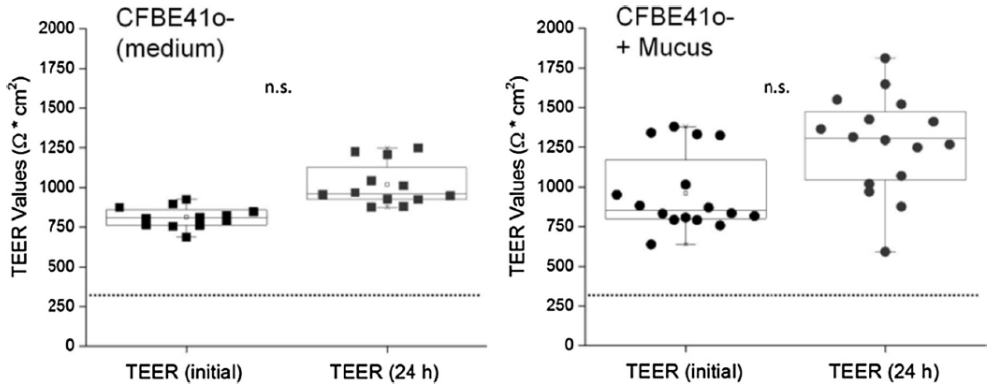

Fig. 4. The barrier properties of the CFBE41o- monolayers grown for at least 10 days under submerged conditions were monitored for 24 h. The TEER values were measured before (initial) and 24 h after addition of (CFBE41o- + Mucus, right). CFBE41o- cells not exposed to mucus but incubated under submerged conditions with regular medium served as controls (CFBE41o-, left). The horizontal line at 300 Ω cm^2 indicates the threshold values deemed to indicate the presence of a tight barrier. The mean ± SE of n = 12 (CFBE41o-) and n = 16 (CFBE41o- + mucus) from three independent experiments are shown. No significant (n.s.) differences were found.

pulmonary mucus may be the common human origin of both materials. In addition, the freeze-drying process may have contributed, in combination with the antibiotics in the cell culture medium, to keep the model sterile and to maintain high cell viability and intact barrier properties. No signs of bacterial contamination were observed with the use of freeze-dried mucus.

3.5. Sodium fluorescein transport

The pulmonary mucus is a selective barrier that allows the permeation of small molecules such as nutrients, growth factors, and antibodies, but significantly hinders the movement of particulates with a size greater than 100–200 nm [8,22,23]. The apical-to-basolateral transport of the small hydrophilic model drug sodium fluorescein (376.3 Da) is routinely used to assess the paracellular transport and the barrier properties of *in vitro* epithelial models [20,41,42]. We hypothesized that sodium fluorescein is small enough to permeate through the mucus pores and would not significantly interact with the mucus fibers due to its negative charge. Therefore, one could expect a similar transport rate of the molecule through the CFBE41o- monolayers, as well as equivalent P_{app} values, in either the presence or absence of mucus. CFBE41o- monolayers, with or without mucus, were indeed observed to act similarly as a barrier to paracellular transport (Fig. 5A), with both conditions resulting in P_{app} values below 1×10^{-6} cm/s. A slight although not significant lower extent of permeation of sodium fluorescein could however be observed in the CFBE41o- monolayers incubated with human mucus (Fig. 5B), most probably due to interactions between the compound and mucus elements in a setting of two unstirred layers of different viscosity within the first hour after sodium fluorescein addition.

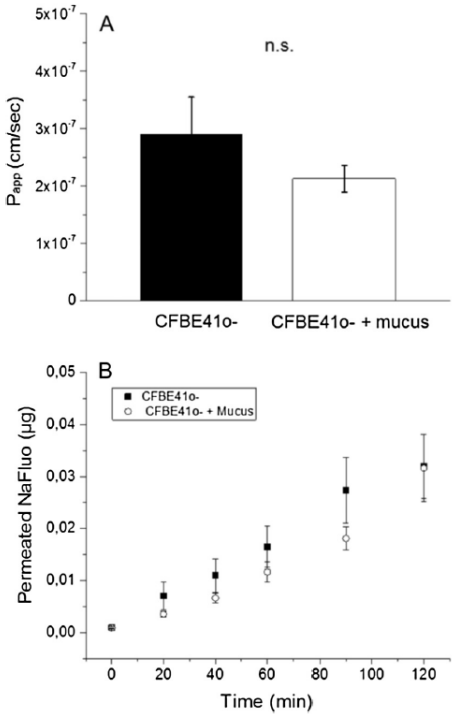

Fig. 5. The barrier properties of the CFBE41o- monolayers after their exposure to mucus were determined by measuring the permeability of sodium fluorescein (NaFluo) over time. (A) Apparent permeability (P_{app}) of sodium fluorescein through CFBE41o- monolayers compared to CFBE41o- monolayers supplemented with human mucus. (B) Permeated total amount of NaFluo over time through CFBE41o- monolayers (solid squares) compared to CFBE41o- monolayers supplemented with human mucus (empty circles). The mean ± SE for n = 20 from 3 independent experiments are shown. No significant (n.s.) differences were found.

3.6. Mucus is a barrier to polymeric nanoparticles

The mesh-like structure of pulmonary mucus is mainly given by a highly cross-linked mucin network (Fig. 6A). The size of the pores of the mucus mesh is highly heterogeneous and ranges from very small pores of just a few nanometers to larger pores on the microscale [22,23]. Therefore, mucus represents a steric barrier to the diffusion of NPs. In addition, mucus can also filter NPs by specific chemical interactions. For instance, the sialic acid-rich glycan side-chains of the mucins confer a negative charge on mucus [43]; mucins also possess non-glycosylated regions with a high capacity for hydrophobic interactions [44]. As a result, a large fraction of NPs with a size above 100 nm that theoretically can chemically interact with mucus will become immobilized within the mucus mesh [3,8,22,23]. These findings highlight the outstanding filtering properties of pulmonary mucus against NP-based drug

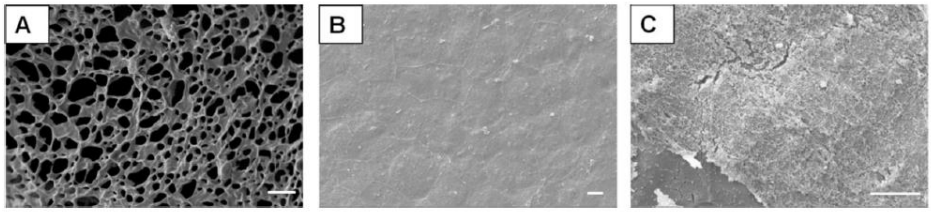

Fig. 6. (A) Scanning electron microscopy (SEM) image of freeze-dried human tracheal mucus. (B) Representative SEM image of a CFBE41o- monolayer; cell boundaries between neighboring cells are visible. (C) SEM image of human tracheal mucus on top of a CFBE41o- cell monolayer; the mucus mesh structure seen in (A) is lost due to the chemical fixation. Scale bar = 4 µm.

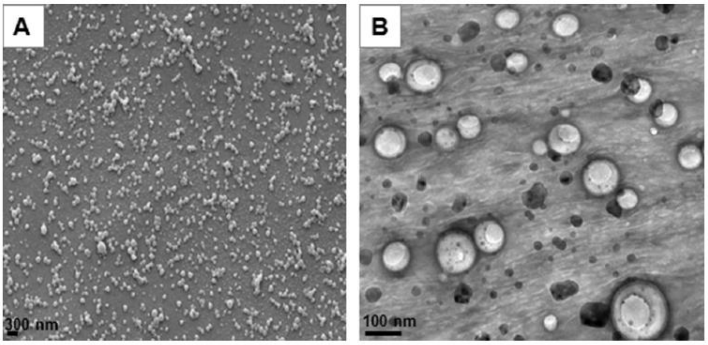

Fig. 7. (A) Scanning electron microscope (SEM) and (B) transmission electron microscope (TEM) images showing the morphology of DiD labeled chitosan-PLGA nanoparticles.

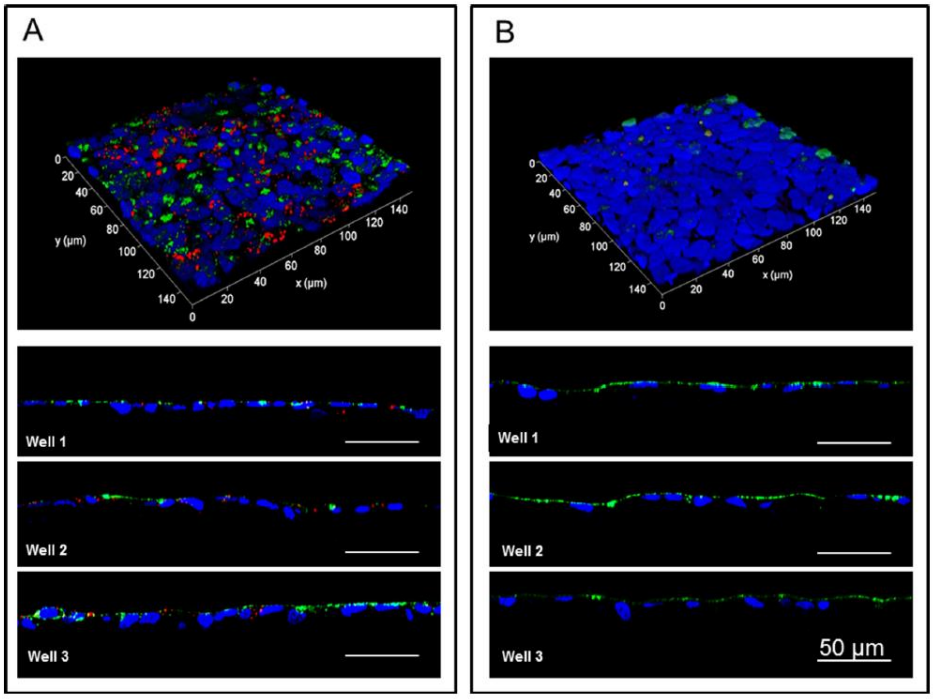

Fig. 8. Confocal laser scanning microscopy images of the cellular uptake study performed with DiD-labeled chitosan-PLGA nanoparticles (NP) on CFBE41o- cells with and without mucus. (A) CFBE41o- monolayers were incubated with 400 µl of the NP suspension (40 µg/ml) for 24 h; after incubation, although the apical surface was thoroughly washed with PBS, a widespread presence of NPs either in close contact with or internalized by cells was noted, as evidenced by the 3D rendering (top) and the X-Z cross-sections (wells 1–3). (B) CFBE41o- monolayers supplemented with human tracheal mucus were incubated with 400 µl of the NP suspension (40 µg/ml) for 24 h. After incubation, the apical surface was thoroughly washed with PBS, resulting in the removal of both mucus and entrapped NPs. The absence of NPs in contact with cells in this case indicates that a vast majority of the NPs were trapped within the mucus and washed away. Nuclei were stained with DAPI (blue), the cell membrane was stained with wheat germ agglutinin (green), and the DiD-labeled chitosan-PLGA NPs were labeled with DiD (red). (For interpretation of the references to color in this figure legend, the reader is referred to the web version of this article.)

delivery systems. As a proof of concept for the developed *in vitro* model, we incubated chitosan coated PLGA NPs for 24 h together with "naked" CFBE41o- cell monolayers (Fig. 6B), as well as with CFBE41o- cell monolayers supplemented with an additional mucus layer (Fig. 6C). Thereafter we qualitatively addressed NP uptake by means of confocal microscopy.

The produced chitosan-PLGA NPs had a size of 167.8 ± 3.6 nm (PDI 0.1 ± 0.01, Fig. 7) and were positively charged, as evidenced by a ζ-potential of 12.9 ± 1.9 mV.

This type of NPs was chosen because they have been already used for several applications of pulmonary nucleic acid delivery [45–47]. Additionally, chitosan coatings have been shown to induce efficient transfection in various cell lines [27,28], including CFBE41o- [12]. We hypothesized, however, that with a NP diameter close to 200 nm and due to the known mucoadhesive properties of chitosan [48], most of the NPs would be trapped within the mucus layer, precluding their cellular uptake. When NPs were incubated with the "naked" CFBE41o- cell monolayers, a significant uptake could be observed from the confocal images (Fig. 8A). On the other hand, when the chitosan-PLGA NPs were incubated with CFBE41o- monolayers that were supplemented with a layer of mucus, the number of NPs in close proximity to the cells was negligible, indicating that most of the NPs had been entrapped by the mucus layer (Fig. 8B) which was itself washed away during the staining/fixation procedure. This finding further confirmed our hypothesis, and indicates that the drug delivery efficiency of NP-based systems is dramatically reduced in mucosal tissues.

4. Conclusion

The aim of this work was to develop an *in vitro* model of the bronchial region comprising minimally an epithelial cell layer and a layer of pulmonary mucus. As a cellular element, we used the CF cell line CFBE41o-, which possesses a number of interesting features for pharmaceutical research such as the expression of tight junction proteins and proteins relevant for pulmonary drug transport. Nevertheless, this cell line is unable to secrete mucus, and therefore the cell monolayer alone as an *in vitro* model lacks a key protective element found in the airways *in vivo*. To complement the cell monolayer, small amounts of freeze-dried human tracheal mucus were placed on top of the CFBE41o- cells, creating an air-mucus interface. The rheological properties of the re-hydrated mucus were very similar to the native material. Moreover, the biocompatibility of the exogenous mucus with the cells could be demonstrated. The re-hydrated mucus behaved as a semi-permeable layer, allowing the small molecule sodium fluorescein to permeate but severely hindering the passage of positively-charged 168 nm diameter polymeric NPs, as evidenced by the low degree of particle uptake by CFBE41o- cells in the presence of mucus. Hence, this model combines the excellent epithelial barrier properties of CFBE41o- cells with the option to implement an additional mucus barrier. Moreover, the relatively short culture time needed to achieve a tight epithelial monolayer allows having a cell line-based mucus-containing *in vitro* model ready for experiments within a timeframe of less than a week. The model may therefore prove a useful tool to study inhalation pharmaceuticals targeted to the bronchial mucosa and in particular to address the role of mucus in this context.

Acknowledgements

The authors would like to acknowledge the excellent technical assistance of Dr Chiara de Rossi, Petra König, Peter Meiers, and Jana Westhues. This work was partly supported by the Marie Curie Initial Training Network PathChooser (PITNGA-2013-608373).

References

[1] B.K. Rubin, Physiology of airway mucus clearance, Respir. Care 47 (2002) 761–768.
[2] C.A. Ruge, J. Kirch, C.M. Lehr, Pulmonary drug delivery: from generating aerosols to overcoming biological barriers-therapeutic possibilities and technological challenges, Lancet Respir. Med. 1 (2013) 402–413.
[3] B.S. Schuster, J.S. Suk, G.F. Woodworth, J. Hanes, Nanoparticle diffusion in respiratory mucus from humans without lung disease, Biomaterials 34 (2013) 3439–3446.
[4] M.B. Antunes, N.A. Cohen, Mucociliary clearance – a critical upper airway host defense mechanism and methods of assessment, Curr. Opin. Allergy Clin. Immunol. 7 (2007) 5–10.
[5] B. Button, L.H. Cai, C. Ehre, M. Kesimer, D.B. Hill, J.K. Sheehan, R.C. Boucher, M. Rubinstein, A periciliary brush promotes the lung health by separating the mucus layer from airway epithelia, Science 337 (2012) 937–941.
[6] M.R. Knowles, R.C. Boucher, Mucus clearance as a primary innate defense mechanism for mammalian airways, J. Clin. Invest. 109 (2002) 571–577.
[7] F.L. Ramos, J.S. Krahnke, V. Kim, Clinical issues of mucus accumulation in COPD, Int. J. Chron. Obstruct. Pulmon. Dis. 9 (2014) 139–150.
[8] N.N. Sanders, S.C. De Smedt, E. Van Rompaey, P. Simoens, F. De Baets, J. Demeester, Cystic fibrosis sputum: a barrier to the transport of nanospheres, Am. J. Respir. Crit. Care Med. 162 (2000) 1905–1911.
[9] S. Yuan, M. Hollinger, M.E. Lachowicz-Scroggins, S.C. Kerr, E.M. Dunican, B.M. Daniel, S. Ghosh, S.C. Erzurum, B. Willard, S.L. Hazen, X. Huang, S.D. Carrington, S. Oscarson, J.V. Fahy, Oxidation increases mucin polymer cross-links to stiffen airway mucus gels, Sci. Transl. Med. 7 (2015) 276ra227.
[10] A.L. Innes, S.D. Carrington, D.J. Thornton, S. Kirkham, K. Rousseau, R.H. Dougherty, W.W. Raymond, G.H. Caughey, S.J. Muller, J.V. Fahy, Ex vivo sputum analysis reveals impairment of protease-dependent mucus degradation by plasma proteins in acute asthma, Am. J. Respir. Crit. Care Med. 180 (2009) 203–210.
[11] J.S. Elborn, Cystic fibrosis, Lancet 388 (2016) 2519–2531.
[12] E. Fernandez Fernandez, B. Santos-Carballal, W.M. Weber, F.M. Goycoolea, Chitosan as a non-viral co-transfection system in a cystic fibrosis cell line, Int. J. Pharm. 502 (2016) 1–9.
[13] R.J. Fields, C.J. Cheng, E. Quijano, C. Weller, N. Kristofik, N. Duong, C. Hoimes, M. E. Egan, W.M. Saltzman, Surface modified poly(beta amino ester)-containing nanoparticles for plasmid DNA delivery, J. Contr. Release 164 (2012) 41–48.
[14] N. Bangel-Ruland, K. Tomczak, E. Fernandez Fernandez, G. Leier, B. Leciejewski, C. Rudolph, J. Rosenecker, W.M. Weber, Cystic fibrosis transmembrane conductance regulator-mRNA delivery: a novel alternative for cystic fibrosis gene therapy, J. Gene Med. 15 (2013) 414–426.
[15] C. Ehrhardt, E.M. Collnot, C. Baldes, U. Becker, M. Laue, K.J. Kim, C.M. Lehr, Towards an in vitro model of cystic fibrosis small airway epithelium: characterisation of the human bronchial epithelial cell line CFBE41o, Cell Tissue Res. 323 (2006) 405–415.
[16] M. Kong, P. Maeng, J. Hong, R. Szczesniak, E. Sorscher, W. Sullender, J.P. Clancy, Respiratory syncytial virus infection disrupts monolayer integrity and function in cystic fibrosis airway cells, Viruses 5 (2013) 2260–2271.
[17] H.E. Nilsson, A. Dragomir, L. Lazorova, M. Johannesson, G.M. Roomans, CFTR and tight junctions in cultured bronchial epithelial cells, Exp. Mol. Pathol. 88 (2010) 118–127.
[18] N. Molenda, K. Urbanova, N. Weiser, K. Kusche-Vihrog, D. Gunzel, H. Schillers, Paracellular transport through healthy and cystic fibrosis bronchial epithelial cell lines – do we have a proper model?, PLoS ONE 9 (2014) e100621
[19] C.I. Grainger, L.L. Greenwell, D.J. Lockley, G.P. Martin, B. Forbes, Culture of Calu-3 cells at the air interface provides a representative model of the airway epithelial barrier, Pharm. Res. 23 (2006) 1482–1490.
[20] M. Haghi, P.M. Young, D. Traini, R. Jaiswal, J. Gong, M. Bebawy, Time- and passage-dependent characteristics of a Calu-3 respiratory epithelial cell model, Drug Dev. Ind. Pharm. 36 (2010) 1207–1214.
[21] S. Mura, H. Hillaireau, J. Nicolas, S. Kerdine-Romer, B. Le Droumaguet, C. Delomenie, V. Nicolas, M. Pallardy, N. Tsapis, E. Fattal, Biodegradable nanoparticles meet the bronchial airway barrier: how surface properties affect their interaction with mucus and epithelial cells, Biomacromolecules 12 (2011) 4136–4143.
[22] X. Murgia, P. Pawelzyk, U.F. Schaefer, C. Wagner, N. Willenbacher, C.M. Lehr, Size-limited penetration of nanoparticles into porcine respiratory mucus after aerosol deposition, Biomacromolecules 17 (2016) 1536–1542.
[23] J. Kirch, A. Schneider, B. Abou, A. Hopf, U.F. Schaefer, M. Schneider, C. Schall, C. Wagner, C.M. Lehr, Optical tweezers reveal relationship between microstructure and nanoparticle penetration of pulmonary mucus, Proc. Natl. Acad. Sci. USA 109 (2012) 18355–18360.
[24] J.S. Patton, J.D. Brain, L.A. Davies, J. Fiegel, M. Gumbleton, K.J. Kim, M. Sakagami, R. Vanbever, C. Ehrhardt, The particle has landed – characterizing the fate of inhaled pharmaceuticals, J. Aerosol. Med. Pulm. Drug Deliv. 23 (Suppl 2) (2010) S71–87.
[25] H.H. Sigurdsson, J. Kirch, C.M. Lehr, Mucus as a barrier to lipophilic drugs, Int. J. Pharm. 453 (2013) 56–64.
[26] X. Yang, K. Forier, L. Steukers, S. Van Vlierberghe, P. Dubruel, K. Braeckmans, S. Glorieux, H.J. Nauwynck, Immobilization of pseudorabies virus in porcine tracheal respiratory mucus revealed by single particle tracking, PLoS ONE 7 (2012) e51054.

[27] N. Csaba, M. Koping-Hoggard, M.J. Alonso, Ionically crosslinked chitosan/tripolyphosphate nanoparticles for oligonucleotide and plasmid DNA delivery, Int. J. Pharm. 382 (2009) 205–214.
[28] H.Q. Mao, K. Roy, V.L. Troung-Le, K.A. Janes, K.Y. Lin, Y. Wang, J.T. August, K.W. Leong, Chitosan-DNA nanoparticles as gene carriers: synthesis, characterization and transfection efficiency, J. Contr. Release 70 (2001) 399–421.
[29] M. Thomas, A.M. Klibanov, Non-viral gene therapy: polycation-mediated DNA delivery, Appl. Microbiol. Biotechnol. 62 (2003) 27–34.
[30] B.K. Rubin, B. Finegan, O. Ramirez, M. King, General anesthesia does not alter the viscoelastic or transport properties of human respiratory mucus, Chest 98 (1990) 101–104.
[31] B.K. Rubin, O. Ramirez, J.G. Zayas, B. Finegan, M. King, Collection and analysis of respiratory mucus from subjects without lung disease, Am. Rev. Respir. Dis. 141 (1990) 1040–1043.
[32] A. Mittal, K. Schulze, T. Ebensen, S. Weissmann, S. Hansen, C.M. Lehr, C.A. Guzman, Efficient nanoparticle-mediated needle-free transcutaneous vaccination via hair follicles requires adjuvantation, Nanomedicine 11 (2015) 147–154.
[33] N. Nafee, M. Schneider, U.F. Schaefer, C.M. Lehr, Relevance of the colloidal stability of chitosan/PLGA nanoparticles on their cytotoxicity profile, Int. J. Pharm. 381 (2009) 130–139.
[34] J.L. Sporty, L. Horalkova, C. Ehrhardt, In vitro cell culture models for the assessment of pulmonary drug disposition, Expert Opin. Drug Metab. Toxicol. 4 (2008) 333–345.
[35] M.E. Kreft, U.D. Jerman, E. Lasic, T. Lanisnik Rizner, N. Hevir-Kene, L. Peternel, K. Kristan, The characterization of the human nasal epithelial cell line RPMI 2650 under different culture conditions and their optimization for an appropriate in vitro nasal model, Pharm. Res. 32 (2015) 665–679.
[36] S. Loman, J. Radl, H.M. Jansen, T.A. Out, R. Lutter, Vectorial transcytosis of dimeric IgA by the Calu-3 human lung epithelial cell line: upregulation by IFN-gamma, Am. J. Physiol. 272 (1997) L951–958.
[37] C. Ehrhardt, J. Fiegel, S. Fuchs, R. Abu-Dahab, U.F. Schaefer, J. Hanes, C.M. Lehr, Drug absorption by the respiratory mucosa: cell culture models and particulate drug carriers, J. Aerosol. Med. 15 (2002) 131–139.
[38] J.G. Zayas, G.C. Man, M. King, Tracheal mucus rheology in patients undergoing diagnostic bronchoscopy. Interrelations with smoking and cancer, Am. Rev. Respir. Dis. 141 (1990) 1107–1113.
[39] M. Boegh, S.G. Baldursdottir, A. Mullertz, H.M. Nielsen, Property profiling of biosimilar mucus in a novel mucus-containing in vitro model for assessment of intestinal drug absorption, Eur. J. Pharm. Biopharm. 87 (2014) 227–235.
[40] B.J. Teubl, M. Absenger, E. Frohlich, G. Leitinger, A. Zimmer, E. Roblegg, The oral cavity as a biological barrier system: design of an advanced buccal in vitro permeability model, Eur. J. Pharm. Biopharm. 84 (2013) 386–393.
[41] A. Kuehn, S. Kletting, C. de Souza Carvalho-Wodarz, U. Repnik, G. Griffiths, U. Fischer, E. Meese, H. Huwer, D. Wirth, T. May, N. Schneider-Daum, C.M. Lehr, Human alveolar epithelial cells expressing tight junctions to model the air-blood barrier, Altex 33 (2016) 251–260.
[42] M.I. Hermanns, R.E. Unger, K. Kehe, K. Peters, C.J. Kirkpatrick, Lung epithelial cell lines in coculture with human pulmonary microvascular endothelial cells: development of an alveolo-capillary barrier in vitro, Lab. Invest. 84 (2004) 736–752.
[43] A. Ludwig, The use of mucoadhesive polymers in ocular drug delivery, Adv. Drug Deliv. Rev. 57 (2005) 1595–1639.
[44] S.K. Lai, Y.Y. Wang, J. Hanes, Mucus-penetrating nanoparticles for drug and gene delivery to mucosal tissues, Adv. Drug Deliv. Rev. 61 (2009) 158–171.
[45] A.J. Mahiny, A. Dewerth, L.E. Mays, M. Alkhaled, B. Mothes, E. Malaeksefat, B. Loretz, J. Rottenberger, D.M. Brosch, P. Reautschnig, P. Surapolchai, F. Zeyer, A. Schams, M. Carevic, M. Bakele, M. Griese, M. Schwab, B. Nurnberg, S. Beer-Hammer, R. Handgretinger, D. Hartl, C.M. Lehr, M.S. Kormann, In vivo genome editing using nuclease-encoding mRNA corrects SP-B deficiency, Nat. Biotechnol. 33 (2015) 584–586.
[46] M.N. Ravi Kumar, U. Bakowsky, C.M. Lehr, Preparation and characterization of cationic PLGA nanospheres as DNA carriers, Biomaterials 25 (2004) 1771–1777.
[47] J. Beisner, M. Dong, S. Taetz, N. Nafee, E.U. Griese, U. Schaefer, C.M. Lehr, U. Klotz, T.E. Murdter, Nanoparticle mediated delivery of 2'-O-methyl-RNA leads to efficient telomerase inhibition and telomere shortening in human lung cancer cells, Lung Cancer 68 (2010) 346–354.
[48] S. Dhawan, A.K. Singla, V.R. Sinha, Evaluation of mucoadhesive properties of chitosan microspheres prepared by different methods, AAPS PharmSciTech 5 (2004) e67.

6.3 Starch-Chitosan Polyplexes: A Versatile Carrier System for Anti-Infectives and Gene Delivery

Starch-Chitosan Polyplexes: A Versatile Carrier System for Anti-Infectives and Gene Delivery

Hanzey Yasar [§], Duy-Khiet Ho[§], Chiara De Rossi, Jennifer Herrmann, Sarah Gordon Brigitta Loretz and Claus-Michael Lehr; Polymers (**2018**) 10, 252.

DOI: 10.3390/polym10030252

[§]*Equally contributing authors*

polymers

MDPI

Article

Starch-Chitosan Polyplexes: A Versatile Carrier System for Anti-Infectives and Gene Delivery

Hanzey Yasar [1,2,†], Duy-Khiet Ho [1,2,†], Chiara De Rossi [1], Jennifer Herrmann [1], Sarah Gordon [1], Brigitta Loretz [1,*] and Claus-Michael Lehr [1,2]

1 Helmholtz Institute for Pharmaceutical Research Saarland (HIPS), Helmholtz Center for Infection Research (HZI), Saarland University, D-66123 Saarbrücken, Germany; Hanzey.Yasar@helmholtz-hzi.de (H.Y.); DuyKhiet.Ho@helmholtz-hzi.de (D.-K.H.); Chiara.DeRossi@helmholtz-hzi.de (C.D.R.); jennifer.herrmann@helmholtz-hzi.de (J.H.); S.C.Gordon@ljmu.ac.uk (S.G.); Claus-Michael.Lehr@helmholtz-hzi.de (C.-M.L.)

2 Department of Pharmacy, Saarland University, D-66123 Saarbrücken, Germany

* Correspondence: Brigitta.Loretz@helmholtz-hzi.de; Tel.: +49-681-98806-1030

† These authors contributed equally to this work.

Received: 8 December 2017; Accepted: 27 February 2018; Published: 1 March 2018

Abstract: Despite the enormous potential of nanomedicine, the search for materials from renewable resources that balance bio-medical requirements and engineering aspects is still challenging. This study proposes an easy method to make nanoparticles composed of oxidized starch and chitosan, both isolated from natural biopolymers. The careful adjustment of C/N ratio, polymer concentration and molecular weight allowed for tuning of particle characteristics. The system's carrier capability was assessed both for anti-infectives and for nucleic acid. Higher starch content polyplexes were found to be suitable for high encapsulation efficiency of cationic anti-infectives and preserving their bactericidal function. A cationic carrier was obtained by coating the anionic polyplex with chitosan. Coating allowed for a minimal amount of cationic polymer to be employed and facilitated plasmid DNA loading both within the particle core and on the surface. Transfection studies showed encouraging result, approximately 5% of A549 cells with reporter gene expression. In summary, starch-chitosan complexes are suitable carriers with promising perspectives for pharmaceutical use.

Keywords: polymeric nanoparticles; renewable polysaccharides; anionic starch; cationic anti-infectives; transfection

1. Introduction

Nanoparticulate carrier systems represent a well established platform for vaccination and treatment of severe diseases, such as infection and cancer, by protecting active agents, preventing burst release kinetics, providing the potential to enhance crossing of biological barriers and improving local drug delivery [1–4]. However, the selection of materials or excipients for nanomedical applications remains challenging due to strict requirements of the field. Such materials should be biocompatible and biodegradable, safe and at the same time provide good drug loading capacity as well as a potential to carry diverse bioactive agents [3]. Moreover, for large scale production, the used materials should be environmentally friendly, and able to be manufactured by facile processes. In recent years, a variety of polymeric materials derived from natural biopolymers have been synthesized and investigated to formulate vehicles to deliver bioactive molecules. These molecules have been embedded inside the polymeric matrix or adsorbed onto the colloidal surface [5] by either physical interaction (e.g., electrostatic complexation) or chemical modification. Nevertheless, the number of biodegradable and biocompatible polymers which are further compatible with water (as a solvent suitable for pharmaceutical use) and can form nanoparticles with a high and versatile active agent

encapsulation capacity are still limited. Hence, the production of excipients for nanomedicine with a balance between pharmaceutical requirements and engineering aspects as well as a tunable potential for drug delivery has gained considerable attention. In particular, natural and modified polysaccharides such as chitosan, alginate, starch and dextrin, and their synthetic derivatives, have been considered as efficient candidates for drug carrier systems [1,6,7]. However, achieving a consistent and robust production of polysaccharide nanoparticles is challenging due to the heterogeneous physicochemical properties of natural and synthetic polymers. In addition, depending on the actives to be delivered and the route of administration, different protocols are needed [8] to prepare polysaccharide-based polymeric nanoparticles [9,10]. Thus, the chosen polymers need to be appropriately tailored, chemically modified and optimized to qualify for targeted applications [1].

Among natural polysaccharides, starch and chitosan have many promising properties. Starch is a biocompatible and biodegradable polysaccharide, which is degraded by α-amylase, and available at relatively low cost. It has been widely used in tablets and capsules, e.g., as a binder or diluent [11]. Slightly modified derivatives of starch with fractional molecular weights have previously been studied as a platform to formulate homogenous carrier systems for gene delivery [12]. Other researchers have also studied starch-based particulate systems for drug delivery [13–15]. Chitosan is similarly biodegradable and biocompatible, and has been investigated and widely used in pharmaceutical research for drug [16,17], protein [18] and nucleic acid delivery, and for vaccination purposes [19–21]. It has also been used as a biomedical material for artificial skin and wound healing bandages [22] as a biodegradable polysaccharide [23]. Moreover, chitosan has good biocompatibility as tested in humans [24]. Yamada et al. [12] has reported the preparation of anionic starch derivatives by mild chemical modification, and the separation of different molecular weights by a fractional cut-off protocol, which was later aimed for transfection study. The research showed promising perspectives of starch derivatives as drug carrier system. However, the charge mediated complexation of fractional starch derivatives was not fully explored in that study; the carrier capacity of such system thus remains to be investigated.

In light of these advantages, the aim of this work was to produce versatile and flexible nanocarriers using both starch and chitosan, with a facile and organic solvent-free preparation method combining the advantages of these two polymers into a carrier system. The investigated systems were composed of starch derivatives of molecular weight (M_w) >100 kDa or with M_w range of 30–100 kDa, and oligochitosan M_w 5 kDa or Protasan M_w 90 kDa as chitosan derivatives. A wide range of molecular weights was used to achieve complex stability. We also explored the design space of the system to obtain particles with high colloidal stability as well as tunable surface charge and size. Thus, the varied production parameters of starch-chitosan polyplexes (Scheme 1A) were: (i) molar ratio of carboxylate and amine functional groups (C/N ratio) of starch and chitosan, respectively; (ii) polymer concentration; and (iii) counter polymer type. The loading capacity and versatility of these simple carriers was then investigated using tobramycin and colistin as clinically relevant models of small molecule and peptide anti-infectives respectively [25,26], as well as nucleic acids (plasmid DNA). Furthermore, to improve encapsulation capacity, we coated the starch-chitosan polyplexes with an additional chitosan (Protasan) layer (Scheme 1B), and explored the loading capacity of the resulting nanoparticles. Coating the polyplexes enabled drug loading on the surface of particles, which led to a better encapsulation particularly in the case of the utilized nucleic acids. This approach also creates the further potential for formulating a multifunctional delivery system. The novel approach of starch-chitosan-based complex-coacervation suggested in this study is a straightforward and promising technique to prepare versatile carrier systems with potential in nanomedicine applications. Therefore, we undertook preliminary studies of design, synthesis, and formulation of such carrier systems, and explored their flexibility and capacity for encapsulating selected model macromolecular drugs.

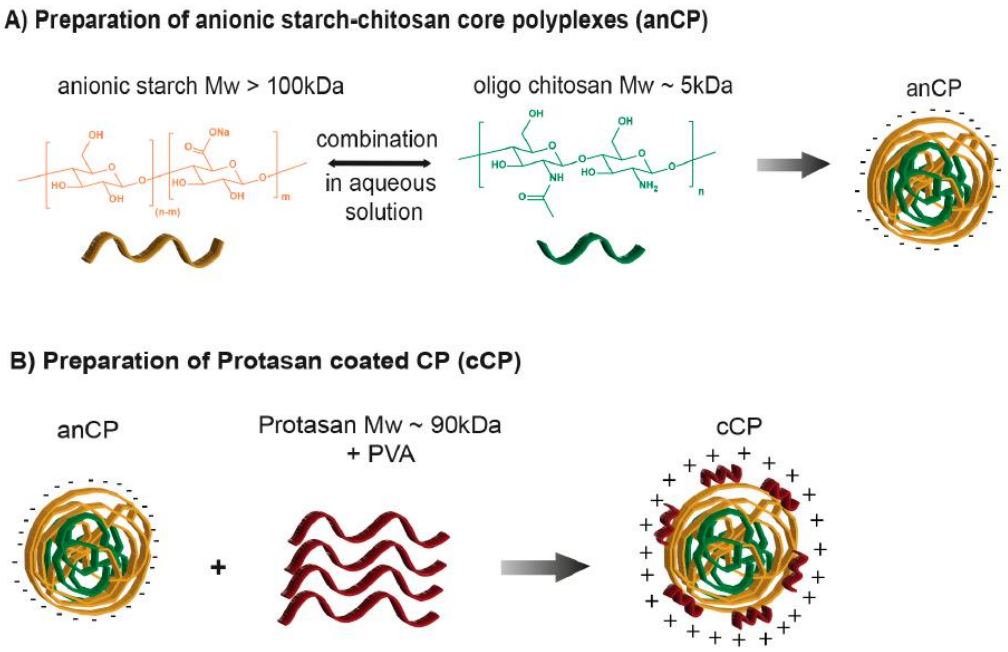

Scheme 1. Illustration of drug-free (plain) starch-chitosan polyplex-preparation.

2. Experimental Section

2.1. Materials

As raw material, partially hydrolyzed potato starch (M_w of 1300 kDa), which was a kind gift from AVEBE (Veendam, The Netherlands), was used. Selective oxidation of the primary alcohol on starch was performed to increase water solubility and obtain an anionic charge. The oxidation procedure and molecular weight fractionation of three M_w samples (5, 30–100, and >100 kDa) was conducted in accordance with the protocol of Yamada et al. [12]. The obtained starch derivatives had an oxidation degree of 45%. The M_w fraction >100 kDa is used unless stated otherwise and is termed "anionic starch" in all further descriptions.

Chitosan oligosaccharide lactate (oligochitosan; M_w 5 kDa), polyvinyl alcohol (PVA; Mowiol® 4-88), sodium hydroxide, trifluoroacetic acid (TFA), acetonitrile and acetic acid were purchased from Sigma-Aldrich (Darmstadt, Germany). Tobramycin sulfate salt and colistin sulfate salt were used as received also from Sigma-Aldrich. Ultrapure chitosan chloride salt (Protasan UP CL113; M_w ~90 kDa, deacetylation degree 75–90%) was obtained from FMC Biopolymer AS NovaMatrix (Sandvika, Norway). Purified water was produced by a Milli-Q water purification system from Merck Millipore (Darmstadt, Germany). O-Phthalaldehyde (OPA), 2-mercaptoethanol, phosphotungstic acid (PTA) and boric acid were used as purchased from Sigma-Aldrich.

Agarose SERVA for DNA Electrophoresis of research grade was bought from Serva (Heidelberg, Germany). Ethidium bromide solution (10 mg/mL), heparin sodium salt from porcine intestinal mucosa, 3-(4,5-dimethylthiazol-2-yl)-2,5-diphenyltetrazolium bromide) (MTT reagent), Triton™ X-100, dimethyl sulfoxide (DMSO) and Dulbecco's phosphate buffered saline solution (PBS) were obtained from Sigma-Aldrich. Gibco Hanks' balanced salt solution (HBSS) buffer was purchased from Thermo Fisher Scientific (Darmstadt, Germany). A549 cells (human lung carcinoma cell line, No. ACC 107) were obtained from DSMZ GmbH (Braunschweig, Germany). Cell culture medium (RPMI 1640) was purchased from PAA laboratories GmbH (Pasching, Austria) and supplemented with 10% fetal calf serum (FCS, Sigma-Aldrich). Plasmid DNA (pDNA) encoding for the fluorescent protein AmCyan was bought from Clontech Laboratories, Inc. (pAmCyan 1-N1, Mountain View, CA, USA). The plasmid

was propagated in *Escherichia coli* DH5α and isolated with Qiagen EndoFree Plasmid Mega Kit (Qiagen, Hilden, Germany) to obtain pDNA of cell culture quality. jetPRIME® transfection reagent was purchased from Polyplus-transfection (Illkirch, France). Rhodamine *Ricinus communis* agglutinin I (RGA I) was obtained from Vector Laboratories. 4′,6-diamidino-2-phenylindole (DAPI) was purchased from Life Technologies (Darmstadt, Germany).

2.2. Preparation, Optimization and Characterization of Starch–Chitosan Core Polyplexes

2.2.1. Preparation and Optimization of Starch-Chitosan Core Polyplexes (CP)

Starch-chitosan core polyplexes (CP) were prepared by self-assembly of anionic starch derivatives and chitosan derivatives in aqueous medium. CP characteristics, including their: (i) surface properties; (ii) size; and (iii) physicochemical stability were varied by: (i) the molecular weight of utilized anionic starch and chitosan derivatives; (ii) polymer concentration; and (iii) molar ratio of carboxylate (COONa) to amine (NH_2) groups (C/N ratio) in oxidized starch and chitosan, respectively. The polyplex formulation procedure is described in Scheme 1A. Briefly, a solution of anionic starch was prepared in Milli-Q water at a defined concentration, while the utilized chitosan derivative was solubilized in 0.02 M acetic acid, followed by pH adjustment to 5.5. The assembly into CP of oxidized starch and its counter excipient occurred by the addition of an appropriate amount of starch polymer solution into the pre-warmed solution of chitosan derivative, followed by 2 min of vortexing and 1 h incubation at room temperature. To prepare anionic core polyplexes (anCP), anionic starch (M_w of >100 kDa) and oligochitosan (M_w of 5 kDa) were employed at various C/N ratios, ranging from 50:1 to 10:1 and further to 1:1, designed to optimize the formulation and stability of the polyplexes. Cationic core polyplexes (cationic CP) were prepared by co-assembly of negative starch (M_w of 30–100 kDa) and Protasan (M_w of 90 kDa) having a higher amount of positively charged amine groups. The optimal C/N ratio was identified by investigating the ratios of 1:30, 1:10 and 1:1. All samples with a solvent pH-value of 5.5 were characterized by dynamic light scattering (DLS), using a Zetasizer Nano from Malvern Instruments (UK) to obtain hydrodynamic size, polydispersity index (PDI), and using laser Doppler velocimetry to obtain ζ-potential. All samples were prepared at least in three different batches.

2.2.2. Preparation and Optimization of Protasan Coated CP (cCP)

Another approach taken to further improve the loading capacity of starch-chitosan carriers was to prepare coated polyplexes with a further layer of Protasan on anCP. The optimized coating method is described briefly as following: anCP were prepared as described and then coated with an additional layer of positively charged Protasan, by an association of amine functional groups of the chitosan and the anionic surface of the anCP (Scheme 1B). The coating solution was prepared by dissolving 3 mg of Protasan in 1 mL PVA 2% (*w/v*) solution, which was then diluted with Milli-Q water to a 1.5 mg/5 mL concentration for coating. A 500 µL volume (6.6 mg/mL) of anCP was added dropwise to the prepared Protasan solution, which was continuously stirred for 30 min at 150 rpm. This was followed by incubation at room temperature for 3 h prior to characterization. The resulting Protasan-coated anCP (cCP, c = 0.87 mg/mL) were kept for further studies. Samples were prepared in at least three different batches. All particle samples were characterized for their hydrodynamic size, PDI and ζ-potential. This method was also applied to investigate the physicochemical stability of anCP and cationic CP under storage conditions of 4 °C for 27 days.

2.2.3. pH-Stability of Drug-Free CP and cCP

The colloidal stability of anCP and cCP at different pH values was investigated by incubating particle suspensions at pH values of 3.5, 4.0, 4.5, 5.5, 6.0, 7.5 and 8.0, all within the physiologically-relevant range. Samples were analyzed to obtain hydrodynamic size, PDI, and ζ-potential, after predetermined incubation times (30 min, 1 h, 3 h and 24 h). The pH-value was adjusted following polyplex preparation at pH 5.5 (as described above) by using either 0.02 M acetic acid solution or 1 M NaOH solution.

All experiments were conducted in triplicates with $n = 3$, and results expressed as mean ± standard deviation (SD).

2.2.4. Morphology

The morphology of all produced polyplexes was visualized by transmission electron microscopy (TEM, JEM 2011, JEOL, St Andrews, UK). Before the TEM visualization, 8.7 µg/10 µL of polyplexes were added on a copper grid (carbon films on 400 mesh copper grids, Plano GmbH, Wetzlar, Germany) and incubated for 10 min to allow an adhesion of polyplexes to the surface. The excess was removed, and polyplexes were further stained with 0.5% (*w/v*) PTA to improve the contrast of TEM images.

2.2.5. Cytotoxicity Study: MTT Assay

A549 cells were seeded in a 96 well plate at a density of 1×10^5 cells per well, in 200 µL of RPMI cell culture medium supplemented with 10% FCS. Cells were grown for 4 days prior to the conduction of the assay to allow for approximately 95% cell confluency. On Day 4, CP and cCP samples were diluted with a suitable amount of RPMI medium (without FCS) to achieve test concentrations of 5, 10, 40, 70, 100, 200 and 500 µg/mL. Cells were then washed twice with 200 µL HBSS buffer (pH 7.4), and polyplex samples were added to cells in triplicate. Cells incubated with only RPMI medium were used as a negative control (determined to result in 100% cell viability) and cells treated with 1% Triton™ X-100 in RPMI medium were used as positive control (designated as 0% cell viability). All samples were incubated with cells for 4 h, on a horizontal shaker with careful shaking at 150 rpm at 37 °C and 5% CO_2. Subsequently, the supernatant was removed, and cells were washed once with HBSS. Then, 200 µL of the MTT-reagent (5 mg/mL) in HBSS was applied to each well and further incubated for 4 h with gentle shaking. The supernatant was then removed and DMSO was immediately added to achieve cell lysis. Cells were incubated in DMSO for 15 min under careful shaking and protected from light. The absorbance of each well at 550 nm was then measured with a plate reader (Infinite® 200 Pro, TECAN, Männedorf, Switzerland). The percentage of viable cells was calculated in comparison to negative and positive controls as described by Nafee et al. [27].

2.3. Cationic Anti-Infective Loaded anCP

2.3.1. Preparation and Optimization of Cationic Anti-Infective Loaded anCP

Isothermal Titration Calorimetry

Two relevant anti-infectives were used to test the loading capacity of anCP. Tobramycin was used as an example of a cationic small molecule antibiotic having a molecular weight of 467.5 Da, and colistin (polymyxin E) was used as an example of a peptide antibiotic with a molecular weight of 1267.5 Da (Scheme 2A).

Interaction between anionic starch and the cationic anti-infectives tobramycin and colistin was investigated by isothermal titration calorimetry (ITC) using a NanoITC 2G (TA Instruments, New Castle, DE, USA). The purpose of such measurement was to optimize excipient to cargo ratio in drug loaded carrier production. Briefly, all drug and anionic starch solutions were prepared in milli-Q water. A 25 mM solution of tobramycin or colistin was prepared in a 250 µL syringe and used to saturate 1.5 mL of anionic starch at a concentration of 0.1 mM filled in the sample cell. Following an initial delay of 300 s, 250 µL of drug solution was repeatedly injected into the sample cell with a spacing of 500 s between injections, and at a reference power of 10 µCal/s. The final thermogram and thermodynamic parameters were produced by subtracting the heat of dilution of either tobramycin or colistin (25 mM in 1.5 mL milli-Q water), followed by fitting using the One Set of Sites model in the data analysis software NanoAnalyze. The free energy of binding (ΔG) was calculated using the equation $\Delta G = \Delta H - T\Delta S$, where ΔH is the enthalpy change, T is temperature (Kelvin), and ΔS is the change in entropy. All measurements were performed at 25 °C.

Preparation and Optimization of Cationic Anti-Infective Loaded anCP

Both tobramycin and colistin were loaded using the same procedure, during formation of anCP, employing various C/N ratios, as follows: (i) 1 mg tobramycin or 3 mg colistin was incubated with an appropriate amount of anionic starch solution for 2 h; and (ii) pre-warmed chitosan solution at pH 5.5 was added, and coacervation was achieved by vortex mixing (2 min).

The anti-infective loaded anCP suspension was then centrifuged at 13,000× *g* and 4 °C for 20 min at least twice and allowed to equilibrate at 4 °C overnight before conducting further experiments. In all experiments the supernatant produced by centrifugation was collected for drug loading quantification.

Loading Quantification

The degree of anti-infective loading in anCP was determined using an indirect quantification method (drug amount inside anCP = initial drug amount − drug amount in the supernatant). Colistin was quantified by high-performance liquid chromatography (HPLC), while tobramycin was quantified based on a protocol for detection of aminoglycosides [28], as detailed below.

HPLC Analysis

The HPLC analysis was performed on a Dionex UltiMate 3000 system (Thermo-Fischer Scientific, Dreieich, Germany) equipped with LPG-3400 SD pump, WPS-3000 autosampler, DAD3000 detector, and TCC-3000 column oven. Chromeleon software (Chromeleon 6.80 SP2 build 9.68, Thermo Scientific Dionex, Dreieich, Germany) was used for data analysis. A column set of LiChrospher® 100 RP-18 (5 µm) LiChroCART® 125-4, consisting of a 125 mm × 4 mm LiChrospher 100/RP-18 column (Merck-Hitachi, Darmstadt, Germany) with a LiChrospher 100/RP-18 guard column (5 µm) (Merck-Hitachi, Darmstadt, Germany) at 30 °C was used as stationary phase for all substances. A gradient method was used starting with 20% A, increasing to 50% A within 2 min, and holding for 1.5 min (A = acetonitrile, B = 0.1% TFA solution in water). Before injection, the samples were filtered through a cellulose acetate 0.2 µm membrane. The flow rate was 1.0 mL/min, and the injection volume was 50 µL. A calibration curve was constructed using eight different concentrations of colistin in water, ranging from 0.2 mg/mL to 0.005 mg/mL (r^2 = 0.9955). All 8 standards were measured 5 times, and a percent relative standard deviation (% RSD) of less than 3.9% was calculated. The run time was 6 min, and a retention time of 3.6 min and 3.9 min was observed for colistin A and colistin B, respectively. As colistin is a mixture of two main fractions, colistin A and colistin B, both were quantified to determine colistin loading. The detection wavelength was 210 nm for colistin A and 214 nm for colistin B.

Aminoglycoside Detection Protocol

The product fluorescence of tobramycin reacted with a fluorescent reagent was measured at 344/450 nm (*Ex*/*Em*) using a Tecan microplate reader following a published method [28]. To prepare the reagent solution, a 0.2 g amount of OPA reagent was dissolved in a mixture of 1 mL methanol, 19 mL boric acid 0.4 M at pH 10.4, and 0.4 mL of 14.3 M 2-mercaptoethanol. A 2 mL of the resulting mixture was then diluted with 16 mL methanol before use. A calibration curve was constructed using five different concentrations of tobramycin in water (0.04–0.005 mg/mL, r^2 = 0.9976).

In both cases, the encapsulation efficiency (EE) and the drug loading rate (LR) were calculated according to the following equations:

$$\begin{aligned} \text{EE} &= \frac{\text{Weight of encapsulated drug in nanoparticles}}{\text{Initial amount of drug in the system}} \times 100 \\ \text{LR} &= \frac{\text{Weight of drug in nanoparticles}}{\text{Weight of nanoparticles}} \times 100 \end{aligned} \quad (1)$$

where "weight of nanoparticles" was calculated as weight of polymeric material + weight of encapsulated drug in nanoparticles.

Each sample was assayed at least in triplicate, and results are reported as the mean ± SD.

Drug Release Study

Tobramycin or colistin release profiles from tobramycin loaded anCP or colistin loaded anCP was performed in PBS (pH 7.4) at 37 °C. Briefly, either tobramycin loaded anCP or colistin loaded anCP was diluted in PBS to have final tobramycin or colistin concentration at 10% (*w/w*) and loaded into dialysis membrane (MWCO 1 kDa, Spectrum Labs, Rancho Domiguez, CA, USA) in the case of tobramycin, or dialysis membrane (MWCO 3.5–5 kDa, Spectrum Labs, USA) in the case of colistin. After that, the whole system was put into 20 mL PBS and placed on a shaker at 400 rpm at 37 °C. The concentration of released drug was analyzed by collecting samples from the supernatant during the period from 1 h to 24 h. The amount of colistin and tobramycin were determined by HPLC and aminoglycoside detection protocol, respectively. The volume was kept constant by refilling with an identical volume of PBS. The cumulative released drug (%) was calculated (mean ± SD of n = 3). Three independent experiments were conducted in triplicates, and results expressed as the mean ± standard deviation (SD).

2.3.2. Minimum Inhibitory Concentration (MIC) Assay

The antimicrobial properties of anCP, anti-infective loaded anCP, and free drugs were performed by standard microbroth dilution assays with *Escherichia coli* (DH5α) and *Pseudomonas aeruginosa* (PA14) in 96 well plates. A suspension of *E. coli* or *P. aeruginosa* prepared from mid log cultures in Mueller-Hinton broth or Lysogeny Broth medium (at 25 °C) was first diluted to OD_{600} (absorption at 600 nm) 0.01, which corresponds to approximately 5×10^6 CFU/mL (CFU, colony-forming units). Polyplex samples (anCP, drug-loaded anCP), free drug solution and PBS as control were then added to bacteria-containing wells by serial dilution over a range of 0.03–64 µg/mL. After incubation for 16 h at 37 °C, inhibitory concentration (IC) IC_{90} values were determined by sigmoidal curve fitting of absorption values (600 nm) that were measured on a Tecan microplate reader. The experiments were conducted in duplicate.

2.4. Preparation of pDNA Loaded cCP

Plasmid DNA pAmCyan was incorporated into the polyplexes to evaluate the potential of the carrier system with respect to nucleic acid actives. A ratio of amine groups (chitosan) to phosphate groups (pDNA) of 20/1 was chosen and is referred to as N/P ratio. The preparation was performed in three steps: first, an appropriate amount of pAmCyan was added to a solution of anionic starch and mixed thoroughly. A 1 mL volume of this pAmCyan-starch solution was added to 1 mL of oligochitosan solution (650 µg/mL) and mixed immediately by vortex for 15 s. A further incubation for 1 h at room temperature was then carried out, leading to the formation of pAmCyan-loaded anCP. In the second step, the pAmCyan loaded anCP were coated by Protasan as described in Section 2.2, to form pAmCyan-loaded cCP. In the third step, a further layer of pAmCyan was applied to pAmCyan-loaded cCP (1:30 *w/w*) resulting in pAmCyan double loaded cCP (Scheme 2B). The pDNA encapsulation efficiency of each step was analyzed by pelleting the samples down and measuring the absorbance of unbound pDNA (at 260/280 nm with NanoDrop Spectrophotmeter) remaining in the supernatant after centrifugation for 30 min at 24,400× g. Thus, the amount of bound pDNA was examined indirectly. The products of each step were characterized to obtain hydrodynamic size, PDI, and ζ-potential, and their morphology was observed by TEM.

2.4.1. Determination the Complexation of pAmCyan in Starch-Chitosan Polyplexes

Complexation and stability of pAmCyan in starch-chitosan polyplexes was evaluated by a gel retardation assay using agarose gel electrophoresis. Further, to facilitate DNA fragmentation, the endonuclease BamHI was used, which linearizes the plasmid, and heparin addition to cause the release of pDNA from the complex. Polyplexes containing 500 ng of pDNA per sample from each step of the formulation process were first digested with 0.5 µL BamHI for 2 h at 37 °C with

shaking. Afterward, 3 µL (30 mg/mL) heparin was added to solutions of digested polyplexes, incubated for 15 min at room temperature and then mixed with 2 µL of orange DNA loading dye (6×; Thermo Fisher Scientific, Waltham, MA, USA). These mixtures were then loaded into 0.75% (*w*/*v*) agarose gel containing 5 µL of ethidium bromide and run for 60 min at 50 V in 0.5× TBE-buffer. The visualization of the bands was performed with a UV illuminator, Fusion FX7 imaging system from Peqlab (Erlangen, Germany).

2.4.2. In Vitro Transfection Studies in A549 Cells

To test the efficiency of the pAmCyan loaded polyplexes, in vitro transfection studies were performed in A549 cells. Briefly, A549 cells were seeded in 24-well plates, at a density of 25 × 10^4 cells per well in 500 µL of RPMI cell culture medium with 10% FCS. Cells were grown for 2 days to reach a cell confluency of 60–70%. Polyplexes of the pAmCyan double loaded carrier system (see Section 2.4) containing 1 µg of pAmCyan (polyplex concentration ~60 µg/mL) were prepared with a ratio of 1:30, 1:50 and 1:100 between pDNA:polyplexes in 500 µL of HBSS buffer. Then, cells were washed twice with HBSS buffer and incubated with the polyplexes for 6 h. After 6 h of incubation, polyplexes were removed and replaced with RPMI containing 10% FCS. Cells were further grown for 2, 3 and 4 days to identify the time point of maximum reporter gene expression. For comparison, the commercially available transfection reagent jetPRIME® was used as positive control. Cells treated with pAmCyan-free cCP and cell culture medium alone were used as negative controls. For confocal laser scanning microscope (CLSM; Leica TCS SP 8, Leica, Wetzlar, Germany) visualization, cell membranes were stained using RGA I (15 µg/mL), and cell nuclei were stained with DAPI (0.1 µg/mL). Samples were then fixed with 3% paraformaldehyde and stored at 4 °C until analysis. All images were acquired using a 25× water immersion objective at 1024 × 1024 resolution and further processed with LAS X software (LAS X 1.8.013370, Leica Microsystems, Leica, Germany). The percentage efficiency of transfected cells was quantified using flow cytometry (BD LSRFortessa™ Cell Analyzer, Biosciences, Heidelberg, Germany). Fifty thousand cells per sample were counted by the cytometer and data were analyzed using FlowJo software (FlowJo 7.6.5, FlowJo LLC, Ashland, OR, USA). Three independent experiments were performed in triplicates, and results expressed as the mean ± standard deviation (SD).

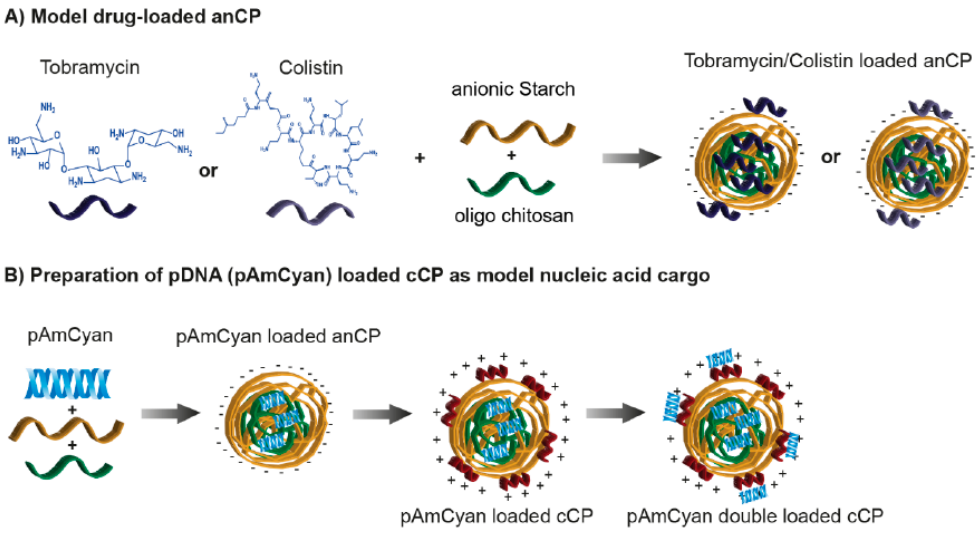

Scheme 2. Illustration of starch-chitosan polyplex-preparation for drug-loaded polyplexes.

3. Results and Discussion

3.1. Preparation and Characterization of Drug-Free Starch-Chitosan Polyplexes

This study represents an extension in comparison to the particle preparation approach of Barthold et al. [29], in which the large poly dispersity index modified starch was employed for colloidal formation. Furthermore, the chemical modification in that reported study, which was used to produce cationic starch derivative, resulted in unfavorably additional synthesis step. Although the particle preparation was well established, the lack of cationic strength due to an obviously low converting yield of cationic starch synthesis limited the carrier capacity for anionic net charge actives of such system. Thus, we used fractionally modified starch derivatives to have better control of colloidal stability, and different molecular weight chitosan derivatives as strong counter excipient for the polyplexes produce. Both excipients are polysaccharides and therefore have favorable characteristics with respect to biological safety, biocompatibility and biodegradability. The simple production of polyplexes using these excipients has the perspective to be readily up-scaled. In the first series of preparations, we studied the plain polymeric complexes by combining both excipients in aqueous solution, with the electrostatic interaction between opposite charges of the individual polymers resulting in polyplex self-assembly. During the optimization of this process, various combinations of types of polymers, C/N ratio, and initial polymer solution concentration were investigated to find a stable and narrow size distribution of the produced colloidal structures (details of the optimization can be found in the Supplementary Materials, Tables S1 and S2). The best of several stable polyplex formulations was produced using a C/N ratio of 10:1, utilizing anionic starch and oligochitosan. Starch-chitosan polyplexes were obtained with an anionic surface charge evidenced by a ζ-potential of around −30 mV. The size of polyplexes could be varied from 150 nm to 350 nm by changing of polymer concentration, with a narrow PDI (<0.3) in all cases. The impact of polymer concentration on polyplex size was expected and already described for comparable systems [30,31]. Spherical polyplex morphology was visualized using TEM (Figure 1A).

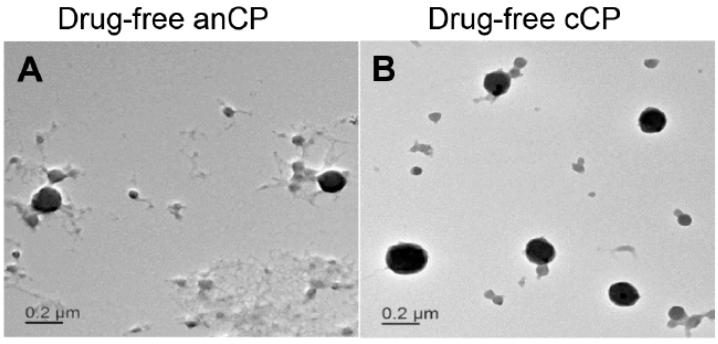

Figure 1. Transmission electron microscope (TEM) images of drug-free starch-chitosan polyplexes stained by 0.5% phosphotungstic acid solution: (**A**) drug-free anCP; and (**B**) drug-free cCP.

Reversing the C/N ratio to 1:10, and using starch (M_w 30–100 kDa) and Protasan (M_w ~90 kDa) resulted in a switch of the surface charge from anionic to cationic (further termed as cationic CP), with a ζ-potential of around +40 mV. The size of particles varied from 214.3 nm to approximately 400 nm depending on the polymer concentration and C/N ratio (Supplementary Materials, Tables S1 and S2). As both anCP and cationic CP systems formed as a result of attractive forces of polymer functional groups, further aggregation of systems over time may potentially occur; the physical stability of the polyplexes was therefore studied over a time course with storage at 4 °C. The colloidal characteristics of both, anCP and cationic CP, remained stable for 27 days with a PDI of ~0.18 and a ζ-potential of −30 mV and +35 mV for anCP and cationic CP, respectively (Supplementary Materials,

Figure S1). Consequently, the utilized preparation process represents a straightforward approach for the formulation of versatile nanoparticles.

The possibility to control the surface charge of a nanocarrier is advantageous for both improving the interaction with the drug to be encapsulated as well as in a later stage the interaction with the target cell [32]. Therefore, the ability to tune surface charge by changing the C/N ratio and molecular weight of starch and chitosan derivatives is a distinct advantage of this novel type of carrier. The ability to load drug molecules of differing structure size and charge, such as e.g., low-M_w anti-infectives as well as high-M_w plasmid DNA, into these carriers was then investigated. Furthermore, a simple coating process was employed to minimize the use of cationic polymer, while still allowing for positive surface charge tuning of particles. The anCP were coated with an additional layer of Protasan (M_w of 90 kDa) resulting in cationic coated polyplexes, cCP. The organic solvent-free procedure was performed in aqueous solution in the presence of PVA as a stabilizer, and led to stable cationic particles with a ζ-potential of +27.1 mV, and a spherical morphology (Figure 1B). The hydrodynamic size and PDI decreased in comparison to anCP (Table 1, Supplementary Materials Table S3) due to the improved electrostatic interaction between the excipients. Furthermore, the anionic, cationic and coated polyplexes overall indicated ζ-potential values of around ±30 mV at which the value ensures improved colloidal stability [33–35], giving the polyplexes the possibility to survive and overcome various biological barriers and reach a specific site of interest.

Table 1. Summary of characteristics of representative drug-free (plain) polyplexes. All measurements were conducted in triplicates. $n = 3$, mean ± SD.

Polyplexes	Size (nm)	PDI	ζ-potential (mV)
Drug-free anCP	287.9 ± 5.0	0.22 ± 0.01	−29.7 ± 0.4
Drug-free cCP	205.4 ± 3.9	0.14 ± 0.02	27.1 ± 1.0

3.1.1. Colloidal Stability of Drug-Free anCP and cCP

To explore the potential to administer anCP and cCP by various routes, the physicochemical stability of these systems was investigated at pH values ranging from 3.5 to 8.0, as relevant for various drug administration pathways. The stability of the polyplexes in different conditions of pH was investigated following 30 min, 1 h, 3 h and 24 h of incubation. As the assembly of the polysaccharide nanoparticulate systems was based on electrostatic interaction, stability of such systems mainly depends on its surface properties which are, in turn, influenced by surrounding environmental factors, e.g., ionic strength and pH values [35,36]. anCP showed stable characteristics regarding size, PDI and ζ-potential, even at the lowest investigated pH value of 3.5 after 3 h incubation (Supplementary Materials, Figure S2). In agreement with the results of Yamada et al. [12], the relatively high M_w (>100 kDa) of the anionic starch clearly aids in stabilization of the particles.

However, the possible dissociation of carboxylate groups on particle surfaces may have eventually led to colloidal aggregation [36] at pH 3.5 and hence destabilized the polyplexes, as indicated by stability data after 24 h of incubation. By contrast the anCP remained stable at all other, higher, pH values after a 24 h incubation (Figure 2), which could be explained by an enhanced repulsive force among anionic particles due to increasing deprotonation of surface carboxylate groups at high pH values. The stability test performed on cCP revealed a stable particle size and PDI at all pH values after 24 h, however a reduction in cCP ζ-potential was seen from pH 3.5 to 8.0 (Figure 2). This behavior is explained by protonation of chitosan molecules, which, being a weak polyelectrolyte with a pK_a of approximately 6.5, has a changing protonation degree depending on the pH of the surrounding solution [37]. An increase in pH value up to 8.0 resulted in a diminishing protonation degree of the chitosan polymer [37,38], thereby resulting in a decrease ζ-potential. Nevertheless, a continued stability of cCP at all tested pH values, especially at pH 7.5 and 8, which are higher than the chitosan pK_a value, could be conferred by the presence of PVA, as a stabilizer that interrupts colloid interaction and aggregation. The stability of both anCP and cCP over a broad range of pH values clearly indicated

flexibility in the potential application of such a tunable carrier system, for drug delivery via various routes of administration. The system could be considered for use in pulmonary delivery, where the local pH is nearly neutral; for gastrointestinal and vaginal delivery, where a low pH environment is encountered [39–41]; and in other applications.

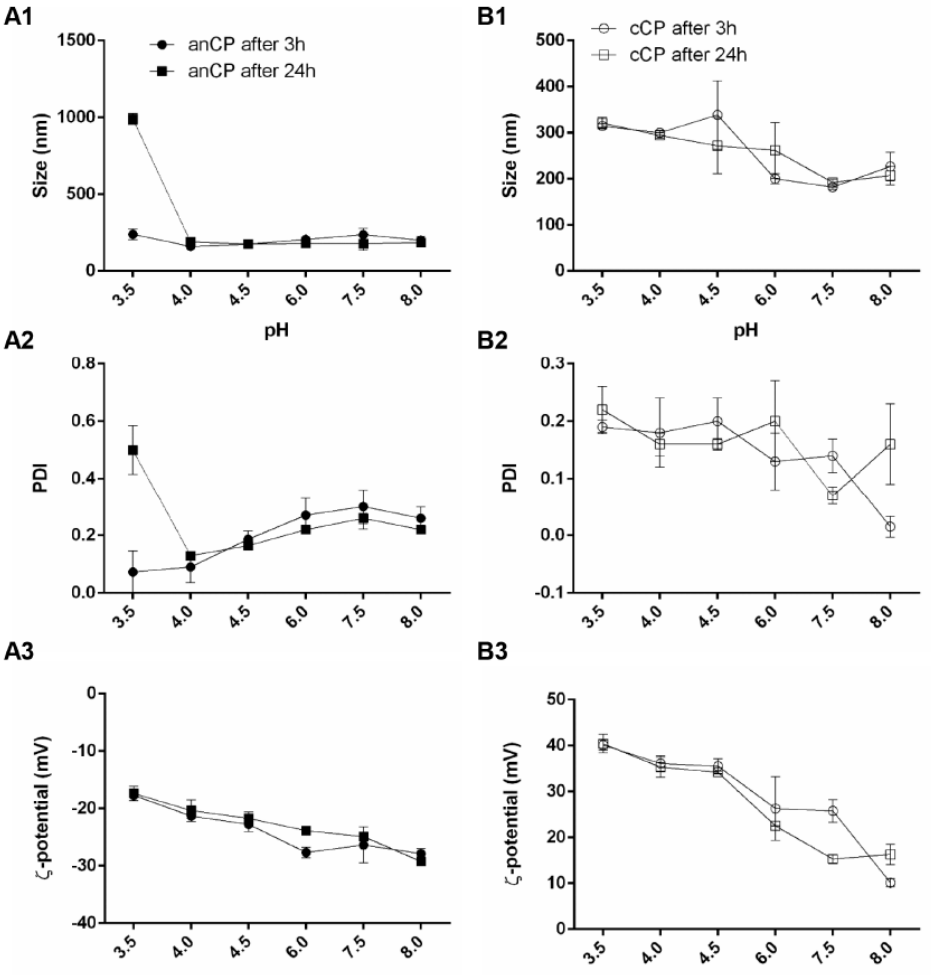

Figure 2. Characteristics of anionic core polyplexes (anCP, **A1**, **A2** and **A3**) and Protasan-coated core polyplexes (cCP, **B1**, **B2** and **B3**) after 3 h and 24 h incubation in pH conditions ranging from 3.5 to 8.0. The pH-values changed accordingly starting from an initial pH-value of the samples of 5.5. $n = 3$, mean ± SD.

3.1.2. Cytotoxicity Assessment

A549 cells were used in our study as a model cell line to test the potential of our carrier system. Figure 3 shows the viability of A549 cells exposed to anCP and cCP with concentrations up to 500 µg/mL, with the light grey area marking the concentration used for later MIC assays and the dark grey showing the concentration employed in subsequent transfection studies. The anCP demonstrated almost no cytotoxicity over the tested concentration range, with an observed cell viability of nearly 100% at all concentrations. However, in contrast, cell viability decreased markedly following treatment with increasing concentrations of cCP. This may be due to their cationic surface charge [42], which, on the other hand, could potentially facilitate a higher cellular uptake of cCP [43], as is particularly relevant for pDNA delivery applications. Ultimately, the cationic surface charge of such pDNA polyplex must be carefully tuned towards an acceptable compromise between transfection efficacy and biocompatibility.

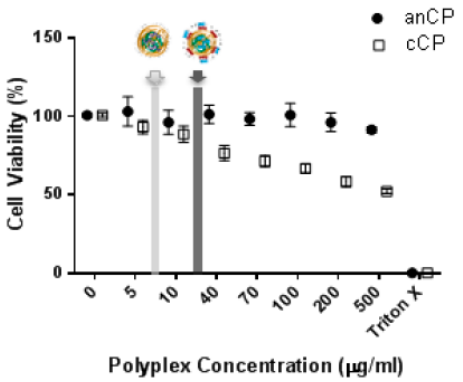

Figure 3. Cell viability assayed by MTT after 4 h incubation (mean ± SD, n = 9 from three independent experiments).

3.2. Loading of anCP with Low-Mw Anti-Infectives

3.2.1. Optimization of the Preparation Process and Drug-Loading

To explore the potential of anCP as a carrier for diverse drug cargos, the aminoglycoside tobramycin (M_w = 467.5 Da), and the oligopeptide colistin (M_w = 1267.5 Da) were chosen as low molecular weight cargos. Tobramycin and colistin are active against Gram negative bacteria, and are two of the four drugs specifically approved in Europe for application as inhaled therapies for chronic bronchopulmonary *P. aeruginosa* infection in cystic fibrosis patients [25,26,44]. Fast elimination and poor permeability however often limit the delivery of hydrophilic anti-infectives, such as tobramycin and colistin, requiring frequent and high dosing with the risk of adverse drug effects and the development of bacterial resistance. Approaches to encapsulate these essential anti-infectives within drug carrier systems to avoid such delivery problems and preserve their activity have therefore been described [30,45]. Tobramycin and colistin both have net positive charges at a neutral pH value due to the presence of amine functional groups in their structures. Thus, it was hypothesized that their properties would be conducive to incorporation into anionic starch-based particles. Consequently, the interaction of further applied chitosan molecules and anionic starch would be affected, which would eventually lead to unstable colloids and aggregation of the resulting system. Therefore, before coacervation, the potential binding of anti-infective molecules to oxidized starch polymer (M_w of >100 kDa), was investigated by isothermal titration calorimetry (ITC), which revealed the thermodynamics of the binding and helped to estimate the optimal drug amount for loading in anCP. Tobramycin and colistin respectively were injected as aqueous solutions to saturate an anionic starch solution, as shown in Figure 4. Values in the inset tables were calculated by the software NanoAnalyze, yielding the same Gibbs free energy (ΔG) for the interaction of around −17.12 kJ/mol for both tobramycin and colistin respectively with the anionic starch polymer. Moreover, based on the thermograms from the ITC analysis, the amount of tobramycin or colistin needed to completely saturate the anionic starch polymer is known. To completely saturate the fixed amount of anionic starch (e.g., 5 mg), there is a need of 1 mg tobramycin, while the needed amount of colistin is 3 mg. The interaction between drug molecule-anionic starch, as well as the number of amine groups on each drug molecule are similar; their molecular weight, however, are nearly three times different. Thus, the amount of the used colislin was three times higher than that of tobramycin. With the aforementioned optimization, the amounts of drugs were selected and for further investigation of drug-loaded anCP.

Having illustrated a clear interaction of tobramycin and colistin with anionic starch, preparation of drug-loaded anCP using chitosan as a counter polymer was investigated. Anionic starch and the selected anti-infective were first incubated, followed by the addition of an appropriate amount of pre-warmed chitosan solution, leading to the formation of polyplexes by self-assembly of these polyelectrolytes. A comparable particle preparing procedure was described by Deacon et al. for

tobramycin and alginate [30]. The C/N ratio and the initial concentrations of the three components (anionic starch, chitosan, and tobramycin or colistin) were varied, and the characteristics of the resulting polyplexes were investigated in order to achieve an optimal formulation. The results of this optimization work are highlighted in Table 2, with additional data shown in the Supplementary Materials (Tables S4 and S5).

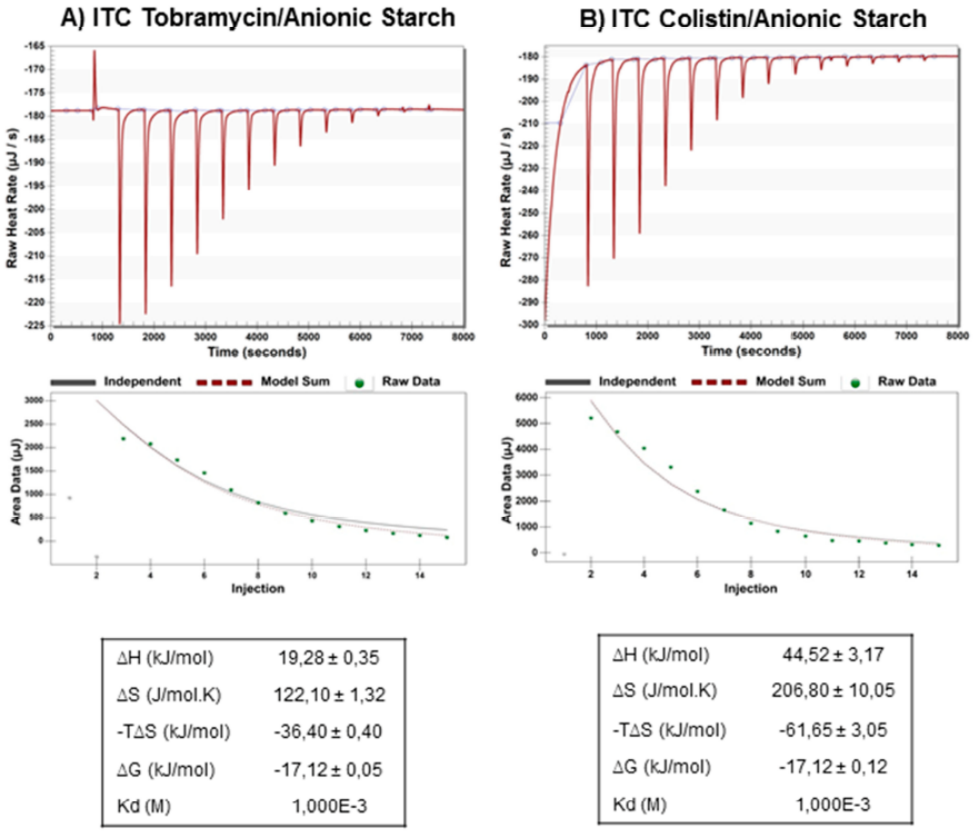

Figure 4. Isothermal titration calorimetry (ITC): (**A**) titration of tobramycin (25 mM) into anionic starch derivative (M_w of >100 kDa) (0.1 mM); and (**B**) titration of colistin (25 mM) into anionic starch derivative (M_w of >100 kDa) (0.1 mM).

The loading capacity of tobramycin and colistin in anCP was then evaluated. Encapsulation of these molecules into anCP was based on the association of anionic ions of oxidized starch and cationic ions of drug molecules. Hence, by using a fixed amount of drug molecules, and varying the C/N ratio (by varying the amount of added chitosan derivative) as well as the initial concentration of polymer solution, stable drug-loaded colloids could be produced. As shown in Table S4, tobramycin-loaded anCP ranging in size from 165.8 ± 0.8 nm to 375.9 ± 1.8 nm with a homogenous distribution (PDI < 0.3) were formed. The ζ-potential of tobramycin-loaded anCP generally increased from nearly −30 mV to average −17 mV, which suggested the presence of cationic drug molecules not only within the polyplex matrix, but also on the surface of polyplexes. An increasing C/N ratio also resulted in a tendency for decreasing particle size from 375.9 ± 1.8 nm to 175.2 ± 2.8 nm. This decrease in size could be due to a condensing effect when using a higher amount of starch, which introduced an excess of available anionic ions for interaction with chitosan, even after incubation with tobramycin. As a result, the colloidal characteristics of tobramycin-loaded nanoparticles were not significantly different to those of unloaded systems. To obtain colistin-loaded anCP, an amount of colistin three times higher in comparison to tobramycin was employed for pre-incubation with anionic starch, due to the molecular

weight difference between the two drugs. Colistin-loaded anCP were prepared again using varying polymer concentrations. As the final concentration decreased, while C/N ratio was maintained at 40/1, the particle size decreased from 324.4 ± 3.6 nm to 266.3 ± 6.5 nm (Table S5). The colistin loaded systems were also stable and homogenous with PDI values lower than 0.3. The results, therefore, clearly show that a reduction in polyplex size resulted from a decrease in employed polymer concentration; this is also in accordance with observations in previous studies [31]. Overall, there was an increase in the ζ-potential of drug loaded carriers as compared to unloaded, which is evidence for the presence of positive net charge anti-infective molecules on carrier surfaces. The size of colistin-loaded anCP was generally larger than the corresponding tobramycin-loaded anCP, which could be explained by the possible formation of colistin micelles during incubation with starch solution. This is made possible by the amphiphilic molecular structure of colistin, which possesses a lipophilic fatty acyl tail and a hydrophilic head group [46]. Consequently, the addition of chitosan supported the colloidal stability of the polyplex system. The morphology of anti-infective loaded anCP was spherical as investigated by TEM (Figure 5A,B). The encapsulation efficiency (EE) and loading rate (LR) of colistin- and tobramycin-loaded anCP are highlighted in Table 2 and Tables S6 and S7. The EE and LR values were indirectly calculated by collecting supernatants after two washing steps. As determined using HPLC, colistin encapsulated within anCP showed maximum values of 96.57 ± 0.19% and 22.70 ± 0.33% for EE and LR, respectively. Incorporation of tobramycin, determined by product fluorescence at 344/450 nm, also showed an EE higher than 98% in all cases, but comparatively lower LR values (2.9 ± 0.0% maximum). The high EE of both model drugs (>90% in all cases) was a result of pre-determination of the interaction between drug molecules and anionic starch, which allowed estimating the amount of used drug in encapsulation and thereby maximization of the encapsulation efficiency. The LR of tobramycin-loaded anCP showed a rational loading capacity for polymeric nanoparticles with a size of approximately 200 nm, while the LR of colistin-loaded anCP was surprisingly high. This might be due to the aforementioned micelle formation of colistin molecules, stabilized by the starch polymer solution. Hence, colistin could be localized in the core of nanoparticles, covered by starch polymer molecules, and could also be loaded on the surface of the system due to charge interaction. The results clearly demonstrate the capacity of the anCP carrier system to be loaded with either type of low-M_w anti-infectives.

Table 2. Summary of characteristics of drug-loaded anCP, %EE = encapsulation efficiency and %LR = loading rate. All measurements were conducted in triplicates. n = 3, mean ± SD.

Polyplexes	Size (nm)	PDI	ζ-potential (mV)	%EE	%LR
Tobramycin loaded anCP	175.2 ± 2.8	0.18 ± 0.00	−16.8 ± 1.0	98.7 ± 0.1	2.9 ± 0.0
Colistin loaded anCP	266.3 ± 6.5	0.27 ± 0.01	−14.6 ± 0.5	96.6 ± 0.2	17.2 ± 0.1
pAmCyan loaded anCP	271.8 ± 2.4	0.25 ± 0.01	−29.8 ± 0.6	76.6 ± 0.6	0.3 ± 0.002
pAmCyan loaded cCP	214.0 ± 3.5	0.17 ± 0.01	28.0 ± 0.6	67.7 ± 14.1	0.2 ± 0.036
pAmCyan double loaded cCP	204.6 ± 3.5	0.16 ± 0.02	25.5 ± 0.6	93.9 ± 4.5	3.3 ± 0.150

Furthermore, the cumulative release profile of both tobramycin and colistin from drug-loaded anCP were studied in PBS at 37 °C, the results are shown in Figure S3. Clearly, the controlled release of anti-infective in PBS could be observed in both cases, with over 40% and 20% of drug released over the period 16–24 h for tobramycin and colistin, respectively. The initial burst after 4–6 h incubation was recorded as on average nearly 30% for tobramycin and 20% for colistin. The percentage of initial anti-infective released from the anCP would represent the amount of drug molecule loaded on the particles surface. Interestingly, the release of colistin at all time points are relatively lower than that of tobramycin, which would again be explained by the aforementioned micelle formation of colistin molecules that are stabilized and maybe then embedded inside the polymeric polyplex. The release results would help predict the drug carriers behavior in further in vitro experiments. To evaluate the release of the anti-infectives from drug-loaded anCP, and have better insight into the controlled

release in vitro or in vivo, in which other components exist, e.g., bacteria, would require more complex biologically simulated tests that were beyond the scope of the present study.

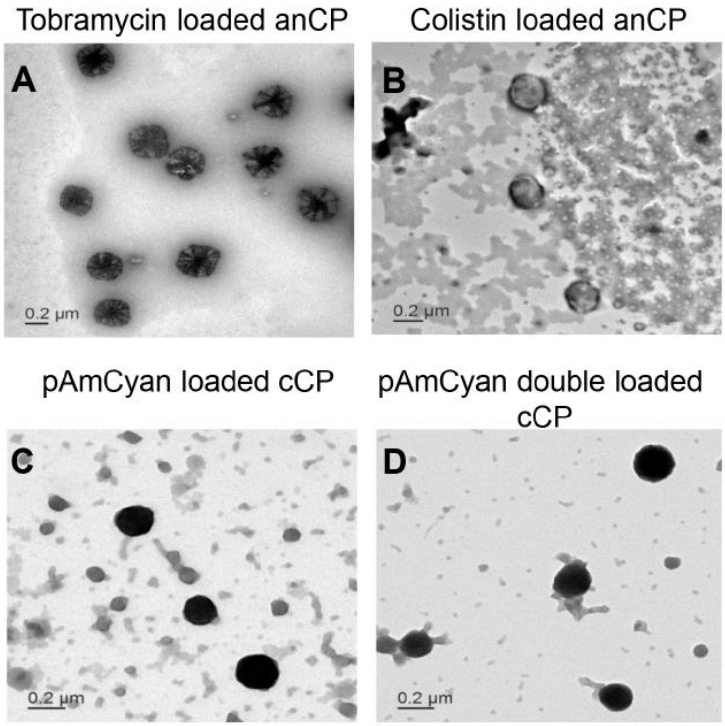

Figure 5. Transmission electron microscope (TEM) images of drug-loaded starch-chitosan polyplexes stained by 0.5% phosphotungstic acid solution: (**A**) tobramycin loaded anCP; (**B**) colistin loaded anCP; (**C**) pAmCyan loaded cCP; and (**D**) pAmCyan double loaded cCP.

3.2.2. Efficacy of Anti-Infective Loaded anCP

While anCP have the capacity to load different types of anti-infectives including small molecule and peptide drugs, it is important that the particle excipients do not interfere with action of active agents which might confound the further evaluation of drug delivery systems. Hence, the anti-microbial activity of blank anCP and anti-infective loaded anCP were studied against *E. coli* and *P. aeruginosa* in comparison to the use of free drugs. As shown in Table 3, the antibacterial activity of drug-loaded anCP was relatively similar to that of the corresponding free drug. MIC values obtained show that blank anCP were not active against *E. coli* and *P. aeruginosa* at the highest tested concentrations, which means the formation of polyplexes with anCP did not compromise the intrinsic anti-microbial efficiency of either antibiotic. To demonstrate a superior safety and efficiency profile of such nanocarriers in comparison to the free drug would require some more complex biological test systems that were beyond the scope of the present study.

Table 3. MIC assay results against *E. coli* and *P. aeruginosa*.

Samples	IC90 against *E. coli* (µg/mL)	IC90 against *P. aeruginosa* (µg/mL)
Tobramycin	0.2–0.3	1.56
Tobramycin loaded anCP	0.2–0.3 *	1.56 *
Colistin	0.4–0.5	3.125
Colistin loaded anCP	0.5 *	3.125–6.25 *
anCP	>64	>64
PBS buffer	no inhibition	no inhibition

* Drug content in anCP.

3.3. Loading of anCP with High-Mw pDNA

A model plasmid DNA encoding a fluorescent dye (pAmCyan) was further incorporated into the carrier system in a three-step procedure (core formation, Protasan coating and pDNA complexation), to demonstrate the ability of the polyplexes to deliver a broad spectrum of cargos. The three-step procedure also lead to an increase of nucleic acid encapsulation within the polyplexes, protecting nucleic acids from enzymatic degradation. Produced pAmCyan loaded polyplexes were again found to have a spherical structure (Figure 5C,D). The physiochemical characteristics of all intermediate and final polyplexes in this stepwise production can be found in Table 2. Each subsequent step in the preparation procedure results in a denser complexation, with the pAmCyan double loaded cCP showing the smallest size and most narrow size distribution (lowest PDI value). Furthermore, the ζ-potential was observed to switch from negative to positive after coating with Protasan, with a further slight decrease after complexation with negatively charged pAmCyan. The additional complexation with pAmCyan resulted in a 15% higher encapsulation efficiency in comparison to the intermediate step 2 (Table 2). Additionally, agarose gel electrophoresis (Figure 6, left) elucidates that no pDNA could run through the gel, which indicates that pDNA is strongly complexed within the polyplexes. Only further treatment with BamHI and heparin causes pDNA release as seen through the bands (Figure 6, right). Furthermore, pDNA loaded anCP and pDNA associated on the surface of polyplexes (pDNA double loaded cCP) allow an easier intercalation of EtBr and faster release with heparin, whereas pDNA loaded cCP is densely packed impeding pDNA release as no free pDNA bands can be observed in the gel.

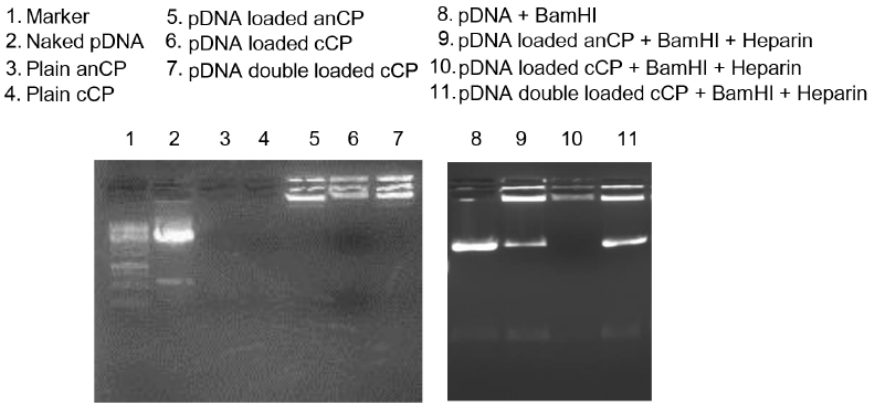

Figure 6. Gel retardation assay using agarose gel electrophoresis of plain and pDNA (pAmCyan) incorporated polyplexes for all three preparation steps in comparison with naked pDNA (undigested pDNA) and digested pDNA (pDNA + BamHI).

Potential of Polyplexes for pDNA Delivery

Using nanoparticles as a non-viral delivery system for gene therapy represents a significant challenge, as nanocarriers need to cross several biological barriers while preserving the functionality of carried pDNA. pDNA condensed inside the nanocarriers must survive the acidic conditions inside the lysosomes and escape the lysosomal compartment in order to cross the nuclear membrane [43]. Current knowledge of polymeric transfection systems suggests that a good pH-buffering capacity (a process known as the "proton sponge effect") [47] is an important factor in the achievement of endosomal escape. Here, the potential of starch–chitosan polyplexes for nucleic acid delivery was explored by in vitro transfection studies using A549 cells. Three different ratios between pDNA:polyplexes have been studied to investigate the best transfection rate. While 1:50 and 1:100 show no significant transfection (data not shown), 1:30 mediated successful transfection, with the highest reporter gene expression observed after 48 h with 5% of transfected cells. In comparison, jetPRIME® as positive

control had a higher transfection efficiency (45%) after 48 h, which rapidly decreased to 30% after 72 h and to 25% after 96 h (Figure 7). The comparatively lower transfection efficiency of the polyplexes may be due to a high stability of condensed pDNA, leading to an incomplete release of pDNA inside the cytoplasmic compartment [48,49]. Further improvement of the transfection efficiency would presumably be achievable by addition of endosomal escape moieties [50,51], or with chitosan derivatives (e.g., trimethylation or amino acid conjugation) [52,53]. However, such efficacy improvements often impact the biocompatibility. Thus, optimization between safety and efficacy should be performed for a selected nucleotide type, target application, and delivery route, since carrier stability, cellular uptake, and functional efficacy are highly dependent on all these factors.

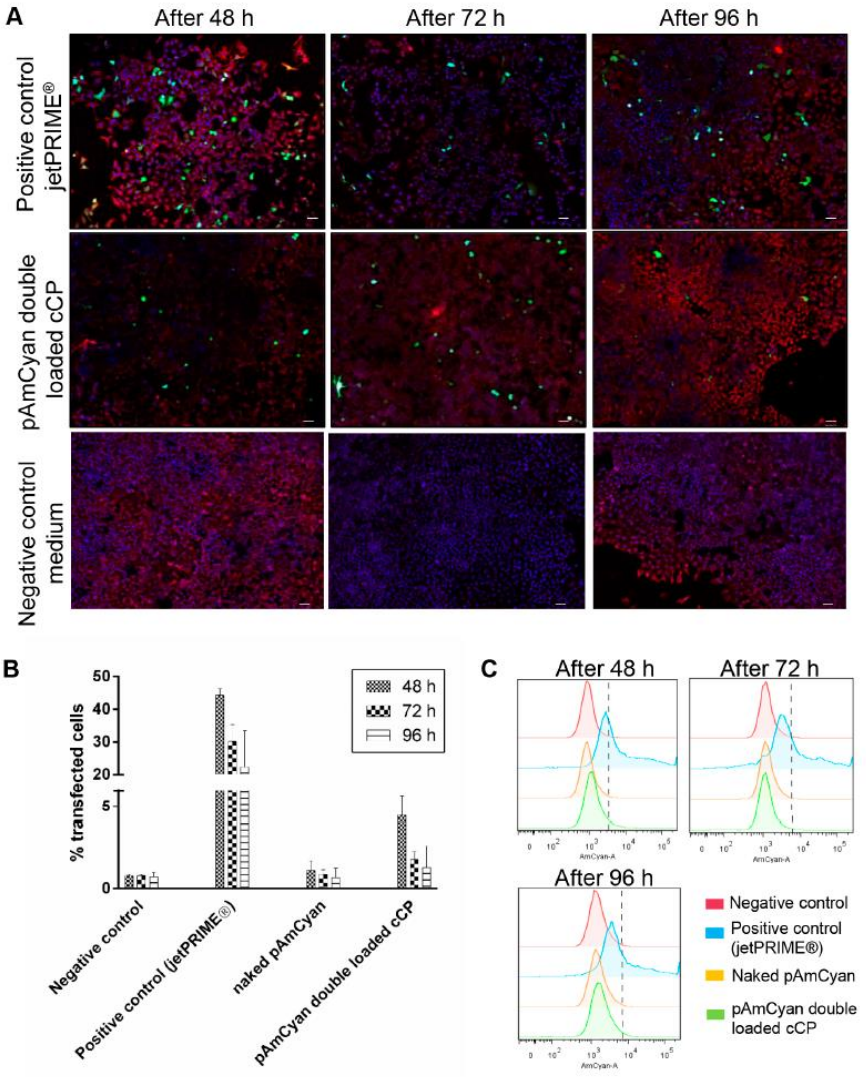

Figure 7. (**A**) Representative confocal images of A549 cells transfected with pAmCyan double loaded pAmCyan by using jetPRIME® as positive control and only cell culture medium as negative control. Transfection was analyzed with CLSM after 48 h, 72 h, and 96 h. Green fluorescence reveals cells successfully transfected with the polyplexes while their morphology remains consistent with non-transfected cells (red: cell membrane; blue: cell nucleus; scale bar 50 µm). (**B**) The transfection efficiency was further quantified using flow cytometry, which indicated the highest amount of transfection after 48 h for pAmCyan double loaded cCP. (**C**) Representative graphs obtained with flow cytometer.

4. Conclusions

In this work, we produced a flexible, straightforward and organic solvent-free procedure for the manufacture of nanocarrier systems based on the natural, biodegradable and biocompatible polysaccharides starch and chitosan. Starch and chitosan derivatives of different M_w ranges were combined by adjusting the molar ratio of carboxyl and amine functional groups, polymer concentration and counter polymer type to obtain a delivery system with tunable properties including surface charge and size. Core polyplexes (CP) were built by complex coacervation of anionic starch (M_w ~100 kDa) with positively charged chitosan derivatives (M_w ~5 kDa) in aqueous solution. The polyplexes with the best colloidal properties were obtained at a molar ratio of carboxyl and amine groups of 10:1. The negatively charged core polyplexes remained stable on storage for over 27 days. We further focused on optimizing anionic CPs by coating them with an additional layer of chitosan (Protasan, M_w ~90 kDa). Cell viability testing of anCPs and cCPs indicated a low level of cytotoxicity acceptable for use in biological systems, and colloidal stability at different tested pH values. The developed anCP system further showed good carrier properties, allowing for high encapsulation efficiency (>90%) of cationic peptide (colistin) and small molecule (tobramycin) anti-infectives without compromising antimicrobial activity. Moreover, the cationic polyplexes, cCP, allowed for double encapsulation of plasmid DNA (pAmCyan) for intracellular delivery as confirmed by gel retardation assay, and facilitating in-vitro transfection in A549 cells.

Starch-chitosan polyplexes show high flexibility for designing multifunctional carriers, in which for example the core polyplexes can encapsulate anti-infectives, while the outer coating layer could be used to incorporate other components like enzymes or nucleases (e.g., deoxyribonuclease I) to enhance drug penetration through biofilms or mucus [30]. For gene therapy purposes the inner polyplex can be used to carry and protect plasmid DNA, while the surface could be decorated with a second polynucleotide.

Supplementary Materials: The following are available online at http://www.mdpi.com/2073-4360/10/3/252/s1, Figure S1: Physicochemical stability of starch-chitosan CP, in which anCP was produced with C/N ratio 10/1, and catCP was produced with C/N ratio 1/10, upon storage (4 °C). The particles were diluted into Milli-Q water at each time point for the measurement of size, PDI and ζ-potential. $N = 3$, $n = 3$, mean ± SD; Figure S2: Physicochemical stability of starch-chitosan anCP and cCP at different pH values ranging from 3.5 to 8.0, after 30 min and 1 h incubation. The initial pH-value of the samples was 5.5. $N = 3$, $n = 3$, mean ± SD; Figure S3: Cumulative release of tobramycin from tobramycin loaded anCP, and colistin from colistin loaded anCP performed in PBS at 37 °C. $N = 3$, $n = 3$, mean ± SD; Table S1: Summary of starch-chitosan CP characteristics obtained by varying polymer types, polymer concentration, and C/N molar ratio. $N > 3$, $n = 3$, mean ± SD; Table S2: Summary of starch-chitosan CP characterization with optimal C/N ratio varied by change of polymer concentration. $N > 3$, $n = 3$, mean ± SD; Table S3: Summary of anionic CP (anCP) and Protasan coated anCP (cCP) characteristics, in which anCP was produced with parameters, namely C/N ratio 10/1, and polymer concentration at 6.5 mg/mL. $N > 3$, $n = 3$, mean ± SD; Table S4: Summary of tobramycin-loaded anCP characteristics achieved by variation of C/N ratio and polymer concentration. $N > 3$, $n = 3$, mean ± SD; Table S5: Summary of colistin-loaded anCP characteristics resulting from variation of polymer concentration. $N > 3$, $n = 3$, mean ± SD; Table S6: Summary of drug loading quantification of tobramycin-loaded anCP. $N > 3$, $n = 3$, mean ± SD; Table S7: Summary of drug loading quantification of colistin-loaded anCP. $N > 3$, $n = 3$, mean ± SD.

Acknowledgments: The authors thank Xabier Murgia Esteve, Florian Gräf, and Arianna Castoldi for fruitful discussions; Petra König and Jana Westhues for support and handling of cell cultures; and Viktoria Schmitt for bacteria culture. This project has received funding from the European Union Framework Programme for Research and Innovation Horizon 2020 (2014–2020) under the Marie Sklodowska-Curie Grant Agreement No. 642028.

Author Contributions: Hanzey Yasar and Duy-Khiet Ho contributed equally in this study in which they initiated the research idea, conceived and designed all experiments. Hanzey Yasar and Duy-Khiet Ho synthesized and prepared molecular weight fractionalized anionic starch, and optimized particles preparing process of starch and chitosan (including negative, positive and coated surface particles), as well as investigated stability of all particles at storage condition and different pH environments. Hanzey Yasar further studied cytotoxicity (by MTT assay) and plasmid (pAmCyan) loading capacity (by a gel retardation assay) of the particles, and performed transfection study on A549 cell line by CLSM and quantification method using flow cytometry. Duy-Khiet Ho further studied and optimized cationic anti-infectives (tobramycin and colistin) loading capacity (by isothermal titration calorimetry) of the particles, and performed the minimum inhibitory concentration (MIC) assay on *E. coli* and *P. aeruginosa*. Hanzey Yasar and Duy-Khiet Ho analyzed all the data and wrote the manuscript with an equal manner. Chiara De Rossi visualized the developed particles by using TEM, performed HPLC, and contributed

her expertise in imaging and analyzing the transfection study by using CLSM. Jennifer Herrmann contributed her expertise in bacteria study and analyzed the data. Sarah Gordon, Brigitta Loretz and Claus-Michael Lehr supervised Hanzey Yasar and Duy-Khiet Ho, initiated the project and have been responsible for the overall scientific approach. All authors contributed with their scientific input to the written manuscript.

Conflicts of Interest: The authors declare no competing financial interest.

Abbreviations

CP	core polyplexes
anCP	anionic core polyplexes
cationic CP (or catCP)	cationic core polyplexes
cCP	coated polyplexes

References

1. Kang, B.; Opatz, T.; Landfester, K.; Wurm, F.R. Carbohydrate nanocarriers in biomedical applications: Functionalization and construction. *Chem. Soc. Rev.* **2015**, *44*, 8301–8325. [CrossRef] [PubMed]
2. Bachmann, M.F.; Jennings, G.T. Vaccine delivery: A matter of size, geometry, kinetics and molecular patterns. *Nat. Rev. Immunol.* **2010**, *10*, 787–796. [CrossRef] [PubMed]
3. Abed, N.; Couvreur, P. Nanocarriers for antibiotics: A promising solution to treat intracellular bacterial infections. *Int. J. Antimicrob. Agents* **2014**, *43*, 485–496. [CrossRef] [PubMed]
4. D'Angelo, I.; Conte, C.; Miro, A.; Quaglia, F.; Ungaro, F. Pulmonary drug delivery: A role for polymeric nanoparticles? *Curr. Top. Med. Chem.* **2015**, *15*, 386–400. [CrossRef] [PubMed]
5. Mahapatro, A.; Singh, D.K. Biodegradable nanoparticles are excellent vehicle for site directed in-vivo delivery of drugs and vaccines. *J. Nanobiotechnol.* **2011**, *9*, 55. [CrossRef] [PubMed]
6. Baldwin, A.D.; Kiick, K.L. Polysaccharide-modified synthetic polymeric biomaterials. *Biopolymers* **2010**, *94*, 128–140. [CrossRef] [PubMed]
7. Wikström, J.; Elomaa, M.; Syväjärvi, H.; Kuokkanen, J.; Yliperttula, M.; Honkakoski, P.; Urtti, A. Alginate-based microencapsulation of retinal pigment epithelial cell line for cell therapy. *Biomaterials* **2008**, *29*, 869–876. [CrossRef] [PubMed]
8. Hans, M.L.; Lowman, A.M. Biodegradable nanoparticles for drug delivery and targeting. *Curr. Opin. Solid State Mater. Sci.* **2002**, *6*, 319–327. [CrossRef]
9. Azzam, T.; Eliyahu, H.; Shapira, L.; Linial, M.; Barenholz, Y.; Domb, A.J. Polysaccharide? Oligoamine Based Conjugates for Gene Delivery. *J. Med. Chem.* **2002**, *45*, 1817–1824. [CrossRef] [PubMed]
10. Sim, H.J.; Thambi, T.; Lee, D.S. Heparin-based temperature-sensitive injectable hydrogels for protein delivery. *J. Mater. Chem. B* **2015**, *3*, 8892–8901. [CrossRef]
11. Builders, P.F.; Arhewoh, M.I. Pharmaceutical applications of native starch in conventional drug delivery. *Starch Stärke* **2016**, *68*, 864–873. [CrossRef]
12. Yamada, H.; Loretz, B.; Lehr, C.-M. Design of starch-graft-PEI polymers: An effective and biodegradable gene delivery platform. *Biomacromolecules* **2014**, *15*, 1753–1761. [CrossRef] [PubMed]
13. Mahmoudi Najafi, S.H.; Baghaie, M.; Ashori, A. Preparation and characterization of acetylated starch nanoparticles as drug carrier: Ciprofloxacin as a model. *Int. J. Biol. Macromol.* **2016**, *87*, 48–54. [CrossRef] [PubMed]
14. Balmayor, E.R.; Baran, E.T.; Azevedo, H.S.; Reis, R.L. Injectable biodegradable starch/chitosan delivery system for the sustained release of gentamicin to treat bone infections. *Carbohydr. Polym.* **2012**, *87*, 32–39. [CrossRef]
15. Santander-Ortega, M.J.; Stauner, T.; Loretz, B.; Ortega-Vinuesa, J.L.; Bastos-González, D.; Wenz, G.; Schaefer, U.F.; Lehr, C.M. Nanoparticles made from novel starch derivatives for transdermal drug delivery. *J. Control. Release* **2010**, *141*, 85–92. [CrossRef] [PubMed]
16. Bernkop-Schnurch, A.; Dunnhaupt, S. Chitosan-based drug delivery systems. *Eur. J. Pharm. Biopharm.* **2012**, *81*, 463–469. [CrossRef] [PubMed]
17. Grenha, A.; Gomes, M.E.; Rodrigues, M.; Santo, V.E.; Mano, J.F.; Neves, N.M.; Reis, R.L. Development of new chitosan/carrageenan nanoparticles for drug delivery applications. *J. Biomed. Mater. Res. Part A* **2010**, *92*, 1265–1272. [CrossRef] [PubMed]

18. Gan, Q.; Wang, T. Chitosan nanoparticle as protein delivery carrier—Systematic examination of fabrication conditions for efficient loading and release. *Colloids Surf. B Biointerfaces* **2007**, *59*, 24–34. [CrossRef] [PubMed]
19. Wen, Z.-S.; Xu, Y.-L.; Zou, X.-T.; Xu, Z.-R. Chitosan nanoparticles act as an adjuvant to promote both Th1 and Th2 immune responses induced by ovalbumin in mice. *Mar. Drugs* **2011**, *9*, 1038–1055. [CrossRef] [PubMed]
20. De Campos, A.M.; Sánchez, A.; Alonso, M.J. Chitosan nanoparticles: A new vehicle for the improvement of the delivery of drugs to the ocular surface. Application to cyclosporin A. *Int. J. Pharm.* **2001**, *224*, 159–168. [CrossRef]
21. Van der Lubben, I.M.; Verhoef, J.C.; van Aelst, A.C.; Borchard, G.; Junginger, H.E. Chitosan microparticles for oral vaccination: Preparation, characterization and preliminary in vivo uptake studies in murine Peyer's patches. *Biomatrials* **2001**, *22*, 687–694. [CrossRef]
22. Dodane, V.; Vilivalam, V.D. Pharmaceutical applications of chitosan. *Pharm. Sci. Technol. Today* **1998**, *1*, 246–253. [CrossRef]
23. Onishi, H.; Machida, Y. Biodegradation and distribution of water-soluble chitosan in mice. *Biomaterials* **1999**, *20*, 175–182. [CrossRef]
24. Aspden, T.J.; Mason, J.D.; Jones, N.S.; Lowe, J.; Skaugrud, O.; Illum, L. Chitosan as a nasal delivery system: The effect of chitosan solutions on in vitro and in vivo mucociliary transport rates in human turbinates and volunteers. *J. Pharm. Sci.* **1997**, *86*, 509–513. [CrossRef] [PubMed]
25. Elborn, J.S.; Vataire, A.-L.; Fukushima, A.; Aballea, S.; Khemiri, A.; Moore, C.; Medic, G.; Hemels, M.E.H. Comparison of Inhaled Antibiotics for the Treatment of Chronic *Pseudomonas aeruginosa* Lung Infection in Patients with Cystic Fibrosis: Systematic Literature Review and Network Meta-analysis. *Clin. Ther.* **2016**, *38*, 2204–2226. [CrossRef] [PubMed]
26. Elborn, S.; Vataire, A.-L.; Fukushima, A.; Aballéa, S.; Khemiri, A.; Moore, C.; Medic, G.; Hemels, M. Efficacy and safety of inhaled antibiotics for chronic pseudomonas infection in cystic fibrosis: Network meta-analysis. *Eur. Respir. J.* **2016**, *48*, PA4863. [CrossRef]
27. Nafee, N.; Schneider, M.; Schaefer, U.F.; Lehr, C.-M. Relevance of the colloidal stability of chitosan/PLGA nanoparticles on their cytotoxicity profile. *Int. J. Pharm.* **2009**, *381*, 130–139. [CrossRef] [PubMed]
28. Benson, J.R.; Hare, P.E. *O*-phthalaldehyde: Fluorogenic detection of primary amines in the picomole range. Comparison with fluorescamine and ninhydrin. *Proc. Natl. Acad. Sci. USA* **1975**, *72*, 619–622. [CrossRef] [PubMed]
29. Barthold, S.; Kletting, S.; Taffner, J.; de Souza Carvalho-Wodarz, C.; Lepeltier, E.; Loretz, B.; Lehr, C.-M. Preparation of nanosized coacervates of positive and negative starch derivatives intended for pulmonary delivery of proteins. *J. Mater. Chem. B* **2016**, *4*, 2377–2386. [CrossRef]
30. Deacon, J.; Abdelghany, S.M.; Quinn, D.J.; Schmid, D.; Megaw, J.; Donnelly, R.F.; Jones, D.S.; Kissenpfennig, A.; Elborn, J.S.; Gilmore, B.F.; et al. Antimicrobial efficacy of tobramycin polymeric nanoparticles for *Pseudomonas aeruginosa* infections in cystic fibrosis: Formulation, characterisation and functionalisation with dornase alfa (DNase). *J. Control. Release* **2015**, *198*, 55–61. [CrossRef] [PubMed]
31. Dul, M.; Paluch, K.J.; Kelly, H.; Healy, A.M.; Sasse, A.; Tajber, L. Self-assembled carrageenan/protamine polyelectrolyte nanoplexes-Investigation of critical parameters governing their formation and characteristics. *Carbohydr. Polym.* **2015**, *123*, 339–349. [CrossRef] [PubMed]
32. Radovic-Moreno, A.F.; Lu, T.K.; Puscasu, V.A.; Yoon, C.J.; Langer, R.; Farokhzad, O.C. Surface charge-switching polymeric nanoparticles for bacterial cell wall-targeted delivery of antibiotics. *ACS Nano* **2012**, *6*, 4279–4287. [CrossRef] [PubMed]
33. Mandzy, N.; Grulke, E.; Druffel, T. Breakage of TiO_2 agglomerates in electrostatically stabilized aqueous dispersions. *Powder Technol.* **2005**, *160*, 121–126. [CrossRef]
34. Jonassen, H.; Kjoniksen, A.-L.; Hiorth, M. Stability of chitosan nanoparticles cross-linked with tripolyphosphate. *Biomacromolecules* **2012**, *13*, 3747–3756. [CrossRef] [PubMed]
35. Honary, S.; Zahir, F. Effect of Zeta Potential on the Properties of Nano-Drug Delivery Systems—A Review (Part 2). *Trop. J. Pharm. Res.* **2013**, *12*, 265–273. [CrossRef]
36. Yoo, M.K.; Sung, Y.K.; Chong, S.C.; Young, M.L. Effect of polymer complex formation on the cloud-point of poly(*N*-isopropyl acrylamide) (PNIPAAm) in the poly(NIPAAm-*co*-acrylic acid): Polyelectrolyte complex between poly(acrylic acid) and poly(allylamine). *Polymer* **1997**, *38*, 2759–2765. [CrossRef]
37. Fan, W.; Yan, W.; Xu, Z.; Ni, H. Formation mechanism of monodisperse, low molecular weight chitosan nanoparticles by ionic gelation technique. *Colloids Surf. B Biointerfaces* **2012**, *90*, 21–27. [CrossRef] [PubMed]

38. Shu, X.; Zhu, K. The influence of multivalent phosphate structure on the properties of ionically cross-linked chitosan films for controlled drug release. *Eur. J. Pharm. Biopharm.* **2002**, *54*, 235–243. [CrossRef]
39. Ensign, L.M.; Cone, R.; Hanes, J. Nanoparticle-based drug delivery to the vagina: A review. *J. Control. Release* **2014**, *190*, 500–514. [CrossRef] [PubMed]
40. Evans, D.F.; Pye, G.; Bramley, R.; Clark, A.G.; Dyson, T.J.; Hardcastle, J.D. Measurement of gastrointestinal pH profiles in normal ambulant human subjects. *Gut* **1988**, *29*, 1035–1041. [CrossRef] [PubMed]
41. Melis, G.B.; Ibba, M.T.; Steri, B.; Kotsonis, P.; Matta, V.; Paoletti, A.M. Ruolo del pH come modulatore dell'equilibrio fisiopatologico vaginale. *Min. Ginecol.* **2000**, *52*, 111–121.
42. Fischer, D.; Li, Y.; Ahlemeyer, B.; Krieglstein, J.; Kissel, T. In vitro cytotoxicity testing of polycations: Influence of polymer structure on cell viability and hemolysis. *Biomatrials* **2003**, *24*, 1121–1131. [CrossRef]
43. Frohlich, E. The role of surface charge in cellular uptake and cytotoxicity of medical nanoparticles. *Int. J. Nanomed.* **2012**, *7*, 5577–5591. [CrossRef] [PubMed]
44. Maiz, L.; Giron, R.M.; Olveira, C.; Quintana, E.; Lamas, A.; Pastor, D.; Canton, R.; Mensa, J. Inhaled antibiotics for the treatment of chronic bronchopulmonary *Pseudomonas aeruginosa* infection in cystic fibrosis: Systematic review of randomised controlled trials. *Expert Opin. Pharmacother.* **2013**, *14*, 1135–1149. [CrossRef] [PubMed]
45. Bargoni, A.; Cavalli, R.; Zara, G.P.; Fundaro, A.; Caputo, O.; Gasco, M.R. Transmucosal transport of tobramycin incorporated in solid lipid nanoparticles (SLN) after duodenal administration to rats. Part II—Tissue distribution. *Pharmacol. Res.* **2001**, *43*, 497–502. [CrossRef] [PubMed]
46. Wallace, S.J.; Li, J.; Nation, R.L.; Prankerd, R.J.; Velkov, T.; Boyd, B.J. Self-assembly behavior of colistin and its prodrug colistin methanesulfonate: Implications for solution stability and solubilization. *J. Phys. Chem. B* **2010**, *114*, 4836–4840. [CrossRef] [PubMed]
47. Akinc, A.; Thomas, M.; Klibanov, A.M.; Langer, R. Exploring polyethylenimine-mediated DNA transfection and the proton sponge hypothesis. *J. Gene Med.* **2005**, *7*, 657–663. [CrossRef] [PubMed]
48. Truong, N.P.; Jia, Z.; Burgess, M.; Payne, L.; McMillan, N.A.J.; Monteiro, M.J. Self-catalyzed degradable cationic polymer for release of DNA. *Biomacromolecules* **2011**, *12*, 3540–3548. [CrossRef] [PubMed]
49. Hartono, S.B.; Phuoc, N.T.; Yu, M.; Jia, Z.; Monteiro, M.J.; Qiao, S.; Yu, C. Functionalized large pore mesoporous silica nanoparticles for gene delivery featuring controlled release and co-delivery. *J. Mater. Chem. B* **2014**, *2*, 718–726. [CrossRef]
50. Truong, N.P.; Gu, W.; Prasadam, I.; Jia, Z.; Crawford, R.; Xiao, Y.; Monteiro, M.J. An influenza virus-inspired polymer system for the timed release of siRNA. *Nat. Commun.* **2013**, *4*, 1902. [CrossRef] [PubMed]
51. Sanz, V.; Coley, H.M.; Silva, S.R.P.; McFadden, J. Protamine and Chloroquine Enhance Gene Delivery and Expression Mediated by RNA-Wrapped Single Walled Carbon Nanotubes. *J. Nanosci. Nanotechnol.* **2012**, *12*, 1739–1747. [CrossRef] [PubMed]
52. Kean, T.; Roth, S.; Thanou, M. Trimethylated chitosans as non-viral gene delivery vectors: Cytotoxicity and transfection efficiency. *J. Control. Release* **2005**, *103*, 643–653. [CrossRef] [PubMed]
53. Zheng, H.; Tang, C.; Yin, C. Exploring advantages/disadvantages and improvements in overcoming gene delivery barriers of amino acid modified trimethylated chitosan. *Pharm. Res.* **2015**, *32*, 2038–2050. [CrossRef] [PubMed]

6.4 Kinetics of mRNA Delivery and Protein Translation in Dendritic Cells using Lipid-Coated PLGA Nanoparticles

Kinetics of mRNA delivery and protein translation in dendritic cells using lipid-coated PLGA nanoparticles

Hanzey Yasar, Alexander Biehl, Chiara De Rossi, Marcus Koch, Xabi Murgia, Brigitta Loretz, Claus-Michael Lehr; Journal of Nanobiotechnology 2018, **16**:72

DOI.org/10.1186/s12951-018-0401-y

Yasar *et al. J Nanobiotechnol (2018) 16:72*
https://doi.org/10.1186/s12951-018-0401-y

Journal of Nanobiotechnology

RESEARCH Open Access

Kinetics of mRNA delivery and protein translation in dendritic cells using lipid-coated PLGA nanoparticles

Hanzey Yasar[1,2], Alexander Biehl[1,3], Chiara De Rossi[1], Marcus Koch[4], Xabi Murgia[1,2], Brigitta Loretz[1*] and Claus-Michael Lehr[1,2,3]

Abstract

Background: Messenger RNA (mRNA) has gained remarkable attention as an alternative to DNA-based therapies in biomedical research. A variety of biodegradable nanoparticles (NPs) has been developed including lipid-based and polymer-based systems for mRNA delivery. However, both systems still lack in achieving an efficient transfection rate and a detailed understanding of the mRNA transgene expression kinetics. Therefore, quantitative analysis of the time-dependent translation behavior would provide a better understanding of mRNA's transient nature and further aid the enhancement of appropriate carriers with the perspective to generate future precision nanomedicines with quick response to treat various diseases.

Results: A lipid–polymer hybrid system complexed with mRNA was evaluated regarding its efficiency to transfect dendritic cells (DCs) by simultaneous live cell video imaging of both particle uptake and reporter gene expression. We prepared and optimized NPs consisting of poly (lactid-*co*-glycolid) (PLGA) coated with the cationic lipid 1, 2-di-*O*-octadecenyl-3-trimethylammonium propane abbreviated as LPNs. An earlier developed polymer-based delivery system (chitosan-PLGA NPs) served for comparison. Both NPs types were complexed with mRNA-mCherry at various ratios. While cellular uptake and toxicity of either NPs was comparable, LPNs showed a significantly higher transfection efficiency of ~ 80% while chitosan-PLGA NPs revealed only ~ 5%. Further kinetic analysis elicited a start of protein translation after 1 h, with a maximum after 4 h and drop of transgene expression after 48 h post-transfection, in agreement with the transient nature of mRNA.

Conclusions: Charge-mediated complexation of mRNA to NPs enables efficient and fast cellular delivery and subsequent protein translation. While cellular uptake of both NP types was comparable, mRNA transgene expression was superior to polymer-based NPs when delivered by lipid–polymer NPs.

Keywords: mRNA, Transfection, Gene delivery, Chitosan-PLGA, Cationic lipid, Live cell imaging

Background

Messenger RNA (mRNA)-based therapeutics and vaccine strategies have gained impressive attention as an innovative, promising and alternative strategy to DNA-based therapies [1, 2]. With the unique advantages of mRNA over plasmid DNA (pDNA) preventing the requirement of nuclear entry and thereby less possibility for genomic integration, which enables transient protein translation within the cytoplasm. Thus, mRNA yields faster protein expression within the cytoplasm and serves as a favorable, effective and safe candidate with a predictable outcome for the use in biomedical research.

Viral vectors have been traditionally used as mRNA carriers due to the instability of nucleic acid macromolecules under physiological conditions [3]. Nevertheless, their use might be associated to important limitations in terms of immunologic side effects and toxicity [1].

*Correspondence: Brigitta.Loretz@helmholtz-hzi.de
[1] Department of Drug Delivery (DDEL), Helmholtz-Institute for Pharmaceutical Research Saarland (HIPS), Helmholtz Center for Infection Research (HZI), Campus E8.1, 66123 Saarbrücken, Germany
Full list of author information is available at the end of the article

Hence, non-viral vectors availing nanotechnological advances are in the focus of investigation to improve cellular uptake and subsequent transfection of target cells. Therefore, a variety of different biocompatible and biodegradable nanoparticles (NPs) have been developed including lipid-based [4–7] and polymer-based [8, 9] systems, featuring a cationic surface charge and thereby facilitating complexation of anionic mRNA. While these approaches rendered significant progress to overcome drawbacks resulting from mRNA-based delivery in vitro as well as in vivo [10–13], designing of suitable systems with low cytotoxicity and high transfection rate [14] remains crucial parameters and sets an indispensable precondition for mRNA-delivery. However, among all these delivery systems, a new class of nanoparticles combining the beneficial properties of both lipids and polymers termed as lipid–polymer hybrid particles (LPNs) [15] has gained momentum. Although LPNs have been commonly used for siRNA (small interfering RNA) [16–20] or pDNA [21, 22] delivery, their utility as reagents for mRNA delivery has only recently been investigated. Su et al. [11] produced a phospholipid-coated poly-(β-amino ester) (PBAE) hybrid system mediating a transfection rate of around 30% in a dendritic cell line (DC2.4 cell line), while Perche et al. [23] improved the transfection efficiency, even further, up to 60% with mannosylated histidylated lipoplexes. Besides these criteria of manufacturing safe and efficient systems, an auxiliary knowledge about the mRNA translation kinetics is important for a better understanding of mRNA's transient course [9] for tailoring therapeutic strategies. Moreover, versatile, robust and adaptable nanocarriers are needed for scalable production. To our knowledge, the first studies evaluating the kinetics of mRNA translation were reported from Leonhardt et al. [9], in which eGFP coding mRNA complexed to Lipofectamine2000® particles were used to transfect cells revealing their property as transient cargo reaching the highest protein expression rate 3 h post-transfection in A549 cells [9]. Further characterization of transgene expression kinetics has been quantified using commercially available transfection reagents, among others Stemfect®, in DCs [6]. Additionally, Su et al. [11] analyzed the release kinetics of surface-loaded mRNA from phospholipid coated PBAE hybrid systems and hypothesized faster release kinetics for surface adsorbed mRNA in comparison to encapsulated mRNA. Moreover, mRNA adsorbed to the particle surface showed increased stability compared to the naked one. Zhadanov et al. [24, 25] employed commercially available transfection reagents to establish a kinetic model to understand the intracellular delivery of mRNA to single cells and their subsequent release behavior within the cytoplasm. Nonetheless and to our knowledge, there is still no study available, which quantifies protein translation kinetics using tailor-made mRNA nanocarriers.

Therefore, the aim of the study was to understand and evaluate the time-dependent internalization behavior of mRNA in vitro in DCs using two different types of tailor-made nanocarriers as illustrated in Fig. 1. DCs represent potent antigen presenting cells (APCs) and are the most essential targets for mRNA vaccines [26]. Therefore, it is also the purpose of this study to transfer the gained knowledge for future NP-based vaccination strategies. Hence, (i) we produced core–shell structured lipid–polymer hybrid nanoparticles (LPNs), co-formulated with the biodegradable and biocompatible polymer poly (lactid-*co*-glycolid) (PLGA) as the core surrounded by the well-known cationic lipid 1,2-di-*O*-octadecenyl-3-trimethylammonium propane (DOTMA) [27]. LPNs were then complexed with mRNA-mCherry, which provided a reliable read-out to evaluate transfection efficiency. Additionally to that, (ii) the internalization kinetics of LPNs to DCs was characterized and systematically compared with a well-established delivery system consisting of a cationic polymer chitosan coating PLGA [10, 28] (CS-PLGA NPs). mCherry encoding mRNA was applied as a proof of concept model for facile observation and post-loaded onto the nanoparticles to achieve the expected fast, desired release kinetics and hence protein expression. Additionally to that, we monitored real-time transfection by, (iii) applying live cell video imaging in order to simultaneously analyze both the time-dependent uptake of fluorescently labeled, mRNA-loaded LPNs and the translation of the mCherry protein within DCs.

Experimental methods

Preparation and characterization of blank lipid-PLGA (LPNs) and chitosan-PLGA (CS-PLGA) nanoparticles

Both types of nanoparticles used in this study have been produced in the same way using a modified double-emulsion method as described previously [28]. PLGA (50:50; Resomer RG 503H, Evonik Industries AG, Darmstadt, Germany) served as the core polymer and 1,2-di-*O*-octadecenyl-3-trimethylammonium propane (DOTMA) or chitosan as the cationic surface layer. All deployed organic solvents in the experiments were purchased from Sigma-Aldrich (Darmstadt, Germany).

Lipid-PLGA NPs (LPNs) were produced by taking a protocol described by Jensen et al. as starting point [17], but replacing the cationic lipid 1,2-dioleoyl-3-trimethylammonium-propane (DOTAP) by DOTMA and few further modifications.

Briefly, a solution composed of 125 µL of DOTMA (13 mg/mL; Avanti polar lipids, INC, AL, USA) and 250 µL of PLGA (30 mg/mL) was prepared in chloroform and mixed thoroughly. A volume of 250 µL of milli-Q

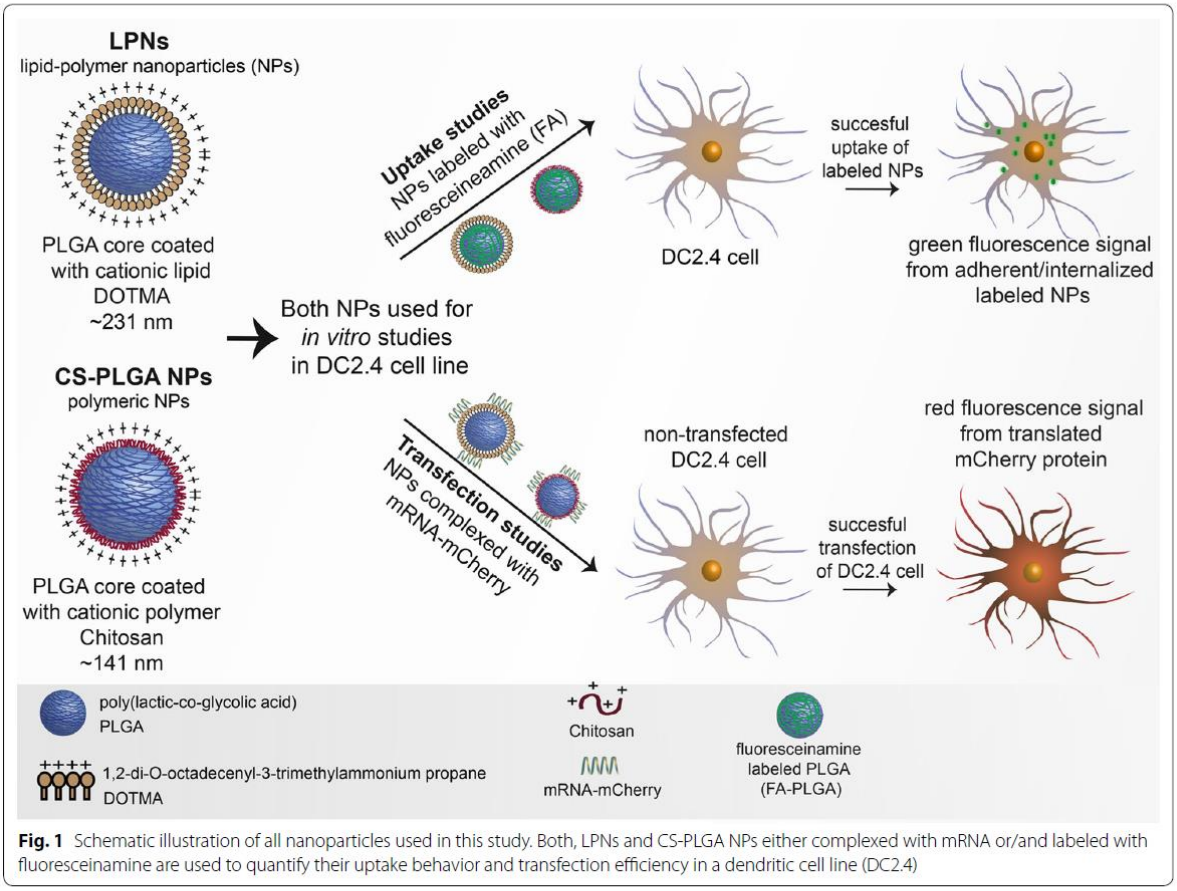

Fig. 1 Schematic illustration of all nanoparticles used in this study. Both, LPNs and CS-PLGA NPs either complexed with mRNA or/and labeled with fluoresceinamine are used to quantify their uptake behavior and transfection efficiency in a dendritic cell line (DC2.4)

water (Merck Millipore, Billerica, MA) was then added to the DOTMA:PLGA organic phase followed by a subsequent sonication with ultrasound (Branson Ultrasonic Corporation, USA) at 30% amplitude for 30 s enabling the primary w/o emulsion. Immediately afterwards, 1 mL of a 2% (w/v) polyvinyl alcohol (PVA, Mowiol® 4-88, Sigma-Aldrich, Darmstadt, Germany) solution was applied to the primary emulsion and sonicated under the same settings resulting in the secondary w/o/w emulsion. Further, 5 mL of the PVA solution were then added to the secondary emulsion under continuous stirring overnight to allow organic solvent evaporation. Resulting DOTMA coated PLGA NPs (2.15 mg/mL) were purified using a dialysis membrane (MWCO 1 kDa, Spectrum Labs, CA, USA).

Chitosan-PLGA NPs were prepared according to [28, 29]. Briefly, 0.2% (w/v) of chitosan solution was prepared by dissolving Protasan UP CL 113 (FMC Biopolymer AS NovaMatrix, Sandvika, Norway) in a 2% (w/v) PVA solution. Afterwards, 50 mg of PLGA was dissolved in 2 mL of ethyl acetate and 400 µL of milli-Q water was then added to the PLGA organic phase followed by a subsequent sonication to obtain the primary w/o emulsion. The chitosan-PVA solution was immediately afterwards added to the w/o emulsion and sonicated once again resulting in the secondary w/o/w emulsion. A volume of 20 mL of milli-Q water was additionally added to the w/o/w emulsion to allow organic solvent evaporation with a further purification of resulting chitosan coated PLGA NPs (2 mg/mL) by centrifugation at 15,000*g* for 15 min. To examine the cellular localization of the NPs, fluorescently labeled NPs were produced using fluoresceinamine (FA; Sigma-Aldrich, Darmstadt, Germany) covalently coupled to PLGA [30] and simply substituted against PLGA in the above mentioned production-procedure resulting in FA-LPNs and CS-FA-PLGA NPs.

The physicochemical properties of all NPs were characterized by dynamic light scattering (DLS; Zetasizer Nano, Malvern Instruments, UK) to attain their hydrodynamic size (referred to the hydrodynamic diameter), polydispersity index (PDI) and ζ-potential. All values obtained by DLS are the mean values of the peak

intensity distribution. All samples were measured at least in four different batches and results are shown as the mean ± standard deviation (SD).

Structural characterization of blank nanoparticles using SEM, TEM and Cryo-TEM

The morphological appearance of all nanoparticles was visualized using a variety of different microscopical methods including conventional Scanning Electron Microscopy (SEM, EVO HD15, Zeiss, Germany) and Transmission Electron Microscopy (TEM, JEM 2011, JEOL, St Andrews, UK). Before TEM-visualization, 10 µL of each NP dispersion was applied on a carbon coated copper grid (type S160-4 from Plano GmbH, Wetzlar, Germany) and the excess solution was removed after 10 min incubation time. In order to improve the contrast of the TEM-images, adhered NPs on the copper grid were in another experimental setting further stained with 0.5% (w/v) phosphotungstic acid solution (PTA; Sigma-Aldrich, Darmstadt, Germany) according to our previous studies described in Yasar et al. [31]. For SEM visualization, the copper grid with applied NPs were then placed onto a carbon disc and gold-sputtered. For cryo-TEM investigations 3 µL of the NPs solution were placed onto a holey carbon film (type S147-4 from Plano GmbH, Wetzlar, Germany), plotted for 2 s to a thin film and plunged into liquid ethane using a cryo plunge 3 system from Gatan (Pleasanton, CA, USA) operating at T = 108 K. The frozen samples were transferred under liquid nitrogen to a cryo-TEM sample holder (Gatan model 914) and imaged in bright-field low-dose mode (JEOL JEM-2100) at T = 100 K and 200 kV accelerating voltage.

Physical stability of LPNs and CS-PLGA nanoparticles under physiological conditions

The physical stability of blank LPNs was tested over a time course of 62 days upon storage at 4 °C and room temperature. Additionally, the stability of both blank NPs was characterized in Hanks's Balanced Salt Solution (HBSS buffer, pH 7.4) and in Dulbecco's Modified Eagle Medium (DMEM; Thermo Fisher Scientific, Darmstadt, Germany) with and without 10% fetal calf serum (FCS; Sigma-Aldrich, Darmstadt, Germany) at different time-points in order to find the best conditions for in vitro cell culture studies. Briefly, 0.215 mg/100 µL of blank LPNs and 0.2 mg/100 µL of CS-PLGA NPs were mixed with 800 µL of appropriate medium. The samples were incubated at 37 °C with 5% CO_2 under slightly shaking for 2 h, 4 h, and 24 h. Immediately afterwards, the hydrodynamic size, PDI, and ζ-potential were measured from three independent samples and results are presented as mean ± SD.

Preparation of mRNA-mCherry loaded NPs

mRNA-mCherry (CleanCap™ mCherry mRNA (5moU); TriLink BioTechnologies LLC, CA, USA) was loaded at different ratios to both LPNs and CS-PLGA NPs to evaluate their potential as efficient mRNA delivery systems. Thus, the anionic mRNA was loaded onto the surface of both cationic NPs (following our previous protocol described in Yasar et al. [31]) using mRNA:NPs weight ratios of 1:10, 1:20 and 1:30. A volume of 1 µg/µL mRNA-mCherry was mixed with an appropriate amount of each NPs and further incubated at room temperature for 1 h. This carried out in mRNA complexed NPs (mRNA:LPNs and mRNA:CS-PLGA NPs). The encapsulation efficiency (%EE) of bound mRNA:LPNs and mRNA:CS-PLGA NPs was evaluated indirectly by pelleting all samples down at 24,400*g* for 30 min and determining the concentration of unbound mRNA in the supernatant by measuring absorbance at 260/280 nm with a NanoDrop Spectrophotometer. This enabled the calculation of bound mRNA multiplied by a factor of 100 to receive the percentage encapsulation efficiency. Four independent batches of mRNA-loaded NPs were produced and characterized to obtain the hydrodynamic size, PDI and ζ-potential while the morphology assessed with conventional SEM and TEM after staining with 0.5% w/v PTA solution.

Determination of mRNA Binding and release by gel retardation assay

The determination of mRNA binding and its stability within the nanoparticles were analyzed by a gel retardation assay using 0.75% (w/v) agarose gel electrophoresis and tested for all mRNA complexed NPs with varying weight ratios (1:10, 1:20 and 1:30). To further induce a release of complexed mRNA, 5 µL heparin (30 mg/mL; Sigma-Aldrich, Darmstadt, Germany) was added to the mRNA complexed NPs and incubated for 15 min at room temperature. All samples were then mixed with 2 µL of orange DNA loading dye (6×, Thermo Fisher Scientific, Waltham, MA, USA), loaded into the agarose (Serva, Heidelberg, Germany) gel containing 3 µL of ethidium bromide (10 mg/mL; Sigma-Aldrich, Darmstadt, Germany) and run for 25 min at 90 V using 0.5× TBE buffer. The mRNA bands were then visualized with a UV illuminator (Fusion FX7 imaging system from Peqlab, Erlangen, Germany).

Cell cultures

Bone-marrow-derived murine dendritic cell line (DC2.4 cell, Cat# SCC142, Merck Millipore, Darmstadt, Germany) was maintained in complete media comprised of DMEM supplemented with 10% FCS, 10 mM HEPES, 2 mM L-glutamine and cultured in a humidified incubator at 37 °C with 5% CO_2. A human lung carcinoma cell

line (A549 cells; NO. ACC 107, DSMZ GmbH, Braunschweig, Germany) was grown in complete cell culture medium (RPMI 1640; PAA laboratories GmbH, Pasching, Austria) with 10% FCS and used as model cell line to test the transfection efficiency of mRNA complexed NPs. Both cell lines were passaged with trypsin–EDTA upon reaching ~ 85% confluency and used for the experimental settings as described in the next sections.

Cell viability and cytotoxicity assay: live-dead staining

DC2.4 cells were seeded in a 24 well plate at a density of 3×10^5 cells/well, in 500 µL of DMEM with 10% FCS and incubated overnight at 37 °C with 5% CO_2 to allow complete adherence of cells to the well. The next day, cell culture medium was removed, and cells were washed twice with HBSS. Prior to the experiment, blank LPNs and CS-PLGA NPs were prepared at appropriate concentrations (10, 20, 40, 60, 100 and 160 µg/mL) in HBSS and cells were incubated with 500 µL of each concentration for 4 h under slightly shaking at 37 °C with 5% CO_2. Cells treated with HBSS buffer only were used as negative control. For the positive control (dead cells), cells were plated in a separate 24 well plate and incubated for 1 h at 56 °C. Immediately after incubation, cells were washed twice with PBS, detached with trypsin–EDTA and placed in round-bottom falcon tubes (Falcon, A Corning Brand, Tamaulipas, Mexico). A volume of 200 µL of FACS-buffer (containing 2% FCS in PBS) and 1 mL of PBS were added to cells and centrifuged at 4 °C and 300*g* for 5 min. The supernatant was discarded, and the pellets were washed once again with 1 mL PBS and centrifuged respectively. A Live/Dead Fixable Staining Kit 568/583 (PromoKine, Promocell, Heidelberg, Germany)—suitable for flow cytometry—was used to quantify cell viability and cytotoxicity. The dye within the kit was reconstituted, and cells were further treated according to manufacturer's protocol. Thus, the remaining pellet after the second centrifugation was re-suspended in 1 mL PBS, and thereafter, 1 µL of fixable dead cell stain was added to the cells, mixed well and further incubated protected from light at 4 °C for 30 min. Cells were then washed with 1 mL PBS, fixed in 1% paraformaldehyde (Electron Microscopy, PA, USA) and stored until analysis. Cell viability and cytotoxicity of tested NPs was quantified using flow cytometry (BD LSRFortessa™ Cell Analyzer, Biosciences, Heidelberg, Germany) in the PE-channel. Fifty thousand cells per sample were measured by the cytometer and obtained data were analyzed using FlowJo software (FlowJo 7.6.5, FlowJo LLC, OR, USA). Three independent experiments were conducted, and results are expressed as the mean ± SD.

Cellular uptake in DC2.4 cell line

To quantify the cellular localization of blank and mRNA complexed LPNs and CS-PLGA NPs, a green fluorescent dye (fluoresceinamine, FA with a peak emission wavelength of 530 nm) was first covalently coupled to PLGA before nanoparticle-production. DC2.4 cells were seeded and grown as described for the live-dead staining assay. Prior to the experiments, fluorescent NP types, with and without mRNA (FA-LPNs, mRNA:FA-LPNS, CS-FA-PLGA and mRNA:CS-FA_PLGA NPs) were prepared in HBSS buffer at different concentrations (20, 40 and 60 µg/mL). A volume of 500 µL of each NP suspension was then applied to the cells at 37 °C and 5% CO_2 2 h or 4 h on a shake at 150 rpm.

Right after each time-point, cells were rinsed twice with HBSS buffer in order remove excess of NPs, detached from the well with trypsin, placed in round-bottom tubes, and centrifuged down to receive the cell pellets. Cells were then re-suspended and fixed for flow cytometry. Fifty thousand cells were assessed using the FITC fluorescence channel. The percentage of cells positive to FA-labeled NPs were determined with FlowJo. Results are presented as the mean ± SD of four independent experiments.

In vitro transfection and kinetics

To test whether mRNA complexed NPs would efficiently transfect dendritic cells, DC2.4 cells were seeded in 24 well plates at a density of 3×10^5 cells per well in 500 µL DMEM cell culture medium with 10% FCS. Non-labeled LPNs and CS-PLGA NPs containing 1 µg of mRNA were prepared with a mRNA:NPs weight ratio of 1:10, 1:20 and 1:30 in 500 µL HBSS buffer. The cells were then washed twice with HBSS buffer and incubated with the mRNA complexed NPs for 2 h and 4 h. In an modified experimental setting, cells were exposed to NPs for 4 h, NPS were removed by washing, and cells were then incubate with NP-free DMEM plus 10% FCS for 24 h and 48 h. The different mRNA:NPs weight ratios and time-points were used to identify the maximum transgene expression. A commercially available transfection reagent, JetPRIME®, was used as positive control, whereas cells treated with naked mRNA-mCherry and medium alone were used as negative control. The efficiency of mCherry transgene expression was quantified using flow cytometry, and cytometer settings were adjusted to differentiate between transfected and non-transfected cells. Data were analyzed with FlowJo and results are shown as mean ± SD of four independent experiments.

Furthermore, DC2.4 cells incubated for 24 h and 48 h post-transfection were visualized by confocal laser scanning microscope (CLSM; Leica TCS SP 8, Leica, Wetzlar, Germany). Here, cell membranes were stained

with Wheat Germ Agglutinin linked to Alexa Fluor 488 fluorescent dye (WGA, 10 µg/mL) and cell nuclei with 4′,6-diamidino-2-phenylindole (DAPI, 0.1 µg/mL). Samples were then fixed with 3% paraformaldehyde and stored at 4 °C until imaging. The images were acquired with a 25× water immersion objective at 1024 × 1024 resolution and afterwards processed with LAS X software (LAS X 1.8.013370, Leica Microsystems, Leica, Germany). CLSM visualization of transgene expression was repeated in three independent experiments and images were processed using the software ImageJ (Fiji).

Live cell video microscopy: recording NP uptake and protein translation

To analyze the transgene expression kinetics of single cells over a time-course of 4 h, live cell imaging was performed in DC2.4 cells using fluorescently-labeled and mRNA complexed mRNA:FA-LPNs with a weight ratio of 1:30. NP uptake could be tracked due to the green fluorescent signal of FA-PLGA, while transgene expression of cells could be determined by following the red fluorescence emitted by the peptide translated from mCherry-mRNA. Here, 3×10^5 cells/well were seeded overnight in a µ-Slide 8 well glass bottom chamber (ibidi, Martinsried, Germany) in DMEM with 10% FCS. CLSM facility was set to maintain constant physiological conditions for cells. The entire microscope was enclosed in a humidified incubation chamber enabling temperature regulation to 37 °C. The specimen was placed under a perfusion chamber to maintain a CO_2 atmosphere at 5% with a flow speed of 3 L/h. Before recording, cell culture medium was replaced by HBSS and DC2.4 cells were placed under the microscope. Images were acquired using a 25× water immersion objective at 1024 × 1024 resolution with an interval of 3 min/image for a time frame of 4 h. Image acquisition was started Immediately after applying mRNA:FA-LPNs. Images were processed, compiled with the LAS X software and four different videos were produced with at 6 frames/s. NP uptake and the time-dependent change of transgene expression within single cells were analyzed by plotting the red (transgene expression) and green (FA-PLGA of NPs) fluorescence signals against time. To extract arbitrary fluorescence values from the microscopy images, we used a science-distribution tool of the software ImageJ. Each video was loaded and split in its three channels (bright field microscopy, red fluorescence and green fluorescence). All videos were captured at four focal planes, which were merged with Z Project, while keeping the maximum intensity across the planes for each pixel. The videos were converted to 8-bit grayscale and saved as Tagged Image File format (TIF). To analyze the transgene expression kinetics, the aforementioned channels of each video were opened in the 80th frame corresponding to the 4 h time-point after the start of the experiment. In this particular frame, successfully transfected cells could be easily identified in the red channel. For each video, we located 8 red-fluorescent (transfected) and 2 non-fluorescent cells (non-transfected) in the 80th frame, matching the 8:2 transfection ratio observed by flow cytometry. With the selection tool of *Fiji*, the boundaries of these 10 cells were selected in the bright filed channel and saved as regions of interest (ROI). These ROIs were subsequently used in the green and red fluorescence channel to determine the fluorescence intensity in several frames. The same analysis was repeated for frames 70, 60, 50, 40, 30, 20, 10 and 1 (matching with the time-points of: 3.5 h, 3 h, 2.5 h, 2 h, 1.5 h, 1 h, 0.5 h and 0 h). Finally, the time-dependent change of the signal-intensity was plotted using the mean value of fluorescence intensity.

Potential of LPNs and CS-PLGA NPs for functional mRNA-delivery in A549 cells

A549 cells were used to show the potential of both NPs to efficiently transfect epithelial cells. A549 cells were seeded at a density of 1×10^5 cells/well in 24 well plates. The experimental setting with further quantification and visualization of transgene expression in A549 cells was performed as described before for DC2.4 cell. The used mRNA complexed non-labeled NPs were incubated for 4 h and transfected cells were counted 24 h and 48 h post-transfection with flow cytometry and further visualized using CLSM.

Statistical analysis

Statistical analysis was performed using two-way ANOVA followed by a Tukey's multiple comparison test with the software Graph Pad Prism 6 for Windows (Version 6.01, GraphPad Software Inc.). Data were considered as statistical significant for $p < 0.05$ ($^*p < 0.05$, $^{**}p < 0.01$, $^{***}p < 0.001$ and $^{****}p < 0.0001$). N is the number of independent experiments and n is the number of technical replicates.

Results and discussion

Design and characterization of blank lipid-coated and chitosan-coated PLGA nanoparticles

Two different core–shell structured delivery systems have been manufactured using either PLGA, a biodegradable and biocompatible polymer as the core, which was coated with a cationic lipid (DOTMA), or a cationic polymer (chitosan), to achieve a positive surface charge. In either case, we produced the blank (i.e. mRNA-free) particles first and complexed them with mRNA in a second step before application. The production procedure and all related settings for both NPs were kept equal to

enable a good foundation for comparison. In the first experimental setting, we designed blank lipid-coated PLGA nanoparticles (LPNs) as described previously [17, 27] and chitosan-coated PLGA Nanoparticles (CS-PLGA NPs) [10, 28] using a modified double-emulsion method with PVA as stabilizer and analyzed their physicochemical properties in regards to hydrodynamic size, polydispersity index (PDI) and ζ-potential. The size as well as surface charge of nanoparticles are likely to influence pharmacokinetics, accumulation behavior, tissue distribution, cellular internalization [20, 32] and their cytotoxic effect [14]. Therefore, these two parameters were diligently taken in consideration. Particle sizes were kept below 250 nm to qualify endocytosis, and the surface potential not to exceed +25 mV as strong cationic surface charge correlates with higher cytotoxic effects [14]. The mean hydrodynamic size of LPNs was 230 nm, with a narrow PDI of approximately 0.09 revealing a cationic surface potential of around +16 mV respectively (Table 1). In comparison to the lipid–polymer NPs, CS-PLGA NPs exhibit a smaller particle size of about 140 nm (PDI: 0.12) with an equal surface charge in the positive range of + T25 mV (Table 1).

Keeping in mind the potential biopharmaceutical application, we investigated the storage stability of LPNs at 4 °C and room temperature (RT) post-preparation for a time-period of 62 days by measuring the particle size, PDI, and ζ-potential, respectively, which revealed no significant difference for all tested conditions (Additional file 1: Figure S1).

The stability and hence aggregation behavior of the particles under different physiological conditions was further investigated following 2 h, 4 h and 24 h incubation time at 37 °C, which is essential to understand the behavior of nanoparticles in a biologically relevant environment. LPNs and CS-PLGA NPs were incubated in HBSS buffer, DMEM, and DMEM plus 10% FCS and their colloidal stability was measured after the predetermined time-points. LPNs remained overall stable in all tested media. A significant decrease in the hydrodynamic size from approx. 220 nm to approx. 150 nm with an increase in PDI to approx. 0.35 was observed in serum containing medium only (Additional file 1: Figure S2A1, A2). By contrast, CS-PLGA NPs show a significant increase in size and PDI after exposure to all tested media compared to the untreated control (Additional file 1: Figure S2B1, B2) while the addition of serum to DMEM resulted in a decreased size with a substantial strong increase of PDI from approx. 0.1 up to around 0.5. The significant change in colloidal characteristics after addition of serum, especially the decrease in size was already reported in Schulze et al. [33]. This effect is evoked by adsorption of negatively charged serum proteins onto the surface of the positively charged nanoparticles, causing destabilization of the particles. However, for both NP types the hydrodynamic size showed some changes upon transfer in buffer or medium on the short time scale but then remained stable for 24 h.

Table 1 Physicochemical characteristics of blank and mRNA complexed nanoparticles (NPs) with the percentage encapsulation efficiency (%EE) of mRNA

Nanoparticles	Size (nm)	PDI	ζ-potential (mV)	%EE
Blank LPNs	231 ± 7.0	0.09 ± 0.02	16.25 ± 3.24	–
*mRNA:LPNs_1:10	322.2 ± 26.1	0.21 ± 0.02	−0.05 ± 6.54	91.3 ± 1.5
*mRNA:LPNs_1:20	217.5 ± 11.6	0.16 ± 0.04	19.62 ± 1.13	87.0 ± 2.0
*mRNA:LPNs_1:30	*243.5 ± 45.3*	*0.18 ± 0.08*	*22.97 ± 0.68*	*92.8 ± 2.0*
Blank CS-PLGA NPs	141.2 ± 6.2	0.12 ± 0.01	25.20 ± 3.84	–
*mRNA:CS-PLGA_1:10	176.4 ± 5.5	0.32 ± 0.00	13.30 ± 2.76	87.0 ± 0.4
*mRNA:CS-PLGA_1:20	158.6 ± 1.7	0.23 ± 0.00	20.42 ± 1.22	95.4 ± 0.6
*mRNA:CS-PLGA_1:30	*151.3 ± 3.4*	*0.18 ± 0.02*	*25.55 ± 1.22*	*94.2 ± 0.3*

Samples highlighted in italics indicate the NPs with best colloidal properties.
*mRNA:NPs weight ratio. *N* = 4, mean ± SD

Structural visualization of blank nanoparticles

Besides the criteria of well-defined size and ζ-potential, the shape and structure of nanoparticles are further important parameters impacting cellular internalization [34]. Hence, we have employed a variety of techniques using conventional imaging by scanning electron microscopy (SEM), transmission electron microscopy (TEM) and cryo-TEM to visualize NP morphology and structure, as all of the techniques have their specific advantages and limitations. We further improved the TEM-images by staining the nanoparticles with PTA. As SEM produces images of the sample by scanning the surface with an electron beam, blank LPNs and CS-PLGA NPs revealed a smooth and evenly shaped spherical surface structure (Fig. 2a1, b1). We then analyzed the inner structure of the nanoparticles by using TEM (Fig. 2a2, b2) in order to characterize the arrangement of used excipients as it was discussed in literature that lipid–polymer nanoparticles have a core–shell like structure [35]. Here, the images reveal a darker and hence electron dense layer surrounding a brighter core. The anionic PTA stain showed strong adherence to the cationic particles surface without entering the particle core, which may further emphasize a core–shell structure of both NPs (Fig. 2a3, b3). Furthermore, Cryo-TEM was implemented as a technique with minimal risk of artifact formation [36] (e.g. agglomeration, particle size shrinkage) and confirmed the spherical

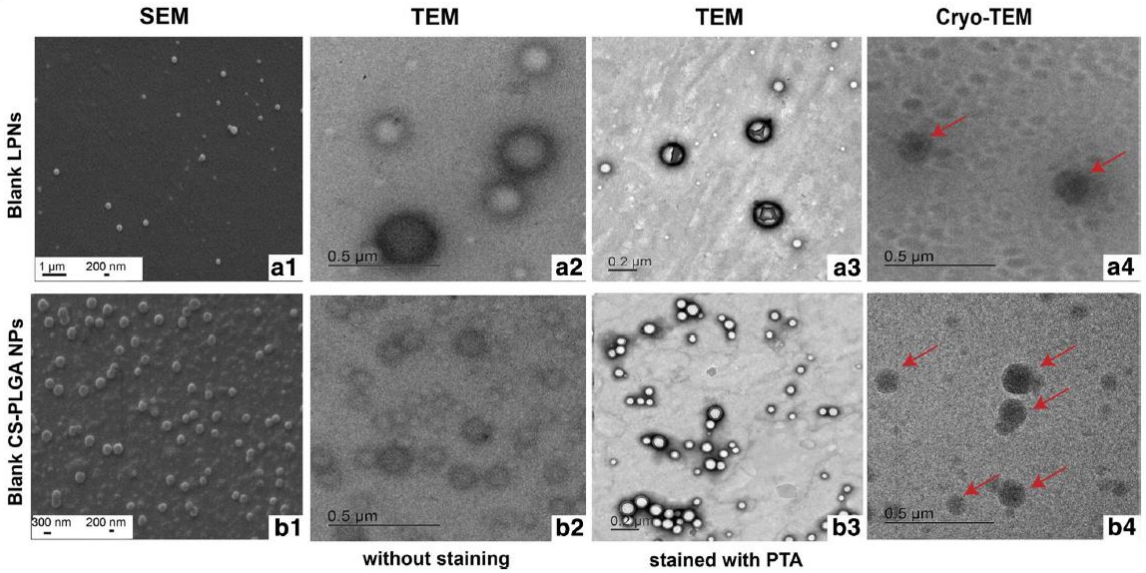

Fig. 2 A variety of different microscopic methods used to visualize blank LPNs (**a1**–**a4**) and CS-PLGA NPs (**b1**–**b4**). **a1**, **b1** SEM images show a smooth, spherical morphology of the nanoparticles, **a2**, **b2** TEM images of particles without staining give a hint about the core–shell structure, seen in a dark electron dense layer surrounding a brighter core. **a3**, **b3** To emphasis this structure and increase the contrast, the particles were stained with 0.5% wt/V PTA and imaged with TEM and further unstained nanoparticles were visualized with a less harsh method using Cryo-TEM with red arrows pointing to the particles (**a4**, **b4**). Scanning electron microscopy (SEM), transmission electron microscopy (TEM)

structure of the NPs (Fig. 2a4, b4). The size of both NPs found by Cryo-TEM was in the range of 50–200 nm.

Complexation and characterization of mRNA-loaded LPNs and CS-PLGA NPs

The cationic head group of the lipid and the cationic amine group of chitosan facilitates the electrostatic interaction and hence binding of the net anionic charged mRNA to the surface of the nanoparticles.

The NPs have different ζ-potential depending on the cationic coating and the usage of fluorescence labeled PLGA. Thus, same weight ratios of mRNA loading lead to different charge neutralization and destabilization. The ratio of mRNA:NP affects the colloidal stability since the nucleotides neutralize the cationic particle charge either partly, fully or reverse it to anionic, implicating a risk of particle-aggregation when the ζ-potential approaches zero. For reasons of better comparability, mRNA:NPs weight ratios (w/w) of 1:10, 1:20 and 1:30 were arbitrary selected. A model mRNA encoding for the red fluorescent reporter gene mCherry was used and hence complexed onto the surface of LPNs and CS-PLGA NPs. This design has the following advantages (i) to avoid exposure of mRNA to the harsh conditions of NP production (e.g. high shear stress), (ii) to protect mRNA after complexation against nucleases and (iii) for fast release upon certain physiological triggers (e.g. competing endogenous anions) as necessary for effective translation.

The physicochemical properties in terms of hydrodynamic size, PDI, ζ-potential were characterized and the encapsulation efficiency quantified respectively (Table 1). mRNA-loaded LNPs (mRNA:LNPs) at a ratio of 1:10 show an increment of the size from ~ 230 nm (blank LPNs) to ~ 322 nm, following a broader size distribution profile (highest PDI value of 0.21) and a strong decrease in the ζ-potential from ~ 16 mV to nearly 0 mV (Table 1) indicating a destabilized system. Besides, the studied weight ratios of 1:20 and 1:30 resemble in their colloidal properties regarding size and ζ-potential, while the PDI shows a slight increase. The same tendency upon various tested weight ratios was observable for mRNA-loaded CS-PLGA NPs (mRNA:CS-PLGA NPs). Both delivery systems complexed the mRNA up to ~ 90% (Table 1), maintaining spherical morphology (Fig. 3a1, a2, b1 and b2). The increment of NPs concentration correlates with higher amount of amine groups of the used cationic excipients, enabling a better saturation and hence stronger and improved condensation of the anionic mRNA. Additionally, agarose gel electrophoresis elucidated the efficiency of both NPs to bind mRNA-mCherry

(Fig. 4). For mRNA-loaded LPNs of 1:10 w/w, a band of free mRNA was observable in the gel in contrast to 1:20 and 1:30, indicating stronger condensation of mRNA with increasing amount of NPs (Fig. 4a).

Surprisingly, a fluorescence signal of EtBr in the bags for all ratios of mRNA:LPNs, as an indicator for the presence of mRNA with the nanoparticles, was not seen (Fig. 4a, mRNA binding). This is presumably attributed to the used lipid DOTMA interacting stronger with the mRNA and hence impeding the further intercalation of EtBr. The presence of mRNA-mCherry associated onto the surface of LPNs was, however, demonstrated using heparin, which causes a fast release of mRNA within 15 min as seen through the free bands in the gel (Fig. 4a, mRNA release). In comparison, mRNA:CS-PLGA NPs allow intercalation of EtBr as seen in Fig. 4b, as no band could run through the gel, while the addition of heparin just partially released the mRNA from CS-PLGA NPs (Fig. 4b, mRNA release). Furthermore, the visible bands at the bottom of agarose gel pockets of Fig. 4 can be explained by an incomplete release of mRNA from the NPs after heparin treatment, preventing the motion of particle-bound mRNA through the gel. The mRNA migrating deeper into the gel is only a fraction of a total amount of mRNA bound to the particle. This effect is even more pronounced in the chitosan sample than the LNP sample.

Cell viability and cytotoxicity assay

It is common knowledge that cationic charged particles are associated with higher cytotoxic effects [37], partly explicable due to potentially enhanced interaction of

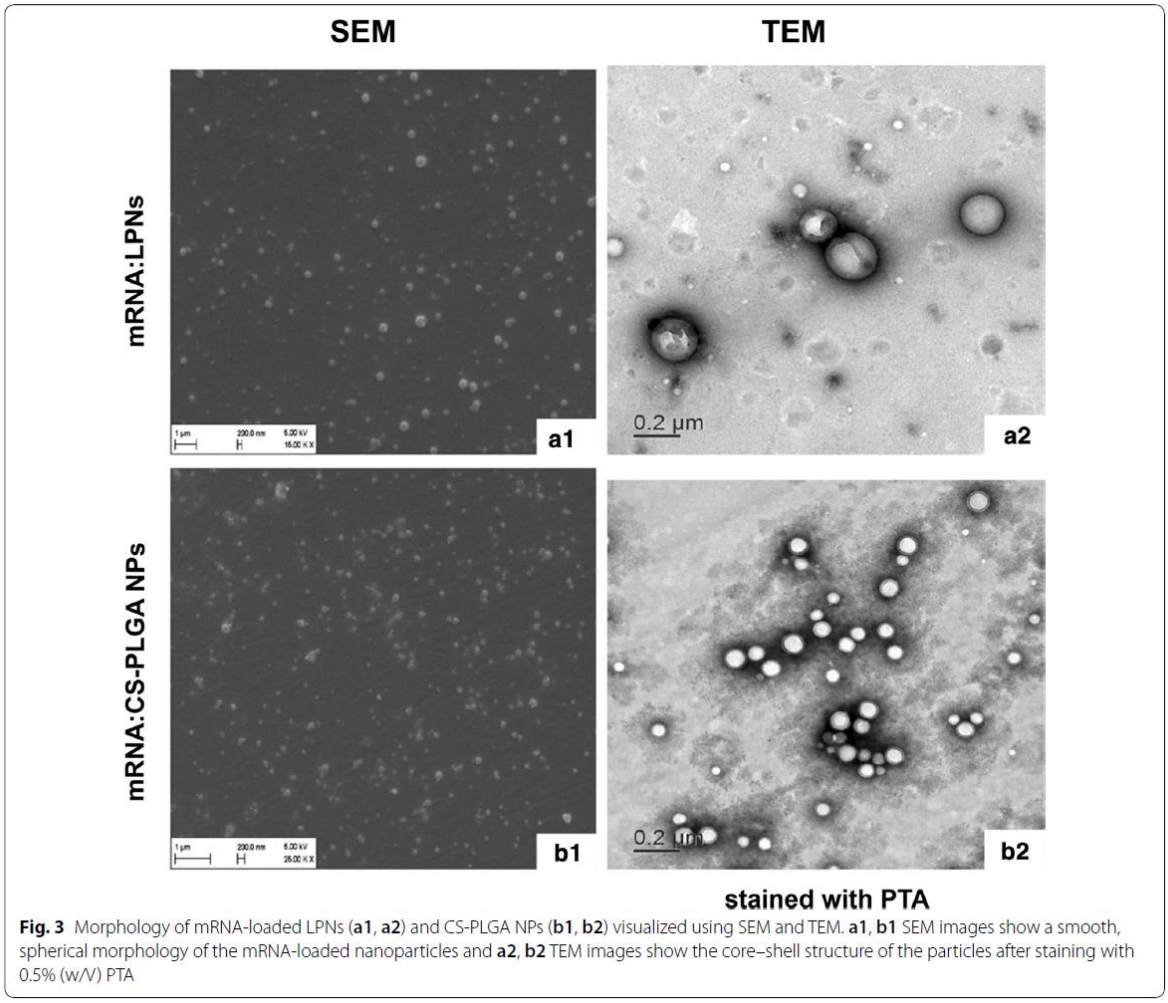

Fig. 3 Morphology of mRNA-loaded LPNs (**a1**, **a2**) and CS-PLGA NPs (**b1**, **b2**) visualized using SEM and TEM. **a1**, **b1** SEM images show a smooth, spherical morphology of the mRNA-loaded nanoparticles and **a2**, **b2** TEM images show the core–shell structure of the particles after staining with 0.5% (w/V) PTA

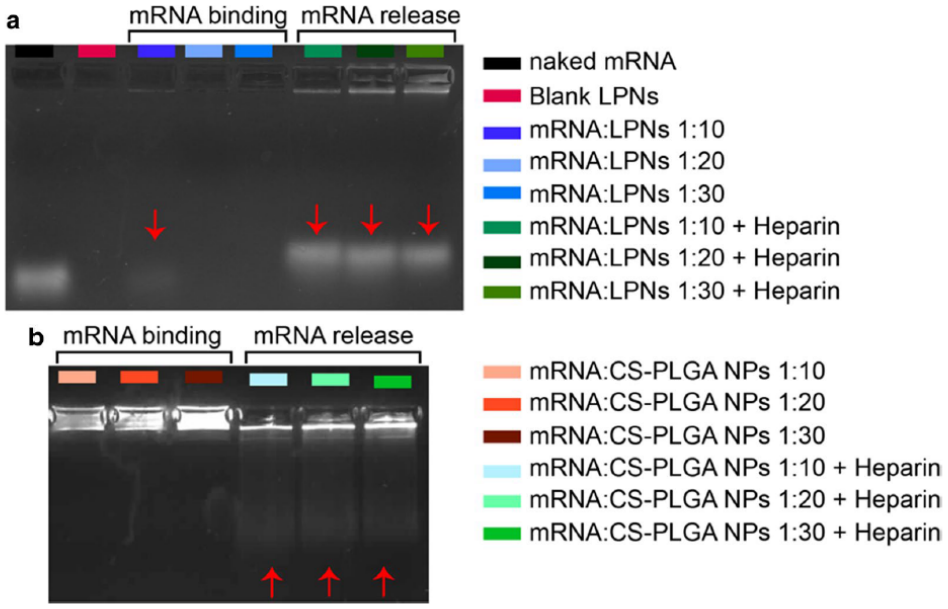

Fig. 4 Gel retardation assay of mRNA complexed with different nanoparticles (NPs) at various ratios: **a** LPNs and **b** CS-PLGA NPs. Both images indicate mRNA binding to NPs and their appropriate release using heparin

cationic particles with the anionic charged cell membrane, which however also facilitate cellular uptake [38]. Therefore, we have analyzed the cell viability of blank LPNs and CS-PLGA NPs on DC2.4 cells, by nanoparticle incubation at different concentrations for 4 h (Fig. 5a, b) and differentiated dead from living cells by staining with a live-dead staining kit with an appropriate gating strategy (Additional file 1: Figure S3). Under such conditions, lipid-PLGA nanoparticles showed no cytotoxic effects up to a concentration of 100 µg/mL, which were only observed at 160 µg/mL, as reflected by a drop of cell viability to ~ 50%. CS-PLGA NPs demonstrated no toxic effects over the tested concentration ranges. In order to keep a well-tolerated concentration range for our further cell studies, we used the ranges marked with green rectangles (Fig. 5a, b). The toxicity difference at a higher concentration between lipid-PLGA and chitosan-PLGA nanoparticles might be associated with the pH sensitivity of the primary ammonium group in chitosan showing changing deprotonation degree depending on the surrounding pH value in comparison to the quaternary ammonium group in DOTMA. The HBSS-buffer used for the toxicity studies has a pH of 7.4 a value in which chitosan reveals a slight diminishing protonation degree resulting in a decrease of ζ-potential and presumably less cellular interaction [31]. Additionally to that, the hydrophobic nature of the DOTMA envelope might elicit a better interaction with cells and hence uptake.

Kinetics of cellular internalization for blank and mRNA-loaded nanoparticles

Prior to transfection studies, we evaluated the kinetics of cellular internalization for blank and mRNA-loaded NPs, as the knowledge about the efficiency of uptake towards dendritic cells might help to understand the subsequent transfection. To quantify the internalization of nanoparticles into cells, we used fluorescently labeled particles, by first covalently coupling fluoresceinamine to PLGA and subsequently designing and characterizing appropriate nanoparticles. Labeled blank LPNs (FA-LPNs) show similar colloidal characteristics as non-labeled LPNs, while labeled blank CS-PLGA NPs (CS-FA-PLGA NPs) indicated a drop of ζ-potential from approx. + 25 mV (for non-labeled) to + 10 mV (Additional file 1: Figure S4). The attachment of chitosan to the PLGA core is mainly driven by charge interaction. As the conjugation of FA to the carboxyl group decreases the anionic charge of the PLGA core, less chitosan can bind to PLGA causing a decrease in ζ-potential. In comparison, DOTMA can additionally attach to the PLGA core by hydrophobic interaction and might be less dependent on the anionic nature of the PLGA core. mRNA-loaded labeled NPs (either mRNA:FA-LPNs or mRNA:CS-FA-PLGA NPs) were prepared at three different mRNA:NPs ratios 1:10, 1:20 and 1:30 comparable to a particle concentration of 20 µg/mL, 40 µg/mL and 60 µg/mL, resp., and characterized for their physicochemical properties. While the size

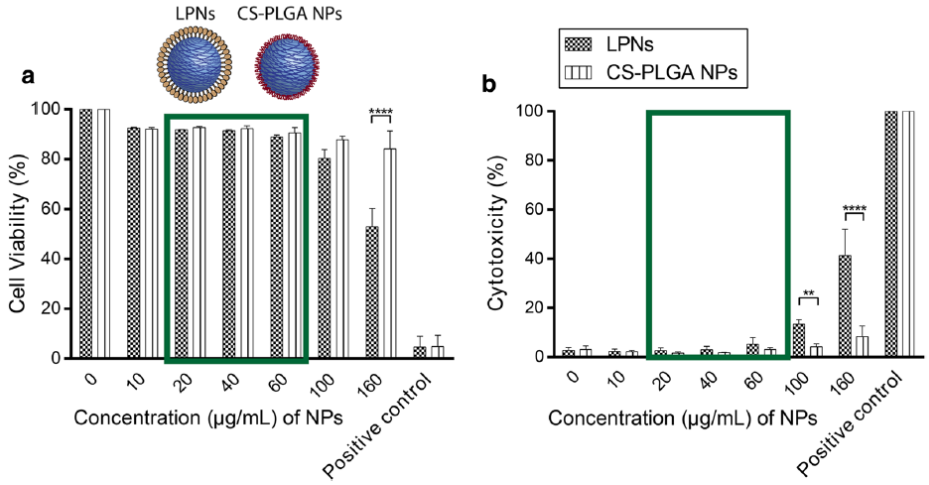

Fig. 5 **a** Cell viability and **b** cytotoxicity studies assayed with a live-dead staining kit on DC2.4 cells using blank LPNs and CS-PLGA NPs. Particles were incubated for 4 h: LPNs reveal a slightly higher cytotoxicity than CS-PLGA NPs. Green rectangles represent the concentration range used for cellular localization and transfection studies. $N = 3$, mean ± SD (**$p < 0.01$, ****$p < 0.0001$)

and PDI for both mRNA-loaded labeled NPs at different ratios show no significant difference, the ζ-potential indicates a strong decrease to a negative range for the tested ratios, only mRNA:LPNs 1:30 remaining in the positive range (Additional file 1: Figure S4). The ζ-potential of the FA-labeled NPs was lower than the non-labeled NP of the same type. Thus, lower mRNA ratios already neutralize the particle charge. The effect of NPs internalization by dendritic cells was then analyzed at the same three concentrations for labeled blank and mRNA-loaded NPs and at two different time-points, i.e. after 2 h and 4 h exposure to cells at 37 °C. Right after NPs exposure, cells were trypsinized and analyzed by flow cytometry. We could first observe a higher cell association for FA-LPNs over CS-FA-PLGA NPs (Fig. 5a1). FA-LPNs showed a cell association with nearly 95% of the cells for concentrations ≥ 40 µg/mL and hence a strong fluorescence shift (Fig. 6a1, a2). CS-FA-PLGA NPs revealed no concentration-dependent cellular internalization and lower percentage (approx. 70%) of cells with particle association. Although CS-FA-PLGA NPs show some increase NP positive cells after 4 h, no clear time-dependent cell association of the particles was observable.

When either type of labeled NPs was complexed with mRNA and exposed to DCs, the cell association behavior changed in comparison to the labeled blank particles. All mRNA-loaded particles indicate no significant concentration or time-dependent association, but enhanced cellular association as seen in the higher amount of particle-positive cells (Fig. 6b1, b2). Hence, for all tested nanoparticles the surface charge does not play a role in the efficiency of cell association, as mRNA-loaded FA-labeled nanoparticles show a negative surface charge in comparison the blank ones. Another point needed to be taken in consideration is the type of cells used in this study. DC2.4 cells belong to phagocytic and professional antigen presenting cells. Once a foreign material is recognized by immature DCs it will be endocytosed, DCs mature with changed metabolism and downregulated phagocytosis [39]. Thus, in their immature state, they have a higher phagocytic and thereby higher uptake activity compared with non-phagocytic cells [38] and hence show a similar uptake behavior towards negatively and positively charged nanoparticles. After reaching a saturation state following a downregulated metabolism, the phagocytic activity decreases and NPs are no further taken up, which explains the concentration- and time-independence of the NPs internalization. We further assume that the adsorption of mRNA improves the cell association due to better stabilization of the nanoparticles after mRNA adsorption onto the surface. Sue et al. did observe similar effect for a comparable system [11]. This behavior is clearly seen in the higher cell internalization of mRNA:CS-FA-PLGA NPs compared with the blank particles. The high amount of positive cells upon incubation with FA-LPNs compared to CS-FA-PLGA is assumedly a result of the hydrophobic nature of FA-LPNs.

Kinetics of protein translation in dendritic cells

A variety of different non-viral systems has been introduced to deliver safe and efficiently mRNA to the site of action, especially for mRNA-therapeutics and

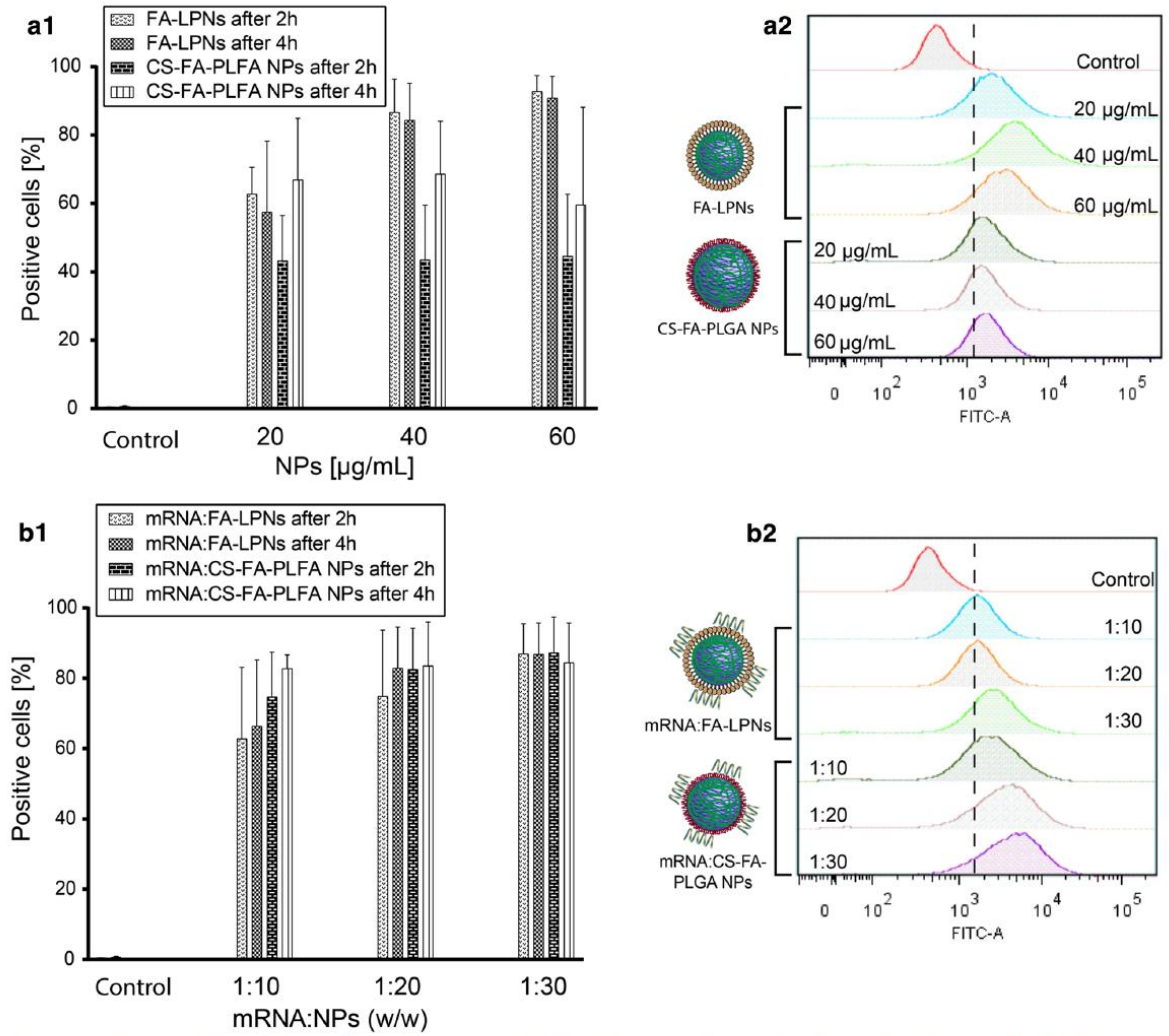

Fig. 6 Quantification of cellular NP association for fluoresceinamine (FA) labeled blank (**a1**, **a2**) and mRNA complexed nanoparticles (**b1**, **b2**) tested in DC2.4 cells. NPs were incubated for 2 h and 4 h at different concentrations (20, 40 and 60 µg/mL corresponding to the weight ratios 1:10, 1:20 and 1:30 used for transfection). **a1**, **b1** Green NP fluorescent signal quantified by flow cytometry. Blank LPNs tend to show more uptake then blank CS-PLGA NPs, whereas for mRNA-loaded nanoparticles the opposite was observed. None of the samples showed a significant difference between 2 and 4 h incubation. **a2**, **b2** Representative graphs obtained for NP samples after 4 h incubation. $N = 4$, mean ± SD

mRNA-vaccination strategies. However, most of them still show limitation regarding their efficiency to transfect cells, as they have to cross several biological barriers while maintaining the functionality of the carried mRNA. As mRNA represents a transient cargo [6, 9] to be delivered into the cytoplasm, the kinetics of mRNA transgene expression was explored by taking measurements 2, 4 h after NPs exposure to DCs and additionally 24 and 48 h post-transfection. We further quantified and compared the efficiency of both mRNA-loaded LPNs and CS-PLGA NPs, with jetPRIME® used as positive control. At a w/w ratio of 1:10, mRNA:LPNs revealed a transfection rate in DCs of around ~ 40%, which increased to nearly 80% at w/w ratios of 1:20 and 1:30 (Fig. 7a1). Correspondingly, a strong shift in the red fluorescence signal was seen in the dot-plots (Additional file 1: Figure S5). Already after 2 h, we could observe almost 20% transfected cells for ratio 1:10 following nearly 60% for the weight ratios of 1:20 and 1:30.

While mRNA:CS-PLGA NPs showed similar uptake behavior, protein translation rate was significantly less than for mRNA:LPNs, reaching only 5% of cells with a maximum after 24 h (Fig. 7a2). Translation rates for naked mRNA was almost same as the background of untreated cells and JetPRIME® transfection efficacy was comparable to mRNA:CS-PLGA NP (Fig. 7a3). Furthermore, mRNA:LNPs elucidated the highest transfection efficiency already after 4 h with a decay after 24 h and 48 h post-transfection, which is emphasized in the strong red fluorescence shift (Fig. 7a4). The difference between both nanoparticles can be further seen in the fluorescence microscopy images (Fig. 8a, b) with highest mCherry protein expression resulting in red fluorescence signal for mRNA:LPNs of ratio 1:20 and 1:30. Nanoparticle sizes of LPN and CS-PLGA changed in the range of 50–100 nm (see Table 1), the increase in PDI was modest and the tendency of size increase could not be related to the observed transfection efficacy. The mRNA:LNPs_1:20 re smaller in size but efficient in transfection. The more likely reason for the stronger transfection efficacy is the availability of remaining cationic groups at the particle surface at ratios of 1:20 or 1:30, which are important for the interaction with cell and endosomal membranes.

Lipid-coated PLGA nanoparticles show a higher transfection efficiency over chitosan-coated PLGA nanoparticles, which may be due to the high stability of complexed mRNA onto CS-PLGA nanoparticles presumably leading to an incomplete release (seen in the gel, Fig. 5b) within the cytoplasmic compartment. mRNA:LPNs correspondingly show fast transfection kinetics as shown in the agarose gel by using heparin (Fig. 4a) releasing the mRNA after 15 min of incubation. Hence, we can suppose that the LPNs survive the acidic condition of the lysosome and escape this compartment slowly over time causing a transient mRNA translation within the cytoplasm reaching a transfection rate already after 2 h with an increment in time and highest transgene expression rate after 4 h. The fluorescence microscope images further indicate a variation of the red fluorescence intensity of mCherry

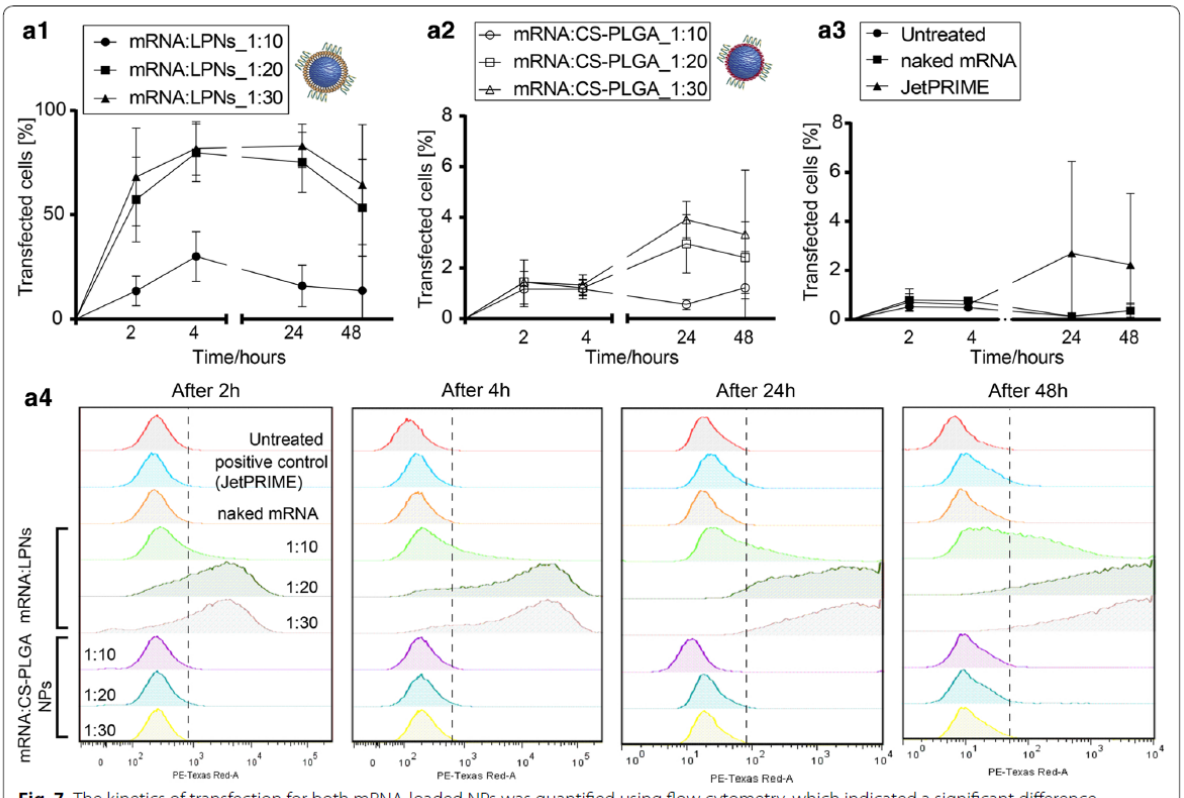

Fig. 7 The kinetics of transfection for both mRNA-loaded NPs was quantified using flow cytometry, which indicated a significant difference between **a1** mRNA:LPNs over **a2** mRNA:CS-PLGA NPs, while mRNA:LPNs with a ratio of 1:20 and 1:30 elucidated a significant higher transfection rate over 1:10. **a3** Control samples for transfection studies were JetPRIME® as positive control and naked mRNA as negative control. (Note the enlarged y-axis, $N = 4$, mean ± SD.) **a4** Representative graphs for evaluated time-points demonstrate a strong fluorescence shift for mRNA:LPNs with an increment in time and hence a higher transgene expression

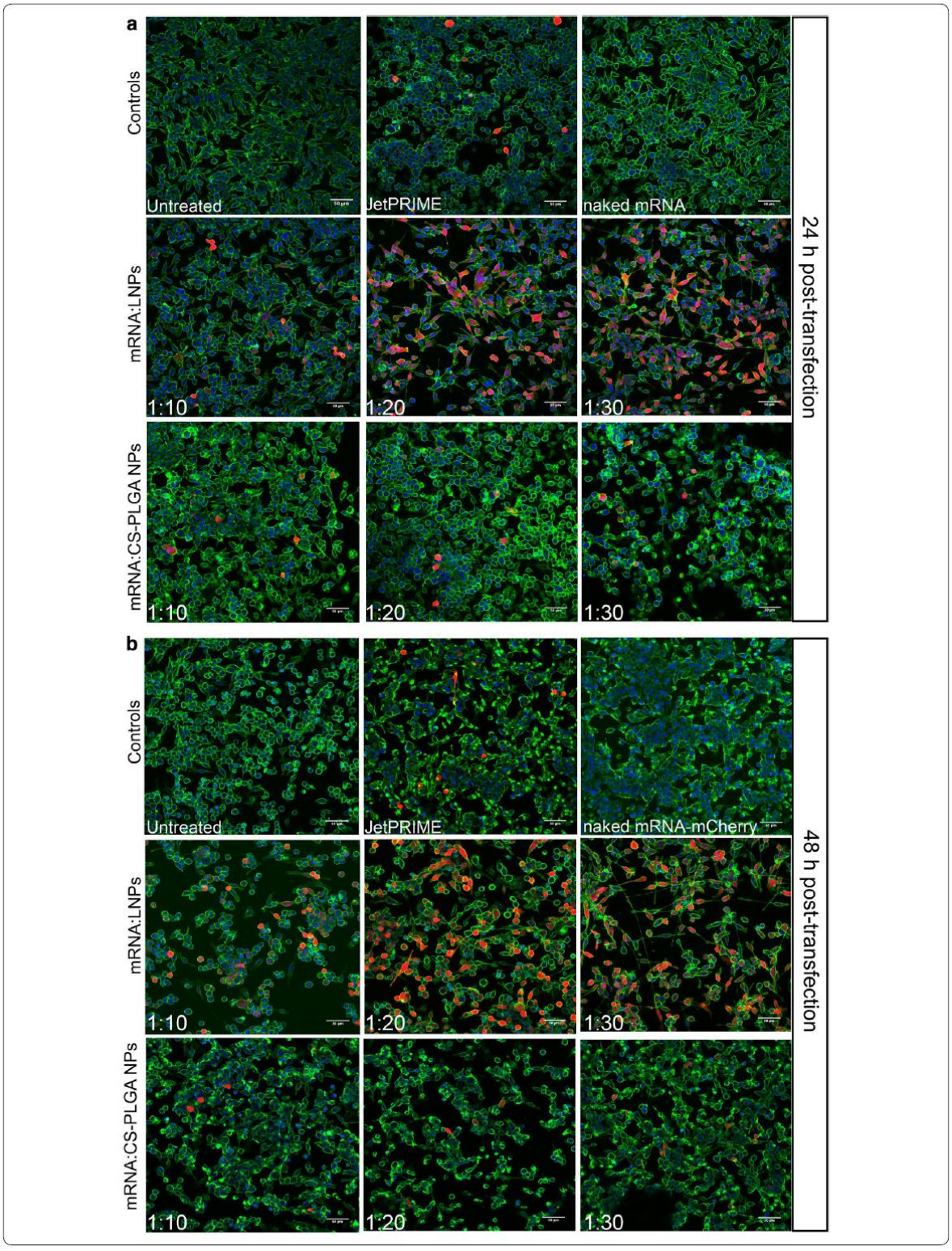
a
Controls
Untreated
JetPRIME
naked mRNA
mRNA:LNPs
1:10
1:20
1:30
mRNA:CS-PLGA NPs
1:10
1:20
1:30
24 h post-transfection
b
Controls
Untreated
JetPRIME
naked mRNA-mCherry
mRNA:LNPs
1:10
1:20
1:30
mRNA:CS-PLGA NPs
1:10
1:20
1:30
48 h post-transfection

(See figure on previous page.)
Fig. 8 Representative confocal images of DC2.4 cells transfected with both mRNA complexed NPs and by using jetPRIME® as a positive control, naked mRNA as negative control. Transfection was analyzed with CLSM **a** 24 h and **b** 48 h post-transfection. Red fluorescence reveals cells successfully transfected with the nanoparticles while their morphology remains consistent with non-transfected cells (staining: green: cell membrane; blue: cell nucleus; scale bar: 50 µm)

between different cells of the same image. These differences may reflect different metabolic stages of these cells, leading to differences in particle uptake and protein translation, resp., possibly depending on the cell cycle [40].

The transient course observed within this experiments mirrors the behavior of mRNA as reported by Leonhardt et al. [9], in which the transfection kinetics of pDNA and mRNA delivered by the commercial available transfection reagent Lipofectamine2000® was compared. It was shown that mRNA has a faster onset by reaching its maximum transfection efficiency after 3 h. This observation is predictable as pDNA needs enter the nucleus to cause further protein translation while mRNA's protein expression takes place within the cytoplasm. A further criteria of a rapid transfection rate might be due to method for mRNA loading as it has been already hypothesized by Su et al. [11] that surface-adsorbed mRNA shows a faster release kinetics then encapsulated mRNA. This coincides with the observation made in this in vitro cell study, as LPNs show a faster and complete release (see Fig. 4) and hence the rapid transfection rate compared with mRNA encapsulated within the used positive control JetPRIME® revealing its maximum transfection rate 24 h post-transfection. In contrary, Zhdanov et al. [24, 25] is working on generic models to predict the impact of nanoparticles as nucleotides carriers and their release kinetics on the translation. However, his theoretical models, e.g. using lipid nanoparticles predict only a minor role for the translation kinetics performed in in vitro assays.

Furthermore, while particle-uptake appeared to be similar for mRNA:LPNs and mRNA:CS-PLGA NPs, protein translation of the LPNs mRNA-delivery system was more efficient. Nevertheless, even the weaker performing CS-PLGA NPs had already shown their potential to deliver nuclease-encoding mRNA in vivo in a transgenic mouse model resulting in an efficient genome editing, indicating that the necessary level of delivery efficiency may vary with the therapeutic application [10]. Similar performance of mRNA depending on the application route was observed further by Pardi et al. [41] using commercial lipid particles from an ionizable cationic lipid, PC, and cholesterol-PEG to deliver mRNA in vivo with a variety of delivery routes. The reporter gene luciferase was used to monitor the time of transgene expression. Intravenous and intratracheal delivery showed shorter expression times, with a half-life of mRNA translation ~ 7 h, in comparison to intramuscular and intradermal with a half-life of mRNA translation > 20 h. Knowing the kinetics of both NP-uptake and protein translation of NP-delivered mRNA is equally crucial to develop such tailor-made precision nanomedicines in future.

Live cell video microscopy: recording NP uptake and protein translation

In order to simultaneously visualize and quantify both cellular uptake and protein translation NP-mediated mRNA-delivery, we decided to perform live cell video microcopy of this process. DC2.4 cells were exposed to mRNA:FA-LPNs of weight ratio 1:30 and continuously observed over a time-range of 4 h. Figure 9a1 shows representative images depicted from the video after nine different time-points (Additional file 2: Movie S1), with strong particle association to cells seen in green fluorescence and transfected cells signaling in red. Cells showing first a green (= particle binding/uptake) and later a red (= protein translation) fluorescence signal within the 4 h time-frame were counted as transfected cells. Cells showing only a green, but no red fluorescence, were counted as non-transfected cells. As the video analysis shows, particle-cell association starts after 15 min upon exposure while first protein translation signals were recorded after 1 h. After this time-lack, the protein translation (red fluorescence signal) of the transfected cells, as visualized in Fig. 9a2, appeared to increase exponentially until the end of the experiment. As expected, the red fluorescence signal of non-transfected cells remained at the background level. Surprisingly, NP-uptake kinetics (green fluorescence signal) was comparable for both transfected and non-transfected cells with a slow linear increase over time (Fig. 9a3). As live cell video microscopy reveals, some cells start earlier with the transgene expression while others start at later time-point. Quite a few cells do not show transgene expression, even after NPs binding/uptake. This confirms the earlier observed heterogeneity of transgene expression as discussed in the previous section.

Comparison of transfection efficacy for a non-phagocytic cell line

To compare the potential of the LPNs to transfect a non-phagocytic cell line by using the same settings as applied

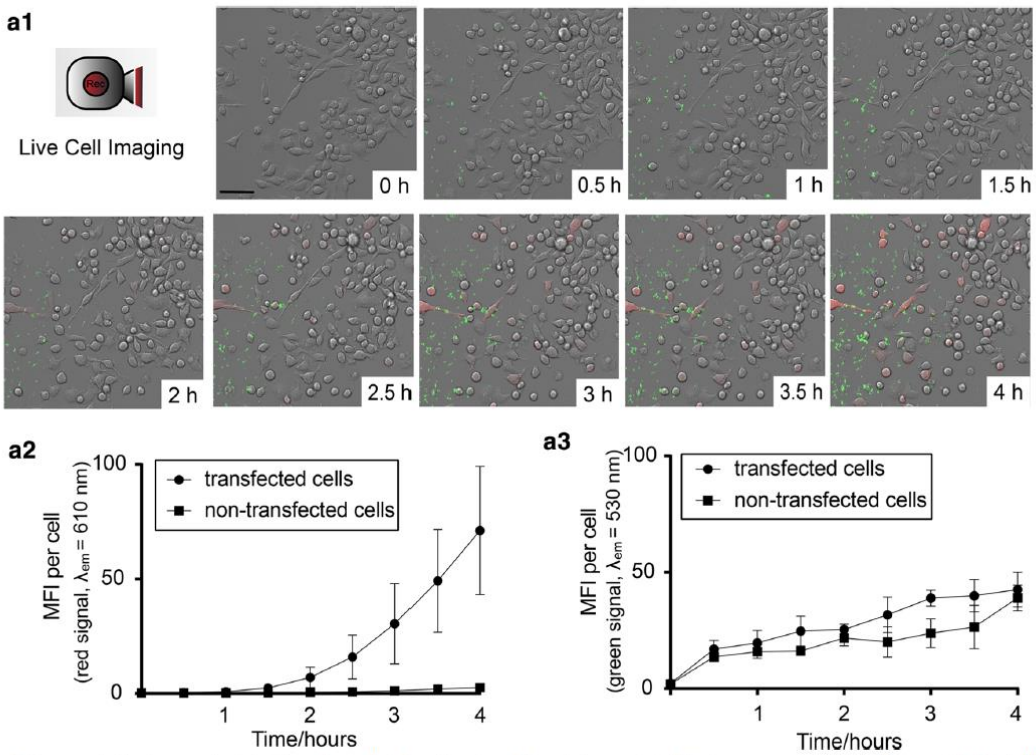

Fig. 9 **a1** Representative images depicted from live cell video after nine different time-points. The images are part of a video provided in Additional file 2: Movie S1. DC2.4 cells were incubated with mRNA:FA-LPNs for a complete time duration of 4 h and with an interval of 3 min/image. Green dots on the images represent the fluorescence signal of labeled LPNs, while the cells signaling in red are the ones with successful mCherry expression. Scale bar = 100 µm. **a2** Time-dependent change of the red fluorescence signal resulting from transfected cells and non-transfected, which are correlated with **a3** green fluorescence signal of labeled nanoparticles. The tendency of each single cell being transfected is independent of the NPs uptake, as no significant difference between the uptake-behavior of transfected and non-transfected cells was observable. λ_{em} = peak emission wavelength, *MFI* mean fluorescence intensity (mean ± SD, data from n = 32 fluorescent cells, n = 8 non-fluorescent cells, obtained from 4 independent videos)

for DC2.4 cells, the human alveolar epithelial cell line A549 was chosen, which is a commonly used model for transfection studies. They were grown to ~ 70% confluency in well-plates and then incubated for 4 h with mRNA:LPNs and mRNA:CS-PLGA NPs, resp. The number of transfected cells was counted by flow cytometer 24 and 48 h post-transfection. Similar as for DC2.4 cells, mRNA complexed LPNs revealed a higher efficiency over CS-PLGA NPs with a steadily increasing transfection rate up to ~ 60% for w/w of 1:30 (Fig. 10) with a strong red fluorescence shift (Additional file 1: Figure S6A). Fluorescence confocal images additionally support this observation for mRNA:LPNs (Additional file 1: Figure S6 B). Notably, however, the level of transfected A549 cells still increased up to 48 h post-transfection, whereas transfection of DC2.4 cells started to decrease again after 24 h post-transfection.

Conclusions

In this study, we have investigated delivery of mRNA into dendritic cells by two different types of cationic nanoparticles. Using fluorescently labeled particles as carriers and mRNA-mCherry as cargo, it was possible to distinguish the different kinetics of NP-uptake and mCherry protein translation. Live cell video microscopy even allowed to follow both processes within the same experiment. The chitosan-PLGA NPs were well internalized by the cells, but relatively inefficient in transfection. Lipid-PLGA hybrid nanoparticles showed superior efficiency transfecting dendritic cells with up to 80% and epithelial cells up 60% transfection rate at concentrations that were not causing any cytotoxic effects. Transgene expression of mRNA:LPNs started in single cells 1 h after particle exposure with an exponential increase during the 4 h of recording. Providing good transfection efficacy and rapid transgene expression, hybrid lipid–polymer

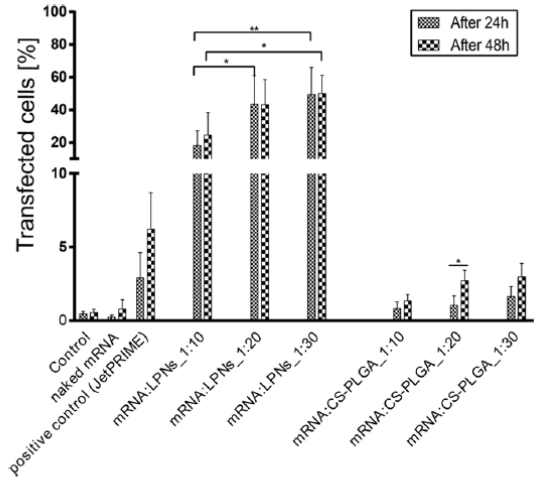

Fig. 10 Transfection of non-phagocytic cells, using mRNA:LPNs and mRNA:CS-PLGA at different ratios performed in epithelial A549 cells for 24 h and 48 h post-transfection using flow cytometer. mRNA complexed LPNs reveal a significant higher transgene expression over CS-PLGA NPs. Both NPs show higher transfection rates with higher mRNA:NP ratios and increasing transfection until 48 h post-transfection N = 4, mean ± SD (*p < 0.05 and **p < 0.01)

nanoparticles, like e.g. the DOTMA LPN delivery system, appear as an interesting platform for mRNA-based therapeutics and vaccination strategies.

Additional files

Additional file 1: Figure S1. Physicochemical characterization for the storage stability of blank LPNs at 4 °C and room temperature (RT) tested over a time-course of 62 days post-preparation **(A)** hydrodynamic size, **(B)** PDI and **(C)** ζ-potential. Colloidal properties reveal stability of LPNs for all tested time-points and temperatures. *N* = 3, mean ± SD. **Figure S2.** (**A1, A2**) Physicochemical characteristics of blank LPNs and (**B1, B2**) blank CS-PLGA NPs tested under different physiological conditions using HBSS buffer, cell culture medium DMEM with and without 10% FCS following 2 h, 4 h and 24 h of incubation. While LPNs show only a significant change in colloidal properties after incubation in DMEM plus 10% FCS, CS-PLGA NPs elicit a significant difference in colloidal parameter for all tested buffers compared with untreated samples. However, the observed size changes are immediate but not increasing within the 24 h of observation. *N* = 3, mean ± SD. **Figure S3.** Representative dot plots and appropriate gating strategy for cytotoxicity assay in DC2.4 cells using blank LPNs and CS-PLGA NPs indicate a fluorescence shift and hence higher cytotoxicity for particles of higher concentrations (160 µg/mL). **Figure S4.** Summary of physicochemical properties for fluoresceinamine labeled blank and labeled mRNA complexed nanoparticles wit mRNA:NPs w/w ratio of 1:10, 1:20 and 1:30. **(A)** Indicates the hydrodynamic size, **(B)** PDI and **(C)** ζ-potential. *N* = 4, mean ± SD. **Figure S5.** Representative dot plots and corresponding gating strategy for the transfection studies in DC2.4 cells using mRNA:LPNs and mRNA:CS-PLGA NPs with JetPRIME® as the positive control, untreated and naked mRNA as negative control. Fluorescence shift reveals cells with mRNA-mCherry transgene expression. **Figure S6.** (**A**) Representative graphs obtained 24 h and 48 h post-transfection of A549 cells with mRNA:LPNs and mRNA:CS-PLGA NPs at different mRNA:NPs weight ratios using flow cytometry. **(B)** Representative confocal images of A549 cells 48 h post-transfection using mRNA:LPNs, JetPRIME® as positive control, naked mRNA as negative control. Red fluorescence reveals cells successfully transfected while their morphology remains consistent with non-transfected cells (green: cell membrane; blue: cell nucleus; scale bar 50 µm).

Additional file 2: Movie S1. The movie displays the interaction of fluorescence labeled and mRNA complexed LPNs (weight ratio of 1:30) with DC2.4 cells with the subsequent mCherry protein translation signaling in red fluorescence.

Abbreviations

DOTMA: 1, 2-di-*O*-octadecenyl-3-trimethylammonium propane; PLGA: poly (lactic-*co*-glycolic acid); NPs: nanoparticles; LPNs: lipid-PLGA NPs; CS-PLGA NPs: chitosan-PLGA NPs; FA-LPNs: fluoresceinamine labeled lipid-PLGA NPs; CS-FA-PLGA NPs: fluoresceinamine labeled chitosan-PLGA NPs; mRNA:LPNs: mRNA-loaded lipid-PLGA NPs; mRNA:CS-PLGA NPs: mRNA-loaded chitosan-PLGA NPs; mRNA:FA-LPNs: mRNA-loaded fluoresceinamine labeled lipid-PLGA NPs; mRNA:CS-FA-PLGA NPs: mRNA-loaded fluoresceinamine labeled chitosan-PLGA NPs.

Authors' contributions

HY, BL and CML conceived and designed the study and discussed the results. HY performed the experiments, analyzed the data, and drafted the manuscript. CDR and MK performed electron microscopy studies. AB and XM did quantification of fluorescence signal from the life cell imaging. All authors read and approved the final manuscript.

Author details

[1] Department of Drug Delivery (DDEL), Helmholtz-Institute for Pharmaceutical Research Saarland (HIPS), Helmholtz Center for Infection Research (HZI), Campus E8.1, 66123 Saarbrücken, Germany. [2] Department of Pharmacy, Saarland University, 66123 Saarbrücken, Germany. [3] Center for Bioinformatics, Saarland Informatics Campus, Saarland University, 66123 Saarbrücken, Germany. [4] INM-Leibniz Institute for New Materials, 66123 Saarbrücken, Germany.

Acknowledgements

The authors gratefully acknowledge Petra Koenig and Jana Westhues for support and handling in cell cultures and Patrick Carius for helping in live cell imaging and fruitful discussions.

Competing interests

The authors declare that they have no competing interests.

Availability of data and materials

All data generated and materials used in this study are included in the manuscript and corresponding additional files.

Consent for publication

Not applicable within this study.

Ethics approval and consent to participate

Not applicable within this study.

Funding

Not applicable for this study.

Publisher's Note

Received: 28 May 2018 Accepted: 15 September 2018
Published online: 19 September 2018

References

1. Islam MA, Reesor EKG, Xu Y, Zope HR, Zetter BR, Shi J. Biomaterials for mRNA delivery. Biomater Sci. 2015;3:1519–33. https://doi.org/10.1039/c5bm00198f.
2. Pardi N, Hogan MJ, Porter FW, Weissman D. mRNA vaccines—a new era in vaccinology. Nat Rev Drug Discov. 2018;17:261–79. https://doi.org/10.1038/nrd.2017.243.
3. Palamà IE, Cortese B, D'Amone S, Gigli G. mRNA delivery using non-viral PCL nanoparticles. Biomater Sci. 2015;3:144–51. https://doi.org/10.1039/c4bm00242c.
4. Malone RW, Felgner PL, Verma IM. Cationic liposome-mediated RNA transfection. Proc Natl Acad Sci USA. 1989;86:6077–81.
5. De Temmerman M-L, Dewitte H, Vandenbroucke RE, Lucas B, Libert C, Demeester J, de Smedt SC, Lentacker I, Rejman J. mRNA-Lipoplex loaded microbubble contrast agents for ultrasound-assisted transfection of dendritic cells. Biomaterials. 2011;32:9128–35. https://doi.org/10.1016/j.biomaterials.2011.08.024.
6. Phua KKL, Leong KW, Nair SK. Transfection efficiency and transgene expression kinetics of mRNA delivered in naked and nanoparticle format. J Control Release. 2013;166:227–33. https://doi.org/10.1016/j.jconrel.2012.12.029.
7. De Haes W, van Mol G, Merlin C, de Smedt SC, Vanham G, Rejman J. Internalization of mRNA lipoplexes by dendritic cells. Mol Pharm. 2012;9:2942–9. https://doi.org/10.1021/mp3003336.
8. Rejman J, Tavernier G, Bavarsad N, Demeester J, de Smedt SC. mRNA transfection of cervical carcinoma and mesenchymal stem cells mediated by cationic carriers. J Control Release. 2010;147:385–91. https://doi.org/10.1016/j.jconrel.2010.07.124.
9. Leonhardt C, Schwake G, Stögbauer TR, Rappl S, Kuhr J-T, Ligon TS, Rädler JO. Single-cell mRNA transfection studies: delivery, kinetics and statistics by numbers. Nanomed Nanotechnol Biol Med. 2014;10:679–88. https://doi.org/10.1016/j.nano.2013.11.008.
10. Mahiny AJ, Dewerth A, Mays LE, Alkhaled M, Mothes B, Malaeksefat E, Loretz B, Rottenberger J, Brosch DM, Reautschnig P, et al. In vivo genome editing using nuclease-encoding mRNA corrects SP-B deficiency. Nat Biotechnol. 2015;33:584–6. https://doi.org/10.1038/nbt.3241.
11. Su X, Fricke J, Kavanagh DG, Irvine DJ. In vitro and in vivo mRNA delivery using lipid-enveloped pH-responsive polymer nanoparticles. Mol Pharm. 2011;8:774–87. https://doi.org/10.1021/mp100390w.
12. Cheng C, Convertine AJ, Stayton PS, Bryers JD. Multifunctional triblock copolymers for intracellular messenger RNA delivery. Biomaterials. 2012;33:6868–76. https://doi.org/10.1016/j.biomaterials.2012.06.020.
13. Kaczmarek JC, Kowalski PS, Anderson DG. Advances in the delivery of RNA therapeutics: from concept to clinical reality. Genome Med. 2017;9:60. https://doi.org/10.1186/s13073-017-0450-0.
14. Lv H, Zhang S, Wang B, Cui S, Yan J. Toxicity of cationic lipids and cationic polymers in gene delivery. J Control Release. 2006;114:100–9. https://doi.org/10.1016/j.jconrel.2006.04.014.
15. Hadinoto K, Sundaresan A, Cheow WS. Lipid–polymer hybrid nanoparticles as a new generation therapeutic delivery platform: a review. Eur J Pharm Biopharm. 2013;85:427–43. https://doi.org/10.1016/j.ejpb.2013.07.002.
16. de Groot AM, Thanki K, Gangloff M, Falkenberg E, Zeng X, van Bijnen DCJ, van Eden W, Franzyk H, Nielsen HM, Broere F, et al. Immunogenicity testing of lipidoids in vitro and in silico: modulating lipidoid-mediated TLR4 activation by nanoparticle design. Mol Ther Nucleic Acids. 2018;11:159–69. https://doi.org/10.1016/j.omtn.2018.02.003.
17. Jensen DK, Jensen LB, Koocheki S, Bengtson L, Cun D, Nielsen HM, Foged C. Design of an inhalable dry powder formulation of DOTAP-modified PLGA nanoparticles loaded with siRNA. J Control Release. 2012;157:141–8. https://doi.org/10.1016/j.jconrel.2011.08.011.
18. Colombo S, Cun D, Remaut K, Bunker M, Zhang J, Martin-Bertelsen B, Yaghmur A, Braeckmans K, Nielsen HM, Foged C. Mechanistic profiling of the siRNA delivery dynamics of lipid–polymer hybrid nanoparticles. J Control Release. 2015;201:22–31. https://doi.org/10.1016/j.jconrel.2014.12.026.
19. Hasan W, Chu K, Gullapalli A, Dunn SS, Enlow EM, Luft JC, Tian S, Napier ME, Pohlhaus PD, Rolland JP, et al. Delivery of multiple siRNAs using lipid-coated PLGA nanoparticles for treatment of prostate cancer. Nano Lett. 2012;12:287–92. https://doi.org/10.1021/nl2035354.
20. Thanki K, Zeng X, Justesen S, Tejlmann S, Falkenberg E, van Driessche E, Mørck Nielsen H, Franzyk H, Foged C. Engineering of small interfering RNA-loaded lipidoid-poly(DL-lactic-*co*-glycolic acid) hybrid nanoparticles for highly efficient and safe gene silencing: a quality by design-based approach. Eur j Pharm Biopharm. 2017;120:22–33. https://doi.org/10.1016/j.ejpb.2017.07.014.
21. Díez S, Miguéliz I, Tros de Ilarduya C. Targeted cationic poly(D, L-lactic-*co*-glycolic acid) nanoparticles for gene delivery to cultured cells. Cell Mol Biol Lett. 2009;14:347–62. https://doi.org/10.2478/s11658-009-0003-7.
22. Bose RJC, Arai Y, Ahn JC, Park H, Lee S-H. Influence of cationic lipid concentration on properties of lipid–polymer hybrid nanospheres for gene delivery. Int J Nanomed. 2015;10:5367–82. https://doi.org/10.2147/IJN.S87120.
23. Perche F, Benvegnu T, Berchel M, Lebegue L, Pichon C, Jaffrès P-A, Midoux P. Enhancement of dendritic cells transfection in vivo and of vaccination against B16F10 melanoma with mannosylated histidylated lipopolyplexes loaded with tumor antigen messenger RNA. Nanomed Nanotechnol Biol Med. 2011;7:445–53. https://doi.org/10.1016/j.nano.2010.12.010.
24. Zhdanov VP. Kinetics of lipid-nanoparticle-mediated intracellular mRNA delivery and function. Phys Rev E. 2017;96:42406. https://doi.org/10.1103/PhysRevE.96.042406.
25. Zhdanov VP. mRNA function after intracellular delivery and release. Bio Syst. 2018;165:52–6. https://doi.org/10.1016/j.biosystems.2018.01.003.
26. Reichmuth AM, Oberli MA, Jeklenec A, Langer R, Blankschtein D. mRNA vaccine delivery using lipid nanoparticles. Ther Delivery. 2016;7:319–34. https://doi.org/10.4155/tde-2016-0006.
27. Takashima Y, Saito R, Nakajima A, Oda M, Kimura A, Kanazawa T, Okada H. Spray-drying preparation of microparticles containing cationic PLGA nanospheres as gene carriers for avoiding aggregation of nanospheres. Int J Pharm. 2007;343:262–9. https://doi.org/10.1016/j.ijpharm.2007.05.042.
28. Mittal A, Raber AS, Schaefer UF, Weissmann S, Ebensen T, Schulze K, Guzmán CA, Lehr C-M, Hansen S. Non-invasive delivery of nanoparticles to hair follicles: a perspective for transcutaneous immunization. Vaccine. 2013;31:3442–51. https://doi.org/10.1016/j.vaccine.2012.12.048.
29. Murgia X, Yasar H, Carvalho-Wodarz C, Loretz B, Gordon S, Schwarzkopf K, Schaefer U, Lehr C-M. Modelling the bronchial barrier in pulmonary drug delivery: a human bronchial epithelial cell line supplemented with human tracheal mucus. Eur J Pharm Biopharm. 2017;118:79–88. https://doi.org/10.1016/j.ejpb.2017.03.020.
30. Weiss B, Schaefer UF, Zapp J, Lamprecht A, Stallmach A, Lehr C-M. Nanoparticles made of fluorescence-labelled poly(L-lactide-*co*-glycolide): preparation, stability, and biocompatibility. J Nanosci Nanotechnol. 2006;6:3048–56. https://doi.org/10.1166/jnn.2006.424.
31. Yasar H, Ho D-K, de Rossi C, Herrmann J, Gordon S, Loretz B, Lehr C-M. Starch-chitosan polyplexes: a versatile carrier system for anti-infectives and gene delivery. Polymers. 2018;10:252. https://doi.org/10.3390/polym10030252.
32. Shang L, Nienhaus K, Nienhaus GU. Engineered nanoparticles interacting with cells: size matters. J Nanobiotechnol. 2014;12:5. https://doi.org/10.1186/1477-3155-12-5.
33. Schulze C, Kroll A, Lehr C-M, Schäfer UF, Becker K, Schnekenburger J, Schulze Isfort C, Landsiedel R, Wohlleben W. Not ready to use—overcoming pitfalls when dispersing nanoparticles in physiological media. Nanotoxicology. 2009;2:51–61. https://doi.org/10.1080/17435390802018378.
34. Salatin S, Maleki Dizaj S, Yari Khosroushahi A. Effect of the surface modification, size, and shape on cellular uptake of nanoparticles. Cell Biol Int. 2015;39:881–90. https://doi.org/10.1002/cbin.10459.
35. Mandal B, Bhattacharjee H, Mittal N, Sah H, Balabathula P, Thoma LA, Wood GC. Core-shell-type lipid–polymer hybrid nanoparticles as a drug delivery platform. Nanomed Nanotechnol Biol Med. 2013;9:474–91. https://doi.org/10.1016/j.nano.2012.11.010.
36. Franken LE, Boekema EJ, Stuart MCA. Transmission electron microscopy as a tool for the characterization of soft materials: application and interpretation. Adv Sci (Weinheim, Baden-Wurttemberg, Germany). 2017;4:1600476. https://doi.org/10.1002/advs.201600476.
37. Fischer D, Li Y, Ahlemeyer B, Krieglstein J, Kissel T. In vitro cytotoxicity testing of polycations: influence of polymer structure on cell viability and hemolysis. Biomaterials. 2003;24:1121–31. https://doi.org/10.1016/S0142-9612(02)00445-3.

38. Fröhlich E. The role of surface charge in cellular uptake and cytotoxicity of medical nanoparticles. Int J Nanomed. 2012;7:5577–91. https://doi.org/10.2147/IJN.S36111.
39. Lipscomb MF, Masten BJ. Dendritic cells: immune regulators in health and disease. Physiol Rev. 2002;82:97–130. https://doi.org/10.1152/physrev.00023.2001.
40. Kim JA, Åberg C, Salvati A, Dawson KA. Role of cell cycle on the cellular uptake and dilution of nanoparticles in a cell population. Nat Nanotechnol. 2011;7:62–8. https://doi.org/10.1038/nnano.2011.191.
41. Pardi N, Tuyishime S, Muramatsu H, Kariko K, Mui BL, Tam YK, Madden TD, Hope MJ, Weissman D. Expression kinetics of nucleoside-modified mRNA delivered in lipid nanoparticles to mice by various routes. J Control Release. 2015;217:345–51. https://doi.org/10.1016/j.jconrel.2015.08.007.

7 List of Publications, Oral and Poster Presentations

List of publications

Yasar, H.; Duran, V.; Becker, J.; Loretz, B.; Kalinke, U.; Lehr, C-M. Preferential uptake of chitosan-coated PLGA nanoparticles by antigen presenting cells. Nanomedicine-Nanotechnology, Biology, Medicine, **2018**, in reply.

Haque, A. K. M. Ashiqul; Dewerth, A.; Antony, J.S.; Riethmüller, J.; Schweizer, G.R.; Weinmann, P.; Latifi, N.; **Yasar, H**.; Pedemonte, N.; Sondo, E.; Weidensee, B.; Ralhan, A.; Laval, J.; Schlegel, P.; Seitz, C.; Loretz, B.; Lehr, C.-M.; Handgretinger, R.; Kormann, M.S.D. Chemically modified h CFTR mRNAs recuperate lung function in a mouse model of cystic fibrosis. Scientific Reports, **2018**, 8, 16776.

Yasar, H.; Biehl, A.; Rossi, C. de; Koch, M.; Murgia, X.; Loretz, B.; Lehr, C.-M. Kinetics of mRNA delivery and protein translation in dendritic cells using lipid-coated PLGA nanoparticles. Journal of Nanobiotechnology, **2018**, 16, 72.

Yasar, H.; Ho, D.-K.; Rossi, C. de; Herrmann, J.; Gordon, S.; Loretz, B.; Lehr, C.-M. Starch-Chitosan Polyplexes: A Versatile Carrier System for Anti-Infectives and Gene Delivery. Polymers, **2018**, 10, 252.

Murgia, X.; **Yasar, H.**; Carvalho-Wodarz, C.; Loretz, B.; Gordon, S.; Schwarzkopf, K.; Schaefer, U.; Lehr, C.-M. Modelling the bronchial barrier in pulmonary drug delivery: A human bronchial epithelial cell line supplemented with human tracheal mucus. European journal of pharmaceutics and biopharmaceutics: official journal of Arbeitsgemeinschaft fur Pharmazeutische Verfahrenstechnik e.V, **2017**, 118, 79–88.

Yasar, H.; Schulze, K.; Gordon, S.; Loretz, B.; Guzman,C. A.; Lehr, C-M. Follicular Drug Delivery: a Root to Success, The Medicine Maker, **2016**.

Guzman,, C. A.; Lehr, C-M.; Schulze, K.; Loretz, B.; Gordon, S.; **Yasar, H.** Perspectives of non-invasive vaccine delivery, *Research Report HZI* (2014/2015), **2016**.

Wei, H.; **Yasar, H**.; Funk, N.W.; Giese, M.; Baz, E.-S.; Stengl, M. Signaling of pigment-dispersing factor (PDF) in the Madeira cockroach Rhyparobia maderae. *PloS one*, **2014**, *9,* e108757.

Selected Talks and Poster Presentations on Conferences

Talk*: Hanzey Yasar (May 2017)"From top to bottom-Uptake behavior of Chitosan-PLGA Nanoparticles within the skin structure"*; Skin Vaccination Summit in Leiden/Netherlands

Talk:* Hanzey Yasar (Sep. 2016*) "*Invisible patches*", Event about "Shakespeare lives in Science" organized from Erasmus Medical Centre in Rotterdam/Netherlands-

***Talk:* Hanzey Yasar (June 2016)** *"Crème for Vaccination";* FameLab -International Science and Communication competition, Cheltenham Science Festival, Cheltenham/UK

Talk*: Hanzey Yasar (Oct. 2015) "Vaccination through the hair follicles",* Meeting of SFB1102 of Saarland University/, Saarbrücken/Germany

Hanzey Yasar, Chiara De Rossi, Brigitta Loretz, Claus-Michael Lehr **(Sep. 2017)** *Comparing two polymeric core-shell nanocarriers for mRNA delivery*; Deutsche Pharmazeutische Gesellschaft (DPhG) Meeting in Saarbrücken/Germany

Hanzey Yasar, Khiet Ho-Duy, Chiara De Rossi, Sarah Gordon, Brigitta Loretz, Claus Michael Lehr **(Nov. 2016)** *Starch-Chitosan polyplexes as versatile drug carrier system for transfollicular vaccination*; Globalization of Pharmaceutics Education Network (GPEN) in Lawrence /USA

Hanzey Yasar, Xabi Murgia, Konrad Schwarzkopf, Christiane Carvalho, Sarah Gordon, Brigitta Loretz, Claus-Michael Lehr **(March 2016)** *Mucus penetration and cellular uptake of nanoparticles in a cystic fibrosis cell model*; BioBarriers 2016 in Saarbrücken/Germany

Awards

September 2017: House of Pharma & Healthcare (6th Annual Meeting): *Science Slam:* ***3rd runner*** (Title of Talk: *"Schmerzlose Impfungen*)

May 2016: *FameLab* - International Science and Communication competition; National*,* ***1st runner*** *in Germany (*Title of first Talk: *"*Wundheilung wie im Film*"* and Title of second Talk: "Mit Nanokugeln gegen Allergien")

April 2016: *FameLab* - International Science and Communication competition; *Regional* Heats in Braunschweig*,* ***1st runner*** *in the regionals* (Title of Talk: "*Impfcreme"*)

8 Scientific Collaborations

I would like to acknowledge our external collaboration partners for their dedicated contribution to this project, their support, scientific expertise and the fruitful, constructive plus enjoyable conversations and meetings to improve the outcome of the projects.

The group of Prof. Dr. Carlos A. Guzman (Department of Vaccinology and Applied Microbiology from Helmholtz Centre for Infection Research/Braunschweig) were our main collaborator for the in vivo studies within this project. I gratefully would like to thank Dr. Kai Schulze and my PhD-fellow Simon Delandre with their contribution to this project, their support and fruitful conversations. I very much enjoyed the time working together with Simon even if the experiments always had a completely different outcome then our hypothesis and I do believe that “Nature” is still waiting for us. I further thank to Andreas Müller (Institute for Molecular and Clinical Immunology, Otto-von-Guericke-University of Magdeburg) for his support in *in vivo* live cell imaging in mice using TPEM and all the constructive and helpful discussions.
I would like to thank Dr. Joop van den Heuvel and Margitta Schürig (Department of Structure and Function of Proteins at the HZI) for the devoted attempt to produce Hemagglutinin.

I would like to further acknowledge our successful corporation with Prof. Dr. Ulrich Kalinke and Veronica Duran from Twincore/Hannover, who welcomed me in their lab, were we conducted together all results for the *ex vivo* experiments and treated me as one of theirs. Veronica helped and supported me in the experimental settings and analysis of the results. We had great discussions and it was always fun working together with her. We enjoyed going to lab even very late in the evening and despite the sometimes not expected experimental results. “Pokemon Go” did not always solved the problems but “what can we do … its science” and we continued working.

I further would highly acknowledge the company CureVac-the RNA people® from Tübingen, who provided us the mRNA-HA used within our studies and additionally to the meaningfully conversations and meetings we had.

9 Acknowledgments

After an intensive period of almost four years, I am delighted to write the last words of my dissertation and gratefully acknowledge many people, who had helped and supported me on this path to successful accomplish this chapter of my life. The list of people to whom I owe to thank is quite long, so that I would like to mention a few of them.

I would like to primarily acknowledge my “Doktorvater” Prof. Dr. Claus-Michael Lehr, who gave me the opportunity to be a member of his department and to work on such a fascinating project taking the public’s attention and involving so many different corporation partners from academic and industrial field, from whom I have gained so much more than just scientific expertise. He has helped me to advance and grow professionally and personally and never failed to forgive me, whenever I had forgotten to inform him about my participation in “Science-Slams”, for which he always supported me. Alongside of him, I am very much thankful to Dr. Brigitta Loretz and her devotion to the project, her never-ending patience, who morally guided me through these tough times. She taught me a lot so that I could improve my scientific expertise, and always had an open door and ear for troubles of scientific but also personal nature. She gave many useful and competent advices and I am very grateful of her very fast working style of revising our manuscripts within a few days.

I further would like to thank to Dr. Sarah Gordon, who additionally supervised me in the first two years. I owe her a big “thank you” for helping me to improve my English, the perfect corrections of the manuscripts, listening to my problems and for her warm hugs, whenever she saw tears slowly welling in my eyes. She never refused to correct my E-Mails before sending away. Our DDEL-department was a cheerful environment full with committed and engaged young-scientists from all over the world and various fields, who continuously taught me something knew and made me loving to come to work. This was not only an excellent working environment but also the place where I met Patrick, a great scientist, my boyfriend, partner and best friend.

The time in Saarbrücken and in our department made me to meet Sara M. and Jing, who grow to be a family for me. Girls, I will never forget your patience with me, for your continuous support, helping hands, wonderful style and travel tips, the very long-

lasting poker nights. Sarah N. joined and broadened our family in my last year and we had great times going out for dinner, trying international food, enjoying coffee or black tea together on our Sunday-meetings. I further thank to my lovely friend Nashravan, who taught me a lot and made my life here in Saarbrucken much easier through her valuable advises, her presence whenever I needed help even in times of huge disagreements, her commitment and engagement in my personal growth. I loved and appreciated the work together with my dear friends and scientific companions Khiet and Xabi, whom I owe big hugs and huge thanks. I enjoyed the time with you of working and joking around in lab. Even when things got serious, you always had a smile and amazing stories to tell. I will never forget our funny sushi dinners and the dream-stories of Khiet, the fantastic political and philosophical discussions with Xabi. Further, I will never forgot the scientific conversations with my friends Olga, Carlos and Cristina, mainly about the next Marvel or Sci-Fi-Movies, the establishment of a journal to publish only negative/failed results and playing with dry-ice. To Karin and Sarah M. and further our technical colleagues Chiara, Jana and Petra my greatest thank for your continuous support during my PhD-period, for your help in solving any upcoming questions of bureaucratic, analytic and cell cultural nature.

I would like to thank Prof. Dr. Alexandra Kiemer for reviewing my thesis, her support and willingless accompany throughout my PhD time.

However, I would have not come so far without the continuous and willingness support of my family and my boyfriend.

Bütün çalişmalarim boyunca arkamda duran, akadamik kariyerime devam etmemde, bana her yönden maddi ve manevi destek çikan, beni hiçbir zaman yalniz birakmayan, yardiminlarini hiç esirgemeyen ailemeye ve özelikle Annem ve Babama sonsuz teşekür borcundayim. Benimle saatlerce telefonda konuşan, destekleyen, en tatli ve büyük fanatiklerim ve bana bir gün nobel ödülü verileceğine inanan kiz ve erkek kardeşlerime çok teşekür ederim.

Zor günlerimde ellerini bana uzatan ve yanimda olan, tezimin başindan sonuna kadar desteklerine esirgemeyen, tezime okuyup gereken düzeltmeleri yapmamda yardimci olan çok değerli arkadaşim Patricke sonsuza kadar teşekür ederim.

THANK YOU ALL! DANKESCHÖN! TEŞEKÜRLER!